

# High-Fidelity Simulation and Analysis of a Floating Offshore Wind Turbine under Extreme Wave and Wind Conditions

A thesis accepted by the Faculty of Aerospace Engineering and Geodesy of the  
University of Stuttgart in partial fulfillment of the requirements for the degree of  
Doctor of Engineering Sciences (Dr.-Ing.)

by

Friedemann Borisade (né Beyer)

born in Stendal, Germany

Main referee: Prof. Dr. Po Wen Cheng  
Co-referee: Prof. Dr. Henrik Bredmose

Date of defence: 21.09.2021

Institute of Aircraft Design  
University of Stuttgart  
2022



# Acknowledgements

Although this acknowledgement is at the very beginning of my dissertation, it cannot be read without relating to the end of this work and the journey I had to take to get to this point. Countless hours of pondering about proper words and shiny graphs, sleepless nights of checking models and progress monitors of simulation tools, and challenging times juggling between family, work and academic research have been a major part of this project. But also enlightening moments of having found a solution to a particular problem, satisfaction at seeing expected but also unexpected outcomes in colourful pictures, and the once in a life opportunity for deep diving into doctoral research shaping my personality and character. With great gratitude I step back and thank all who have supported me in climbing this mountain.

Prof. Dr. Po Wen Cheng, I clearly remember the day when we were talking for the first time about floating wind in a café and my plans for pursuing a doctorate. You have been providing me with the necessary people, tools and project work to build up my research from this moment on. Your openness and input to my ideas have helped me to challenge assumptions and keep focusing on the outcomes. I also thank Prof. Dr. Henrik Bredmose of DTU for providing his academic feedback by reviewing my dissertation and offering fruitful technical discussions at various project meetings and conferences.

It has been a pleasure being part of the team at Stuttgart Wind Energy (SWE). Many former colleagues have contributed to this dissertation with talks on the meaning and impact of this research but also practical tips and tricks for looking for solutions behind the corners. Matthias Kretschmer, you really have been a gift when you supported me as a student and later fellow at the institute by building and running first simulations and reviewing parts of my work. Furthermore, thank you Dr. Matthias Arnold for providing a baseline tool chain I could rely on for this research. Dr. Birger Luhmann, Dr. Frank Lemmer, Florian Haizmann, Dr. Denis Matha, Dr. Ines Würth, Prof. Dr. David Schlipf, Dr. Steffen Raach, Dr. Kolja Müller, Fiona Lüdecke, and others at the SWE, thank you for many enlightening discussions in the past years. Many thanks also to Alexander Schön for his IT support and help in setting up and maintaining simulation clusters at the institute which have allowed me to conduct computationally demanding simulations. Further thanks to all students contributing to this

project and giving me the opportunity to learn and grow as a supervisor. Thanks as well to my colleagues at Ramboll for technical advice on general floating wind topics: Jannis Espelage, Fabian Wendt, Simon Tiedemann and Michael Karch.

Providing this dissertation as open access contribution is a way of acknowledging the public funding this work has received. In particular, the European Commission's Seventh Framework Programme (FP7) has provided partial funding under the grant agreement number 295977 (project acronym: FLOATGEN). BW Ideol being part of the project consortium is acknowledged for supporting this research by supplying experimental data for validation. In particular, many thanks to Thomas Choisnet for his interest in my research, openness in reviewing this work and providing helpful technical comments guiding the evaluation of the results. Special thanks to Dr. Amy Robertson of NREL for discussing about floating wind simulation code comparisons and experimental testing in the IEA Wind OC4 to OC6 projects.

Finally, I thank my wife Tosin for leading the list of supporters. There are no words that can describe my sincere gratitude for your selfless support in backing me up, encouraging me in difficult times and enjoying the fruits of success together. You are the most important but hidden figure behind this research work, and you are what holds this project together like the glue between the following pages. To my children Naemi and Nilaja: You have not only helped me to keep track of the important things in life, such as family, but also inspired me with your endless quest for understanding contexts in your surrounding world. You are true researchers with your continuous, childlike search for answers to why questions. I am also grateful for my family who provided me with mental, physical and spiritual support throughout this research project.

S. D. G.

# Contents

<b>Abbreviations</b>	<b>ix</b>
<b>List of Symbols</b>	<b>xi</b>
<b>Abstract</b>	<b>xv</b>
<b>Kurzfassung</b>	<b>xvii</b>
<b>1 Introduction</b>	<b>1</b>
1.1 Motivation . . . . .	1
1.2 Related Work . . . . .	3
1.2.1 Bottom-fixed Offshore Wind Turbines . . . . .	4
1.2.2 Floating Offshore Wind Turbines . . . . .	5
1.3 Research Objectives and Assumptions . . . . .	7
1.4 Outline . . . . .	10
<b>2 Background and Modelling of Floating Offshore Wind Turbines</b>	<b>13</b>
2.1 Status of Floating Offshore Wind Energy . . . . .	13
2.2 Floating Substructure Concepts . . . . .	14
2.3 Floating-Specific Design Modifications . . . . .	16
2.4 Simulation Techniques for Load Analysis . . . . .	17
2.4.1 Standards and Design Load Cases . . . . .	18
2.4.2 Structural Dynamics . . . . .	19
2.4.3 Aerodynamics . . . . .	21
2.4.4 Hydrodynamics . . . . .	23
2.4.5 Mooring Dynamics . . . . .	29
2.5 Metocean Environment . . . . .	31
2.5.1 Wind . . . . .	31
2.5.2 Regular and Irregular Waves . . . . .	32
2.5.3 Extreme Waves and Wave Focusing . . . . .	35
2.6 Experimental Model Testing . . . . .	37
<b>3 Simulation Environment and Setup</b>	<b>41</b>
3.1 Multibody Approach and Model Topology . . . . .	41
3.1.1 Substructuring of Multibody Model . . . . .	42
3.1.2 Model Degrees of Freedom . . . . .	42

3.1.3	Force Elements . . . . .	43
3.2	Coupling of Multibody and CFD Model . . . . .	45
3.2.1	Motivation . . . . .	45
3.2.2	Coupling Methodology . . . . .	46
3.2.3	Iteration Scheme . . . . .	47
3.2.4	Code Implementation . . . . .	49
3.3	Modelling of Numerical Wave Tank in CFD . . . . .	50
3.3.1	Wave Generation . . . . .	51
3.3.2	Numerical Beach . . . . .	54
3.3.3	Boundary Conditions . . . . .	55
3.3.4	Mesh Properties . . . . .	57
3.3.5	Mesh Deformation . . . . .	58
3.3.6	Initial Conditions . . . . .	62
3.3.7	Additional Solver Settings . . . . .	63
3.4	Sensitivity Analysis in 2D Numerical Wave Tank . . . . .	65
3.4.1	Temporal discretisation . . . . .	66
3.4.2	Spatial discretisation . . . . .	67
3.4.3	Turbulence model . . . . .	68
3.5	Baseline Simulation Procedure . . . . .	69
3.6	Recommended Practices for Modelling . . . . .	73
3.6.1	Simulation Procedure . . . . .	73
3.6.2	Wave Generation and Damping . . . . .	74
3.6.3	Fluid and Solver Settings . . . . .	74
3.6.4	MBS-CFD Coupling . . . . .	75
<b>4</b>	<b>Experiments and Validation</b>	<b>77</b>
4.1	Wave Tank Model Test Setup . . . . .	77
4.1.1	Wave Tank Description . . . . .	78
4.1.2	Model Characteristics and Test Matrix . . . . .	78
4.1.3	Measurements and Sensor Locations . . . . .	79
4.2	Description of Coupled MBS-CFD Model . . . . .	79
4.2.1	MBS Model Topology . . . . .	81
4.2.2	Mooring System Calibration . . . . .	81
4.3	Investigated Load Cases . . . . .	82
4.4	Free-Decay Test . . . . .	83
4.4.1	Procedure for Evaluation of Hydrodynamic Damping . . . . .	84
4.4.2	Pitch Free-Decay . . . . .	86
4.4.3	Heave Free-Decay . . . . .	94
4.4.4	Surge Free-Decay . . . . .	102
4.5	Regular Wave Test . . . . .	106
4.5.1	Discussion of Platform Kinematics . . . . .	108
4.5.2	Discussion of Relative Wave Elevation . . . . .	109
4.5.3	Flow Field Visualisation . . . . .	110
<b>5</b>	<b>Extreme Wave and Wind Conditions</b>	<b>115</b>
5.1	Description of Coupled MBS-CFD Model . . . . .	115
5.1.1	MBS Model Topology for Extreme Wave Conditions . . . . .	117

---

5.1.2	MBS Model Topology for Extreme Wave and Wind Conditions . . . . .	118
5.1.3	Reference Wind Turbine and Reference Site . . . . .	119
5.2	Investigated Load Cases . . . . .	121
5.3	Measurements and Sensor Locations . . . . .	123
5.4	Extreme Wave . . . . .	124
5.4.1	Discussion of Focused Wave Development . . . . .	124
5.4.2	Discussion of Relative Wave Elevation . . . . .	126
5.4.3	Discussion of Platform Kinematics . . . . .	127
5.4.4	Discussion of Integrated Forces on the Structure . . . . .	130
5.4.5	Flow Field Visualisation . . . . .	131
5.4.6	Discussion of Impact of Wave Run-up on Structure . . . . .	136
5.5	Extreme Wave and Wind . . . . .	142
5.5.1	Discussion of Relative Wave Elevation . . . . .	142
5.5.2	Discussion of Platform Kinematics . . . . .	143
5.5.3	Discussion of Integrated Forces on the Structure . . . . .	144
5.5.4	Discussion of Impact of Wave Run-up on Structure . . . . .	144
5.5.5	Discussion of Wind Turbine Motion and Loads . . . . .	145
5.6	Summary and Final Remarks . . . . .	150
<b>6</b>	<b>Conclusions and Outlook</b>	<b>153</b>
6.1	High-Fidelity Simulation Environment . . . . .	153
6.2	Validation by Experiment . . . . .	154
6.3	Extreme Environmental Conditions . . . . .	156
6.4	Recommendations . . . . .	158
<b>A</b>	<b>Appendix</b>	<b>159</b>
A.1	Derivation of Mesh Deformation Transition Function . . . . .	160
A.2	Comparison of Influence of Time Stepping Scheme . . . . .	161
A.3	Maxima and Time of Occurrence for Extreme Wave Analysis . . . . .	163
	<b>Bibliography</b>	<b>165</b>
	<b>Curriculum Vitae</b>	<b>181</b>





# Abbreviations

1P	One-per-revolution
3P	Three-per-revolution
ALS	Accidental Limit State
API	American Petroleum Institute
BEM	Blade Element Momentum
BRF	Body Reference Frame
CCL	CFX Command Language
CEL	CFX Expression Language
CFD	Computational Fluid Dynamics
COB	Centre of Buoyancy
COG	Centre of Gravity
DEL	Damage Equivalent Load
DES	Detached Eddy Simulation
DLC	Design Load Case
DLL	Dynamic Link Library
DLR	German Aerospace Center
DNS	Direct Numerical Simulation
DNV	Det Norske Veritas
DOF	Degree of Freedom
ESS	Extreme Sea State
EWM	Extreme Wind Speed Model
FAST	Fatigue, Aerodynamics, Structures, and Turbulence
FDM	Finite Difference Method
FEM	Finite Element Method
FFT	Fast Fourier Transform
FLOATGEN	Demonstration and benchmarking of a floating wind turbine system for power generation in Atlantic deep waters
FLS	Fatigue Limit State
FMBI	Fluid-Multibody Interaction
FOWT	Floating Offshore Wind Turbine
FSI	Fluid-Structure Interaction
FVM	Finite Volume Method
FVW	Free Vortex Wake
HIL	Hardware-in-the-Loop

---

ID	Identifier
IEA	International Energy Agency
IEC	International Electrotechnical Commission
IFB	Institut für Flugzeugbau (Institute of Aircraft Design)
ISO	International Organization for Standardization
ISYS	Inertial Reference Frame
JONSWAP	Joint North Sea Wave Observation Project
LCT	Load Case Table
LES	Large Eddy Simulation
LIDAR	Light Detection And Ranging
MBS	Multibody System
ME	Morison Equation
MMS	CFX Memory Management System
NB	Numerical Beach
NREL	National Renewable Energy Laboratory
NTM	Normal Turbulence Model
NWP	Normal Wind Profile Model
NWT	Numerical Wave Tank
O&M	Operation and Maintenance
OC3	Offshore Code Comparison Collaboration
OC4	Offshore Code Comparison Collaboration Continuation
OC5	Offshore Code Comparison Collaboration Continuation, with Correlation
OC6	Offshore Code Comparison Collaboration, Continued, with Correlation, and unCertainty
OSS	Offshore Substation
PF	Potential Flow
PM	Pierson-Moskowitz
PSD	Power Spectral Density
QTF	Quadratic Transfer Function
RANS	Reynolds-Averaged Navier-Stokes
RAO	Response Amplitude Operator
RNA	Rotor Nacelle Assembly
SISO	Single-Input-Single-Output
SST	Shear Stress Transport
SWE	Stuttgart Wind Energy
SWL	Still Water Level
TLP	Tension Leg Plattform
TP	Transition Piece
ULS	Ultimate Limit State
URANS	Unsteady Reynolds-Averaged Navier-Stokes
VOF	Volume of Fluid
WINDS	Wake-induced Dynamic Simulator

# List of Symbols

## Greek letters

$\alpha$	Wind shear power law exponent [–]
$\beta$	Wave propagation heading direction [rad]
$\chi$	Yaw rotational displacement [rad]
$\delta$	Damping coefficient [s <sup>-1</sup> ]
$\epsilon$	Phase shift for wave focusing [rad]
$\eta$	Wave elevation [m]
$\lambda$	Wave length [m], tip speed ratio [–], Froude scaling factor [–]
$\Lambda$	Logarithmic decrement [–]
$\nu$	Kinematic viscosity [m <sup>2</sup> s <sup>-1</sup> ]
$\omega$	Angular frequency [rad s <sup>-1</sup> ]
$\Omega$	Rotor speed: angular velocity [rad s <sup>-1</sup> ], displayed as rotational speed [min <sup>-1</sup> ]
$\omega_0$	Undamped natural angular frequency [rad s <sup>-1</sup> ]
$\omega_d$	Damped natural angular frequency [rad s <sup>-1</sup> ]
$\phi$	Roll rotational displacement [rad], wall shear stress [Pa], velocity potential [m <sup>2</sup> s <sup>-1</sup> ]
$\psi$	Pitch rotational displacement [rad]
$\rho$	Volumetric mass density [kg m <sup>-3</sup> ]
$\sigma$	Standard deviation
$\theta$	Phase [rad], rotor blade pitch angle [rad]
$\varphi$	Volume fraction [–], azimuth [rad]

## Roman letters

$a$	Half length of principal longitudinal axis [m]
$A$	Wave amplitude [m], area for force calculation [m <sup>2</sup> ]
$b$	Half length of principal lateral axis [m]
$c$	Half length of principal vertical axis [m]
$C$	Scaling factor for momentum source [m <sup>-1</sup> ]
$C_a$	Added mass coefficient [–]
$C_d$	Drag coefficient [–]
$C_m$	Inertia coefficient [–]
$d$	Water depth [m], damping constant [kg s <sup>-1</sup> ]
$D$	Mesh deformation limiter [–], damping ratio with respect to critical damping [–], diameter [m]
$f$	Function for momentum source calculation of numerical beach [–], frequency [s <sup>-1</sup> ]
$F$	Integrated force on floating substructure [N], Morison force [N]

---

$f_D$	Transition function for mesh deformation [-]
$Fr$	Froude number [-]
$g$	Gravitational acceleration [ $\text{m s}^{-2}$ ]
$h$	Draught or draft of a vessel or floating substructure [m]
$H$	Wave height [m]
$i$	Iteration counter [-]
$k$	Wave number [ $\text{rad m}^{-1}$ ], structural spring stiffness [ $\text{kg s}^{-2}$ ], numerical order of accuracy [-]
$KC$	Keulegan-Carpenter number [-]
$L$	Wave scaling factor [-], length of structure [m]
$m$	Scaling factor for mesh deformation [-], rigid body mass [kg]
$M$	Bending moment [Nm]
$\dot{m}$	Mass flow rate [ $\text{kg s}^{-1}$ ]
$n$	Time step counter [-]
$N$	Number of cells [-], number of spectral amplitudes for wave focusing [-]
$p$	Pressure [Pa]
$r$	Relaxation factor [-], radius [m]
$R$	Ramp function [-]
$Re$	Reynolds number [-]
$S$	Momentum source for numerical beach [ $\text{kg m}^{-2} \text{s}^{-2}$ ], spectral density of wave spectra [ $\text{m}^2 \text{s}$ ]
$t$	Time [s]
$T$	Wave period [s], peak-spectral period of signal [s], kernel function for second-order focused wave [ $\text{m}^{-1}$ ]
$TI$	Turbulence intensity [-]
$t_R$	Time constant for ramp function [s]
$t_{\text{step}}$	Time step size [s]
$u$	Longitudinal velocity in $x$ [ $\text{m s}^{-1}$ ]
$Ur$	Ursell number [-]
$v$	Lateral velocity in $y$ [ $\text{m s}^{-1}$ ]
$V$	Volume [ $\text{m}^3$ ]
$w$	Vertical velocity in $z$ [ $\text{m s}^{-1}$ ]
$x$	Longitudinal coordinate, surge translational displacement [m]
$y$	Lateral coordinate, sway translational displacement [m]
$z$	Vertical coordinate, heave translational displacement [m]

### Subscripts

$(\cdot)_{\text{air}}$	Referring to material properties of air
$(\cdot)_{\text{FS}}$	Referring to full scale
$(\cdot)_{\text{M}}$	Referring to momentum source
$(\cdot)_{\text{MS}}$	Referring to model scale
$(\cdot)_{\text{f}}$	Referring to fluid
$(\cdot)_{\text{hub}}$	Referring to hub
$(\cdot)_{\text{m}}$	Referring to model scale
$(\cdot)_{\text{p}}$	Referring to prototype scale
$(\cdot)_{\text{PTFM}}$	Referring to floating substructure/platform
$(\cdot)_{\text{RBL}}$	Referring to rotor blade

- $(\cdot)_{\text{SWL}}$  Referring to still water level
- $(\cdot)_{\text{TWR}}$  Referring to tower
- $(\cdot)_{\text{water}}$  Referring to material properties of water



# Abstract

The first pre-commercial floating wind farms Hywind Scotland and WindFloat Atlantic demonstrate the technical feasibility of floating wind, while the installed fleet of substructures is still dominated by bottom-fixed foundations. Structural integrity is verified by assessing design load cases. But, especially in extreme conditions and highly transient behaviour, engineering-level simulation models cannot capture all relevant effects. The motivation of the present study is to close the gap between engineering models and experiments by high-fidelity analysis of extreme environmental conditions of a Floating Offshore Wind Turbine (FOWT).

At first, a high-fidelity simulation environment is developed based on a coupled methodology of Multibody System (MBS) (SIMPACT) and Computational Fluid Dynamics (CFD) (ANSYS CFX) solvers. A fully implicit iteration scheme is executed with modules for sending, receiving and translating of loads and deformations. A moderator controls the iteration process. The methodology provides an integrated analysis of a FOWT with consideration of aero- and hydrodynamics, structural dynamics as well as mooring and control system.

A Numerical Wave Tank (NWT) is build in CFD by applying the Volume of Fluid (VOF) approach to assess hydrodynamic loads. Waves are generated at the inlet boundary condition and a Numerical Beach (NB) mitigates wave reflection. Mesh deformations are considered through local deformations calculated by the structural solver. Sensitivity studies on grid resolution, time step size and turbulence model are performed to optimise accuracy and efficiency.

Experimental data from a wave tank model test at a scale of 1:32, conducted in the course of the FLOATGEN project in 2014, are used to validate the simulation approach. Free-decay tests of Ideol's floating substructure in surge, heave and pitch motion are analysed. Moderate settings for grid resolution and time step size are sufficient to accurately predict natural periods. Simulation at model or full scale does not change the results. Heave free-decay is characterised by spectral energy contributions below the natural frequency, caused by the piston mode of the water column inside the moonpool. Small discrepancies in yaw motion during surge free-decay, possibly caused by inaccurate alignment in the experiment, result in underestimation of the natural period by 10%. A regular wave test shows good agreement for the platform kinematics. Hence, second-order wave drift forces are predicted correctly.

One lesson learned is that linear damping is not sufficient to describe the decay of the floating system and additional higher-order terms are needed. However, reliable prediction of hydrodynamic damping is the weak point of the MBS-CFD coupling methodology because the temporal scheme of the fluid solver is limited to first-order discretisation. For higher-order implementations, more than one time step would have to be iterated in the communication to increase the accuracy. However, this cannot be implemented because the internal functions and system calls in the codes are only accessible to a limited extent using user functions.

Finally, extreme wave-only conditions are analysed for a reduced MBS model of the FLOATGEN prototype. Afterwards, complexity is increased and a fully resolved MBS representation of a generic 2.2 MW wind turbine is simulated under extreme wave and wind conditions. Design Load Case (DLC) 6.1 is adapted and a deterministic, phase-focused wave group is generated based on representative metocean conditions with 50-year return period. Design waves are recommended by offshore standards as an alternative to periodic regular waves. A steady Extreme Wind Speed Model (EWM) is used for computation of aerodynamic loads on the flexible rotor by Blade Element Momentum (BEM) theory and wind drag forces on the flexible tower.

Platform surge is highly excited by extreme wave conditions leading to maximum excursions of 75% of the water depth. Significant wave run-up at the Transition Piece (TP) is observed of up to 80% of its height. The additional loading from extreme wind in DLC 6.1 increases the maximum platform surge by 5% and the mean platform pitch by 1°, while the heave is dominated by wave-induced motion. Higher water velocities, surface pressures and wall shear stresses are observed at the TP when extreme wind is taken into account because of a different wave crest development and wave breaking. The tower top experiences higher maximum accelerations of  $4 \text{ m s}^{-2}$  and pitch inclinations up to 14° in incident wave direction compared to the tower base. However, maximum inclinations and accelerations are still within acceptable survival design margins of a barge-type floating substructure.

The results demonstrate that the developed high-fidelity MBS-CFD simulation environment can fill the gap between engineering models and experiments for the design of FOWTs. The methodology provides results, which cannot be obtained from other simulation techniques, such as ringing of the wind turbine after wave slamming, run-up heights along the TP or pressure distributions under extreme conditions. General conclusions for the design of FOWTs are difficult because the design is concept- and site-specific. Wind loads should be included when simulating extreme waves with a high-fidelity method for reliable and conservative prediction of motion and loads. Turbulent wind is not considered, but the EWM is assumed to be conservative because maximum wind speeds during gusts are taken into account. Furthermore, wave impact loads can be smaller compared to bottom-fixed substructures because of the relative movement of the FOWT. More severe excursions, inclinations and accelerations can occur during operational conditions compared to those observed. The simulations show the limitations of the simplified mooring system and it is recommended to implement a dynamic mooring model.



# Kurzfassung

Erste vorkommerzielle Projekte beweisen die technische Machbarkeit schwimmender Offshore-Windparks, wie zum Beispiel Hywind Scotland und WindFloat Atlantic. Jedoch dominieren bodenfeste Fundamente die installierte Anzahl von Substrukturen. Die Bewertung von Entwurfslastfällen ist erforderlich, um die strukturelle Integrität zu verifizieren. Aber insbesondere bei extremen Bedingungen und hohem instationären Verhalten können Ingenieurs simulationsmodelle nicht alle relevanten Effekte erfassen. Daher ist die Motivation dieser Studie, die Lücke zu schließen zwischen Ingenieurmodellen und Experimenten durch eine hochaufgelöste Analyse extremer Umweltbedingungen bei einer schwimmenden Offshore-Windenergieanlage.

Zuerst wird auf der Grundlage einer gekoppelten Methodik von MBS- (SIMPACK) und CFD-Lösern (ANSYS CFX) eine hochaufgelöste Simulationsumgebung entwickelt. Ein vollständig implizites Iterationsschema wird angewandt. Die Methodik ermöglicht eine integrierte Analyse unter Berücksichtigung von Aero-, Hydro- und Strukturmechanik sowie Vertäuungs- und Steuerungssystem.

Zur Beurteilung der hydrodynamischen Belastungen wird ein numerischer Wellentank unter Anwendung des VOF-Ansatzes in CFD aufgebaut. An der Einlassrandbedingung werden Wellen erzeugt und ein numerischer Strand dämpft die Wellenreflexion. Netzdeformationen werden durch lokale Verformungen, die vom Strukturlöser berechnet werden, berücksichtigt. Sensitivitätsstudien zur Gitterauflösung, Zeitschrittgröße und zum Turbulenzmodell werden zur Optimierung von Genauigkeit und Effizienz durchgeführt.

Um den Simulationsansatz zu validieren, werden experimentelle Daten aus einem Wellentankmodellversuch des FLOATGEN-Projekts im Maßstab 1:32 verwendet. Das freie Abklingverhalten bei der Längs-, Tauch- und Stampfbewegung wird analysiert. Moderate Einstellungen für die Gitterauflösung und die Zeitschrittweite reichen aus, um Eigenperioden genau vorherzusagen. Die Abbildung im Modell- oder Vollmaßstab ändert die Ergebnisse nicht. Die Tauchbewegung wird durch die Kolbenmode der Wassersäule im Inneren des Moonpools beeinflusst. Die Eigenperiode der Längsbewegung wird um 10% unterschätzt, vermutlich verursacht durch eine ungenaue Ausrichtung im Experiment. Die Übereinstimmung bei regulärem Seegang ist gut. Daher werden Wellen-Driftkräfte korrekt vorhergesagt.

Eine Erkenntnis ist, dass Dämpfungsterme höherer Ordnung notwendig sind, um den Abklingvorgang des schwimmenden Systems zu beschreiben. Eine zuverlässige Vorhersage der hydrodynamischen Dämpfung ist jedoch der Schwachpunkt der MBS-CFD-Kopplung, da der Fluid-Löser auf eine zeitliche Diskretisierung erster Ordnung beschränkt ist. Bei Implementierungen höherer Ordnung müssten in der Kommunikation mehr als ein Zeitschritt iteriert werden, um die Genauigkeit zu erhöhen. Dies ist jedoch nicht realisierbar, da die internen Funktionen und Systemaufrufe in den Codes nur eingeschränkt zugänglich sind.

Zum Abschluss der Arbeit wird ein reduziertes MBS-Modell des FLOATGEN-Prototyps extremen Wellenbedingungen ausgesetzt. Danach wird die Komplexität erhöht. Eine generische 2.2 MW Windturbine mit voll aufgelöster MBS-Typologie unterliegt extremen Wellen- und Windbedingungen. DLC 6.1 wird angepasst und eine deterministische, phasen-fokussierte Wellengruppe in CFD generiert, basierend auf repräsentativen Metocean-Bedingungen mit 50 Jahren Wiederholungszeitraum. Ein stationäres Extremwindmodell wird zur Berechnung der aerodynamischen Lasten auf den flexiblen Rotor nach der BEM-Theorie und der Widerstandskräfte des Windes auf den flexiblen Turm verwendet.

Die Längsbewegung der Plattform erreicht durch extreme Wellen maximale Auslenkungen von 75 % der Wassertiefe. Am Übergangsstück wird ein signifikanter Wellenhochlauf bis zu 80 % der Höhe beobachtet. Die Windlasten in DLC 6.1 erhöhen die maximale horizontale Auslenkung um 5 % und die mittlere Krängung um die Stampfachse um 1°. Höhere Wassergeschwindigkeiten, Oberflächendrücke und Wandschubspannungen werden am Übergangsstück unter extremen Wellen- und Windbedingungen durch Unterschiede bei der Wellenbrechung verursacht. Die maximalen Beschleunigungen mit  $4 \text{ m s}^{-2}$  und Neigungswinkel bis zu 14° sind an der Turmkopf höher als am Turmfuß. Die Werte liegen jedoch innerhalb zulässiger Designgrenzen.

Die Ergebnisse zeigen, dass die entwickelte hochaufgelöste MBS-CFD Simulationsumgebung die Lücke zwischen Ingenieurmodellen und Experimenten für den Entwurf von schwimmenden Offshore-Windenergieanlagen schließen kann. Die Methodik liefert Ergebnisse, die mit anderen Simulationstechniken nicht erzielt werden können, wie z.B. das Ringen der Windturbine nach einem Welleneinschlag, Wellenhochlauf entlang des Übergangsstück oder Druckverteilungen unter extremen Bedingungen. Allgemeine Schlussfolgerungen für das Design von schwimmenden Offshore-Windenergieanlagen sind schwierig, da das Design konzept- und standortspezifisch ist. Windlasten sollten bei der hochaufgelösten Simulation extremer Wellen zur zuverlässigen und konservativen Vorhersage von Bewegungen und Lasten berücksichtigt werden. Turbulenter Wind wird nicht untersucht, aber das verwendete Extremwindmodell wird als konservativ angenommen, weil maximale Windgeschwindigkeiten von Böen berücksichtigt werden. Die Lasten beim Welleneinschlag können aufgrund der Relativbewegung der Plattform im Vergleich zu bodenfesten Substrukturen kleiner sein. Im Betrieb können auch größere Auslenkungen, Neigungen und Beschleunigungen auftreten als in dieser Studie beobachtet. Die Simulationen zeigen die Grenzen des vereinfachten Vertäuungssystems. Ein dynamisches Modell wird empfohlen.

# 1

## Introduction

This study is introduced by first describing its motivation in Section 1.1, following by highlighting related work and research in Section 1.2. Based on this, the main research question and associated objectives and assumptions are formulated in Section 1.3. The Chapter concludes by addressing the outline of this dissertation in Section 1.4.

### 1.1 Motivation

In recent years offshore wind became an emerging and mature technology to deliver renewable energy to millions of people around the world. In order to meet national and international climate targets for reduction of carbon dioxide, renewable energy, especially from offshore wind, is an important enabler. On the one side this is justified by an immense energy potential from offshore wind resources. On the other hand cost of energy is dropping due to industrialisation and optimisation. As a result, first offshore wind farms are built and operated without subsidies, such as Vattenfalls' Hollandse Kust Zuid offshore wind project. Bottom-fixed foundations are dominating the installed fleet of substructures with monopiles representing a share of 81.0% according to statistical analysis of grid-connected offshore wind turbines in Europe at the end of 2019 [1]. Jackets with a share of 8.9% and gravity base foundations with a share of 5.7% only rank second and third place by a considerable margin to monopiles. The average water depth for European offshore wind farms under construction in 2019 was 33.0 m, an increase from 2018 with 27.1 m [2]. Currently, floating offshore wind represents only a marginal share of installed substructures, even though vast amounts of offshore wind resources are available in deep waters, which are economically unattractive for bottom-fixed concepts. For example, two

thirds of the North Sea are characterised by water depths between 50 m and 220 m [3] based on the European research project ORECCA [4]. Operation of the first pre-commercial floating offshore wind farm Hywind Scotland did not start until 2017. Based on the lack of shallow water sites worldwide, upcoming commercial auctions, for instance in France and California (USA), demonstrate the global tendency to deliver several Gigawatts of energy from floating wind within the next decade [5, 6]. The technology gains momentum through industrialisation [7] after pilot floating offshore wind projects were realised recently and benefits from global trends to increase the share of renewable energy.

One of the key challenge for technical optimisation of design is the development, validation and improvement of numerical modelling tools [3], which are capable of simulating the floating system, which represents the floating substructure, the tower and the Rotor Nacelle Assembly (RNA). Common practise for design is the application of an integrated methodology, which accounts for aero- and hydrodynamics, structural dynamics and effects of control and mooring system and is required by international offshore wind design standards, such as IEC 61400-3-1 [8]. Although computation performance is increasing rapidly, also because of recent developments in high performance and cloud computing, designers still need to choose between the accuracy of available computation methods and their associated efficiency. Usually hundreds and thousands of design load cases need to be calculated and assessed during multiple simulation loops in order to predict design load effects and verify structural integrity.

Especially in extreme conditions and highly transient behaviour of the floating system, state-of-the-art simulation models cannot capture all relevant effects as explained, for example, in the European LIFES50+ research initiative by [9], [10] or [11]. Advanced tools are needed to close the gap and minimise design risks and uncertainties. This task, among others, was also addressed within the European research and demonstration project FLOATGEN (grant agreement no: 295977, project full title: *Demonstration and benchmarking of a floating wind turbine system for power generation in Atlantic deep waters*), which concluded with the installation of a 2 MW Floating Offshore Wind Turbine (FOWT) prototype at the SEM-REV offshore test site, 20 km off the coast from Le Croisic, France, in April 2018 as shown in Figure 1.1. The mooring lines were pre-laid in July 2017. During the subsequent operational campaign, the floating system experienced extreme environmental conditions with waves up to 12.5 m maximum height, measured in the second half of 2019<sup>1</sup>.

---

<sup>1</sup>Press release by Ideol from January 14<sup>th</sup>, 2020:  
floatgen-achieves-total-6-gwh-power-production-2019

<https://floatgen.eu/en/actualites/>

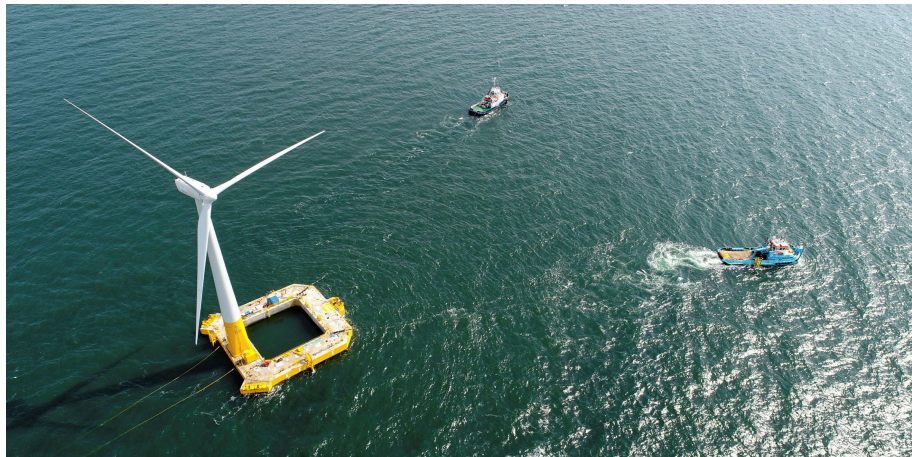


**Figure 1.1:** Tow-off of the FLOATGEN prototype to the offshore test site SEM-REV, 20 km off the city of Le Croisic, France, in April 2018 using tug boats. [source: Ideol]

## 1.2 Related Work

This dissertation describes the development, validation and application of a high-fidelity simulation environment for analysis of extreme wave and wind conditions of FOWTs. In the following, the term high-fidelity refers to the application of Computational Fluid Dynamics (CFD) methods for numerical studies.

Only a limited amount of hydrodynamic analyses on loads and dynamics of FOWTs using CFD modelling techniques were published in research. In industry, the methodology is only used to a very small extent for special problems, mainly because of the high computing costs and resource demands. For example, the engineering consultancy Ramboll applied the Numerical Wave Tank (NWT) approach in CFD for optimisation of monopile substructures for offshore wind farms<sup>2</sup>. Floating substructures possess additional Degrees of Freedom (DOFs) compared to their bottom-fixed counterparts. Thus, the modelling is even more complex and the transient behaviour more pronounced. This is also a reason for the limited use of CFD in the relatively young history of floating wind industry. More advances in CFD for offshore wind in academia with a focus on aerodynamics is presented in [12, 13].

---

<sup>2</sup>Article by Søren Juel Petersen and Ronnie Refstrup Pedersen from May 15<sup>th</sup>, 2018: <https://ramboll.com/ingenuity/smarter-calculations-new-new>

### 1.2.1 Bottom-fixed Offshore Wind Turbines

The potential of CFD calculations to predict wave impact loads on bottom-fixed support structures for offshore wind turbines, such as monopiles, was studied by Bredmose and Jacobsen [14] or Ghadirian et al. [15]. The Volume of Fluid (VOF) approach is applied using OpenFOAM and breaking waves are generated using a second-order focused wave group technique. It is based on linear superposition and phasing of wave components in order to create a breaking wave at a specific focus location and instance in time. Impact loads from the vertical wave run-up flow on a horizontal inspection platform are investigated for five different platform levels. Results show slamming pressure from the overturning wave front and wave run-up at the rigid monopile substructure. Semi-empirical Morison equation only provides good load estimates on monopiles for non-breaking waves of moderate amplitude but cannot estimate impact loads for the presented case as the vertical loads are generated from wave-structure interaction. In addition, vertical impacts may excite structural ringing at high frequencies because of their short-duration contributions to the overturning moment and in-line force. Bredmose concluded that an accurate prediction of vertical loads is very important for the design. Related to this research, Paulsen et al. [16, 17] presented results of the impact of two-dimensional irregular waves on a bottom-fixed circular cylinder. CFD calculations using OpenFOAM are validated against experimental results. Both the free surface elevation and the inline force can be accurately predicted using CFD. Paulsen showed that good load estimates can also be achieved for moderately steep irregular waves using Morison equation in combination with a non-linear two-dimensional potential flow solver. For near-breaking waves, however, the inline force at the monopile is more accurately predicted with the CFD solver.

A comparison of experimental model tests at  $1/12^{\text{th}}$  scale and numerical simulations using the CFD solver ANSYS CFX was described by Hildebrandt [18] for a bottom-fixed tripod substructure. Wave breaking is achieved in the experimental setup by a sloped seabed and different load cases are investigated for a broken wave, curled wave front and partly vertical wave front. A two-dimensional NWT without substructure reproduces the physical wave propagation from the wave maker until breaking. This procedure can save computational resource by extracting the velocity profile of the fluid at a location shortly before wave breaking occurs and implementing it as boundary condition in the three-dimensional CFD domain with a tripod model. Hildebrandt found a good agreement between numerical and experimental results and compared derived slamming coefficients to the load calculations based on guidelines. With decreasing distance of wave breaking in front of the tripod, an increase of local peak forces and associated peak locations is observed. In addition, the difference between the external line forces and impact pressures is highlighted because the line force takes the complete pressure field of the circumference into account. Thus, the maximum force does not necessarily occur at the same instance in time as the maximum impact pressure.

### 1.2.2 Floating Offshore Wind Turbines

A generic floating wind turbine system based on a spar-buoy substructure was analysed in [19] with a coupled methodology involving solvers for Multibody System (MBS) and CFD. Results show the shedding of three-dimensional vortices along the depth of the structure and their influence on the platform pitch motion. It is found that even for a very simple free-decay test in surge direction, differences to the state-of-the-art hydrodynamic methods based on potential flow theory are noticeable. The findings demonstrate that a correlation between simulation techniques applying different levels of modelling fidelity is not achieved easily because results depend on numerical parameters, which need to be assessed and validated during experimental tests. For example, for the CFD method, the temporal and spatial discretisation, the applied turbulence model and other solver settings affect the simulation results. Potential flow methods rely heavily on hydrodynamic coefficients, determined by experiment, for additional consideration of the viscous drag using Morison's equation [20]. Furthermore, the drag coefficients are usually distributed along submerged sectional elements of a floating substructure, but are set to a fixed value for Design Load Cases (DLCs) after model testing or literature research. However, this is a simplification as the drag force is a function of the geometry and flow regime, which are load case dependent [21–23].

As part of this research, a barge-type floating substructure was analysed at 1/32<sup>th</sup> model scale in regular waves and compared to experimental data [24,25]. Different geometries of the mooring foundation and the associated impact on platform motion are investigated, showing effects on the pitch response. In general, global motion of the floating substructure are predicted by the coupled MBS-CFD methodology with only small discrepancies to the experimental results. The same methodology was applied to the substructure of the LIFES50+ Nautilus-DTU10 [26] in [10] for forced oscillation tests and free-decay in heave. The solution of the linear radiation problem in potential-flow theory provides good results for the added mass of a floating substructure over a wide range of oscillation frequencies. Heave added mass values from forced oscillations using MBS-CFD are calculated with good agreement to the potential flow results. However, the magnitude of radiation damping in heave direction, calculated by the potential-flow solution, is considerably smaller than the magnitude of viscous damping in the MBS-CFD results. As flow velocities increase for higher oscillation frequencies and constant amplitude viscous effects become more and more relevant.

A code-to-code comparison was shown by Benitz [27] for the Offshore Code Comparison Collaboration Continuation (OC4) DeepCwind semi-submersible [28]. The floating substructure is modelled in CFD using OpenFOAM and the hydrodynamic loads are compared to those assessed by the potential flow theory and Morison's equation, in order to explain discrepancies between different engineering tools and experimental data. Current-only, wave-only and free-decay load cases are simulated for the substructure at 1/50<sup>th</sup> model scale. Three grid variations

with approximately three million cells are compared with the full geometry, small components only and large components only. For current-only cases, the platform is fixed in space and engineering tools predicted larger drag forces than shown by CFD. Combined effects of a free surface, a free end and the multiple member arrangement were analysed. Differences in load predictions are found due to the transverse forces from vortex shedding and shadowing effects of downstream floater members, which are inherently simulated in CFD. These effects are not captured by the solutions obtained using potential flow theory and the Morison's equation. In addition, predictions of drag coefficients differ if calculations are performed at model and full scale because of a mismatch of the Reynolds number. Benitz's study emphasises that the geometry impacts the load predictions significantly and a careful selection of input parameters for engineering tools is required. Simulation results for wave-only conditions with a stationary substructure show a better agreement between engineering models and high-fidelity CFD method than for current-only. This is explained by the fact that wave loads on a fixed platform are dominated by diffraction, which is captured well by the panel method, and the drag forces from Morison's equation are almost negligible. In conclusion, load predictions are less sensitive to poorly chosen drag coefficients for wave-only loads cases of a stationary substructure. At last, free-decay tests of the semi-submersible are analysed for the pitch and the heave DOF and the results show a good agreement with the experimental data for the platform pitch. However, the heave motion in CFD is highly impacted by the choice of Fluid-Structure Interaction (FSI) numerical coupling method. This is also found for regular wave cases because the mean position about which the body oscillates is not correct using loose coupling between fluid and structural solvers, while the frequency and magnitude of the oscillation is consistent to engineering tools. Numerical instability from artificial added mass from weakly coupled FSI solvers was also seen by Sarlark et al. [10, 29, 30] using OpenFOAM and the LIFES50+ OO-Star Wind Floater Semi 10 MW [26]. Free-decay simulations of the substructure are performed and compared to an engineering model. Loads on a free-floating and moored platform are investigated and a good agreement is found for the natural period and the damping value.

Furthermore, Dunbar et al. [31] carried out an analysis based on tightly coupled solvers using OpenFOAM to eliminate the artificial added mass instability. Dunbar validated his approach with a benchmark case. Results using both translational and rotational motion for the Deep-Cwind semisubmersible platform show good agreement with engineering models.

Other researchers, for instance Quallen et al. [32], modelled both aero- and hydrodynamics of a 5 MW FOWT on a spar-buoy substructure with a single Unsteady Reynolds-Averaged Navier-Stokes (URANS) CFD solver using 5.75 million grid nodes in the computational domain. A comparison is presented against numerical data from free-decay and wave-only tests of the Offshore Code Comparison Collaboration (OC3) Phase IV campaign [33] using engineering tools. Results show differences between predicted natural periods of state-of-the-art methods and high-fidelity simulations, originating from different restoring forces from the mooring lines.



Also, predicted surge amplitudes are considerably smaller compared to the OC3 Phase IV results (load case 4.1 in Table 17 [33]), while frequencies and mean values are similar.

The Offshore Code Comparison Collaboration, Continued, with Correlation, and unCertainty (OC6) project was started in 2019 under the framework of International Energy Agency (IEA) Task 30 and investigates the under-prediction of the loads and motion response of a semi-submersible floating substructure at its surge and pitch natural period by engineering tools. It was demonstrated in the preceding Offshore Code Comparison Collaboration Continuation, with Correlation (OC5) project [34] that the underestimation in the low-frequency region outside the linear wave excitation originates from non-linear hydrodynamic loading. This is created by the interaction of wave components at the sum and difference frequency components. Two model test campaigns were conducted to assess the different contributions from diffraction and radiation to non-linear hydrodynamics by towing tests, forced oscillations and regular and irregular waves with a fixed configuration. It is found that approaches, such as second-order potential flow solutions with a quadratic-transfer function, improve the modelling of the excitation outside the linear wave excitation region. In addition, tuning of the drag coefficients to account for flow acceleration around the bottom of the platform is critical to obtain the appropriate pitch moment [35]. A group working on high-fidelity CFD solutions joined the project to improve the understanding of discovered discrepancies [36].

Recently, the Innovative Training Network (ITN) FLOAWER (project full title: *FLOAting Wind Energy netwoRk*) received funding under the Horizon 2020 work programme Marie Skłodowska-Curie actions (MSCA) with the scope to design better performing, economically viable floating wind turbines. One of the researchers in FLOAWER will focus on determination of wave load and load effects for floating wind turbine hulls subjected to severe wave conditions applying validated high-fidelity simulation models.

### 1.3 Research Objectives and Assumptions

Based on the motivation described above and the review of related studies, knowledge gaps are identified. They are converted into research questions and objectives to be addressed in this research.

## Objectives

Advanced tools are needed to capture the relevant effects in extreme conditions. High-fidelity simulation techniques based on CFD methods were applied to bottom-fixed substructures for analysis of extreme and breaking waves. For FOWTs, researchers applied CFD to gain a better understanding of the differences between engineering-level design tools and experimental data by focusing on the load cases: current-only, waves-only, combined wind and waves, forced oscillations, etc. Extreme events can generate design driving loads, for example during storm periods as shown exemplary in Figure 1.2, but their analysis with CFD is not mature in the research of FOWTs.



**Figure 1.2:** Image of the FLOATGEN demonstrator, recorded from the tower, during a winter storm on December 22<sup>nd</sup>, 2019. [source: Ideol]

On this basis the main research question is formulated as follows:

**How do extreme environmental conditions influence the system response of a FOWT and how can it be captured accurately using a high-fidelity simulation environment?**

This question shall be answered by addressing the following objectives:

1. **Development** of an **integrated, high-fidelity simulation environment** which is capable of modelling a FOWT system in combined extreme wave and wind conditions and predicting the response and behaviour of the FOWT.
2. **Validation** of the developed methodology using **experimental data** obtained from a model scale wave basin test.
3. **Application** of the simulation environment in order to assess the **loads and motion response from extreme wave and wind conditions** on a FOWT. Evaluation of differences between wave-only and combined wind and wave environmental conditions.

4. **Analysis of the results** to provide recommended practices and general conclusions. Review the limits of applicability of the proposed methodology and definition of future research needs.

## Assumptions

Assumptions and simplifications are made to limit the scope of this research and reduce the number of influencing parameters. Thus, possible variations are narrowed down and the computational efforts are limited to an acceptable level.

First, this research relies on a simulation environment based on coupled MBS and CFD solvers. High-fidelity CFD calculations are only performed to assess hydrodynamic loads on the floating substructure in order to limit the computational grid. Much more resources are needed to consider also the aerodynamic loads on the wind turbine rotor using CFD. Thus, wind loads on the rotor are calculated using Blade Element Momentum (BEM) theory with correction models. Tower wind loads are modelled using a simplified approach based on drag forces on sectional elements. In summary, a combination of engineering and high-fidelity models is applied.

Symmetry of the analysed floating substructure in lateral direction (coordinate  $y$ ) is exploited in the CFD mesh, which further reduces the number of cells and the computational effort. However, this simplification implies that wave propagation is limited to a single heading direction towards the positive longitudinal coordinate  $x$ .

As discussed in the course of this dissertation, the CFD solver is restricted to first-order time stepping scheme within the MBS-CFD coupling methodology. This results in higher numerical damping than for higher-order temporal discretisations. The effect is quantified in this study and can only be partially mitigated by increased temporal and spatial resolution.

In addition, the rigid body DOFs of the platform are limited to account only for surge and heave translational displacement as well as pitch rotational displacement. Thus, sway, roll and yaw motion are neglected. The substructure is modelled as rigid, although in principle the structural flexibility of the floating substructure can be included as demonstrated in [37] for the analysis of fluid-structure interaction on tidal current turbines. A rigid model is justified because floating substructures are either made of massive reinforced concrete and/or stiffened steel plates with high structural stiffness as in shipbuilding. A detailed finite element analysis is usually part of the design process and out of scope of this study. Furthermore, structural data to build a detailed finite element model were not available here. Further reduction of the number of DOFs is done in the MBS model by combination of all wind turbine bodies as a lumped mass. A fully resolved setup with separate MBS bodies for rotor blades, hub, nacelle, tower and floating substructure is only applied for the analysis of combined extreme wave and wind conditions.

In order to put the focus on analysis of high-fidelity modelling of hydrodynamics, the mooring system is simplified and represented in MBS by a global linear stiffness matrix derived from experiment. This assumption introduces inaccuracies especially at extreme conditions when non-linear effects become relevant. However, the as-designed or as-built mooring system of the FLOATGEN prototype was not available in this study.

This study is closely linked to the tasks in the European research and demonstration project FLOATGEN. Therefore, only the barge-type floating substructure designed by Ideol is studied. Extreme environmental conditions with a return period of 50 years based on metocean data of the SEM-REV offshore test site are used for the study, as well as recommendations from design standards. Irregular waves are not examined because their analysis relies on statistically relevant timescales, which requires very long run times of several weeks with the applied MBS-CFD simulation environment. Furthermore, effects of current, tides, marine growth etc. are not addressed here.

Due to the lack of public and suitable measurements for the considered floating substructure under extreme wave and wind conditions, results of the proposed test case are presented and discussed solely for the numerical simulation. However, experimental data of a model scale test are used to validate the simulation methodology for loads and motion response of free-decay and regular wave tests. Finally, the wind turbine is assumed to be in idling mode without any controller action, meaning that the rotor is idling and a fixed blade pitch angle of  $90^\circ$  is set as initial condition. This assumption is valid because the cut-out wind speed is usually  $25 \text{ m s}^{-1}$ , which is significantly lower than the extreme wind conditions analysed here.

## 1.4 Outline

For addressing the above defined research questions and objectives, this study is structured as follows. At first, background information is given on FOWTs and currently applied simulation techniques for load analysis in Chapter 2.

This is the basis for the subsequent development of a simulation environment based on a coupling between MBS and CFD solvers in Chapter 3. In addition, a two-dimensional NWT is setup and a sensitivity analysis is presented with respect to numerical parameters, such as grid spacing, temporal resolution and turbulence modelling. A description of the applied simulation procedure and recommended practices for modelling of a NWT completes the Chapter.

In the next step, the coupled MBS-CFD simulation environment is validated in Chapter 4 using experimental data from a model scale test in a wave basin. The influence of mesh discretisation, scaling factor, time step size and initial conditions is investigated for free-decay tests for the platform pitch, heave and surge motion. A special focus is put on the evaluation of natural periods and the damping behaviour of the high-fidelity numerical solution. Flow field visualisations show predominant characteristics of fluid velocity and vortex shedding to facilitate the

---

understanding of the findings. The validation concludes with the presentation of a regular wave test and discussion of computed platform kinematics and relative wave elevations around the floating substructure.

The assessment of loads and motion response under extreme conditions is discussed in Chapter 5. Therein, differences between the MBS model topology of load cases for extreme wave-only and combined extreme wave and wind conditions are analysed. The simulation results of extreme wave impact on the floating system are studied by analysing platform kinematics, relative wave elevations, integrated forces on the structure and effects of wave run-up. Visualisations of the flow field during wave impact are provided for illustration purpose and to support the discussion. Subsequently, combined extreme wave and wind conditions are evaluated and differences to the previously described wave-only case are highlighted.

This dissertation concludes with major findings, final remarks, recommendations and future research needs from the author's opinion in Chapter 6.



# 2

## Background and Modelling of Floating Offshore Wind Turbines

After introducing the main research question, focus is drawn in this Chapter on the background. At first, a summary of the current status of floating offshore wind energy is presented in Section 2.1 before a categorisation of floating substructures is introduced in Section 2.2. Afterwards, common modelling techniques for load case simulations are addressed in Section 2.4. The metocean environment with wind and waves is covered in Section 2.5 and the experimental model testing is explained in Section 2.6.

### 2.1 Status of Floating Offshore Wind Energy

Hywind Scotland was the first pre-commercial floating offshore wind farm, installed 29 km east off Peterhead, Scotland, in 2017. Five units of Siemens SWT-6.0-154 wind turbines with a total capacity of 30 MW are attached to Equinor's Hywind spar floating substructure and moored at a water depth between 95 to 120 m [38]. The project represents a further development of the 2.3 MW Hywind demonstrator from 2009 [39, 40]. The second pre-commercial floating offshore wind farm WindFloat Atlantic, located 20 km off the coast from Viana do Castelo, Portugal, was installed in 2019/2020 with a higher rated capacity and is based on a different substructure concept. It comprises three MHI Vestas V164-8.4 MW wind turbines with Principle Power's three-column semi-submersible substructure at 100 m water depth. Similar to Hywind, the WindFloat concept was verified by a pilot project, which started in 2011 with a 2 MW demonstrator and was operational for five years [41].

France’s first offshore wind turbine FLOATGEN was installed at 32m water depth at the SEM-REV offshore test site, located 20 km off the coast from Le Croisic, France, in 2018. It is a barge-type floating substructure designed by Ideol and equipped with a Vestas V80-2.0 MW, see Figure 1.1. The project was partially funded by the European Commission and this dissertation is based on the research carried out by the author in the FLOATGEN project. Choisnet et al. presented the barge-type floating substructure made of concrete in [42] and compared the FLOATGEN design to a steel hull of comparable shape and displacement in [43]. Significantly more ballast is needed in operation because the steel structure is much lighter, so that half of the compartments of the platform are filled with sea water. More recently, Choisnet et al. [44, 45] demonstrated a stepwise validation of innovations introduced in the FLOATGEN prototype, for example the hybrid mooring lines with a chain-polyamide-chain setup. In addition, a code-to-code verification of two coupled analysis approaches with focus on the platform modelling was shown by [46], whereas Jestin et al. [47] highlighted the design and construction process of the concrete hull of FLOATGEN. Courbois et al. [48] studied the wave drift loads of Ideol’s substructure concept and compared numerical results from OpenFOAM with wave canal tests. A general overview of floating wind technologies and projects is presented in [49–52].

## 2.2 Floating Substructure Concepts

One approach to categorise floating substructures on a conceptual level is based on how stability is achieved. One can generally distinguish between three basic concepts, buoyancy-, ballast- and mooring-stabilised systems. An illustration of general platform concepts is presented in Figure 2.1.

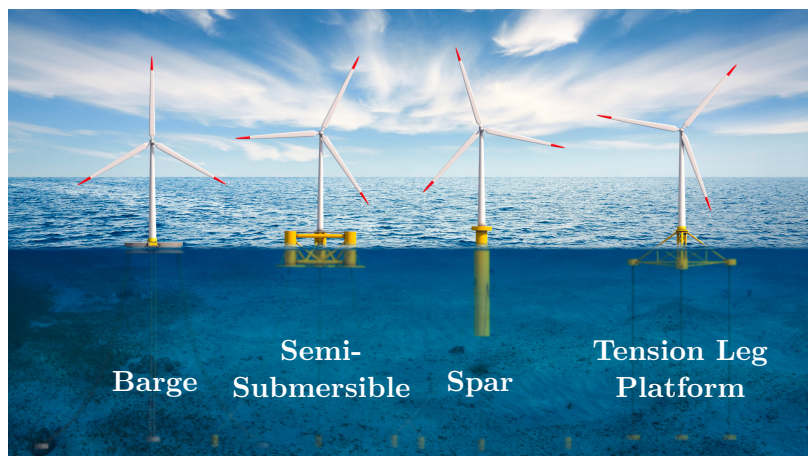


**Figure 2.1:** Illustration of general floating substructure concepts. [modified from: WindEurope [53]]

In the following principal design concepts of FOWTs are introduced together with a description of the major advantages and drawbacks. In this dissertation, a barge-type floating substructure is analysed in details.



1. **Barge:** Barge-type concepts are characterised by large rectangular or cylindrical structures with low draft, which results in higher sensitivity to wave excitation around the heave, pitch and roll natural frequencies. Large waterplane area and area moment of inertia of the buoyancy-stabilised system provide the hydrostatic restoring forces and moments. However, natural periods are usually within the main wave excitation region so that additional hydrodynamic and viscous damping must be generated by geometric measures, such as a moonpool and/or skirt, to mitigate the motions. Barges scale up favourably and are advantageous in terms of quayside assembly operations with small water depths.
2. **Spar:** Substructures of type spar consist of a slender, cylindrical structure of large draft and small waterplane area, which makes them less sensitive to the wave excitation. Hydrostatic restoring forces are created by large gravitational forces acting at the Centre of Gravity (COG), which is located below the Centre of Buoyancy (COB) due to the additional ballast at the bottom of the structure. They are not suitable for shallow water sites and impose substantial draft restrictions for turbine integration inshore. One of the drawbacks is the lower platform yaw stiffness, which is partially compensated by mooring lines with delta connections.
3. **Semi-Submersible:** Semi-submersibles represent a hybrid concept, because they receive hydrostatic stability from both buoyancy and gravity due to large waterplane area and area moment of inertia and low COG. Designs vary from three to four columns of cylindrical or rectangular shape with centric or eccentric arrangement of the wind turbine. One of the columns supports the tower and RNA and pontoons or bracings are used to connect columns with each other. Semi-submersibles are characterised by a large total displacement and a draft in between barges and spars of comparable rating. The Transition Piece (TP) and joints are more complex, thus, fatigue of the structure requires special attention during the design. Active ballast systems may adjust the quasi-static platform pitch depending on the rotor thrust.
4. **Tension Leg Platform:** A Tension Leg Platform (TLP) is a mooring-stabilised concept with taut mooring lines. The substructure with excess buoyancy is held under a large pre-tension of the tendon system, which transfers loads to the anchors and has a vertical or inclined arrangement. The hull shape comprises either a column with cantilevered pontoons or a lattice structure. Compared to other concepts, TLPs are lighter and have a smaller total displacement. Depending on the tendon system, slack events are prevented and individual DOFs are restricted with comparable motion characteristic in vertical direction as bottom-fixed foundations. Also wave excitation is lower and the system eigenfrequencies are usually above the wave frequency range. However, hy-

drostatic restoring stiffness is much smaller compared to the mooring restoring stiffness, which makes tow-out and installation more complex for TLPs because of increased risks associated with stability.

5. **Suspended Counterweight Concept:** Finally, suspended counterweight concepts recently gained more interest in the industry, for example the TetraSpar concept by Stiesdal Offshore Technologies A/S [54–57] – a 3.6 MW prototype is planned for installation in 2020. It represents a ballast-stabilised concept with the COG much lower than the COB similar to a spar. In contrast, the deep COG does not originate from ballast at the bottom but by a counterweight, which is suspended by tendons and introduces additional challenges and risks. The design of the top structure usually resembles slender semi-submersibles or TLPs and is designed for mass production. Dynamic behaviour is similar to spar concepts but with the possibility for an easy turbine installation at quayside. However, installation is more complex than for barges and semi-submersible due to the suspension process of the counterweight.

## 2.3 Floating-Specific Design Modifications

Floating-specific design modifications are necessary, in particular for the tower because compared to bottom-fixed wind turbines, additional rigid body motions of the floating substructure increase the loads. Furthermore, the tower support changes to a free-free boundary condition because the representation of a one-mass oscillator with a fixed tower base and free tower top mass is modified to a two-mass oscillator with a system of two free masses – RNA and floating substructure. A floating system cannot be characterised by a one-mass oscillator with decreased soil stiffness, which in principle would lead to a decrease in the structural eigenfrequencies, because the stiffness from the mooring system and hydrostatics is several magnitudes of order smaller than the soil stiffness for bottom-fixed foundations. However, if a standard soft-stiff offshore tower design is applied to a floating system, the first eigenfrequency of the tower fore-aft mode is moved from the One-per-revolution (1P) to the Three-per-revolution (3P) region because usually typical design margins of 10% are used. Thus, the tower is usually re-designed and stiffened to increase the eigenfrequencies to above the 3P region, which results in heavy towers and a stiff-stiff tower design. As a consequence, fatigue at the tower base is more critical than for the soft-stiff tower configurations.

A second design modification refers to the control system. For wind speeds above rated, the rotor speed controller will increase the blade pitch angle to limit the aerodynamic rotor torque and rotor thrust. However, when the controller responds (sufficiently fast) to the change in wind speed, the oscillation in platform pitch, induced by wave excitation, will become unstable [21, 58]. This so called “negative damping” effect can be avoided by reducing the controller

bandwidth by “detuning of gains” [59,60]. Using a simplified approach, which has the advantage of keeping the general Single-Input-Single-Output (SISO) controller layout, the rotor closed-loop eigenfrequency is selected to be lower than the critical pitch eigenfrequency of the floating substructure. This method was evaluated, for example by [61,62]. However, instabilities may still exist for certain operating points because the considered rotor eigenfrequency can differ from the coupled rotor eigenfrequency and the overall system stability is not guaranteed [21]. Recommended practices on controller development and floating-specific challenges is provided in [63].

Design modifications for mechanical components involving oil, lubrication system, pumps and sealings may be required if extreme accelerations or inclinations exceed certain limits. In general, this is technically feasible but economically viable only for large volume projects if major modifications are required. Electrical equipment, such as converter, transformer, switchgear, generator, etc., is less critical to increased dynamics of floating systems because of high design margins for accelerations. Thus, no floating-specific modifications are required.

## 2.4 Simulation Techniques for Load Analysis

In general, FOWTs are characterised by three translational rigid body DOFs called surge, sway and heave and three rotational ones called roll, pitch and yaw, as illustrated for an exemplary floating substructure in Figure 2.2. As a result of the additional DOFs in comparison to bottom-fixed foundations, a floating system shows much more dynamic behaviour, which results in necessary modifications, especially of the tower and control system. Typical natural periods of different floating substructures are presented in [63]. Generic values for barge concepts are 100–150 s for surge/sway, 5–15 s for heave, 10–20 s for roll/pitch and 50–100 s for yaw.

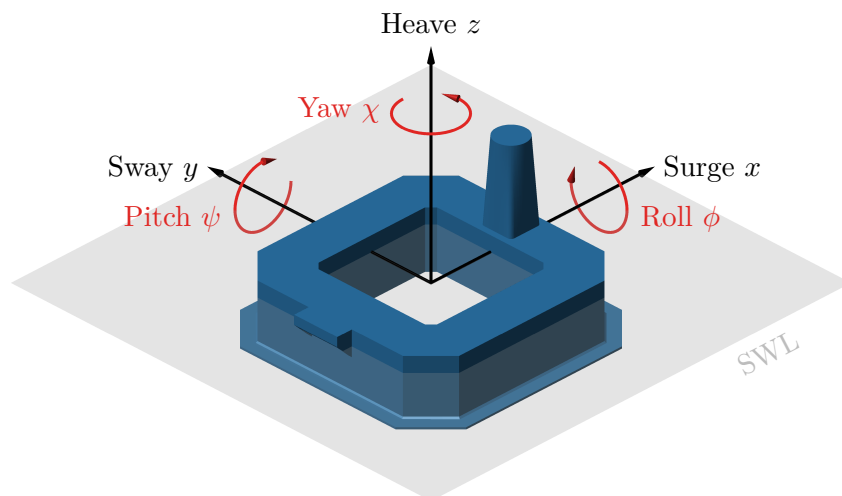


**Figure 2.2:** Schematic view of a barge-type floating substructure with a TP. The global coordinate system is shown with translational (black) and rotational (red) rigid body DOFs.

### 2.4.1 Standards and Design Load Cases

Design standards provide the technical requirements to ensure the integrity of the structural, mechanical, electrical and control systems of a floating wind turbine and apply to design, manufacturing, installation and Operation and Maintenance (O&M). Specific floating wind design standards, service specifications and recommended practices exist for different components and procedures, some of them are compared in [9, 64, 65].

Design requirements for FOWTs are specified by the International Electrotechnical Commission (IEC) in IEC 61400-3-2 [66], which is based on the previous standard for bottom-fixed offshore wind turbines IEC 61400-3-1 [8]. In addition, reference is made for definition of wind models to IEC 61400-1 [67], which also represents the design standard for onshore wind turbines. Certification bodies, such as Det Norske Veritas (DNV), provide similar standards, for example DNV-ST-0119 [68] for floating wind turbine structures, DNV-ST-0126 [69] for onshore and bottom-fixed offshore support structures, DNV-ST-0437 [70] for loads and site conditions to name a few. Furthermore, certification principles and procedures of FOWTs are described in detail in service specifications, for instance DNV-SE-0422 [71]. Whenever a conflict between requirements exist, a precedence list must be followed.

Structural integrity needs to be assessed by design load calculations, which are based on site-specific environmental conditions as summarised in the design basis. Relevant combinations of environmental conditions and design situations must be analysed and are defined in a Load Case Table (LCT). A variety of design tools are available to predict dynamic loads and deformations of FOWTs, an overview of state-of-the-art models and their capabilities is presented in [9, 34, 63, 72–74]. During conceptual design, a reduced set of DLCs, which are expected to have major impact and cover key operating conditions, is evaluated based on experience and recommendations. For detailed design, a full set of DLCs consists of thousands of relevant combinations, which are analysed during several design iteration loops. Critical DLCs distinguish between Ultimate Limit State (ULS), Fatigue Limit State (FLS) and Accidental Limit State (ALS) and are design- and site-specific for FOWTs. For example, Müller et al. [75] describe critical design conditions for two conceptual FOWTs of the LIFES50+ project, in particular DLC 1.2 (fatigue loads during power production and normal sea state), DLC 1.6 (ultimate loads during power production and severe sea state) and DLC 6.1 (ultimate loads during parked conditions and extreme wind and wave environment). DLC 6.1 is evaluated and discussed in Chapter 5 because extreme design conditions are focused in the present study.

## 2.4.2 Structural Dynamics

Structural dynamics models are required for design load calculations of FOWTs [66]. Usually, a coupled approach is applied that models aero-, hydro- and structural dynamics as well as control and mooring system in a time-domain analysis. This is to account for non-linear load effects and transient behaviour from, for example, large deformations or non-linear dynamic properties. For each of the mentioned disciplines, several numerical implementations exist, which are always a trade-off between accuracy and efficiency. Depending on the available level of detail of structural and geometric information during concept, basic or detailed design, one must choose between analytical, reduced, engineering and high-fidelity models. An overview of modelling techniques is presented in [49].

The most commonly used discrete mechanical system models are finite element model and multibody model or a combination of both. While the Finite Element Method (FEM) provides local stress distributions but relies on a detailed structural and geometrical description of the components, MBS is used for high-level assessment of loads and deformations, whose modelling requires only global information, such as mass, stiffness distribution etc. [37]. An introduction on rigid MBS is given in [76, 77], whereas books by [78] provide more details on flexible MBS and by [79, 80] on FEM.

For very fast concept analyses, controller development or global system optimisation even simpler (reduced) structural models are needed with only a handful of DOFs. This is discussed for example in [21] or [81], which describe both non-linear time-domain and linear frequency-domain approaches.

### Multibody System

A classical MBS describes rigid bodies with specified mass, whose motion is constrained by massless joints and which experiences discrete or distributed forces and moments. Flexible MBS also considers flexible (elastic) bodies. Joints either restrain or allow certain DOFs. External forces are applied by massless springs, dampers or actuators, while internal forces at the rheonomic and scleronomic connections originate from the reaction forces. Properties of inertia, elasticity, damping and forces are associated with individual elements, which are combined to a discretised global system. As a result, a relatively simple set of equations of motion describe a simplified mechanical system. Due to the small number of DOFs compared to the finite element models, even large dynamic systems can be simulated in the time domain. The floating substructure is usually modelled as a rigid body with six DOFs for all rigid platform motions, see Figure 2.2. Recent research by [82] also considered substructure flexibility in a dynamic simulation using a reduced set of selected modes, which are represented by a superelement. Furthermore, nacelle, hub, gearbox and generator are often modelled as rigid bodies, while

main bearings are represented by different types of connections, for example, the yaw actuator by a rotational spring-damper element.

Flexible bodies are used to model the rotor blades, tower and drivetrain. Modal reduction is applied to describe flexible bodies with a reduced number of mode shapes, which are calculated by modal analysis using finite element models, see for example in [78]. Modes shapes depend not only on the individual properties of the component but also on the remaining components of the coupled system.

Design tools, such as OpenFAST by National Renewable Energy Laboratory (NREL) [83], are limited in the available numbers of rigid body and flexible DOFs, while general purpose MBS tools, such as SIMPACK, enable more detailed and complex topologies. Common design tools consider at least the first two flapwise bending modes of the rotor blades and the first edgewise mode because rotor blades are stiffer in the edgewise direction. Torsional modes are necessary to account for the bend-twist coupling of the modern large and flexible rotor blades. New MBS developments nowadays support elements with full geometric non-linearities and large deflections and include bending, torsion, shear, and extensional DOFs, such as NREL's module BeamDyn [84], which was validated in [85]. Moreover, tower flexibilities are included by at least the first two modes in the fore-aft and side-side direction.

## **Finite Element Method**

A higher level of fidelity can be achieved by using FEM models. A finite element model is a result of the discretisation of a flexible continuous body into a large number of geometrically simple elements with specified properties. The elements are connected with discrete nodes at which external forces and moments are applied and where bearing conditions are defined such as fixed or free structural support. Finite elements can be, for example, one-dimensional beams or rods, two-dimensional triangles or three-dimensional cuboids with specific volume. The fundamental idea of FEM is to associate properties, such as inertia, elasticity and force, with a discrete element of simple geometry, for which the local equations of motion are defined. The overall system is assembled from the single finite elements by connecting the nodes. By combining the mass, damping and stiffness matrices, which correspond to the global DOFs, the static and dynamic structural behaviour can be predicted. The FEM generally represents an approximation method similar to MBS because of the use of discrete elements with associated basis functions. However, in contrast to MBS usually a large number of elements is required for the finite element method, which increases the number of DOFs and the computational requirements. In addition, detailed information of the investigated component such as geometry and material properties is required, which makes a pure FEM model less applicable in early design phases. A more practical approach is to solve the equations of motion for the rigid body motions of a FOWT system applying a MBS approach and combine it with beam finite

elements for tower and rotor blades to solve the remaining elastic DOFs. This approach captures sufficiently the overall dynamics of the floating wind turbine while providing some details on the global load distribution.

### 2.4.3 Aerodynamics

Different levels of model fidelity exist for the calculations of aerodynamic forces and the resulting loads on the wind turbine rotor blades.

#### **Blade Element Momentum Method**

Most commonly applied in loads analysis of wind turbine aerodynamics is the state-of-the-art BEM method with corrections, see for example [86]. The BEM method relies on the conservation of linear and angular momentum and calculates the thrust and torque on the annular sections of the wind turbine rotor. The rotor is represented as an actuator disk with the axial and tangential (angular) induction factors. Induction factors indicate the amount of reduction of wind speed and flow redirection by each blade element. Momentum theory is combined with blade element theory, which calculates the normal and tangential force on a specified number of blade elements. The aerodynamic forces are a function of the local flow angle at the rotor blades and airfoil characteristics [87]. The flow angle depends on the sectional pitch angle and local angle of attack. The induction factors, which are influenced by aerodynamic loads, are solved iteratively until the convergence criteria are reached. Definition of the blade geometry with the chord length and twist angle as well as airfoil polars with lift and drag coefficients are required. However, aerodynamic interactions between blade elements are neglected, which means the radial flow is neglected, and the forces are determined by the airfoil polars. The derivation of the classical BEM theory is described in [88].

Empirical correction models are needed because of the simplifications made in the BEM theory. Unsteady aerodynamics such as dynamic stall models need to be incorporated. Furthermore, corrections of airfoil polars are needed to include three-dimensional flow, especially at the blade root. Hub- and tip-loss models, for example by Prandtl, are required because the rotor is assumed as an actuator disk with an infinite number of blades in the classical BEM theory. Furthermore, dynamic wake effects, which account for the induction dynamics from transient conditions, can be accounted for with a time delay. Furthermore, Glauert's empirical correction is applied for heavily loaded rotors with large axial induction factors. Finally, corrections for skewed wake effects, for example by Pitt and Peters, were developed for yawed inflow [89,90].

### Advanced Aerodynamic Models

Advanced aerodynamic models are applied for high-fidelity analysis of, for example, rotor-wake interactions, simulation of flow development at wind-farm level or investigation of new blade designs to overcome the limitations of the BEM theory. CFD methods for aerodynamics of wind turbines are widely used in academia but also in industry, as presented in [12, 13, 91–93]. The underlying theory is addressed in Section 2.4.4 with more detail.

Less computationally expensive than CFD is the grid-free Free Vortex Wake (FVW) method, which originates from the helicopter and aircraft aerodynamics, as shown in [94, 95], but it can also be applied for wind turbines [96]. Based on the potential flow theory with an inviscid, incompressible and irrotational fluid, the Laplace's equation is solved by a mathematical representation for vortex filaments. They are characterised by concentrated vorticity and, according to the Biot-Savart law, induce a velocity field on a fluid particle depending on the radial distance. The induced velocities are superimposed by the external three-dimensional velocity field. Vortex core models are needed to correct the singularity in the induced velocity field at the vortex filament. The wake of the wind turbine rotor is represented by a vortex lattice of discrete shed vortices, which account for the flow unsteadiness, and trailing vortex filaments, which are associated with the spanwise variation in lift. The evolving wake convects and deforms freely and is coupled to a lifting-line or -surface model of the rotor blades, which relates the lift distribution to the strengths of the vortex filaments according to the Kutta-Joukowski theorem. Unlike BEM, corrections for wake-induced aerodynamic effects, such as tip loss or dynamic and yawed inflow, are implicitly included in FVW method. But similar to BEM, airfoil data are required for blade sections on the rotor blade and blade element theory is used to evaluate the distribution of the lift coefficient as a function of the angle of attack. Application of the FVW method in aerodynamic studies of FOWTs is described in [97, 98]. Moreover, investigation of two-bladed onshore wind turbines with FVW is discussed in [99].

For this study, the classical BEM method with Prandtl's hub- and tip-loss model but without corrections for dynamic inflow or dynamic stall is applied to compute aerodynamic loads on an idling rotor in extreme conditions. In addition, wind drag loads on the tower are considered as described in Section 5.1.2.



## 2.4.4 Hydrodynamics

Restoring forces from linear hydrostatics as a result of the hydrostatic pressure field around submerged parts of the floating substructure, also known as Archimedes' principle of buoyancy, is important for static stability of FOWTs. Lemmer [21] summarises the calculation of the hydrostatic restoring stiffness in heave and pitch. In contrast, hydrodynamics are associated to the dynamic pressure of the water over the wetted surface of a floating substructure [100]. Thus, hydrodynamic loads on a FOWT arise from water fluid and its interaction with the floating substructure, which could be exposed to wave run-up. In general, a classification according to [8] can be made, which divides the hydrodynamic loads in viscous drag, inertia, diffraction, wave radiation, slapping and slamming as well as vortex shedding and other non-linear contributions. Additional influences from sea current and for FOWTs, especially sloshing and green water, need to be assessed [66]. Other literature, such as [63], recommend a division of hydrodynamic loads into viscous and non-viscous parts, or as in [74] in linear and non-linear components. Two general techniques are most commonly applied for hydrodynamic load calculations of FOWTs, Morison's equation and potential-flow theory or a combination of both. Their applicability is limited and depends on the dimensions of the investigated components and the water flow regime. Morison's equation and potential-flow theory are introduced in the following Sections. They are described in more detail in standard literature for offshore engineering such as [23, 101–104].

With respect to hydrodynamic damping, two contributions are considered – viscous damping of the fluid and radiation damping. The first is a result of the relative velocity of the wetted structure and the surrounding fluid and relates to the drag force term in Morison's equation. The second source of damping originates from the vibration of the submerged part of the structure, which generates waves radiating away from the body and, thus, inducing an energy loss.

### 2.4.4.1 Morison's Equation

Morison's equation is a coefficient-based, semi-empirical hydrodynamic force model for slender, vertical piles [20]. It accounts for viscous drag, added mass and wave excitation loading and provides the longitudinal (or lateral) force on the cylindrical can sections in the normal direction of the body surface:

$$\frac{F}{L} = \frac{\pi}{4} D^2 \rho_f C_m \dot{u}_f + \frac{1}{2} D \rho_f C_d u_f |u_f|, \quad (2.1)$$

here displayed per unit length  $L$  with the diameter  $D$ , fluid density (of water)  $\rho_f$ , inertia coefficient  $C_m$ , drag coefficient  $C_d$ , fluid velocity  $u_f$  and fluid acceleration  $\dot{u}_f$ . The first term is associated to the linear inertia force, which is proportional to the fluid acceleration, and

the second term to the quadratic drag force, which depends on the fluid velocity squared and accounts for flow separation. Journée and Massie describe in [103], that the drag and inertia force components in Equation 2.1 are 90° out of phase with each other if considered as a function of time, which directly follows from the phase shift between fluid velocity and acceleration in an oscillating flow. This effect is exploited during experimental determination of the drag and inertia coefficients, see again [103]. Morison force is calculated for every strip of the cylindrical body (strip theory) and the values are integrated to obtain the total hydrodynamic force on the structure [105]. By substituting the inertia coefficient in Equation 2.1 with the added mass coefficient  $C_a$  using  $C_m = 1 + C_a$  and multiplying by the unit length, the Equation becomes:

$$F = \underbrace{\rho_f V \dot{u}_f}_{1.} + \underbrace{\rho_f V C_a (\dot{u}_f - \dot{u}_s)}_{2.} + \underbrace{\frac{1}{2} \rho_f A C_d (u_f - u_s) |u_f - u_s|}_{3.}, \quad (2.2)$$

with the following force components: 1. Froude-Krylov force, 2. hydrodynamic mass force and 3. quadratic drag force. The Froude-Krylov force refers to the dynamic (unsteady) pressure field generated by undisturbed waves and represents, together with the diffraction force, the total non-viscous forces acting on a floating body in regular waves. In contrast to Equation 2.1, Equation 2.2 accounts for the body motion with the structure velocity  $u_s$  and acceleration  $\dot{u}_s$ . The dimensionless coefficients  $C_a$  and  $C_d$  are a function of the surface roughness, Reynolds number (see Equation 2.24) and Keulegan-Carpenter number  $KC$ :

$$KC = \frac{uT}{D} \quad (2.3)$$

with a characteristic velocity  $u$  and wave period  $T$ . They are determined by experiment or based on standard geometries in literature, for instance [22,23]. A formulation of the Morison's equation for the vertical forces is presented in [28], which is applicable for heave plates.

Furthermore, diffraction effects are neglected in Morison's equation, which limits its applicability to hydrodynamic transparent structures. That means, a diameter to wave length ratio of  $D/\lambda < 0.2$  must not be exceeded, as described in the literature [90,103,104]. In addition, the simplification, that the first acceleration-dependent force component in Equation 2.1 is independent of the frequency, is only valid for slender cylinders, which are characterised by small radiation forces [21]. Finally, hydrodynamic forces on multiple bodies are calculated separately and their interaction is neglected by the Morison's equation.

One of the advantages of applying the Morison's equation is, that pre-processing of frequency-dependent hydrodynamic coefficients using a panel code is not required. Additionally, hydrodynamics of FOWTs are usually modelled by a combination of Morison's equation and potential flow, which considers diffraction effects, to avoid restrictions on platform geometry. Thus, the quadratic drag force from Morison's equation is included in load calculations [74,100].

#### 2.4.4.2 Potential-Flow Theory

As mentioned before, the applicability of Morison's equation is limited to hydrodynamic transparent offshore structures. With increasing diameter of the cylindrical pile this assumption is no longer valid because the wave field is disturbed by the presence of the structure and the diffraction effects become more significant. The same applies for large, non-cylindrical bodies under hydrodynamic loads, such as the square-shaped barge-type floating substructure shown in Figure 2.2.

#### Diffraction Problem

The diffraction problem can be solved analytically or numerically for the modified flow field around the structure. The resulting velocity potential distribution must satisfy the condition that there is no flow perpendicular to the surface of the structure. Also important to mention is that only the inertia loads are determined by the diffraction analysis while drag loads are not considered. Diffraction theory is limited to linear waves, because the velocity potential is solved for linearised boundary conditions at the free water surface. But solutions for non-linear waves can be approximated by scaling the hydrodynamic loads by the ratio of the non-linear wave particle acceleration to the linear wave particle acceleration at each element [96].

For large monopiles or some gravity-base foundations the MacCamy-Fuchs correction from [106] can be applied, for example in [107,108]. It represents an analytical solution to the linear diffraction problem of the potential flow theory for vertical circular cylinders, which are fixed to the seabed. The model is limited to the first-order (or linear) wave theory (Airy wave) and only applicable to elements up to the still water level. In addition, if the structures deviates significantly from a cylindrical shape, for example for ice cones, the model may lead to incorrect results [8]. MacCamy-Fuchs approximation provides an exact solution for the inertia coefficient  $C_m$ , which varies with the diameter to wave length ratio  $D/\lambda$  as shown in [96]. After an initial peak, the inertia coefficient decreases significantly as  $D/\lambda$  increases. Dean and Dalrymple [109] describe the derivation of the MacCamy-Fuchs approximation for the velocity potential and loading on a cylinder.

However, closed-form (analytical) solutions cannot be applied for offshore structures other than vertical circular cylinders. Therefore, numerical methods are necessary to provide approximate results of the diffraction analysis. In general, the velocity potential is split in two parts, which are superimposed: First, a velocity potential that would exist in the absence of the structure (incident wave potential) and second, a velocity potential that leads to zero flow across the surface of the structure (scattering potential) as described in [101]. In consequence, the diffraction loads are a result of the undisturbed pressure field (Froude-Krylov force) and wave scattering at the structure [100]. The structure is divided into  $N$  surface elements, which have their own uniformly distributed oscillating flow source. Subsequently, the second velocity potential is

calculated by summing up  $N$  velocity potentials, each from an oscillating source. Finally, a set of  $N$  equations is solved to obtain the intensity of each flow source by preventing flow across the surface elements.

Results of diffraction analysis should be checked to ensure that unrealistic frequencies are avoided [8]. This applies especially to gap problems when multiple offshore structures are close to each other or are equipped with a moonpool. Consequently, spikes in the Response Amplitude Operator (RAO) and Quadratic Transfer Function (QTF) of individual bodies can be caused by resonant fluid motions [90]. Simulating gap problems using the diffraction analysis can result in unrealistic free surface motions. This is an inherent shortcoming of the diffraction method and relates to its integral formulation limiting the minimum spatial dimensions which can be simulated without considerably increasing the number of discretised panel elements. Unrealistic resonance of gap problems can be mitigated by imposing an artificial damping on the free surface motions at the gap. For example, Guignier et al. [110] place an external lid on the moonpool of the barge-type floating substructure to avoid standing waves.

### **Radiation Problem**

Besides the diffraction problem of potential flow theory, which determines loads on the floating substructure when it is fixed at its mean position and the incident waves are scattered by the structure, the radiation problem must also be solved numerically for evaluation of the linear hydrodynamics [101]. The solution of the radiation problem provides the loads on the floating substructure when it is forced to oscillate in its different modes of motion without the presence of incident waves. As a consequence, radiation loads are generated when the structure radiates outgoing waves away from itself. They entail contributions from wave-radiation damping and the added mass. The governing equations included in the diffraction and radiation analysis for FOWTs are discussed in [100] or [21].

### **Second-Order Loads**

Three-dimensional panel models, such as WAMIT [111, 112], are very common techniques for deriving frequency-dependent hydrodynamic loads from diffraction and radiation analysis. Depending on the model fidelity and investigated geometry, second-order hydrodynamic forces can be taken into account. They are associated to the diffraction problem and proportional to the square of the wave amplitude. Second-order loads result in mean-drift forces, which are applied to the floating substructure, and additional wave excitation at the difference- and sum-frequencies from interaction of pairs of wave frequencies in an irregular sea state. By design, the natural periods of a floating substructure are placed outside the main wave excitation region of the wave energy spectrum. However, hydrodynamic forces from the second-order terms may induce resonance effects, even if their magnitudes are usually smaller than the first-order wave

excitation [72]. Mean-drift forces can be obtained by Newman's approximation, which provides also the slow-drift (difference-frequency) second-order contributions to the hydrodynamic loads. The approach exploits that off-diagonal elements in the full QTF matrices can be estimated using the diagonal elements, so that the slow-drift forces can be calculated. The mean drift forces are obtained by keeping only diagonal terms in the difference-frequency matrix, which are derived from first-order panel calculations. Alternatively but computationally demanding, the difference- and sum-frequency forces can be estimated using the full QTFs [22, 63, 66].

One must take into account that a potential flow model only captures hydrodynamic loads from wave excitation including diffraction and wave-radiation damping and added mass. The viscous damping is neglected in potential flow theory and has to be included in the numerical solution by adding a drag term from Morison's equation or a global quadratic drag applied to the substructure as an approximation [74].

Finally, for transient load case simulations of the hydrodynamic response, the frequency-domain analysis must be transformed in the time domain as described in [21]. The same reference also presents a literature review of studies regarding second-order effects on FOWTs, for example in [113].

#### 2.4.4.3 Computational Fluid Dynamics

CFD represents a high-fidelity method and its application to aerodynamics of wind turbines is introduced in Section 2.4.3. As stated in [63], CFD analyses are becoming more common for investigation of non-linear fluid-structure interactions and complex flow physics with respect to offshore wind turbines, such as slamming and ringing from steep wave impact.

#### **Navier-Stokes Equations**

In general, the conservation of mass, momentum and energy describe the physical model of real flows in fluid dynamics. It can be described mathematically by the Navier-Stokes equations, which are a system of partial differential (conservation) equations for mass, momentum and energy with consideration of the friction and heat transfer effects. An analytical solution of the non-linear and coupled Navier-Stokes equations can be determined only for a small number of cases, for example, for fully developed flows in simple geometries, such as pipes [114]. However, their practical relevance is restricted to the investigation of fundamentals of fluid dynamics. Thus, if empirical studies of the investigated fluid flow are not available, the Navier-Stokes equations need to be solved by numerical methods. In case the fluid density can be considered constant – i.e. the Mach number as the ratio of the flow velocity to the local speed of sound does not exceed a value of 0.3 – the compressible formulation of the Navier-Stokes equations can be simplified to the incompressible system of equations. If friction can be neglected – i.e. the Reynolds number in Equation 2.24 tends to infinity – the Navier-Stokes equations can be

simplified and become the Euler equations. For compressible fluids, the equation of state for an ideal gas and the inner kinetic potential energy (from gas dynamics) can be applied to solve the compressible Navier-Stokes equations.

### **Numerical Schemes**

Different numerical schemes are used for the discretisation and solution of the partial differential equations, for instance the Finite Difference Method (FDM), FEM and Finite Volume Method (FVM) as described in the literature [114,115]. The most commonly applied approach in CFD is the FVM because it allows arbitrary, unstructured grid elements, which makes the method suitable for complex geometries. Furthermore, the basic idea of the FVM is to apply the integral notation of the differential equation of the conservation law, which results in easy handling of strong gradients and discontinuities in the flow. The computational domain is divided into a finite number of grid elements – i.e. control volumes forming a three-dimensional mesh – and the field variables are calculated at the centroid of each element. Numerical integration in space (related to the surface integral in the Navier-Stokes equations) and time is usually approximated by first- and second-order discretisation schemes. The conservation law is solved by evaluation of the numerical flux of mass, momentum and energy across the boundaries of the control volumes. Thus, grid quality is very important for the stability, efficiency and accuracy of the FVM. In addition, boundary and initial conditions are required for the transient solution. In summary, the computation is performed on the integral mean values in each cell for the FVM, whereas the solution is represented by point values for the FDM and by superposition of the basis functions for the FEM. However, because three levels of approximation are required for FVMs – interpolation, differentiation and integration – higher-order discretisations beyond the second order are more difficult to implement [114].

### **RANS Equations and Turbulence Modelling**

If the fluid velocity of the turbulent flows is replaced by the sum of a time-averaged mean value and a fluctuating value, which equals the disturbance, the momentum-conservation equation is characterised by an additional term named the Reynolds stress. Together with the continuity equation the Reynolds-Averaged Navier-Stokes (RANS) equations are defined. The stress tensor of the turbulent fluctuations in the fluid momentum introduces new unknown terms, which need to be determined to close the RANS equations. Therefore, turbulence models are needed and aim to relate the Reynolds stress to the time-averaged velocity field by modelling of the eddy viscosity, as first proposed by Boussinesq [116]. Eddy viscosity models are distinguished by the number of independent turbulence variables. In this study the  $k - \omega$  Shear Stress Transport (SST) turbulence model, developed by Menter [117], is applied. It is a two-equation eddy-viscosity model for the turbulent kinetic energy  $k$  and the specific dissipation  $\omega$  and combines

the  $k - \omega$  model in the viscous boundary layer and the  $k - \epsilon$  model in the free-stream. By assuming that the time-averaged mean value of the fluid velocity changes slowly over time in comparison to the temporal resolution of the numerical integration, the URANS equations are obtained.

### **DNS, LES and DES**

Computationally much more demanding is the Direct Numerical Simulation (DNS), which solves the Navier-Stokes equations without assuming a turbulence model. This implies that turbulent structures are resolved both spatially and temporally, which requires extremely fine mesh, very small time steps and higher-order numerical schemes. Thus, the practical relevance of DNS is limited to fundamental research, such as the analysis of laminar-turbulent transition, and not applicable to high-Reynolds flows of wind turbines.

In contrast, Large Eddy Simulation (LES) models are based on filtering of fluid variables, so that large-scale turbulent structures are directly resolved in time and space, whereas small-scale structures remain unresolved and are modelled. The approach requires higher spatial and temporal resolution of the computational domain than those for a RANS simulation. LES are mainly applied for flows with small Reynolds numbers, such as combustion chambers, and for simulation of weather. A combination of RANS (for the solution in the wall boundary layer) and LES results in Detached Eddy Simulation (DES), which was applied, for example, for simulation of flow interference within an offshore wind farm by [118] or an onshore wind turbine in complex terrain by [119].

The present study employs the URANS approach for CFD modelling because it requires reasonable computational resources for the envisaged evaluation of hydrodynamic loads on a floating substructure at extreme wave conditions.

### **2.4.5 Mooring Dynamics**

The design of a mooring system is an iterative process starting from a conceptual design based on the information and requirements of the design basis. It is followed by a dynamic analysis of the floating system, a subsequent mooring design optimisation and finally, a selection of components and equipment as well as installation, inspection and monitoring procedures, see also [120]. During the design phase, compliance with the design codes and standards, such as DNV-OS-E301 [121], International Organization for Standardization (ISO) 19901-7 [122], American Petroleum Institute (API) RP 2SK [123] etc., needs to be verified.

In general, permanent and temporary mooring systems are available based on the duration of the offshore operation. For FOWT, temporary moorings may be needed during the construction

and installation phase of a commercial-scale project with tens of units to establish a temporary lay-up area [7]. Very early in the design of a mooring system, designers choose between two principle mooring profiles, a catenary system with all-chain or chain-wire-chain setup or a taut (or semi-taut) leg system with chain-wire-chain or chain-polyester-chain setup as described by Ma et al. [124]. There are two main objectives of mooring design: First, station-keeping within specified tolerances under normal and extreme operational conditions and appropriate limitation of the excursions to protect the umbilicals or cables. The second objective is to guarantee the operability and reliability of the floating system by sufficient mooring system strength and fatigue life.

Models with different levels of fidelity are available for the design and analysis of mooring lines. In general, two types of mooring models can be distinguished. Static models neglect the inertia forces and fluid drag loads on the mooring and the sectional forces in the mooring line or at the fairlead and anchor only depend on its position. In contrast, dynamic mooring line models also consider the velocity- and acceleration-dependent mooring line inertial mass, added water mass and damping from vortex shedding at the mooring lines [21]. For floating wind research, the quasi-static model MAP++ [125] and the lumped-mass dynamic model MoorDyn [126,127] are widely used for numerical simulation of the (multi-segmented) mooring lines because both models are coupled to the wind turbine simulation tool OpenFAST. There are more complex higher-order mooring dynamics models based on finite elements. A comparison of underlying theory and review of the dynamic mooring models is discussed in [49,128]. The impact of different quasi-static and dynamic mooring models on the ultimate and fatigue loads of three different floating platform concepts is presented in [129]. The authors conclude that the influence of the applied mooring model depends on the platform topology and increases for elements located closer to the platform. Especially the tower base loads as well as the mooring line tensions are highly dependent on mooring line dynamics so that both fatigue and extreme loads can be significantly affected. Another conclusion is that the mooring dynamics are necessary for the prediction of extreme line tensions, which was also found in [130] by comparison to experimental data. A prediction of the extreme tensions for a 100-year storm can be found in [131].

In this study, a simplified approach is used for modelling of the mooring line loads on the floating substructure based on a global linear stiffness matrix calibrated with experimental data, see Section 4.2.2.



## 2.5 Metocean Environment

Metocean environment relates to the meteorological and oceanographic conditions, which impact the design of an offshore wind turbine. A site-specific metocean database entails information the on wind (speed, direction), wave (height, period, direction), current (speed, direction), water levels, sea ice (drifting speed, direction), air and water temperature and densities, water salinity, site bathymetry, marine growth and other parameters [8]. Most relevant parameters in the context of this study are wind and wave conditions, which are described in the following Sections.

### 2.5.1 Wind

An introduction on the principles of wind generation and local influences is given in standard wind energy books, such as [87, 132, 133]. According to the applicable standard IEC 61400-1 [67], wind regimes for normal and extreme conditions are considered. The first category applies to the normal operation of a wind turbine, while the second relates to events with a 1-year or 50-year return period. By definition, wind conditions are based on a constant mean wind speed, which is combined with either a time-dependent deterministic gust profile or with turbulence.

The atmospheric boundary layer develops as consequence of the ground surface friction. The resulting wind profile, which is a mathematical expression of the wind speed as function of height above ground can be described either by a logarithmic or power law formulation and depends on the local surface roughness. The power law is applied in this study with the power law exponent  $\alpha$  to quantify wind shear, longitudinal wind speed  $u$  and vertical coordinate  $z$ . It refers to the Normal Wind Profile Model (NWP) of IEC 61400-1:

$$u(z) = u_{\text{hub}} \left( \frac{z}{z_{\text{hub}}} \right)^{\alpha} \quad (2.4)$$

Wind speed can be measured using cup or ultrasonic anemometers from a met mast or remote sensing devices, such as Light Detection And Ranging (LIDAR). The data are used for site calibration, resource assessment, power performance measurements according to IEC 61400-12-1 [134], etc. to name a few. Long-term statistics of the mean wind speed – i.e. the Rayleigh or Weibull distribution – can be fitted to the site-specific wind measurement data. Furthermore, the distribution of the wind speed and wind direction at a given site can be described by the wind rose.

On the other hand, an averaging time period of 10 minutes is used for the short-term statistics and the basis of wind binning for design load simulations. Moreover, fluctuations from the 10 minute average mean wind speed is a measure of the turbulence. The turbulence intensity is

defined as the ratio of the standard deviation of the wind speed  $\sigma_x$  to the mean wind speed  $\bar{u}$ , both in the longitudinal direction:

$$TI = \frac{\sigma_x}{\bar{u}}. \quad (2.5)$$

According to the Normal Turbulence Model (NTM), the standard deviation of the longitudinal wind speed is defined as the 90 % quantile of the distribution of the turbulence intensity at the hub height with a reference value  $TI_{\text{ref}}$  at  $15 \text{ m s}^{-1}$  according to standard wind turbine class definitions [67]:

$$\sigma_x = TI_{\text{ref}} (0.75 \overline{u_{\text{hub}}} + 5.6 \text{ m s}^{-1}). \quad (2.6)$$

Common turbulence models characterise the turbulence as a function of the frequency. Two spectra are widely used in the wind energy. First, the Kaimal spectrum, which is a variation of the von Karman spectrum, provides a spectral distribution of the turbulence at one point and with an exponential coherence model for the longitudinal velocity component to account for spatial correlation [67]. The more complex Mann spectrum defines additional coherence models of the lateral and vertical wind speed components. Hence, three-dimensional turbulent wind fields can be generated, which are needed for the design load calculations. Usually, Taylor's frozen turbulence hypothesis is applied, which translates the two-dimensional wind field into three dimensions by transporting it with the mean wind speed.

In this study, extreme wind loads are taken into account for DLC 6.1 by modelling of a steady, uniform inflow with vertical shear as introduced in Section 5.2.

### 2.5.2 Regular and Irregular Waves

Wave modelling is based on the description of water particle kinematics, which are needed for the assessment of wave loads on offshore structures, see Section 2.4.4, and for experimental model testing in a wave basin as discussed in Section 2.6. Deterministic and stochastic approximations of real sea states are used to assess the hydrodynamic loading. While the first relates to regular or focused waves, which can be used for design purposes in some applications [8], the second refers to irregular or random waves, which are based on the statistical and spectral methods.

## Irregular Waves

In principle, a stochastic sea state can be described as a superposition of individual regular waves of different frequency, amplitude, phase and propagation direction. Wave spectra provide the energy density as a function of the wave frequency. Two of the most common spectra in offshore engineering are the Pierson-Moskowitz (PM) [135] and the Joint North Sea Wave Observation Project (JONSWAP) [136] wave spectrum. The later is a modification of the PM spectrum and more applicable to not fully developed sea states in fetch-limited locations [87], which is the case for most sites in the North Sea [137]. Moreover, the JONSWAP spectrum is characterised by a higher peak and a narrower spectrum, as found in a storm situation. A comparison of the two mentioned wave spectra is presented in the ISO 19901-1 standard [138]. Wave spectra are defined as a function of the peak spectral period  $T_p$  and the significant wave height  $H_s$ , which is the average of the highest one third of the recorded wave heights. In addition, the mean wave direction is needed to define a design sea state [8]. Furthermore, the correlation of the wind and wave conditions is considered by long-term joint probability distributions of the sea state parameters. Finally, the mean wind and wave directions should be included to take wind-wave misalignment into account.

## Regular Waves

There are different wave theories to describe the regular waves. These wave theories provide the two-dimensional water particle kinematics. For all regular wave theories, the resulting waveform is periodic, symmetric about the wave crest and its shape does not change during propagation. Based on their formulation, wave theories have a particular range of applicability and guidance on selection is discussed, for example, in [8, 138, 139].

The earliest wave theory with a simple mathematical description of periodic progressive waves was published by Airy [140]. The Airy linear wave theory is based on the potential flow theory and defines the linearised velocity potential  $\phi$ :

$$\phi = \frac{\pi H}{kT} \frac{\cosh(k(z+d))}{\sinh(kd)} \sin(\theta) \quad (2.7)$$

with the wave height  $H$ , wave period  $T$ , vertical coordinate  $z$ , water depth  $d$ , wave number  $k$  and wave phase angle  $\theta$  defined in Equations 2.8 and 2.9:

$$k = \frac{2\pi}{\lambda} \quad (2.8)$$

$$\theta = kx - \omega t. \quad (2.9)$$

In Equations 2.8 and 2.9  $\lambda$  is the wave length,  $x$  is the longitudinal coordinate and  $t$  is the time. The wave frequency  $f$  and the angular frequency  $\omega$  are related as shown in Equation 2.10:

$$\omega = \frac{2\pi}{T} = 2\pi f. \quad (2.10)$$

The linear wave dispersion relation, an implicit equation, describes how the wave speed increases with the wave length:

$$\omega^2 = gk \tanh(kd). \quad (2.11)$$

The surface elevation  $\eta$  is calculated from the velocity potential in Equation 2.7 as a function of time:

$$\eta(t) = \frac{H}{2} \cos(\theta). \quad (2.12)$$

Furthermore, the hyperbolic function in Equation 2.11 can be substituted by approximate expressions leading to a classification of three wave regimes: Shallow water (or long) waves satisfy  $kd < \pi/10$ , which is the same as  $d < \lambda/20$ , deep water (or short) waves satisfy  $kd > \pi$ , which is the same as  $d > \lambda/2$  and intermediate depth waves are found in between [23, 90]. Linear wave theory is in principle only applicable for sinusoidal waves of infinitesimal small amplitude and steepness. In addition, it assumes that the fluid is frictionless (meaning that viscosity is zero), the motion is irrotational without vorticity, the seabed is horizontal and fixed, and the fluid motion is very small to be able to neglect higher-order terms in the equation of motion. In ocean engineering Airy's linear wave theory is used for deep water small-amplitude waves as the wave height must be small compared to the wave length and the water depth. Overestimation of the wave kinematics between the wave crest and the Still Water Level (SWL) can be corrected by stretching methods, for example linear Wheeler stretching.

As Airy waves propagate from deep into shallow waters, their orbital motions and pressure fields begin to interact with the seabed [90]. Airy wave theory is not valid for shallow water and steep waves because the waveform changes from a sinusoidal and becomes asymmetric with higher crests and shallower troughs. For this purpose, non-linear wave theories were developed that describe the finite amplitude waves without linearisation of the kinematic and dynamic surface boundary conditions. Higher-order wave theories are not exact but fulfil the higher-order terms. Common non-linear wave theories in offshore engineering are Stokes 5<sup>th</sup> order wave theory [141, 142], suited for deep water and steep waves, and Fenton's cnoidal wave theory [143, 144], which is applicable for long waves in shallow water. Both wave theories depend on finite power series expansions and might suffer from truncation problems. Applicable over a wide range of water depths is Dean's stream function wave theory [145, 146] because it is a

numerical best-fit method. This means that a set of non-linear equations is solved numerically to fit a stream function to a given wave train, specified by water depth, height and period<sup>1</sup>. A measure for the influence of the water depth on the nonlinearity of waves is given by the dimensionless Ursell number  $Ur$  [104, 144]. The boundary between Stokes and cnoidal theories' range of applicability was showed in [147] and is:

$$Ur = \frac{H\lambda^2}{d^3} = 40. \quad (2.13)$$

For  $Ur < 40$  Stokes wave theory applies, whereas for  $Ur > 40$  cnoidal wave theory should be used. If the wave height is increased or the water depth reduced beyond a certain limit, wave breaking occurs as the horizontal water particle velocity in the wave crest exceeds the wave celerity. The hydrodynamics of wave breaking are non-linear in nature and highly complex. State-of-the-art for estimating wave slamming loads on cylindrical offshore wind turbine support structures are engineering models, as presented in [8, 22]. An alternative would be to perform experiments or high-fidelity fluid simulations.

### 2.5.3 Extreme Waves and Wave Focusing

Extreme waves, which may also be referred to as rogue or freak waves, can occur unexpectedly and may be the design driver in the ULS analysis of offshore wind turbines. Extreme wave development in real sea is still a matter of ongoing research, but in principle several mechanism foster their generation: wave focusing by currents, wind-wave interactions, interference from phase or directional wave focusing, thermal expansion and wave-seabed interactions. In general, extreme waves are characterised by a wave height greater than 2.2 times or wave crest greater than 1.25 times the significant wave height [90]. A well known example is the Draupner wave, which was recorded in the North Sea on New Year's Day 1995, with a wave height of more than 25 m, crest height of more than 18 m and wave length of slightly larger than 200 m [101, 148]. According to the standard [8] a design wave is recommended with a return period of 50 years for the consideration of extreme wave loads. If the extreme wave height and associated wave periods cannot be determined because of insufficient metocean data, the following assumption shall be used for deep water [8]:

$$H_{\max} = 1.86H_s. \quad (2.14)$$

This approximation is based on the most probable maximum wave in a three-hour reference period sea-state assuming a Rayleigh distribution. Wave kinematics of the design wave must be calculated by non-linear wave theories such as stream function theory.

<sup>1</sup>Explained in more detail in the OrcaFlex online manual: <https://www.orcina.com/webhelp/OrcaFlex/Content/html/Waves,Deanstreamfunctiontheory.htm>

## NewWave Theory

Instead of applying a periodic wave theory for design wave estimation, representative waves from a random sea may be used. They can be generated using the NewWave theory, which was developed by Tromans et al. [149] to improve design methods of offshore structures. It is a linear representation of the most probable maximum wave in a severe sea state. It provides the wave elevation and velocity profile of a focused wave group based on selected wave frequencies from a measured or theoretical (continuous) wave spectrum, such as JONSWAP. Wave kinematics of each wave frequency component are calculated with the linear wave theory, superposed and brought into phase at a specified focus location and time to create an extreme wave event. This technique is useful to investigate wave breaking at defined locations and associated loads on offshore structures, because the maximum wave height is a variable input parameter.

Several researchers applied NewWave theory to numerical and experimental analysis of focused-waves and interaction of extreme waves with offshore structures, for example [14, 15, 150–154]. Moreover, the method is recommended by the standard ISO 19901-1 [138] for generation of design waves as an alternative to the periodic regular wave theories. NewWave theory models only a section of a wave record. This limitation was overcome with a constrained NewWave by Cassidy [155] by embedding a NewWave into a random sea at a defined instance in time without changing the statistics of the underlying sea state. A comparison of the different wave generation techniques for the modelling of extreme waves is discussed in [156].

Furthermore, NewWave was extended to second-order Stokes wave theory to improve the accuracy by including non-linear wave-wave interactions for the sum- and difference-frequencies [157–160]. Bredmose and Jacobsen [14] experienced premature wave breaking when implementing only the linear wave spectrum to the focused wave groups. Hence, they applied the second-order solution by Sharma and Dean [158], which is also implemented in this study to generate unidirectional, phase-focused wave groups. It is based on Stokes 2<sup>nd</sup> order wave theory and the first- and second-order free surface elevations are given by  $\eta^{(1)}$  and  $\eta^{(2)}$  respectively:

$$\eta = \eta^{(1)} + \eta^{(2)} \quad (2.15)$$

$$\eta^{(1)}(x, t) = \sum_{i=1}^N a_i \cos \psi_i \quad (2.16)$$

$$\eta^{(2)}(x, t) = \frac{1}{4} \sum_{i=1}^N \sum_{j=1}^N a_i a_j [T_{ij}^- \cos(\psi_i - \psi_j) + T_{ij}^+ \cos(\psi_i + \psi_j)] \quad (2.17)$$

with

$$\psi_i = k_i(x - x_0) - \omega_i(t - t_0) + \epsilon_i \quad (2.18)$$

$$\psi_j = k_j(x - x_0) - \omega_j(t - t_0) + \epsilon_j. \quad (2.19)$$

The kernel functions  $T_{ij}^+$  and  $T_{ij}^-$  are given in [158] and depend on the number of considered wave components  $i$  and  $j$ . With  $\epsilon_i = \epsilon_j = 0$  the phase-tuned components of the discretised wave spectrum have a wave crest at the focus location  $x_0$  and focus time  $t_0$ . A total number of  $N$  wave components is used and the spectral amplitudes  $a_i$  and  $a_j$  correspond to the  $i$ th and  $j$ th wave component at angular frequencies  $\omega_i$  and  $\omega_j$ .

Sriram et al. [161] enforce a constant steepness for the definition of the spectral amplitudes. In contrast, in this study the amplitude of every spectral component is determined similar to [14, 150, 151] as:

$$a_i = A_0 \frac{S_i(f) \Delta f}{\sum_{i=1}^N S_i(f) \Delta f} \quad (2.20)$$

with the spectral density components  $S_i(f)$  of a specified wave spectrum, for example the JONSWAP spectrum. The wave frequency step size  $\Delta f$  is based on the number of wave components  $N$  and the bandwidth with the lower and upper cut-off frequencies, and the target linear amplitude of the phase-focused wave group  $A_0$ . Hence, each spectral amplitude scales as the power density within the assumed frequency band [151].

Finally, the longitudinal and vertical velocity components  $u$  and  $w$  are calculated as the partial derivatives of the velocity potential. Results of equations 2.15, 2.21 and 2.22 are inputs to the numerical wave generator described in Section 3.3.1.2.

$$u(x, z, t) = u^{(1)} + u^{(2)} = \frac{\partial \phi^{(1)}}{\partial x} + \frac{\partial \phi^{(2)}}{\partial x} \quad (2.21)$$

$$w(x, z, t) = w^{(1)} + w^{(2)} = \frac{\partial \phi^{(1)}}{\partial z} + \frac{\partial \phi^{(2)}}{\partial z}. \quad (2.22)$$

## 2.6 Experimental Model Testing

During the design process of FOWT, numerical simulations are usually combined with tests of a scaled model in a wave basin with or without winds. The experiments are necessary for the validation of numerical assumptions and to reduce uncertainties in the load predictions for the prototype testing.

## Literature Review

Several test campaigns were published in the past. Most commonly known are the DeepCwind semi-submersible wind turbine tests by Goupee et al. [162] and from Robertson et al. [163], which are used in the Phase II of the OC5 project [34]. Mueller et al. [164] compare the scaling methodologies and critical issues of various wave tank test campaigns of FOWTs and provide practical recommendations for modelling and building of scaled rotors. In the European project INNWIND.EU model scale tests of a FOWT at 1/45<sup>th</sup> scale, which represents the 5 MW OC4 DeepCwind semi-submersible, and at 1/60<sup>th</sup> scale, which represents a generic 10 MW FOWT, were conducted at École Centrale de Nantes [92, 165]. A low-Reynolds number, pitch-controlled rotor was used. Free decay, tests with regular and irregular waves, wind, and combined wind/wave tests were performed. Another campaign addressed active blade pitch control of the TripleSpar semi-submersible conceptual design with a scaled 10 MW turbine [166, 167]. In the European research project LIFES50+ new methodologies for model testing based on Hardware-in-the-Loop (HIL) were developed to represent either the hydrodynamic [168] or the aerodynamic loads [169–171] using a real-time controlled force actuator. Recommended practices on model testing including additional information on the challenges, guidance on the test selection as well as calibration and validation of the numerical models are provided in [63].

## Similarity Laws

In general, accurate reproduction of the motions and loads of a (full scale) prototype relies on a scale model, which satisfies certain similarity laws related to the geometry (length), kinematics (velocity) and/or dynamics (force). In this context three types of internal forces are considered for the fluids: inertial forces due to fluid particle acceleration, gravitational forces due to the weight of the fluid itself and viscous forces due to the difference in shear forces acting on the fluid particles [90].

In model tests for offshore engineering and also FOWTs, the application of the Froude scaling law is a common approach because the gravity waves are the dominant external disturbance. The Froude number describes the square root of the ratio of the inertial to the gravitational forces and is defined as:

$$Fr = \frac{u}{\sqrt{gL}} \quad (2.23)$$

with characteristic velocity  $u$ , characteristic length  $L$  and gravity  $g$  [101, 103, 104]. For deeply submerged offshore bodies and pipe flow, the Reynolds scaling law is applied. This is also the case for wind tunnel experiments which focus on the aerodynamics of the rotor blades and the airfoils because viscous forces from wall friction and vortex shedding are the dominating forces.



The Reynolds number is defined as the ratio of inertial to viscous forces with the kinematic viscosity  $\nu$  [95, 172]:

$$Re = \frac{uL}{\nu}. \quad (2.24)$$

If both the Froude and Reynolds numbers are the same between the model and the prototype (full) scale, the flow around the floating body can be regarded as similar. However, this requirement cannot be fulfilled in practice for the experimental model testing of FOWT. This can be explained by looking at the Equations 2.23 and 2.24. The assumption of  $Fr_m = Fr_p$  results in  $u_m < u_p$  if  $L_m < L_p$  (with  $g_m = g_p$ ), but for  $Re_m = Re_p$ , this means  $u_m > u_p$  if  $L_m < L_p$  (with  $\nu_m = \nu_p$ ). Hence, the ratio of Froude to Reynolds number cannot be held constant, unless the gravitational acceleration is increased significantly, for example by using centrifugal devices, or the kinematic viscosity, which is temperature dependent, is decreased considerably. For FOWTs the mismatch between the Reynolds and the Froude number can be reduced by re-designing the rotor with airfoils of low Reynolds number, where rotor thrust and structural flexibilities of the blades need to be considered carefully. An alternative would be to use HIL testing methodologies, where hydrodynamics or aerodynamics are represented through real-time simulations. An overview of selected scaling factors applying the Froude scaling is shown in Table 2.1 with  $\lambda = L_p/L_m$  and the fluid density ratio between prototype and model scale  $\rho_p/\rho_m$ , see also [137].

**Table 2.1:** Summary of selected scaling factors applying Froude’s scaling law.

Quantity	Unit	Scaling Factor
Length	[m]	$\lambda$
Mass	[kg]	$\frac{\rho_p}{\rho_m} \lambda^3$
Time	[s]	$\sqrt{\lambda}$
Velocity	[m s <sup>-1</sup> ]	$\sqrt{\lambda}$
Acceleration	[m s <sup>-2</sup> ]	1
Frequency	[s <sup>-1</sup> ]	$\frac{1}{\sqrt{\lambda}}$
Force	[N]	$\frac{\rho_p}{\rho_m} \lambda^3$



# 3

## Simulation Environment and Setup

After the theoretical principles were presented in the previous Chapter, the following Chapter deals with the simulation environment and setup. The Multibody approach is introduced in Section 3.1 and the coupling methodology of the Multibody and CFD models is described in detail in Section 3.2. The setup of a NWT is explained in Section 3.3 together with a sensitivity analysis of the main numerical parameters in Section 3.4. Then, a baseline simulation procedure, applied for coupled simulations in the following Chapters, is highlighted in Section 3.5. Finally, Section 3.6 provides recommended practices with a strong focus on the modelling aspects.

### 3.1 Multibody Approach and Model Topology

A modular simulation environment that allows different levels of model fidelity is set up to analyse the dynamic behaviour of a FOWT system. The physical representation of the structure is coupled to the external loads and the wind turbine control system, using the MBS approach. The software SIMPACK by Dassault Systèmes is selected for this research and coupled to modules for aerodynamics, hydrodynamics and effects of the mooring and control system. The model complexity is increased in this study, for example by representing the RNA and tower of the wind turbine as a lumped mass in Chapter 4 and Section 5.4 and as a full MBS model in Section 5.5. Hence, the number of DOFs differs between the models and complete submodels in the MBS representation are replaced. The baseline MBS model is described with the help of a model topology, shown in Figure 3.2. In general, structural properties such as mass, centre of gravity and moments of inertia are used to specify each wind turbine component.

### 3.1.1 Substructuring of Multibody Model

The main MBS model is organised with the help of separated SIMPACK submodels. A visualisation of a SIMPACK model is presented in Figure 3.1, which shows an exemplary FOWT system. Each major wind turbine component is associated to one submodel allowing a proper model organisation and an easy exchange of variations. Submodels are created for the floating substructure, tower, yaw bearing, nacelle, hub and for every blade. In addition, the ground is included in a submodel to ensure compatibility with the bottom-fixed MBS models. External force elements, for example for the calculation of the aerodynamic rotor loads, are combined in a single submodel to improve the model organisation. The same applies to the result elements that generate output data for selected sensors using different formats.

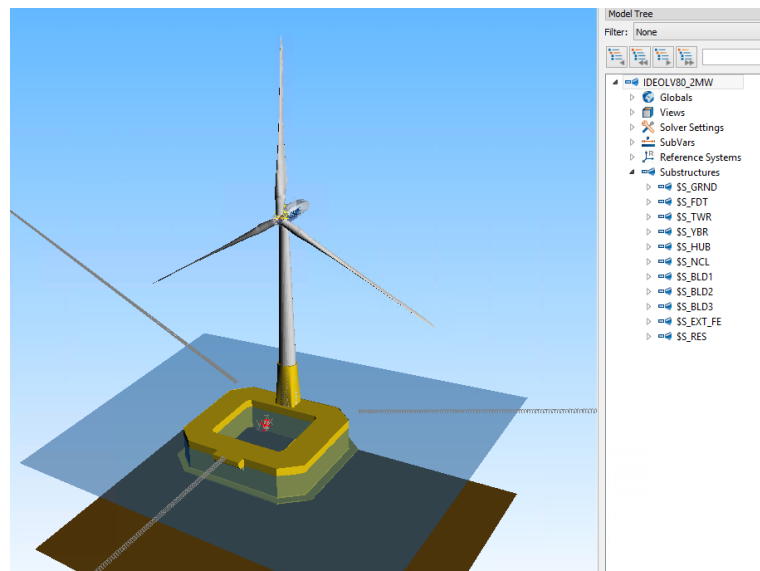


**Figure 3.1:** Illustration of an exemplary SIMPACK model with the topology of submodels.

### 3.1.2 Model Degrees of Freedom

A baseline topology of a MBS model of a FOWT is shown in Figure 3.2. It is modified for the individual simulation objectives in the Sections 4.2.1 and 5.1. In general, stiffness and damping of the components are included as spring-damper elements. A physical model that includes the effects of the ground on bottom-fixed structures, such as monopiles and piles for jackets or anchors, is not necessary but included to comply with a general MBS topology. The floating substructure is free to move and connected to the ground submodel using six rheonomic joints that constrain the movement to selected DOFs. The ground is fixed to the Inertial Reference Frame (ISYS) using a zero DOF joint. Depending on the desired level of complexity and the symmetry of the investigated structure, the kinematics of the floating substructure can be restricted to the three predominant DOFs surge, heave and pitch. The mooring system is

modelled as a set of mooring lines each with an external force acting on the substructure. Each mooring line is anchored to the seabed using a zero DOF joint and connected rigidly to the floating substructure at the fairleads. Hydrodynamic loads are applied as external loading at the substructure based on the results from a hydrodynamic force model – in this study from a CFD model. To simplify the exchange of the submodel variations, the flexible tower is mounted with zero DOFs to the TP (rigid connection) that is included in the substructure. Translational and rotational movement of the tower base connection are modelled with a six DOFs joint and additional stiffness and damping. The yaw bearing connects the nacelle with the tower with rotational DOFs and its yaw-position is calculated by a controller which may be overridden by a fixed value. The high- and low-speed shaft in the nacelle are free to rotate based on the gear ratio. The hub is connected to the nacelle using zero DOFs. It holds the three rotor blades that experience aerodynamic forcing at specified aero markers and are free to rotate in pitch direction. The blade pitch actuators are moved by the control system which is implemented by a Bladed-style dll-Interface. The controller also provides the required generator torque based on the rotor speed. Only the tower and rotor blades are flexible bodies in the MBS model with a maximum eigenfrequency and a maximum number of eigenmodes (modal reduction).

### 3.1.3 Force Elements

External forces on the floating system are included as force elements. Aerodynamic loads can be applied to the rotor blades using the BEM model AeroDyn, developed by NREL. Extreme wind conditions and the resulting wind loads on the tower are implemented calculating the sectional drag forces along the tower sections. Both force elements are calculated locally at specified markers and consider the current wind speed and the relative velocity. The later is due to the rigid body motion of the FOWT as well as to the deformation of the flexible tower and blades. More details on the aeroelastics are included in Sections 2.4.2 and 2.4.3.

Hydrodynamic loads on the floating substructure can be determined using different modelling approaches described in Section 2.4.4. Hydrodynamics based on the Morison equation and the potential flow theory can be incorporated by the HydroDyn model, developed by NREL. The software CFX from ANSYS is used for high-fidelity modelling applying the CFD method. ANSYS CFX is coupled to the SIMPACK solver by using an additional force element, called FLUID2SPCK. It ex-changes motion and loads information between the MBS and CFD solvers during the simulation and is described in more detail in the following section.

Mooring lines are modelled with different physical approximations described in Section 2.4.5. In this study, a simple representation of a global linear stiffness matrix was chosen. Its implementation and calibration is presented in Section 4.2.2. In addition, the required generator torque is set by the control system and applied to the high-speed shaft.

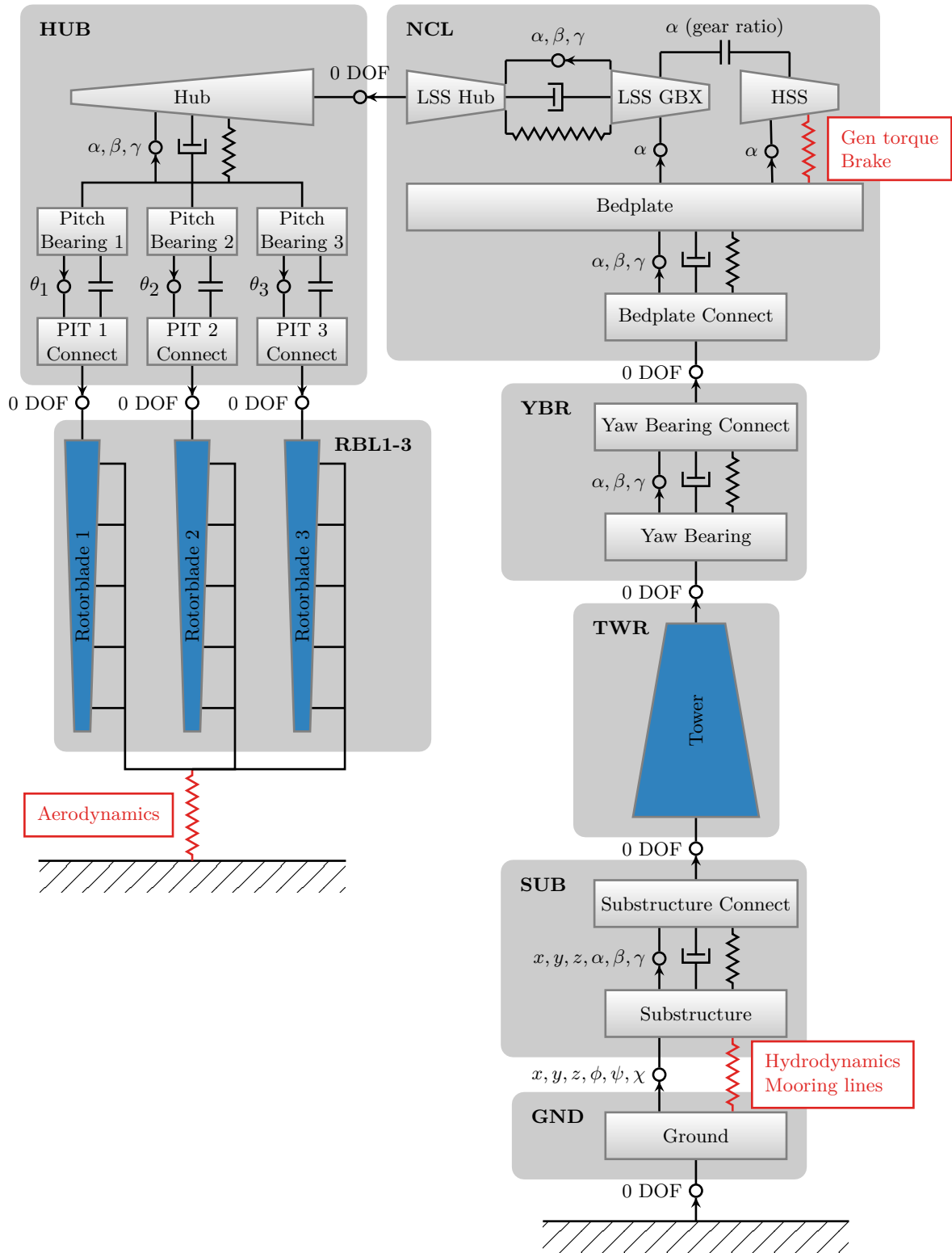


**Figure 3.2:** General topology of an exemplary wind turbine MBS model with flexible bodies displayed in blue and force elements in red. The DOFs are indicated. The submodels are named as GND = Ground, SUB = Substructure, TWR = Tower, YBR = Yaw bearing, NCL = Nacelle, HUB = Hub and RBL = Rotorblade.

## 3.2 Coupling of Multibody and CFD Model

A simulation environment based on a coupling between MBS and CFD was setup for the analysis of a FOWT. Hydrodynamics are calculated with the CFD code ANSYS CFX. It uses the FVM to solve the URANS equations on structured and unstructured grids. The free surface is modelled with the VOF method that computes the shape and location of the free surface on the basis of a fractional volume function [173]. The MBS solver SIMPACK is used to model the structural dynamics, aerodynamics, restoring forces from the mooring system and controller effects.

Besides the analysis of fluid-structure interaction on tidal current turbines [37], the coupling methodology was applied for the investigation of wake-induced aeroelastic effects in wind farm arrays by [174] and [175] using the open source free wake code Wake-induced Dynamic Simulator (WINDS) with SIMPACK. Furthermore, the CFD code FLOWer of the German Aerospace Center (DLR) was coupled to SIMPACK [93] to study aeroelasticity and aeroacoustics of wind turbine rotor blades using a similar methodology.

### 3.2.1 Motivation

The reasons for the development and application of a MBS-CFD coupling are the following. In general, a standard FSI based on FEM and CFD that includes the influence of the flexible bodies has the drawback of very high computational efforts. Modal reduction in MBS provides an elegant and more efficient solution for complex and large structures, such as FOWTs, where body flexibilities of the tower, rotor blades and drive train are very important. However, if CFX is applied as a standalone tool, only rigid bodies can be investigated with very limited complexity such as simple spring-damper elements for the mooring system. The MBS-CFD simulation environment enables an integrated analysis of a complete FOWT considering aero-, servo- and hydrodynamics as well as structural elasticity. Complex and reduced models are possible because rigid and flexible body DOFs as well as different implementations of force elements can be activated or deactivated according to the specific research question. Thus, sensitivity studies with different levels of model fidelity are feasible, for example, from a full CFD application for the aero- and hydrodynamics to combined variations of CFD and engineering methods, such as BEM, for the aerodynamics. The control system can also be taken into account in a coupled MBS-CFD simulation when a full wind turbine model is simulated.

On the other side, the functionality, applicability and accuracy of coupled algorithms have to be validated, ideally by experimental data. In addition, the MBS-CFD approach still requires significant computational resources compared to the state-of-the-art methods in wind turbine engineering and is not suitable for complete design studies with hundreds of simulations, such as a full series of DLCs according to the IEC standard.

### 3.2.2 Coupling Methodology

The baseline code and scripts of the MBS-CFD coupling were developed by Arnold [37] for the simulation of fluid-structure interaction on tidal current turbines. A validation based on submerged free-decay experiments of spring, gravity and bending pendulums in a water tank is presented in [176]. The study demonstrated the validity of the methodology with an excellent agreement between numerical and experimental results. The coupling methodology is introduced in the following Section, more details are described in [37]. This research contributed to the iteration scheme and the monitoring of convergence.

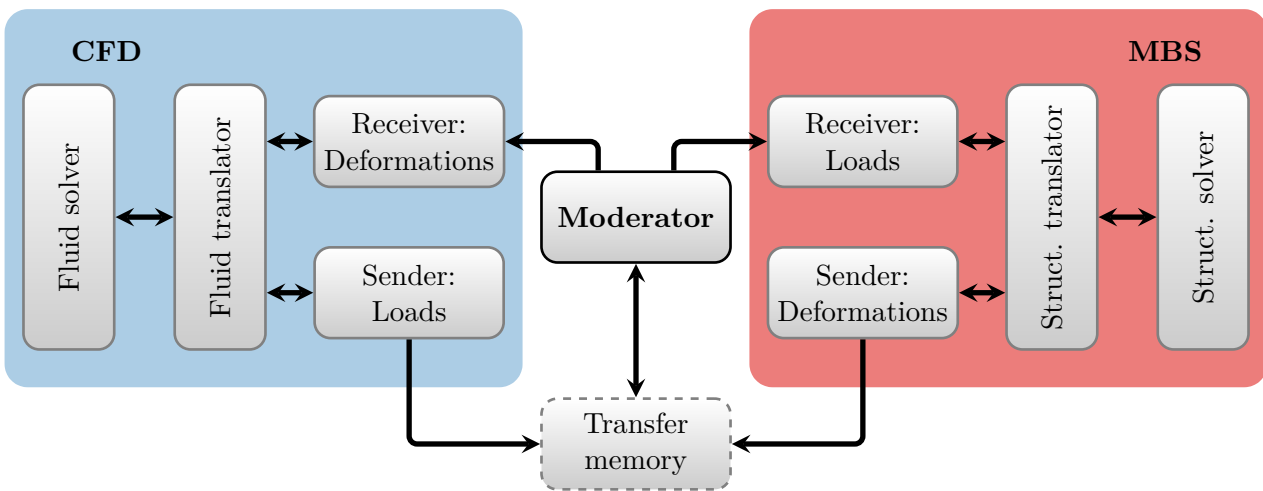


**Figure 3.3:** General scheme of the MBS-CFD coupling methodology.

The methodology of the MBS-CFD coupling is based on four major tasks which are implemented for the existing simulation codes by adding additional functions, see Figure 3.3. The sender, receiver and translator are code-specific while the moderator interacts on a global level in between the codes. In principle, the MBS code calculates the deformations, which are communicated with the CFD code that calculates the fluid loads.

The MBS solution provides response at discrete locations, the so called markers. For data exchange, the communication markers are associated to the MBS bodies at which the three-dimensional translational and rotational vector are available. The interface between the structural solver and the input/output functions is the structural translator. It collects the deformation data at the communication markers in the communication reference frame, with three translational and three rotational values per communicated marker. The structural sender stores the deformation data in the transfer memory. The communication data are written in ASCII-formatted files and stored. The structural receiver reads the loads data from CFD code. The forces and moments of the fluid solver are transformed by the structural translator from the communication reference frame to the body reference frame of the MBS model and are applied at the communication markers.



On the CFD side the fluid translator determines the local deformation of the grid using an inter- or extrapolation of the six available values of the deformation at the communication markers. This procedure is split into two tasks, the coordinate transformation and the surface mapping. In addition, the surface pressure and wall shear distribution from the CFD simulation are integrated on the surface mesh of the body in the communication reference frame as the MBS model has no information on the surface geometry and requires discrete global loads at the communication markers. The resulting three-dimensional hydrodynamic forces and moments, leading to six load components per communication marker, are stored in the transfer memory by the fluid sender, while the fluid receiver reads the deformation data from the MBS simulation.

The moderator controls the iteration process by communicating to the MBS and the CFD solver to wait until the other code has finished the iteration, to continue with the current time step iteration or to move to the next time step. To moderate, status files are used during the coupled simulation. Furthermore, the moderator controls the convergence by using target residuals for the deformation and the loads and checks the minimum and maximum number of iterations per time step.

### 3.2.3 Iteration Scheme

In the case of a FOWT, the volumetric mass density of the fluid water ( $\rho_{\text{water}} = 1,025 \text{ kg m}^{-3}$ ) is in the order of magnitude of the structural density of the wind turbine substructure ( $\rho_{\text{concrete}} = 1,500 \text{ kg m}^{-3}$  to  $2,500 \text{ kg m}^{-3}$ ) and tower ( $\rho_{\text{steel}} = 7,850 \text{ kg m}^{-3}$ ). This can result in a stability problem if an explicit coupling scheme is used as it requires that the fluid density is much smaller than the structural density ( $\rho_{\text{fluid}} \ll \rho_{\text{structure}}$ ). The literature describes the stability problem as artificial added mass effect [37, 177]. Hence, a fully implicit iteration scheme, presented in Figure 3.4, is used in the MBS-CFD coupling for transient simulations.

The coupled simulation is initialised by running the moderator script `.pl`, which is written in Perl programming language. The script is structured in two major loops, one for the transient simulation and the second one for the implicit iteration and relaxation. First, it reads an ASCII-input file `.ipt` that contains information about the simulation case: name, directory, identifier, flags for logging and start-up ramps, relaxation factors for the loads and deformations, target residuals, minimum/maximum number of iterations per time step and backup interval.

Subsequently, the structural solver performs the time integration at time  $t$ , time step  $n$  and iteration number  $i_{\text{struct}} = 1$ . As no loads from CFD exist yet at the beginning of the coupled simulation, the external loads are set to zero in the first structural integration of the first time step. After the structural solver is finished, the deformations are written to the data file `.spck2fluid` and the solver closes. In addition, a status file `.spckready` is sent to instruct the fluid solver to stop waiting for the structural solver.

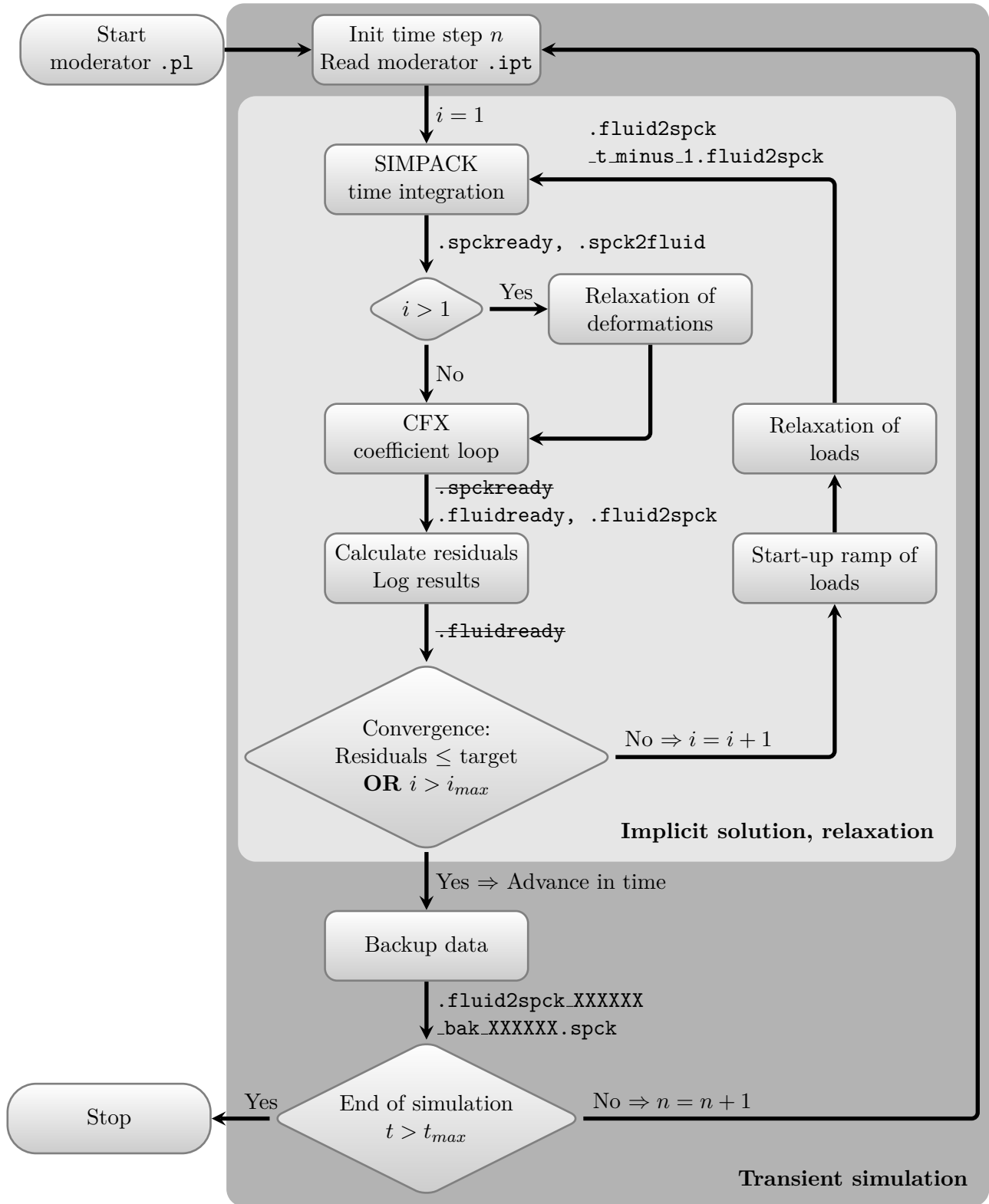


**Figure 3.4:** Flowchart of the MBS-CFD coupling iteration scheme with coupling time  $t$ , time step  $n$  and iteration counter  $i$ . Crossed out names indicate deleted files.

The fluid solver then reads the deformations from `.spck2fluid`, deletes the file `.spckready`, starts its first inner integration ( $i_{\text{fluid}} = 1$ ), called coefficient loop in the ANSYS CFX terminology, calculates the new loads of the current time step  $n$  and stores them in the data file `.fluid2spck`. Again a status file, named `.fluidready`, is generated to indicate that the fluid coefficient loop is finished. Afterwards, the moderator reads the fluid loads from `.fluid2spck`, modifies the values by applying under relaxation ( $0 < r \leq 1$ ) to increase the solver stability and deletes the file `.fluidready`.

The structural time integration of time step  $n$  is then repeated for the second time ( $i_{\text{struct}} = 2$ ) with the updated loads from the first CFD run and the new deformations are calculated. The fluid solver again processes the updated deformations and performs the second coefficient loop ( $i_{\text{fluid}} = 2$ ) to increase the accuracy of the resulting loads. This iteration procedure within one time step is repeated until the convergence criteria for loads and/or deformations are met or the maximum number of iterations is reached.

After the iteration process of each time step is finished the moderator copies the converged loads from `.fluid2spck` to `_t_minus_1.fluid2spck` and jumps to the next time  $t + \Delta t$  (time step  $n + 1$ ). The iteration counter  $i$  is reset to one. The structural solver is restarted but now the loads originating from the previous time step  $n$  are assumed to be constant during the first structural time integration of the time step  $n + 1$ . For all the following structural solver integrations within each time step, the loads are interpolated based on the values of the previous (`_t_minus_1.fluid2spck`) and the current time step (`.fluid2spck`) and the time value of the inner integrator step. The implicit solution advances with alternating runs of the structural and fluid solver until convergence is obtained or a termination criterion is met.

The transient simulation proceeds until the time (or the time step), exceeds a maximum value  $t > t_{\text{max}}$  and the solvers are shutdown. During the coupled simulation the moderator stores backups of the communication data (`.fluid2spck_XXXXXX`) and SIMPACK model `_bak_XXXXXX.spck` to restart the simulation in case the solver aborts, where XXXXXX represents the time step as a six-digit integer. ANSYS CFX saves the backup models at user defined time intervals itself.

### 3.2.4 Code Implementation

The commercial solvers SIMPACK and ANSYS CFX allow interfacing of user defined FORTRAN code to include functionalities required for the MBS-CFD coupling. In case of SIMPACK, the force element FLUID2SPCK is added to the existing library by User Routines. It is evaluated by the structural solver in each inner integration step and is called for measuring and sending the deformations as well as receiving and applying the coupling loads. To implement the implicit iteration scheme with the User Routines in SIMPACK, the structural solver needs to be restarted for each time step iteration from the results of the last converged time step.

One has take into account that the magnitude of the communication time step needs to be identical for the structural and the fluid solver.

For ANSYS CFX the internal CFX Expression Language (CEL) is used to include User Fortran code that is evaluated during an iteration on all grid nodes for the spline based interpolation of the fluid translator. Additional Junction Box Routines for sending and receiving of the communication data, integration of loads and the abortion of the simulation are called at different locations during the solver execution. Based on this functionality and the implicit iteration scheme, inherently included in ANSYS CFX, the fluid solver is started once at the beginning of the coupled simulation and closed after the last coefficient loop of the last time step. Both User CEL Functions and Junction Box Routines are called User Routines in ANSYS CFX.

### 3.3 Modelling of Numerical Wave Tank in CFD

In the CFD simulation environment a NWT is build to capture the hydrostatic and -dynamic effects on the floating substructure. Different characteristics apply to the regions for wave generation, measurements and wave damping, see Figure 3.5. The measuring zone refers to the region where the FOWT is located. In the following Sections, required modelling techniques and important settings are described.

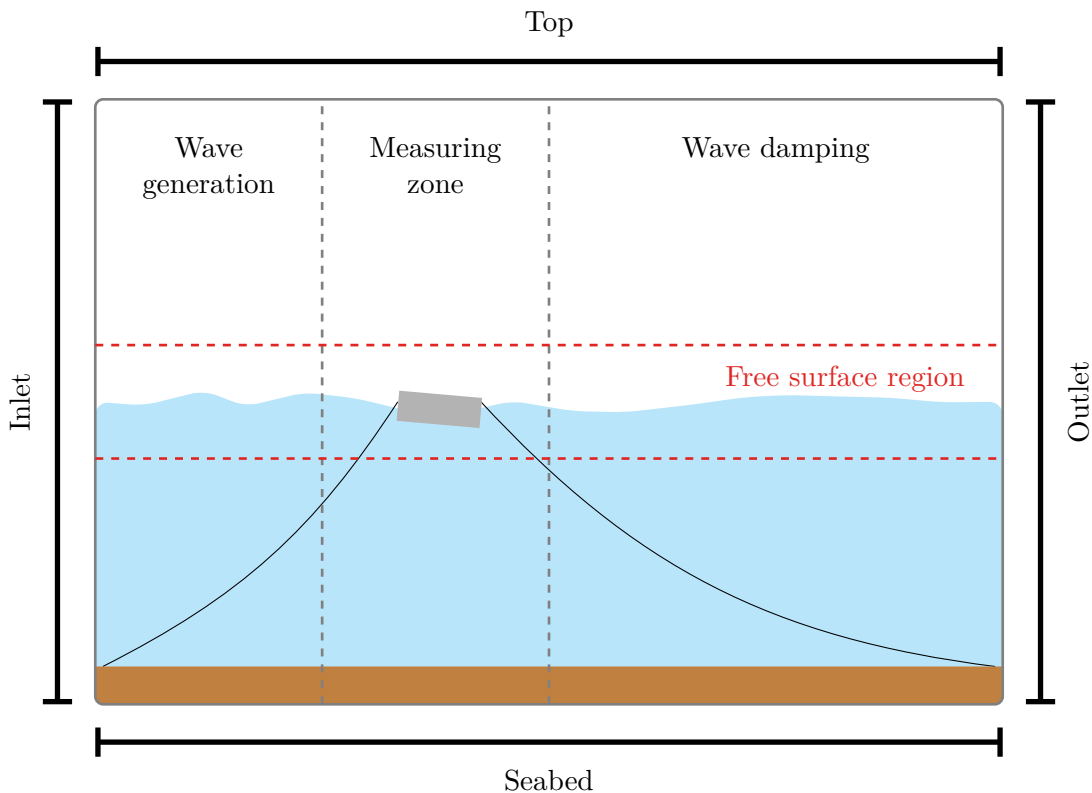


**Figure 3.5:** Schematic view of a NWT with spatial division of the domain and the boundary conditions. The phase boundary between the fluids water and air is located in the free surface region.

### 3.3.1 Wave Generation

Wave generation in ANSYS CFX is not included as a standard toolbox, such as in ANSYS Fluent, that allows the specification of wave properties at a boundary condition in the preprocessor. As consequence, a wave generator is developed and implemented using User Routines, see Figure 3.6. The calculated wave properties are applied at the velocity inlet boundary condition of the NWT. Only unidirectional wave propagation in positive  $x$ -direction is considered.

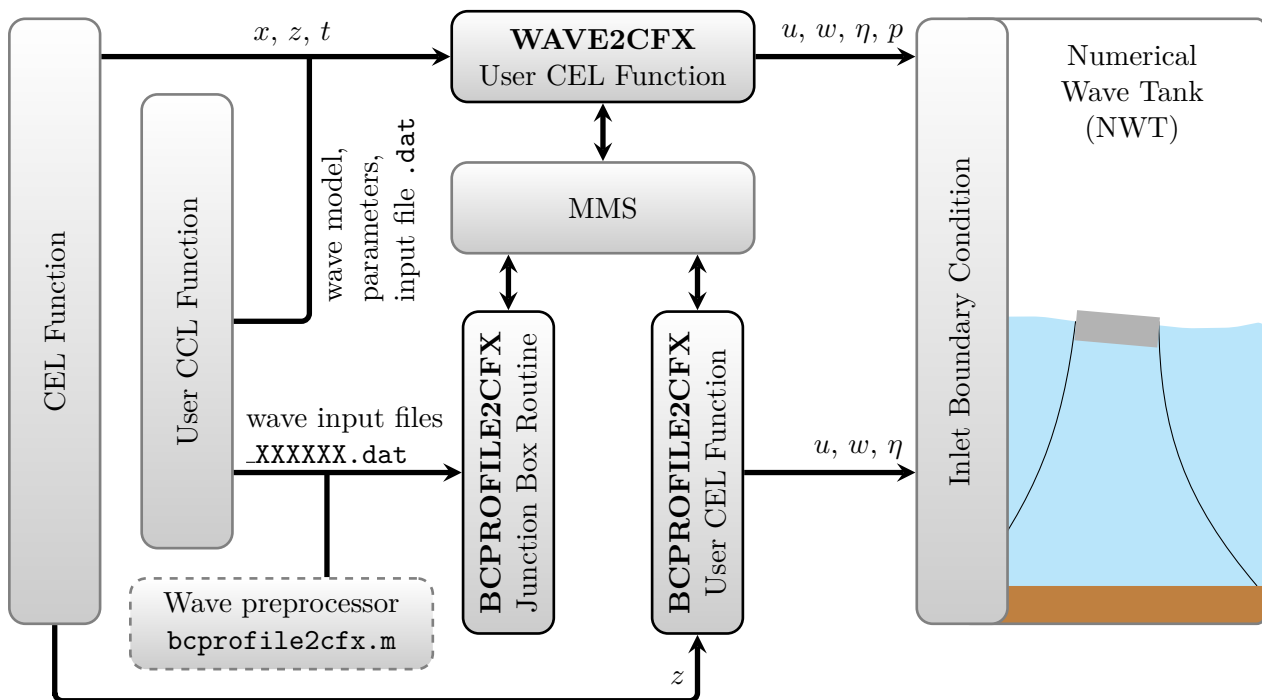


**Figure 3.6:** Scheme of the wave generation implementation in ANSYS CFX based on User Routines. The abbreviations CFX Command Language (CCL), CFX Expression Language (CEL) and CFX Memory Management System (MMS) relate to the ANSYS CFX terminology.

#### 3.3.1.1 WAVE2CFX User Routine

The first implementation called WAVE2CFX is a User CEL Function that is interfaced with the CFX Command Language (CCL) to select a wave theory and set associated parameters, such as wave height  $H$ , wave period  $T$ , wave length  $\lambda$  and phase  $\theta$ . The  $z$ -coordinate of the seabed and the water depth  $d$  define the offset of the wave generation with respect to the global coordinate system. Linear Airy wave theory is implemented with the possibility to define a wave spectrum, and the stream function theory of Fenton (based on Dean's stream function theory) as explained in more detail in Section 2.5.2. WAVE2CFX is evaluated in each iteration to calculate the longitudinal and vertical velocity components  $u$  and  $w$ , wave elevation  $\eta$  and pressure  $p$  as a function of the time  $t$  and the  $x$ - and  $z$ -coordinate of the grid nodes at the inlet.

On this basis the inlet boundary condition is specified with the Cartesian velocity components:

$$u(x, z, t) = \begin{cases} u_{w2c} & \text{if } z \leq z_{SWL} + \eta_{w2c} \\ 0 \text{ m s}^{-1} & \text{if } z > z_{SWL} + \eta_{w2c} \end{cases} \quad (3.1)$$

$$w(x, z, t) = \begin{cases} w_{w2c} & \text{if } z \leq z_{SWL} + \eta_{w2c} \\ 0 \text{ m s}^{-1} & \text{if } z > z_{SWL} + \eta_{w2c} \end{cases} \quad (3.2)$$

$$(3.3)$$

and volume fractions  $\varphi$  for water and air:

$$\varphi_{\text{air}}(x, z, t) = \begin{cases} 1 & \text{if } z > z_{SWL} + \eta_{w2c} \\ 0 & \text{if } z \leq z_{SWL} + \eta_{w2c} \end{cases} \quad (3.4)$$

$$\varphi_{\text{water}}(x, z, t) = \begin{cases} 1 & \text{if } z \leq z_{SWL} + \eta_{w2c} \\ 0 & \text{if } z > z_{SWL} + \eta_{w2c} \end{cases} \quad (3.5)$$

with subscript  $(\cdot)_{w2c}$  indicating values calculated by the CEL function WAVE2CFX and the SWL  $z_{SWL}$ . In order to model a regular wave, which represents a sinusoidal function that starts with zero and increases with the time, the initial phase  $\theta_0$  is calculated according to:

$$\theta_0 = \frac{\pi}{2} - kx_{\text{inlet}} = \frac{\pi}{2} - \frac{2\pi}{\lambda}x_{\text{inlet}}. \quad (3.6)$$

and included in the input file, which is read by WAVE2CFX. Due to its simplicity the User CEL function WAVE2CFX is applied for the generation of regular Airy waves in this research.

### 3.3.1.2 BCPROFILE2CFX User Routine

To be more flexible in terms of the applied wave theories and the inclusion of wave kinematics from experiment, a second wave generator, called BCPROFILE2CFX, is implemented. A Junction Box Routine, that is called during the solver execution at the beginning of each time step, reads wave input data, stored in ASCII-files and generated with a MATLAB preprocessing script `bcprofile2cfx.m`, see Figure 3.6. The base filename is defined by the user in User CCL. Each time step is associated to a unique file containing the wave kinematics  $u(z)$  and  $w(z)$  as well as the wave elevation  $\eta(z)$  as function of the vertical coordinate  $z$ . The wave data are further processed by a User CEL function that calculates the velocity components at all grid nodes at the inlet boundary using linear interpolation. Thus, it is beneficial to set the grid resolution of the wave input data in  $z$ -direction similar to the spatial discretisation at the inlet. This is done by exporting a dummy boundary condition profile at the inlet by ANSYS

CFD-Post and utilise it as a template for the wave preprocessor. In contrast to the wave generation with WAVE2CFX, no dependency on  $x$  and  $t$  is necessary as the water particle velocities and volume fractions are directly imposed at the inlet boundary condition, which results in a boundary profile according to the following equations:

$$u(z) = u_{b2c} \quad (3.7)$$

$$w(z) = w_{b2c} \quad (3.8)$$

$$\varphi_{\text{air}}(z) = \begin{cases} 1 & \text{if } z > z_{\text{SWL}} + \eta_{b2c} \\ 0 & \text{if } z \leq z_{\text{SWL}} + \eta_{b2c} \end{cases} \quad (3.9)$$

$$\varphi_{\text{water}}(z) = \begin{cases} 1 & \text{if } z \leq z_{\text{SWL}} + \eta_{b2c} \\ 0 & \text{if } z > z_{\text{SWL}} + \eta_{b2c} \end{cases} \quad (3.10)$$

with subscript  $(\cdot)_{b2c}$  referring to values calculated by the CEL function BCPROFILE2CFX. The communication between the Junction Box Routine and User CEL function is realised through the CFX Memory Management System (MMS). In principle, arbitrary boundary profiles can be applied to the wave preprocessor. In this research the methodology is used especially for the generation of extreme waves from focused wave groups, described in detail in Section 2.5.3.

### 3.3.1.3 Ramp Function

To avoid unsteadiness and to increase solver stability at the start of the wave generation, a ramp function  $R(t)$  is used, presented Equation 3.11 and Figure 3.7. The time dependent, non-dimensional function value ranges from  $0 \leq R(t) \leq 1$  and is multiplied by the horizontal and vertical velocity components and wave elevation to fade in the waves within a specified time frame  $t_R$ . In general, a value of  $t_R = 2T$  is sufficient.

For tuning of the wave height at specific wave gauges located in the NWT, it is beneficial to apply a linear wave scaling factor  $L$  as the numerical damping of the waves in the CFD domain using Cartesian mesh is almost linear. The ramp function is disadvantageous when using the focused wave groups generated by the BCPROFILE2CFX User Routine and the MATLAB preprocessor because of the unwanted damping of wave components and the resulting shift of focus time and location.

$$R(t) = L \begin{cases} 1 & \text{if } t > t_R \\ 0.5 \left[ 1 - \cos\left(\pi \frac{t}{t_R}\right) \right] & \text{if } t \leq t_R \end{cases} \quad (3.11)$$

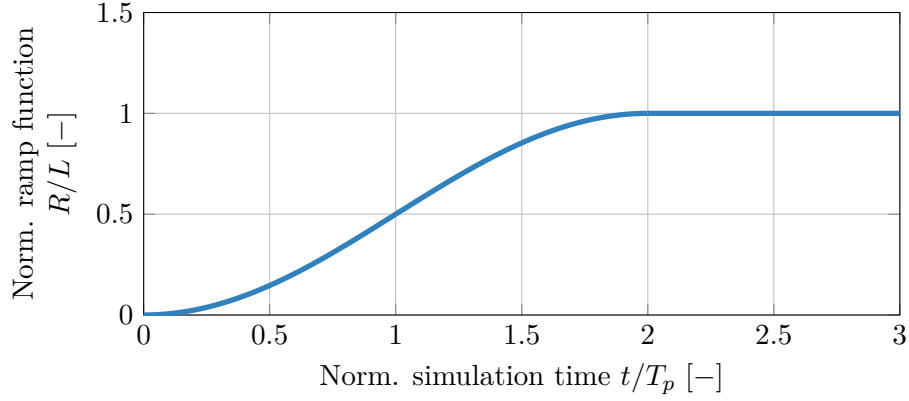


**Figure 3.7:** Ramp function with  $t_R = 2T$  used for the wave generation in transient simulations.

### 3.3.2 Numerical Beach

After the generated waves pass the object to be examined within the measuring zone, wave damping is required to mitigate wave reflection at the end of the NWT. If the damping is insufficient the reflected waves will interfere with incident waves from the wave generator leading to undesired flow phenomena. Wave damping is either accomplished by modelling of a sloped seabed and beach, similar to the reality, or by including an additional numerical damping, implemented in this work. Two approaches are used to implement a numerical damping. First, the size of grid cells in the damping zone is increased towards the outlet. Second, momentum sources  $S_M$  in  $x$ - and  $z$ -direction are added in the computational domain of the Numerical Beach (NB) as defined as:

$$S_{M,x} = \begin{cases} -C_{M,x} 0.5 \rho_f |u| u f_{M,x} \varphi_{\text{water}} & \text{if } x \geq x_s \\ 0 \text{ kg m}^{-2} \text{ s}^{-2} & \text{if } x < x_s \end{cases} \quad (3.12)$$

$$S_{M,z} = \begin{cases} -C_{M,z} 0.5 \rho_f |w| w f_{M,x} f_{M,z} \varphi_{\text{water}} & \text{if } x \geq x_s \\ 0 \text{ kg m}^{-2} \text{ s}^{-2} & \text{if } x < x_s \end{cases} \quad (3.13)$$

with the scaling factors  $C_M$  of unit  $\text{m}^{-1}$  in  $x$ - and  $z$ -direction, the fluid density  $\rho_f$  for either water or air and additional functions  $f_M$ :

$$f_{M,x} = \left( \frac{x - x_{\text{NB},s}}{x_{\text{NB},e} - x_{\text{NB},s}} \right)^2 \quad (3.14)$$

$$f_{M,z} = 1 - \left( \frac{z - z_{\text{SWL}}}{z_{\text{seabed}} - z_{\text{SWL}}} \right). \quad (3.15)$$

The  $x$ -location at the start and end of the NB are defined by  $x_{\text{NB},s}$  and  $x_{\text{NB},e}$  respectively. The vertical position of the seabed boundary condition is considered by  $z_{\text{seabed}}$ . Only water



particles up to the free surface are damped numerically because of the multiplication with the water volume fraction  $\varphi_{\text{water}}$ . The momentum source distribution in the NWT is illustrated in Figure 3.8 for a water velocity of  $1 \text{ m s}^{-1}$  in the  $x$ - and  $z$ -direction without waves. The magnitude of  $S_M$  is negative in the NB and outside zero. The smooth transition from the measuring to the damping zone at  $x_{\text{NB},s}$  avoids wave reflections. To improve the start-up behaviour and to increase the solver stability, a ramp function is implemented for each momentum source, similar to Equation 3.11 with  $t_R = t_{\text{NB},R} = 10n$ .

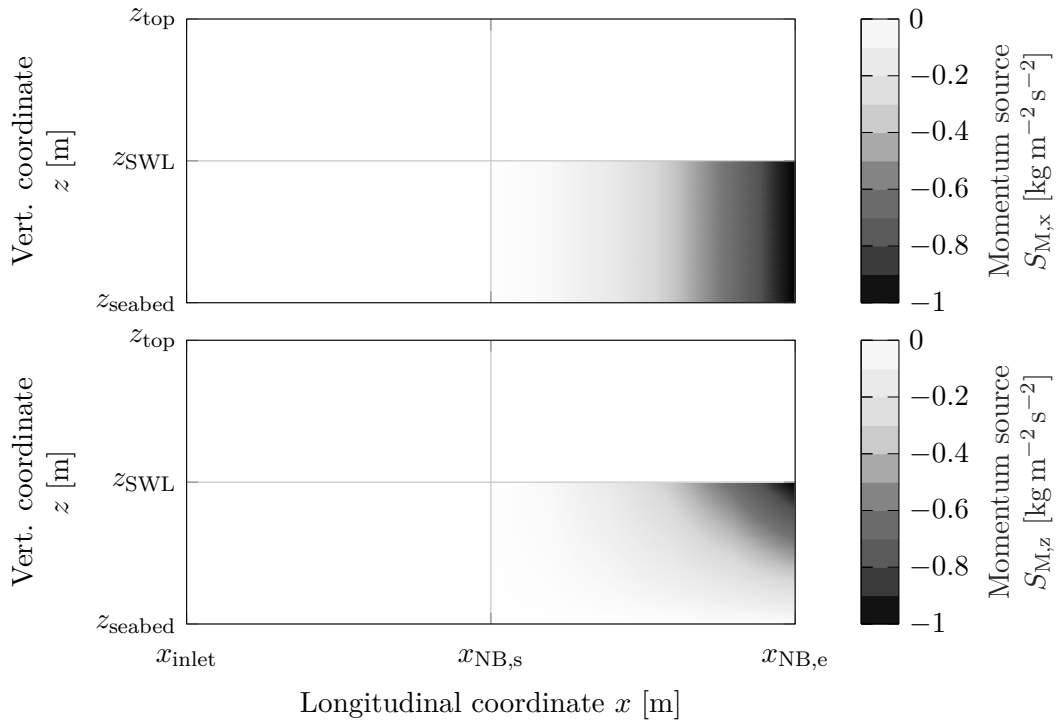


**Figure 3.8:** Illustration of the momentum sources  $S_{M,x}$  and  $S_{M,z}$  for modelling of the NB. The water velocity in the  $x$ - and  $z$ -direction is  $1 \text{ m s}^{-1}$  and waves are not present for illustration purposes. The colour gradient from white to black represents zero and maximum numerical damping.

### 3.3.3 Boundary Conditions

Different configurations of the NWT model are needed. Wave calibration is performed without the floating substructure in a two-dimensional domain extending only one cell in  $y$ -direction. The calibration of the wave conditions is needed because a numerical damping is inherently present and the wave, which is generated at the inlet boundary condition, decreases in height over the length of the CFD domain. In addition, the solver settings, such as the turbulence model or the spatial and temporal discretisation, influence the wave propagation. On the other hand, transient simulations with waves are performed in a three-dimensional domain with the floating substructure located within the measuring zone, see Figure 3.5.

Generally speaking, boundary conditions influence in particular the outcome of the CFD analysis because they are needed to solve the Navier-Stokes equations in the FVM scheme, see Section 2.4.4.3. Therefore, it is important to adjust the boundary conditions for the objectives of the simulation. A summary of the boundary conditions for the implemented setups of the NWT is given in Table 3.1.

**Table 3.1:** Summary of the boundary conditions for different setups of the NWT. Wave calibration is performed in a 2D domain, while free-decay of the substructure or transient motion in waves are simulated in 3D.

Name	Type	Application	Boundary details
Inlet	Inlet	Wave calibration, transient simulation of substr. in waves	Cartesian velocity components: $u, w$ Turbulence: zero gradient (fully developed flow) Volume fractions: $\varphi_{\text{air}}, \varphi_{\text{water}}$ Mesh motion: stationary
	Wall	Free-decay simulation	Free slip wall (without wall friction) Mesh motion: stationary
Outlet	Opening	Wave calibration, transient simulation of substr. in waves	Static pressure and direction: hydrostatic pressure distribution $p_{\text{outlet}}$ (Equation 3.16) Flow direction: normal to boundary Turbulence: zero gradient Volume fractions: $\varphi_{\text{air,init}}, \varphi_{\text{water,init}}$ Mesh motion: stationary
	Wall	Free-decay simulation	Free slip wall Mesh motion: stationary
Seabed	Wall	All cases	No slip wall (with wall friction) Wall roughness: smooth wall Mesh motion: parallel to boundary
Top	Opening	All cases	Entrainment: 0 Pa relative pressure with opening pressure option Turbulence: zero gradient Volume fractions: $\varphi_{\text{air}} = 1, \varphi_{\text{water}} = 0$ Mesh motion: parallel to boundary
Sidewall	Symmetry	All cases	Mesh motion: stationary
Substructure, Transition piece	Wall	All cases except for wave calibration	No slip wall Wall roughness: smooth wall Mesh motion: specified displacement $\Delta x, \Delta y, \Delta z$ according to Eqs. 3.19 to 3.21

The wave properties, calibrated in the initial step, are read by the wave generator at the inlet boundary condition, see Figure 3.6. After the waves develop and pass the measuring zone, they are damped within the NB. To prevent the NWT from filling up with water or running out over the simulation time, if the mass flow rate between the inlet and outlet becomes ei-

ther  $\Delta\dot{m} = \dot{m}_{\text{outlet}} - \dot{m}_{\text{inlet}} < 0 \text{ kg s}^{-1}$  or  $\Delta\dot{m} > 0 \text{ kg s}^{-1}$ , the outlet is modelled with an opening boundary condition. It is described with a pressure distribution  $p_{\text{outlet}}(z)$  depending on whether the fluid air is modelled as compressible or incompressible in CFD:

$$p_{\text{outlet}}(z) = \begin{cases} \rho_{\text{water}}g(z_{\text{SWL}} - z) & \text{if } z \leq z_{\text{SWL}} \\ 0 & \text{if } z > z_{\text{SWL}} \text{ and incompressible air} \\ p_{\text{motion}}(z) & \text{if } z > z_{\text{SWL}} \text{ and compressible air} \end{cases} \quad (3.16)$$

with the acceleration of gravity  $g$  and:

$$p_{\text{motion}}(z) = p_{\text{abs}}(z) - p_{\text{ref}} - \rho_{\text{ref}}g(z - z_{\text{max}}) \quad (3.17)$$

$$p_{\text{abs}}(z) = p_{\text{ref}} \exp \left[ -\frac{\rho_{\text{air}}g(z - z_{\text{max}})}{p_{\text{ref}}} \right] \quad (3.18)$$

with reference pressure  $p_{\text{ref}} = 101,325 \text{ kPa}$ , reference density  $\rho_{\text{ref}} = \rho_{\text{air}} = 1.1837 \text{ kg m}^{-3}$  for air at  $25^\circ\text{C}$  and the absolute pressure  $p_{\text{abs}}(z)$  following the barometric pressure distribution. For free-decay simulations to assess the rigid body platform eigenfrequencies, the inlet and outlet are modelled using a free slip wall boundary condition. Thus, the NB of Section 3.3.2 is located on both sides of the domain in front of the inlet and outlet to damp radiating waves.

The symmetry of the floating structure is used to reduce the simulation domain and the grid is cut in half at  $y = 0$ . This reduces the computational effort by a factor of two and implies a reduction of the platform DOFs to surge  $x$ , heave  $z$  and pitch  $\psi$  only. Additionally, the coupled MBS-CFD studies are limited to a wave propagation heading direction  $\beta$  of zero degrees, corresponding to a wave propagation in positive  $x$ -direction. In MBS a load factor of two is applied to compensate for the reduced, symmetric structure. The load factor is increased over five time steps from zero after initialisation of the simulation to improve solver stability.

### 3.3.4 Mesh Properties

The three-dimensional computational CFD domain is discretised using a structured grid of the software ANSYS ICEM CFD. This type of mesh is chosen because, in general, structured meshes provide a better flow quality and a better scaling of the required CPU resources. However, they are more time consuming in generation than the unstructured meshes. The boundary layer at the hull of the floating substructure and tower is refined and resolved sufficiently. Wall functions are set automatically by the CFD solver for the SST turbulence model, which is used for all simulations in this study except for some cases in the sensitivity analysis in Section 3.4.3. Furthermore, the platform is surrounded by an O-grid to reduce the skewness and increase the mesh quality by using an arrangement of grid cells in an O-shape. An example of the resulting mesh around the floating substructure is presented in Figure 3.9.

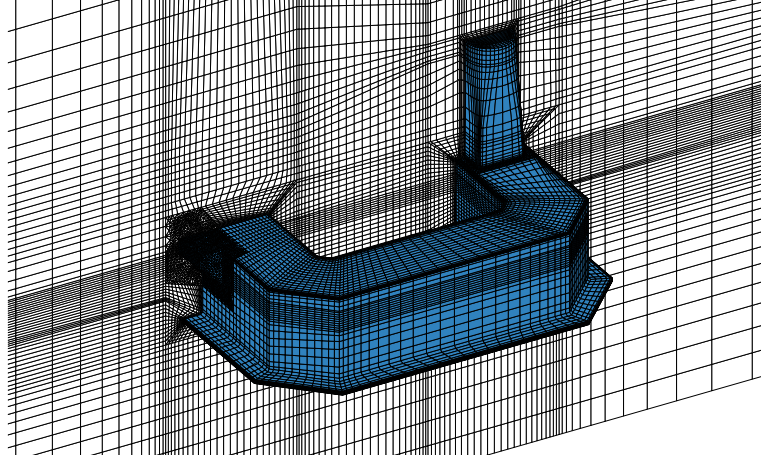


**Figure 3.9:** Illustration of the surface mesh of the floating substructure in blue and the symmetry plane at  $y = 0$  in white.

### 3.3.5 Mesh Deformation

Other studies, such as [19] and [178], defined a global mesh stiffness function in the CFD solver settings with poles at critical regions to reduce the mesh displacement gradient locally to zero. In this research, a different approach is preferred for the complex geometry of the floating substructure. To allow the floating substructure to move freely in the CFD domain under influence of the gravity, hydrodynamics and mooring loads, mesh deformation is included and specified for each individual boundary condition. While the inlet, outlet and symmetry boundary conditions are stationary, the seabed and top are free to slide parallel to the boundary without any deformation normal to it, see Table 3.1. For the floater and tower boundary conditions, the mesh displacements  $\Delta x$ ,  $\Delta y$  and  $\Delta z$  are calculated by the CEL expressions for each Cartesian component relative to the initial mesh:

$$\Delta x = D\Delta x_{f2s} \quad (3.19)$$

$$\Delta y = D\Delta y_{fs2} \quad (3.20)$$

$$\Delta z = D\Delta z_{fs2} \quad (3.21)$$

with local deformations  $\Delta x_{fs2}$ ,  $\Delta y_{fs2}$  and  $\Delta z_{fs2}$  calculated by the force element FLUID2SPCK of the structural solver during the coupled MBS-CFD simulation, see Figure 3.3. The function  $D$  describes a non-dimensional mesh deformation limiter in the CFD domain:

$$D = \begin{cases} 1 & \text{if } f_D > 1 \\ 0 & \text{if } f_D < 0 \\ f_D & \text{if } 0 \leq f_D \leq 1, \end{cases} \quad (3.22)$$

whereby regions without any mesh deformation result from  $D = 0$  and grid nodes with  $D = 1$  are completely translated and rotated based on the local deformations from the structural solver. For  $0 < D < 1$ , the mesh is deformed by a transition function  $f_D$  that describes a three-dimensional geometrical body (volume body) of arbitrary shape. An example of a deformed mesh is presented in Figure 3.10.

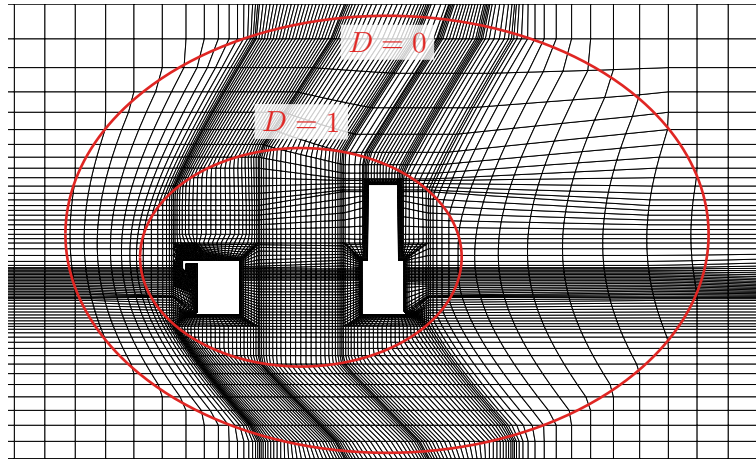


**Figure 3.10:** Deformed mesh, shown in the  $xz$ -plane at  $y = 0$ , as a result of the platform surge motion in the negative  $x$ -direction. The red lines indicate the inner and outer ellipsoidal limits of the mesh deformation with  $D = 1$  and  $D = 0$  respectively.

However, it has been shown to be beneficial to implement a spherical or ellipsoidal transition function as opposed to a rectangular or superellipsoidal shape to reduce the mesh deformation for large platform surge displacements. Hence, the mesh quality in the vicinity of the floating substructure is maintained. The floating substructure is surrounded by a volume of  $D = 1$  to protect the mesh in its vicinity from any stretching or compression, that may result in mesh folding and solver termination from negative volumes. A transition function using non-concentric ellipsoids is preferred to be used in the NWT in contrast to concentric ellipsoids because of the geometrical constraints of the NWT for which the water depth of the investigated model test facility or offshore site location is applied. Figure 3.11 illustrates the non-concentric, ellipsoidal mesh deformation limiter during a surge motion of the floating substructure.

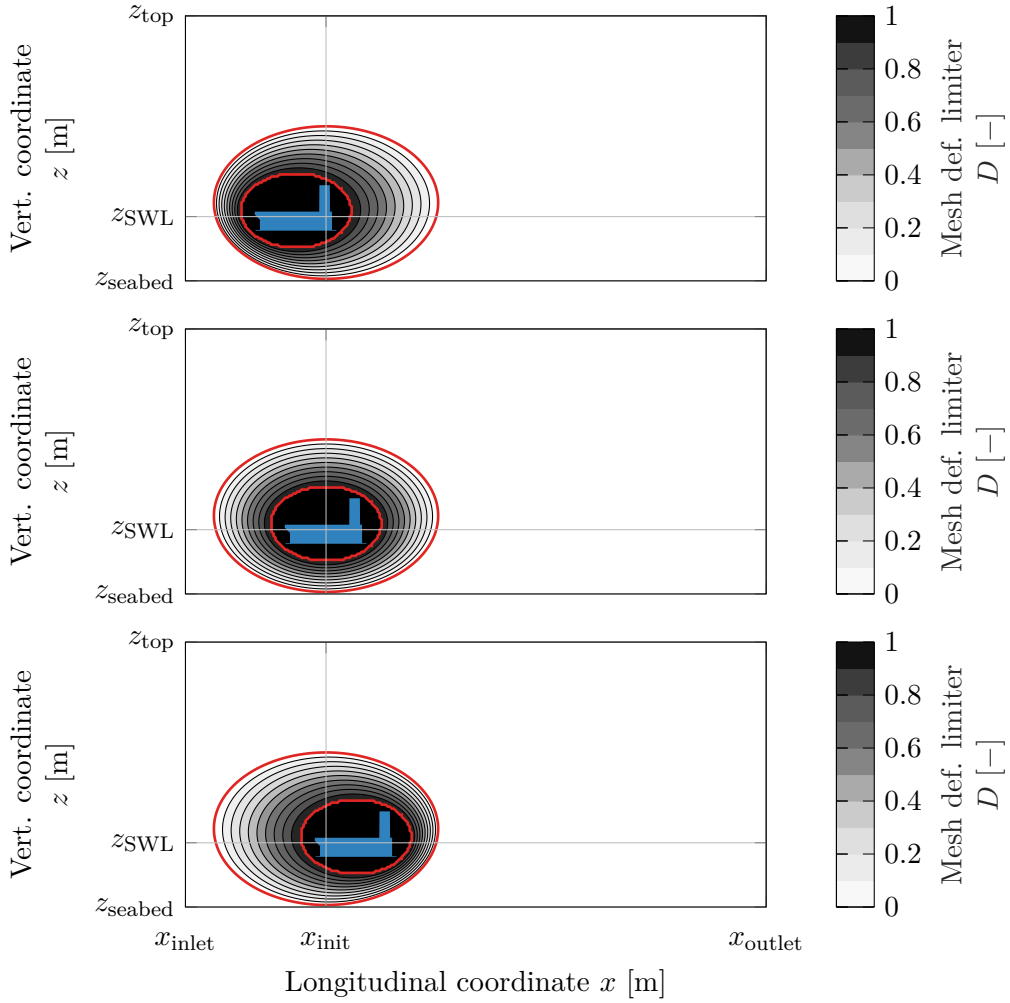


**Figure 3.11:** Illustration of the non-concentric, ellipsoidal mesh deformation limiter  $D$  in the  $xz$ -plane at  $y = 0$  during a surge motion of the floating substructure. The red lines indicate the inner and outer limits of the mesh deformation with  $D = 1$  and  $D = 0$  respectively.

The mesh deformation transition function  $f_D$  is derived from the implicit equation of the ellipsoidal surface, given in the Cartesian coordinates for the radius  $r$ :

$$r = \left[ \left( \frac{x - x_{m,1}}{a} \right)^2 + \left( \frac{y - y_{m,1}}{b} \right)^2 + \left( \frac{z - z_{m,1}}{c} \right)^2 \right]^{1/2} \quad (3.23)$$

with  $a$ ,  $b$  and  $c$  representing the half lengths of the principal axes  $x$ ,  $y$  and  $z$ , and the centre of the inner ellipsoid at  $x_{m,1}$ ,  $y_{m,1}$ ,  $z_{m,1}$ . In case of  $a = b = c$  Equation 3.23 describes a sphere. The geometrical limits of the transition region with  $D = 1$  and  $D = 0$  are represented by an inner and outer ellipsoid with  $r = r_1$  and  $r = r_2$  respectively. This means that the mesh deformation transition function based on the concentric ellipsoids is defined by:

$$f_D(r) = 1 - \frac{r - r_1}{r_2 - r_1} \quad (3.24)$$

in order to achieve  $f_D(r_1) = 1$  and  $f_D(r_2) = 0$  at the inner and outer limits respectively. The values  $r_1$  and  $r_2$  need to be chosen with special attention based on the dimensions of the floating substructure and the NWT to avoid, for example, deformation of the seabed boundary and hull shape geometry. For the implementation of non-concentric ellipsoids, Equation 3.23 is modified to:

$$r = \left[ \left( \frac{x - x_{m,1} - m_x(r - r_1)}{a} \right)^2 + \left( \frac{y - y_{m,1} - m_y(r - r_1)}{b} \right)^2 + \left( \frac{z - z_{m,1} - m_z(r - r_1)}{c} \right)^2 \right]^{1/2} \quad (3.25)$$

with

$$m_x = \frac{x_{m,2} - x_{m,1}}{r_2 - r_1} \quad (3.26)$$

$$m_y = \frac{y_{m,2} - y_{m,1}}{r_2 - r_1} \quad (3.27)$$

$$m_z = \frac{z_{m,2} - z_{m,1}}{r_2 - r_1}. \quad (3.28)$$

The centre of the outer ellipsoid is given by  $x_{m,2}$ ,  $y_{m,2}$  and  $z_{m,2}$ . Equation 3.25 is solved for  $r$  using a symbolic equation and system solver. The resulting analytical function is presented for completeness in Appendix A.1. To take advantage of symmetric ellipsoids in  $y$ -direction, Equation 3.25 is simplified with  $m_y = 0$ . A three-dimensional illustration of the mesh deformation limiter and the implemented non-concentric, ellipsoidal transition function is shown in Figure 3.12 with the floating substructure deflected from the initial displacement.

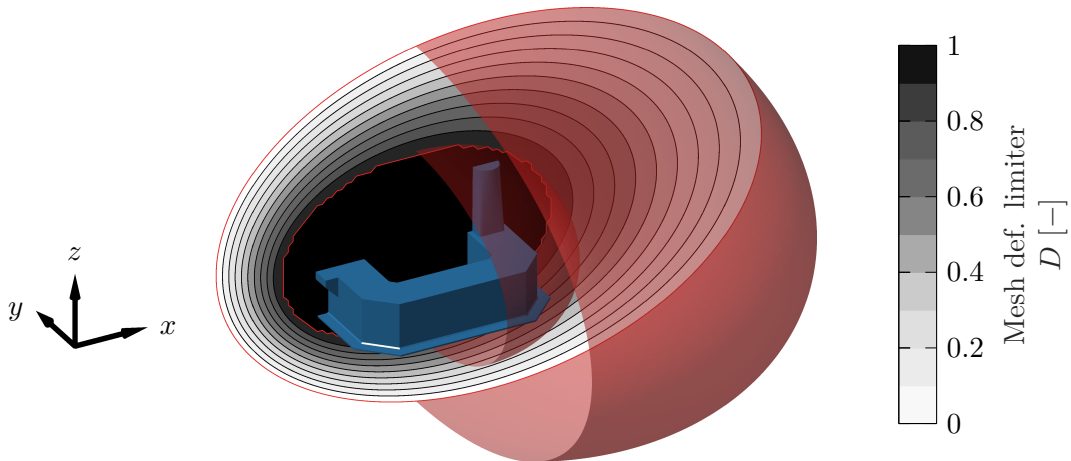


**Figure 3.12:** Illustration of the three-dimensional mesh deformation limiter  $D$ . The isosurfaces at  $D = 1$  and  $D = 0$  in red represent the inner and outer non-concentric ellipsoids, which surround the floating substructure in blue.

### 3.3.6 Initial Conditions

The NWT is filled with water up to the SWL as initial condition. The hydrostatic pressure distribution:

$$p_{\text{init}}(z) = \begin{cases} \rho_{\text{water}}g(z_{\text{SWL}} - z) & \text{if } z \leq z_{\text{SWL}} \\ 0 & \text{if } z > z_{\text{SWL}} \end{cases} \quad (3.29)$$

and the volume fractions of fluids air and water are initialised in the domain as required for the transient FVM simulations, see Section 2.4.4.3:

$$\varphi_{\text{air,init}}(z) = \begin{cases} 1 & \text{if } z > z_{\text{SWL}} \\ 0 & \text{if } z \leq z_{\text{SWL}} \end{cases} \quad (3.30)$$

$$\varphi_{\text{water,init}}(z) = \begin{cases} 1 & \text{if } z \leq z_{\text{SWL}} \\ 0 & \text{if } z > z_{\text{SWL}}. \end{cases} \quad (3.31)$$

The initial velocity field is set to  $u = v = w = 0 \text{ m s}^{-1}$ . An interaction between the boundary conditions, wave generation and damping behaviour can result in transients in the NWT, such as large vortex structures influencing the wave propagation. In this case, it is computationally more beneficial to perform an initial simulation run of long duration and extract the converged velocity field from the postprocessor. To increase efficiency, a two-dimensional domain should be used with decreased grid resolution. Afterwards, the converged velocity distribution in the NWT is loaded as initial values for the full, three-dimensional transient simulation.

If the considered load case contains an initial deflection of the floating substructure, as it is the case for free-decay tests, the initial mesh has to be modified accordingly. In addition, if mean drift is significant for the floating systems, it is beneficial to apply an initial platform surge equal to the mean surge displacement to compensate for the long transients at the beginning of the simulation. The initial position can be determined with experimental data, a previous CFD simulation or results from a calibrated engineering-level tool. When applying the coupled MBS-CFD simulation environment, it is possible to include a spring element in MBS that holds the floating substructure at its initial position until wave generation and damping is fully developed.



### 3.3.7 Additional Solver Settings

In addition to the previously introduced modelling techniques, the following solver settings are applied for the CFD solver as summarised in Table 3.2.

**Table 3.2:** Summary of selected solver settings applied in the CFD code ANSYS CFX.

Category	Setting
Multiphase mode	Homogeneous multiphase model with free surface option
Heat transfer	Homogeneous model with isothermal option and fluid temperature of 25 °C
Turbulence	SST model with automatic wall function
Surface tension	Not included (justification given below)
Solver control	High resolution advection scheme with first-order Backward Euler transient scheme and first-order turbulence numerics
Multiphase control	Volume fraction coupling with volume-weighted initial smoothing
Expert parameters	<p><code>max linsol passes fluids = 5</code>: maximum number of runs in the calculation of hydrodynamic equations with automatic control of under-relaxation if the linear solver does not converge</p> <p><code>overlap relaxation fluids = 0.5</code>: linear solver under-relaxation of overlap equations in a parallel run for hydrodynamics equations</p> <p><code>meshdisp each coefiter = t</code>: solve mesh displacement equation at the start of each coefficient loop to account for strong coupling between mesh motion and fluid solution</p> <p><code>write partition number = t</code>: inclusion of variable <code>Real Partition Number</code> in partition file for postprocessing</p>

All fluids share the same velocity field, turbulence field, etc. by applying a homogeneous multiphase fluid model. This assumption is valid for multiphase flows with very large interphase transfer rate, which is most commonly the case for free surface flows under gravity, where the phases are fully stratified and the interface between air and water is well defined [173]. Thus, the volume fractions of the phases are either one or zero except for the phase boundary and it is more efficient to use a common velocity field. In addition, a homogeneous, isothermal heat transfer model is selected with a fluid temperature of 25 °C.

In order to assess the influence of the grid resolution, time step and solver settings, parameter studies were conducted with a two-dimensional NWT described in the following Section 3.4. As result, turbulence is included in the URANS solver using the SST turbulence model by [117]

with curvature correction and Kato Launder production limiter [173]. The two-equation eddy-viscosity model is chosen because it combines the  $k - \omega$  model in the viscous boundary layer, for example of a floating substructure exposed to waves, and the  $k - \epsilon$  model in the free-stream. Additionally, the sensitivity study in Section 3.4.3 shows that the SST turbulence model is beneficial in terms of numerical damping compared to other models when considering wave propagation in a NWT.

Furthermore, the run mode of the fluid solver is set to parallel to increase the computational efficiency. Consequently, the CFD domain is divided in subdomains during the partitioning process and each partition is associated with a solver thread. However, stability problems can occur if a portion of a partition boundary is aligned with the free surface [173]. Robustness can be increased by implementing expert parameters in the solver control of the CFD code, for example with the parameters `max linsol passes fluids` and `overlap relaxation fluids` as explained in Table 3.2. Moreover, a different partitioning method can be applied to increase solver stability. Good results can be obtained by choosing a partition algorithm that is based on a user specified direction. This direction is defined by vector components with, for example, suitable value pairs of the Cartesian coordinates  $[x, y, z] = [1, 0, 0]$  or  $[1, -1, 1]$  as presented in Figure 3.13.

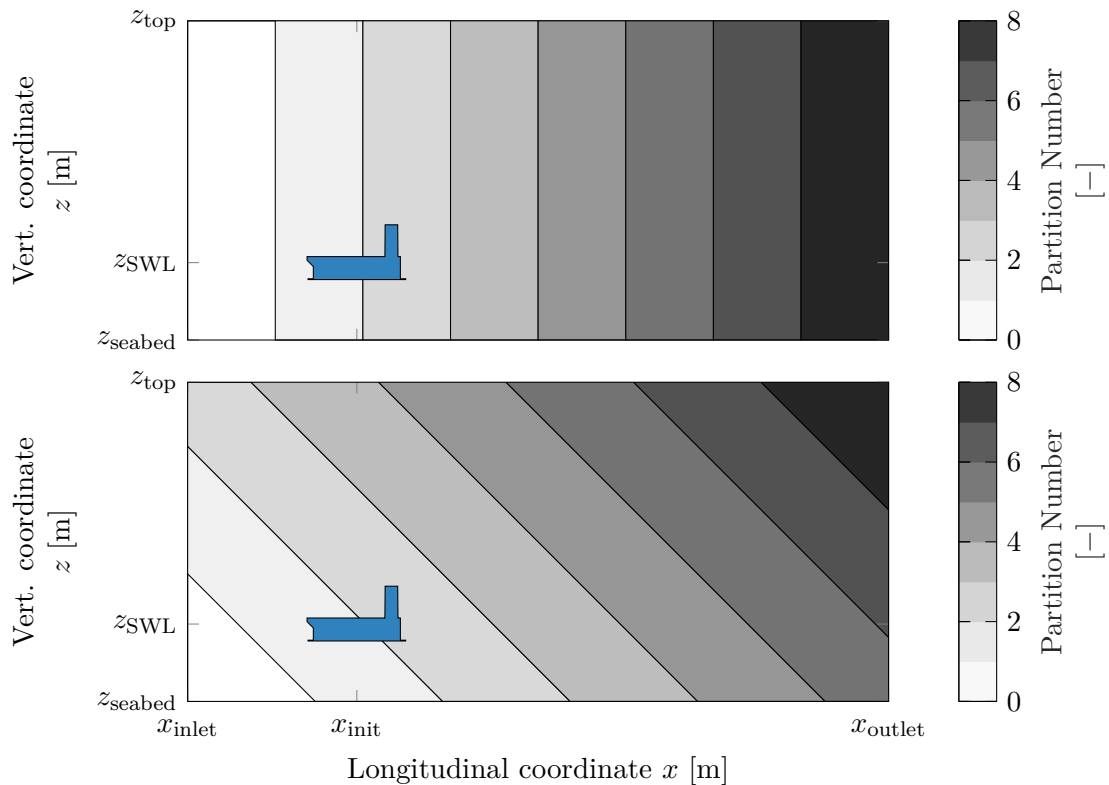


**Figure 3.13:** Exemplary two-dimensional representation of the partitioning of the NWT domain with user specified directions of  $[x, y, z] = [1, 0, 0]$  at the top and  $[1, -1, 1]$  at the bottom. Eight partitions are used with a similar number of grid cells.

The temporal scheme of the fluid solver is limited to first-order discretisation (first-order Backward Euler) in the MBS-CFD coupling methodology. Higher-order implementations require an iteration of more than one time step in the communication to increase the accuracy. However, this cannot be implemented because the internal functions and system calls in the codes are only accessible to a limited extent using user functions. In addition, the parameter study in Section 3.4.1 demonstrates that a fixed time step of a multiple of the wave period is suitable, taking into account the accuracy, stability and efficiency of the simulation. Depending on the investigated environmental conditions, the time step size of, for example,  $t_{\text{step}} = T/100$  as it is the case for focused wave groups is acceptable, see Section 5.4. The implicit iteration scheme of the coupled MBS-CFD simulation is carried out with four coefficient loops in CFD to achieve sufficient convergence.

Surface tension forces are not modelled in the free surface simulations to reduce the computational effort. Preliminary investigations showed that a surface tension model is not necessary to capture the relevant effects when simulating a floating substructure in wave conditions. Moreover, a coupled volume fraction algorithm is used in the multiphase control because it is beneficial for buoyant free surface problems [173].

Finally, the double-precision solver is invoked to increase accuracy of the numerical results because of a wide range of grid dimensions and aspect ratios in the NWT domain. Thus, floating point numbers are stored in 64 bit, occupying twice as much memory as single precision, but it allows an approximate accuracy up to 16 decimal digits.

### 3.4 Sensitivity Analysis in 2D Numerical Wave Tank

Wave generation and damping are crucial for the NWT. It is important to understand the relevant influences on the wave propagation before a floating structure can be analysed using a full setup of high resolution, three-dimensional CFD simulations. In order to determine the sensitivity of the solver settings and spatial discretisation, a parameter study was performed similar to [179] by varying the time step size, turbulence model and grid spacing. A two-dimensional NWT model with a water depth of  $d = 100$  m was created and regular waves with wave height  $H = 6$  m and wave period  $T = 10$  s were generated at the inlet. The NB starts at  $x/\lambda \approx 4$ . The deep water approximations to the linear wave theory are valid because the condition  $d/\lambda > 0.5$  and  $d/(gT^2) > 0.08$  with  $\lambda \approx 155.95$  m according to the dispersion relation is fulfilled, see Section 2.5.2. To be able to transfer findings to three dimensions, it is beneficial to use similar dimensional properties, such as wave tank height and width, SWL and the start location of the NB. A second-order temporal resolution is applied to reduce the numerical damping due to the higher-order transient scheme. This is possible because no coupling to the MBS solver is needed for the sensitivity analysis. Moreover, a discussion on the influence of first- and second-order time stepping schemes is included in Appendix A.2.

### 3.4.1 Temporal discretisation

The wave period is the most characteristic time scale in numerical wave generation, which also allows comparability between the cases. Hence, the impact of the time step size  $t_{\text{step}}$  is evaluated first. Its value is set as a multiple of the wave period, ranging from a coarse temporal discretisation of  $t_{\text{step}} = T/25$  to a relatively fine value of  $t_{\text{step}} = T/200$ . Spatial discretisation is defined by the number of hexahedral grid cells  $N_\lambda$  per wave length  $\lambda$  in  $x$ -direction. For the vertical coordinate  $z$ , the number of elements  $N_H$  is related to the wave height  $H$ . A mesh using  $N_\lambda = 40$  and  $N_H = 120$  is used in combination with the SST turbulence model. A snapshot of the NWT after convergence highlights the wave propagation and is shown in Figure 3.14. In general, the numerical damping reduces with decreasing time step size, which results in higher wave amplitudes  $A = H/2$  in the NWT domain. Coarser time steps, for instance  $t_{\text{step}} = T/25$  and  $t_{\text{step}} = T/50$ , lead to a shift in wave period due to inaccurate temporal discretisation.

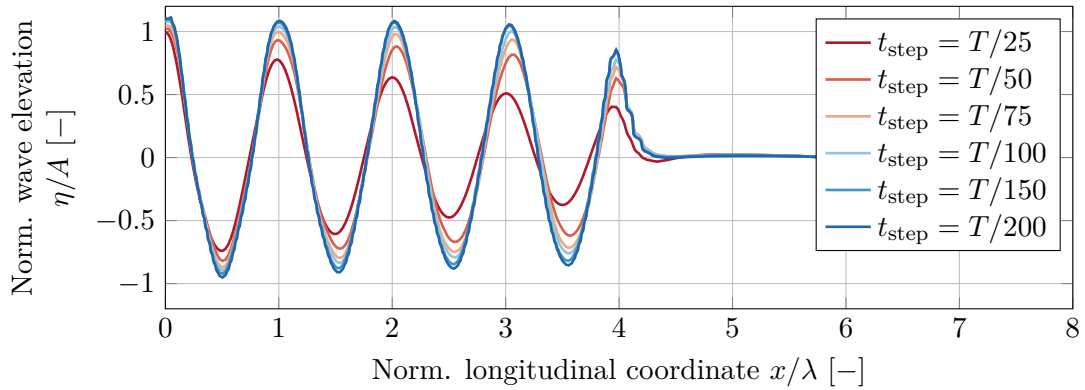


**Figure 3.14:** Series of lines showing the normalised wave elevation over the normalised longitudinal coordinate with a variation of the time step size as multiple of the wave period.

The numerical damping is quantified by evaluation of the magnitude of succeeding wave crests or troughs and the resulting damping ratio  $D$  is calculated as:

$$D = \frac{\Lambda}{\sqrt{(4\pi^2 + \Lambda^2)}} \quad (3.32)$$

with the logarithmic decrement defined as the natural log of the ratio of two successive wave crests:

$$\Lambda = \ln \frac{\eta_{\max}(x)}{\eta_{\max}(x + \lambda)} \quad (3.33)$$

The damping ratio is averaged for succeeding wave crests and included in relation to the critical damping  $D = 1$  in Table 3.3. Comparing the wave propagation between the coarsest temporal discretisation of  $t_{\text{step}} = T/25$  and the finest one of  $t_{\text{step}} = T/200$ , the numerical damping is 16 times higher. In addition, the damping ratio converges with increasing temporal resolution

and is comparable between  $t_{\text{step}} = T/150$  and  $t_{\text{step}} = T/200$ . As result,  $t_{\text{step}} = T/100$  is a good starting point for the temporal discretisation of the NWT, combining both accuracy in the wave propagation and reasonable computational effort. For a higher time step size, the increased damping must be compensated by a wave scaling factor  $L$ , introduced in the ramp function in Equation 3.11.

**Table 3.3:** Damping ratios for the two-dimensional regular wave in relation to the time step size.

Time step size $t_{\text{step}}$ [s]	$T/25$	$T/50$	$T/75$	$T/100$	$T/150$	$T/200$
Damping ratio $D$ [%]	3.36	1.05	0.50	0.29	0.18	0.21

### 3.4.2 Spatial discretisation

The sensitivity of the spatial discretisation on the wave propagation in the NWT is discussed. A temporal discretisation of  $t_{\text{step}} = T/100$  is applied together with the SST turbulence model. The grid resolution is variable in the direction of wave propagation from  $N_\lambda = 20$  to  $N_\lambda = 80$  and vertically from  $N_H = 30$  to  $N_H = 120$ . The wave elevation signal is shown in Figure 3.15 and the resulting damping ratios are summarised in Table 3.4.

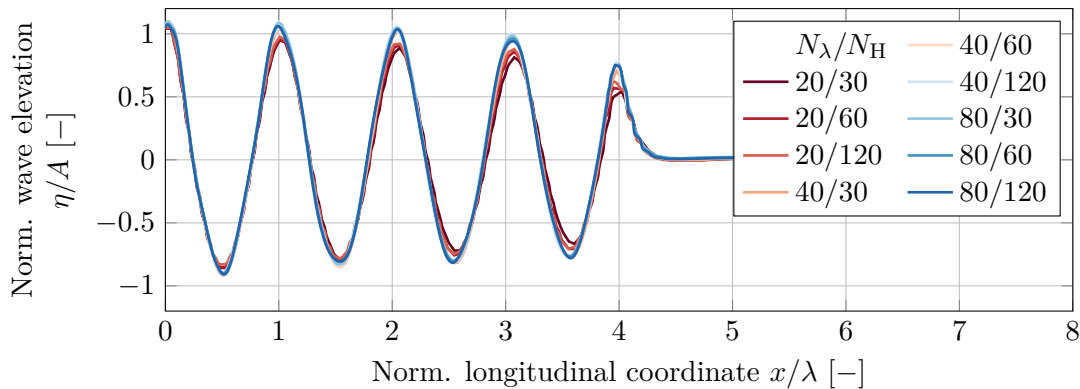


**Figure 3.15:** Series of lines showing the normalised wave elevation over the normalised longitudinal coordinate with a variation of the grid resolution. The number of cells in the  $x$ -direction per wave length versus the  $z$ -direction per wave height is given by  $N_\lambda/N_H$ .

When looking at the data for  $N_\lambda = 20$  and  $N_\lambda = 40$ , a clear trend for the numerical damping is visible: The finer the hexahedral mesh in vertical direction, the smaller the damping value  $D$ . In addition, increasing the number of cells  $N_H$  in longitudinal direction is beneficial for a better resolution of the wave crests and troughs, leading to reduced damping ratios. But a high number of grid elements in  $z$  is not always the best choice, for example, applying  $N_\lambda/N_H = 40/30$  is more accurate than  $N_\lambda/N_H = 20/120$  and at the same time computationally more efficient because of a smaller total number of grid cells, see Table 3.5. Convergence is reached for a fine

spatial discretisation, using  $N_\lambda = 80$ , so that a further reduction of numerical damping is not observed.

**Table 3.4:** Damping ratios for the two-dimensional regular wave in relation to the grid resolution. The number of cells in the  $x$ -direction per wave length versus the  $z$ -direction per wave height is given by  $N_\lambda/N_H$ .

Grid resolution $N_\lambda/N_H$	20/30	20/60	20/120	40/30	40/60	40/120	80/30	80/60	80/120
Damping ratio $D$ [%]	1.26	0.88	0.85	0.66	0.49	0.29	0.77	0.75	0.96

Consequently, a good resolution can be achieved already using a spatial discretisation of  $N_\lambda/N_H = 40/30$  for the free surface region, see Figure 3.5. This applies horizontally from wave generation at the inlet into the measuring zone, see Figure 3.5, and vertically for  $-LA_{\max} \leq z \leq LA_{\max}$  with  $L \approx 1.1 \dots 1.2$  (see the dense hexahedral mesh to model the free surface in Figure 3.10). Grid resolution is decreased intentionally within the NB and towards the seabed of the NWT to increase damping and thin out the mesh.

**Table 3.5:** Number of hexahedral grid elements relative to the minimum value for  $N_\lambda/N_H = 20/30$ .

		$N_\lambda$		
		20	40	80
$N_H$	30	1.00	1.76	3.29
	60	1.59	2.80	5.22
	120	2.76	4.87	9.08

### 3.4.3 Turbulence model

A third parameter, mainly influencing the numerical solution of RANS and URANS, is the turbulence model, which is described with more detail in Section 2.4.4.3. Due to the application of the homogeneous multiphase fluid model, the turbulence model is the same for the fluids water and air. Laminar flow is included as reference and characterised by the absence of turbulence modelling, avoiding the effect on numerical damping. However, for full scale substructures of FOWT, turbulent flow is predominant because of large length scales and resulting Reynolds numbers of several millions as well as vortex shedding. The wave propagation in the CFD domain is shown in Figure 3.16 and the resulting numerical damping is quantified in Table 3.6. A spatial discretisation using  $N_\lambda = 40$  and  $N_H = 120$  is combined with a time step of  $t_{\text{step}} = T/100$ .

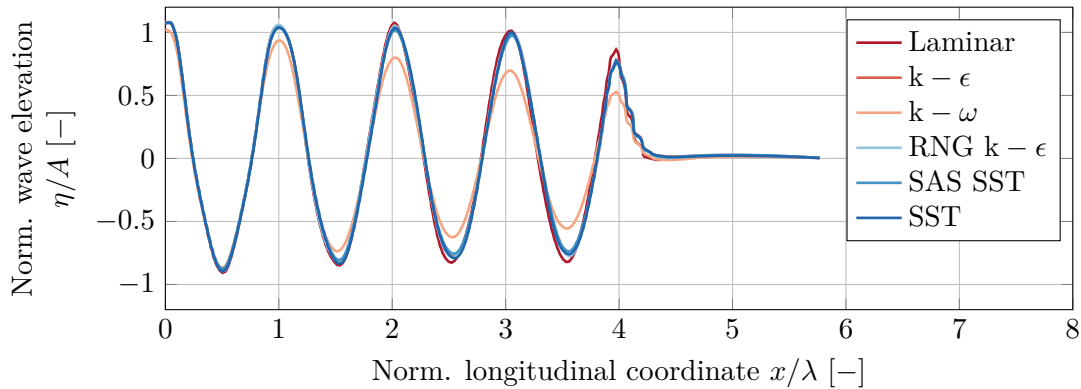


**Figure 3.16:** Series of lines showing the normalised wave elevation over the normalised longitudinal coordinate with a variation of the turbulence model.

The damping ratio of the wave elevation signal is maximum for the  $k - \omega$  turbulence model because of an increase of the eddy viscosity at the water surface. In general, it is applied for flow modelling of the viscous boundary layer. On the other hand, the SST turbulence model results in a similar wave propagation compared to the laminar flow and the damping ratios are minimal. The two-equation eddy-viscosity model applies a blending of the  $k - \omega$  model in the viscous boundary layer and the  $k - \epsilon$  model in the free-stream.

**Table 3.6:** Damping ratios for the two-dimensional regular wave in relation to the turbulence model.

Turbulence model	Laminar	$k - \epsilon$	$k - \omega$	RNG $k - \epsilon$	SAS SST	SST
Damping ratio $D$ [%]	0.32	0.51	2.35	0.54	0.47	0.29

Based on these results, the SST turbulence model is a reasonable choice in terms of accuracy and efficiency. Beyond a two-dimensional NWT, its applicability for the simulation of the flow around floating substructures is validated in Chapter 4.

### 3.5 Baseline Simulation Procedure

During a full analysis of the dynamic response of a floating substructure using the coupled MBS-CFD methodology, presented in Section 3.2, a baseline simulation procedure is followed. It is visualised schematically together with the used main software tools in Figure 3.17. For different applications, such as the wave calibration, the free-decay of the substructure or the transient motion in waves, different steps of the simulation procedure are required. An overview is described below with a summary of relevant considerations from the previous Sections.

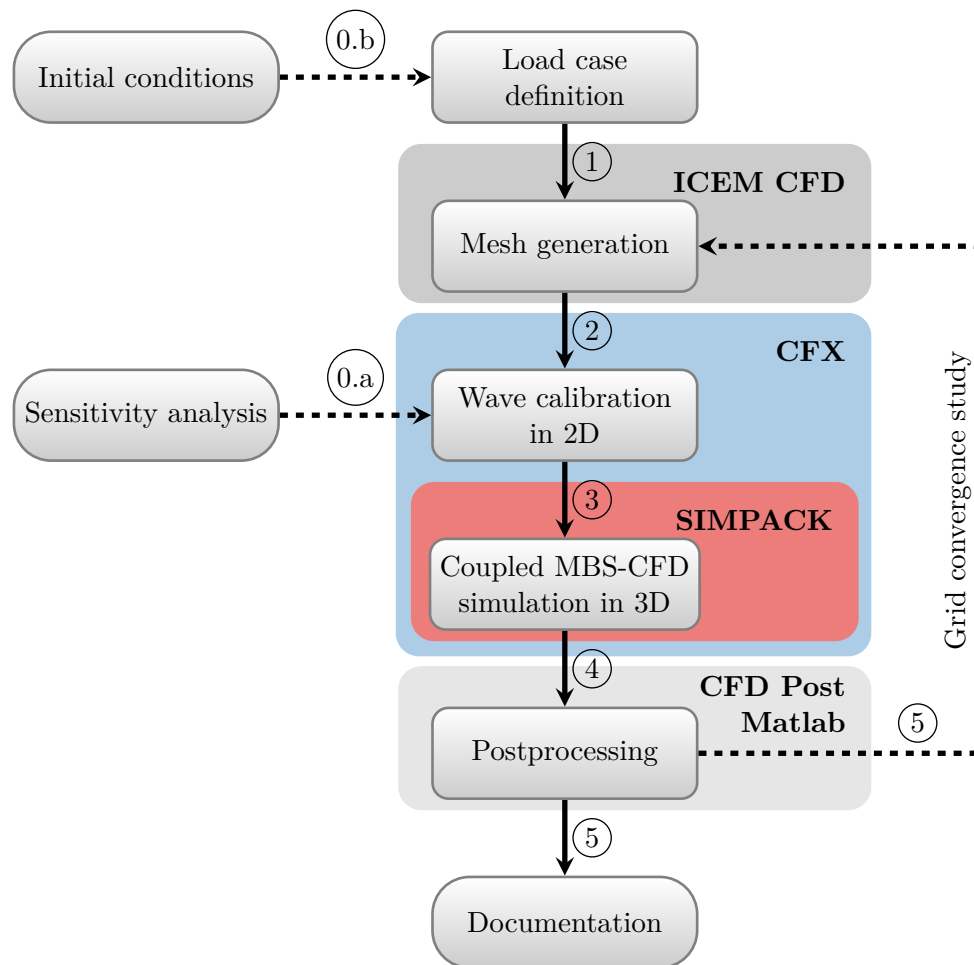


**Figure 3.17:** Flowchart of the simulation procedure and the applied tools to perform a coupled MBS-CFD analysis of a floating substructure in a NWT.

### Steps 0.a and 0.b: Sensitivity analysis and initial conditions

Preliminary steps 0.a and 0.b are required in order to setup the NWT adequately and to perform a CFD simulation successfully. First, a sensitivity analysis is carried out to determine suitable parameters for the grid resolution and wave tank dimensions, time step size, turbulence model, wave generation and damping, number of partitions and additional solver settings. The initial conditions, such as the platform position in surge, heave and pitch, are inherently defined for the free-decay tests. On the other hand, the mean values in case of incident waves are calculated either from experimental data of a wave tank test or approximated from numerical studies using calibrated engineering-level models.



### Step 1: Load case definition

Each simulation study starts with the definition of the investigated load case and the specification of the environmental conditions for wind and waves from a design basis. The initial position and orientation of the floating substructure from the undisplaced conditions is assessed previously in 0.b.

### Step 2: Mesh generation

Based on the geometry of the platform, dimensional properties of wave tank or site location and selected load case, the CFD domain is spatially discretised using the mesh generation software ANSYS ICEM CFD. Two sets of mesh data are created, one for the two-dimensional wave calibration and the other for the three-dimensional coupled MBS-CFD simulation. The floating substructure is excluded from the wave calibration. It is beneficial to apply similar mesh properties, such as NWT dimensions, NB settings and grid resolution with a specified value of  $N_\lambda$  and  $N_H$ , between the two- and three-dimensional domain. Recommendations for the mesh generation are presented in Section 3.4.2 based on a sensitivity analysis.

### Step 3: Wave calibration in 2D

The purpose of wave calibration is to tune parameters, influencing wave propagation, to achieve the desired wave kinematics within the measuring zone of the NWT. It is performed in 2D using ANSYS CFX as standalone software. If the load case is defined without waves, for example, in free-decay tests for system identification, wave calibration is not necessary. A wave scaling factor is used to compensate for the numerical damping, affecting waves from generation at the inlet to the arrival at the floating substructure, see Equation 3.11. Wave gauges are installed in the numerical domain by applying a hydrodynamic transparent surface mesh. It is orientated perpendicular to the wave propagation direction – i.e. parallel to the  $yz$ -plane – and located at the same initial position of the floating substructure as in the three-dimensional NWT. An expression is included in ANSYS CFX-Pre using CEL and is defined as:

$$\text{Monitor1} = \text{areaInt}(\text{Water.Volume Fraction})@\text{WaveGauge1} / \text{dyDomain} - \text{d}. \quad (3.34)$$

Equation 3.34 calculates the instantaneous wave elevation. `WaveGauge1` represents grid nodes, which form a plane at the wave measurement location, `dyDomain` is the dimension of the CFD domain in  $y$ -direction and `d` is the water depth  $d$  defined positively. The expression is applied for monitoring of the wave signal during the simulation or postprocessing. Moreover, the converged flow field of the two-dimensional CFD domain may be imported as initial condition for the full three-dimensional setup to reduce transient effects at the beginning of the simulation.

#### **Step 4: Coupled MBS-CFD simulation in 3D**

After the appropriate wave properties are determined by wave calibration, the coupled MBS-CFD simulation is performed using the provided methodology in Section 3.2. The CFD solver does not run standalone anymore but communicates with the structural model in MBS during the transient simulation. Depending on the investigated load case, the initialisation phase is reduced by initial mesh deformation to increase the computational efficiency. For free-decay tests, the floating substructure is moved from the undisplaced position to the deflected one, see Section 3.3.5 and Figure 3.10, by applying a forced motion in MBS. In conjunction, all irrelevant equation solvers in CFD are deactivated, for example, for hydrodynamics, volume fraction, wall scale, turbulence model, energy, etc. Afterwards, the transient simulation is started with all solvers turned on again using the pre-deformed mesh. If waves are present, the initial mesh is translated and/or rotated based on the initial platform position derived in step 0.b. Thus, one compensates for the simulation time until the waves are fully developed at the wave generator through the ramp function, see Equation 3.11, when the floating substructure oscillates around a mean position. For example, an initial platform surge is considered for regular wave analysis and a spring element is included in the MBS, which releases the floating substructure at the time when the first fully developed wave reaches the structure. The coupled solution process is started by the moderator script that manages convergence and communication of data. The platform position and wave elevation are monitored during the simulation. Backup files are written by the MBS and CFD tools at each wave period to be able to restart the simulation in the event of an unpredicted and sudden solver termination.

#### **Step 5: Postprocessing**

After the simulation is finished, results from CFD, such as velocity, pressure, density and volume fraction, are postprocessed. Additionally, the loads and deformation response from MBS, such as tower top acceleration, tower base loads, platform surge and pitch behaviour, is evaluated. To quantify the sensitivity of the mesh resolution on the solution, different spatial discretisations are simulated in a grid convergence study.

## 3.6 Recommended Practices for Modelling

Recommendations for modelling of hydrodynamics of FOWT using CFD are summarised and categorised according to, first, general aspects and, second, characteristics of the presented coupled MBS-CFD simulation environment.

### 3.6.1 Simulation Procedure

With respect to computational efficiency, it is beneficial to calibrate the properties of regular and irregular waves with a two-dimensional domain excluding the floating substructure because of a reduced number of grid elements. For  $0 \leq t/T \leq 2$ , the ramp function  $R$  in Equation 3.11 and Figure 3.7 is applied for initialisation of waves with  $L = 1$ . Afterwards for  $2 < t/T \leq 4$ , the wave height is kept constant with  $L = 1$  to measure fully developed waves without scaling at the wave gauges in the NWT. Finally, for  $4 < t/T \leq 10$  the wave scaling factor is increased over the simulation time using a step function, demonstrated in Figure 3.18, in order to increase the wave elevation every two periods. As a result, a matching pair of wave scaling factor and desired wave amplitude is obtained by interpolation. After the calibration process is finished, suitable wave properties are available and applied for the full three-dimensional simulation. To transfer findings, similar mesh properties are implemented for 2D and 3D.

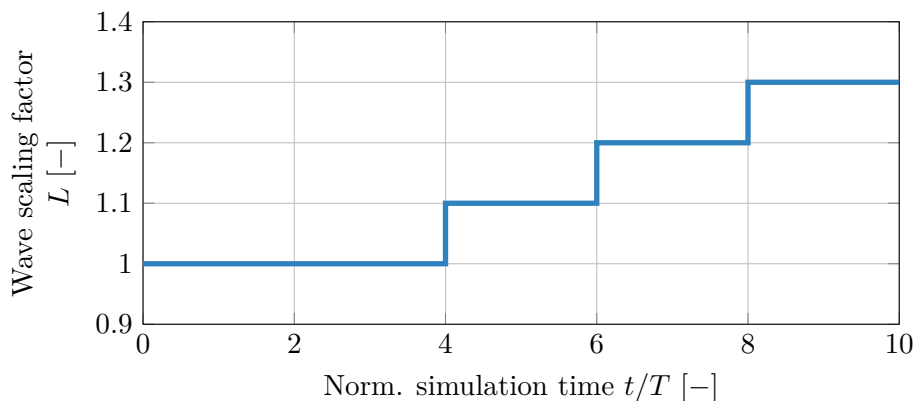


**Figure 3.18:** Ramp function used for the wave calibration in the two-dimensional NWT.

### 3.6.2 Wave Generation and Damping

Besides providing suitable parameters for wave generation and damping, wave calibration results in a converged two-dimensional flow field, which may be imported as initial condition for the full three-dimensional simulation to reduce transient effects at the start. For example, large, slowly moving vortex structures below the SWL may develop as a result of the interaction of wave generation at the inlet and damping in the NB. Their influence on the development of waves in the three-dimensional NWT can be reduced by including an initial velocity field for mesh elements with  $z < z_{\text{SWL}}$ .

In order to increase solver stability and minimize the initial phase until the waves are fully developed, a ramp function, as introduced in Section 3.3.1.3, is applied for the wave generator at the velocity inlet. In addition, the momentum source terms, defined for the NB in Equation 3.12 and 3.13, are start up applying a second ramp function, see Section 3.3.2.

The free surface, resulting from the interface between the fluids water and air, needs to be defined clearly. Consequently, the mesh resolution inside the free surface region, see Figure 3.5, is much finer than outside as shown in section 3.4.2.

### 3.6.3 Fluid and Solver Settings

Both fluids water and air are considered incompressible for the wave calibration, free-decay tests and the analysis of the dynamic response of a floating system. Only if the interaction of the phases water and air is of interest, the fluid air is modelled as an ideal gas and is compressible. This applies, for example, to the compression of air at the submerged mooring interface structure, as shown by [25], or to the numerical resolution of air bubbles from wave impact at the hull of the structure. However, computational resources increase when the compressibility of air is taken into account..

Parallelisation of the numerical calculation is necessary to achieve results in a reasonable time frame because of large CFD meshes of several millions of cells. However, solver stability is an issue for ANSYS CFX if a portion of a partition boundary is aligned with the free surface using the VOF approach. Consequently, an appropriate partitioning method is combined with the inclusion of expert parameters as discussed in Section 3.3.7.

### 3.6.4 MBS-CFD Coupling

To optimise the mesh deformation and to compute a pre-deformed mesh for free-decay tests, it is advantageous to apply a forced motion in MBS and disable all the equation solvers in CFD for hydrodynamics, volume fraction, wall scale, turbulence model, energy, etc.

After the wave propagation is fully developed inside the NWT as a result of the time dependent ramp function, the floating substructure experiences wave drift forces. The structure is pushed in wave propagation direction and oscillates around a mean position if regular waves are present. In order to reduce the transient motion of the platform at the beginning of the simulation, a spring element of high stiffness is included in MBS. It holds the floating substructure at the mean surge position, derived from experiment or other numerical models, until wave generation and damping are fully developed.



# 4

## Experiments and Validation

In this Chapter, the previously setup simulation environment is validated using experimental data of a wave tank model test, which is described at the beginning of this Chapter in Section 4.1. Afterwards, governing parameters of the applied Multibody model are addressed in Section 4.2 and the investigated load cases for validation are summarised in Section 4.3. Free-decay tests in platform pitch, heave and surge are evaluated with varying mesh discretisation, time step size etc. to identify natural periods and damping characteristics in Section 4.4. Complexity is increased by applying regular waves in Section 4.5 .

### 4.1 Wave Tank Model Test Setup

A wave tank model test campaign was conducted in the project FLOATGEN in 2014 at Oceanide's offshore basin BGO FIRST at La Seyne Sur Mer. The objectives of the measurement campaign were to test the mooring system and the dynamic behaviour of Ideol's FOWT floating substructure in extreme wave conditions and shallow water depth. Measurement data from different sensors during the experiment are used for the validation of numerical models.

### 4.1.1 Wave Tank Description

The dimensions of Oceanide's offshore basin BGO FIRST are 40 m in length and 16 m in width with a water depth ranging from 0 m to 5 m. Mono or multi-directional swell with regular and irregular waves with a maximum height of 0.8 m can be generated with a period of 0.6 s to 4 s at model scale. This can be combined with a current collinear or opposite to the swell up to a velocity of  $1.2 \text{ m s}^{-1}$ . A schematic representation of the wave basin is shown in Figure 4.1.

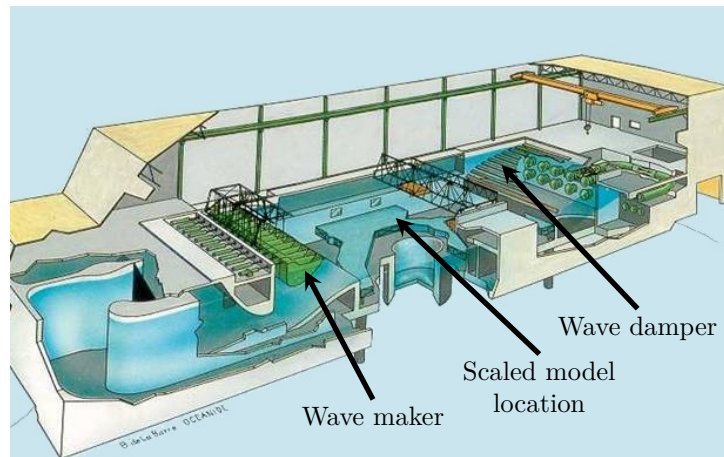


**Figure 4.1:** Offshore basin BGO FIRST at Oceanide, La Seyne sur Mer, France. [modified from source: Oceanide]

### 4.1.2 Model Characteristics and Test Matrix

Froude scaling is applied and a mock-up of the floating substructure with scaling factor  $\lambda = 32$  was tested, see Figure 4.2. The substructure model is fabricated from wood, which is coated to ensure water tightness. The hull is divided into a fore and aft part, which are connected using a mechanical interface with flex sensors to measure the hull global bending moment. Additional masses are attached for the adjustment of weight, COG and inertias. Wind is not taken into account and the wind turbine model is represented by a steel pipe and a steel lumped mass at the top. The mooring system consists of three steel cables that are connected to linear springs at the anchors, separated by an angle of  $120^\circ$ .

The test matrix contains wave and current calibration, free decay tests and combinations of regular and irregular waves and current. Pull-out tests are performed for the characterisation of the mooring stiffness.



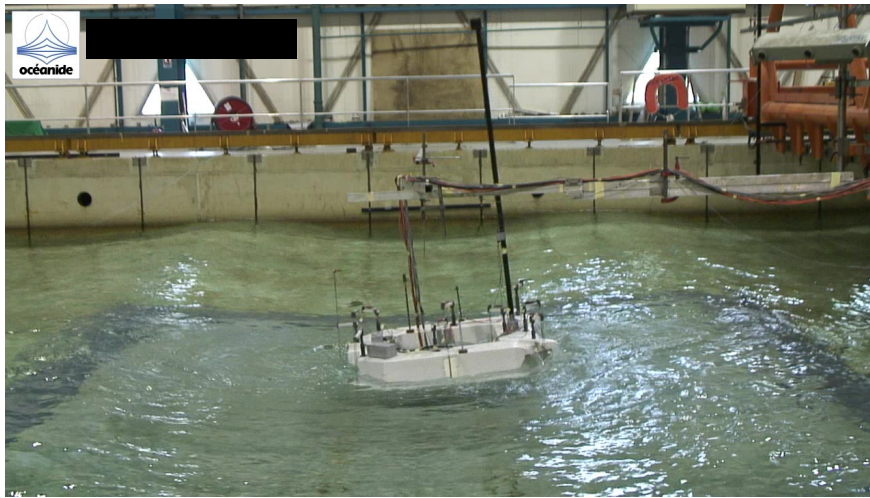


**Figure 4.2:** Mock-up of the floating substructure with instrumentation inside the deep water basin BGO FIRST. [modified from source: Ideol]

### 4.1.3 Measurements and Sensor Locations

The motion of the floating substructure with six DOFs is measured by an infrared camera system. It tracks the motion of three active markers, positioned on the model, and calculates the resulting translation and rotation of the model with respect to the COG. Wave gauges, which are installed around the hull at different locations as shown in Figure 4.2 and 4.3, measure the relative wave elevation during the tests. The incident wave field during the wave calibration and the wave testing is recorded by the reference wave probe  $WP_{ref}$ , located at  $x = 0$  m with respect to global reference system. For evaluation of the axial tension of the mooring lines  $ML_1$  to  $ML_3$ , one-dimensional force sensors are mounted close to the fairleads. Pre-tension was applied to the mooring lines. In addition, the current speed was measured in the wave basin by a current meter. Flex sensors were placed at the base of the steel pipe representing the tower to measure the fore-aft and side-side bending moments. Moreover, the global bending moment in the hull was measured using flex sensors on starboard and portside of the model in the interface between the fore and aft parts. Also, two containers instrumented with a force sensor were attached to the deck at the fore to record the green water loads.

## 4.2 Description of Coupled MBS-CFD Model

The simulation methodology described in Section 3.2 is applied to the coupled MBS-CFD analysis. For simplification, the structural model of the floating system, which represents the floating substructure, the tower and the RNA, is reduced to one rigid body. The structural properties – i.e. mass, COG and moments of inertia – are derived from the measurements of the experimental model. The symmetry of the floating substructure in  $y$ -direction and the

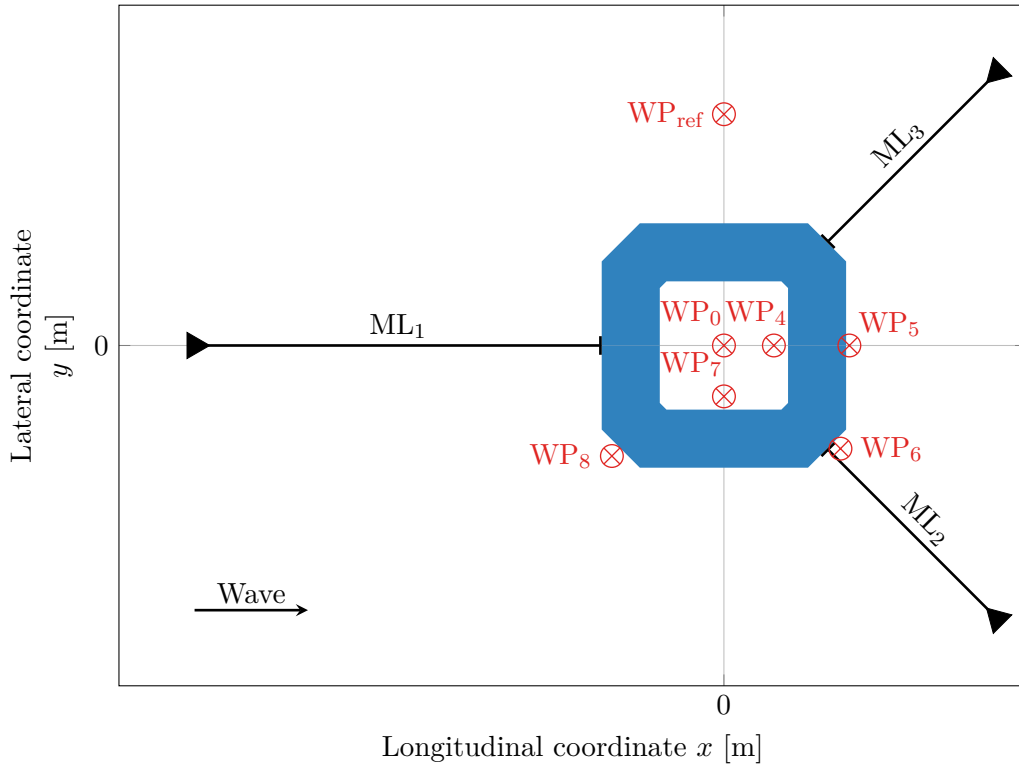


**Figure 4.3:** Schematic arrangement of the model in the wave basin with mooring lines ( $ML_1$  to  $ML_3$ ) and wave probes ( $WP_4$  to  $WP_8$ ) at  $0^\circ$  wave propagation direction and 0 m initial surge displacement. The reference wave elevation is measured at  $WP_{ref}$ .  $WP_0$  is only included in the numerical MBS-CFD simulation for assessment of the water level inside the moonpool during heave free-decay.

exclusive consideration of wave propagation in positive  $x$ -direction are exploited to reduce the computational domain. Therefore, the rigid body DOFs in MBS are reduced to platform surge, heave and pitch, while sway, roll and yaw are neglected, see Table 4.1 and Figure 2.2.

**Table 4.1:** Overview of the considered DOFs in the coupled MBS-CFD simulation model.

Number	MBS submodel	Degree of Freedom	Symbol
1	Substructure	Surge translational displacement	$x$
3		Heave translational displacement	$z$
5		Pitch rotational displacement	$\psi$

### 4.2.1 MBS Model Topology

The reduced MBS topology is shown in Figure 4.4, while the full model is presented in Figure 3.2. Only elements for modelling of the hydrodynamic forces, see FLUID2SPCK in Section 3.2, the restoring forces from the mooring lines, see Section 4.2.2, and a start-up spring-damper force to hold the floating substructure at its initial position, see Section 3.3.6, are included.

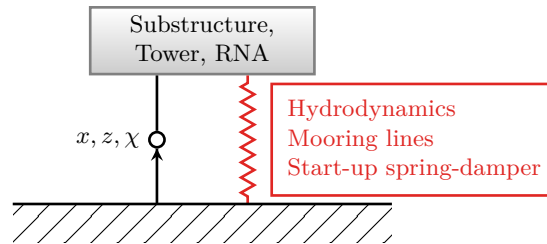


**Figure 4.4:** Topology of the reduced MBS model used for the validation of the MBS-CFD methodology with free-decay and regular wave simulations.

### 4.2.2 Mooring System Calibration

The mooring system was truncated in dimension and not anchored to the ground to fit into the wave basin. Each of the three mooring lines consist of a horizontal steel wire, which is redirected at a pulley and connected to vertical springs. At the end of the wire a threaded rod is installed to anchor the mooring line. Hence, the anchors are located higher above SWL than its associated fairlead on the mock-up of the floating substructure. The MBS model deviates as the fairleads and anchors are placed at the same height above SWL for simplification.

Pull-out tests are performed by pulling on the model in the wave basin with a horizontal cable equipped with a tension sensor. The resulting measurements of the restoring force are used for characterisation of the mooring system stiffness. In the MBS model, restoring forces are calculated by a spring element for each mooring line. An expression is defined that determines the point-to-point force between the anchor and the fairlead. The MBS model is calibrated with respect to the global linear stiffness matrix derived by the experiment. A comparison is presented in Figure 4.5.

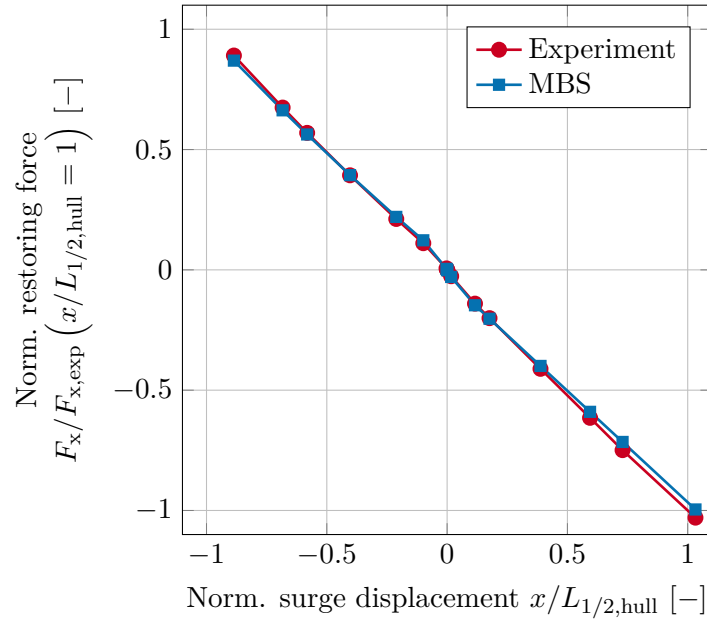


**Figure 4.5:** Surge displacement normalised to the half of the hull length versus the surge restoring force. The later is normalised to the experimental value at  $x/L_{1/2,hull} = 1$  using linear interpolation.

### 4.3 Investigated Load Cases

A summary of load cases used for the validation of the MBS-CFD model is given in Table 4.2. The gravitational acceleration at the location of the wave basin test campaign is  $g = 9.8047 \text{ m s}^{-2}$ .

**Table 4.2:** Overview of the main load cases settings used for the validation of the numerical simulation models with respect to the wave tank model test.

Section	Load case description	Scaling factor	Time step	Wave	Wind	Initial conditions
4.4	Free-decay	$\lambda = 32$ and $\lambda = 1$	$T/200 \leq t_{\text{step}} \leq T/50$	none	none	$x_{0,1} = 8 \text{ m}$ $z_{0,1} = -1.25 \text{ m}$ $z_{0,2} = 0.62 \text{ m}$ $z_{0,3} = 3 \text{ m}$ $\psi_{0,1} = 10^\circ$ $\psi_{0,2} = 3.33^\circ$
4.5	Regular wave	$\lambda = 32$	$t_{\text{step}} = T/100$	$H = 6 \text{ m}$ $T = 10 \text{ s}$ $\beta = 0^\circ$	none	$x_{0,1} = x_{\text{mean}}$

## 4.4 Free-Decay Test

Natural periods of rigid body platform DOFs and associated damping are characteristic properties of a floating system. They can be estimated in preliminary design stages using empirical and numerical models, measurements and databases. However, simplified assumptions need to be verified and tuned during the design phase. Thus, experiments in a wave basin and resulting system identification are crucial [66]. Free-decay tests are used to describe each individual platform configuration in terms of eigenfrequency and damping. Experimental data of such tests are very useful for the validation of numerical models and uncertainty quantification because, for example, the spatial and temporal discretisation have to be of certain quality. In the following analyses, the platform DOFs surge, heave and pitch, presented in Table 4.1, are considered. Although restoring forces from mooring lines mainly impact the surge, sway and yaw motion of the substructure, the mooring system is included in all simulations. During the decay tests in the wave basin the mooring system was installed in intact condition. Damaged mooring conditions with a reduced stiffness of one mooring line were only considered during irregular wave tests.

Results of time series, natural periods and damping are compared between experimental data of the wave basin test, described in Section 4.1, and coupled MBS-CFD simulation. Different spatial and temporal discretisation of the numerical model are applied, see summary in Table 4.2 and 4.3, to assess the impact of the grid resolution and time step size. For example, the mesh variation of medium resolution is illustrated in Figure 3.9. Simulation results from model and full scale are compared to investigate scaling effects. In addition, the influence of the initial displacement on the damping is analysed. Only one experimental data set is available per decay test.

In the following, Identifiers (IDs) are used to distinguish between the measurements and different simulation results. Each plot line is associated with a three-character ID:

- Character 1: “D” representing free-decay load cases,
- Character 2: One digit representing a sensor (“1” for surge translational displacement, “3” for heave translational displacement and “5” for pitch rotational displacement),
- Character 3: One digit that is either “0” for the experiment or of increasing number starting with “1” for a variation of the simulation.

As an example, D56 refers to the platform pitch displacement of the 6<sup>th</sup> variation of the free-decay simulations.

**Table 4.3:** Overview of different mesh variations used for the MBS-CFD simulations of free-decay tests.

Mesh variation	Number of elements	Rel. number of elements
Fine	1,130,698	1.0000
Medium	496,019	0.4387
Coarse	256,101	0.2265

#### 4.4.1 Procedure for Evaluation of Hydrodynamic Damping

Assessment of hydrodynamic damping is carried out by applying the method described by Journée [103], pages 6-15 to 6-17, for free-decay tests or by Piehl [180] for the analysis of ship roll damping. The procedure is introduced below for the platform pitch motion  $\psi$ , but it also applies to the other rigid body DOFs. For a freely oscillating rigid body, the linear equation of motion in pitch  $\psi$  with respect to the COG is:

$$m \frac{d^2\psi}{dt^2} + d \frac{d\psi}{dt} + k\psi = 0 \quad (4.1)$$

with the damping constant  $d$ , structural spring stiffness  $k$  and mass  $m$ , which is the sum of the rigid body mass of the floating substructure and the added mass of water moving with the structure. By dividing Equation 4.1 with the mass, the general form of the second-order differential equation can be written as:

$$\frac{d^2\psi}{dt^2} + 2D\omega_0 \frac{d\psi}{dt} + \omega_0^2\psi = 0 \quad (4.2)$$

with the damping coefficient defined as:

$$\delta = \frac{d}{2m} = \omega_0 D, \quad (4.3)$$

and the undamped natural angular frequency of the system:

$$\omega_0 = \sqrt{\frac{k}{m}}. \quad (4.4)$$

A solution to the damped harmonic oscillator in Equation 4.2 can be expressed as:

$$\psi(t) = \psi_0 e^{-\delta t} \cos(\omega_d t + \theta_0) \quad (4.5)$$

with the natural angular frequency of the damped system:

$$\omega_d = \omega_0 \sqrt{1 - D^2} = \sqrt{\omega_0^2 - \delta^2} = \frac{2\pi}{T_d}. \quad (4.6)$$

By applying the logarithmic decrement of the motion, the non-dimensional damping ratio is defined as:

$$D = \frac{1}{\omega_0 T_d} \ln \left[ \frac{\psi(t)}{\psi(t + T_d)} \right]. \quad (4.7)$$

Under the assumption that the damping is small  $\delta < 0.2$  so that  $\delta^2 \ll \omega_0^2$ , the term  $\delta^2$  is neglected in Equation 4.6 and it is  $\omega_d \approx \omega_0$ . Thus, the damping ratio can be simplified as:

$$D = \frac{1}{2\pi} \ln \left[ \frac{\psi(t)}{\psi(t + T_d)} \right]. \quad (4.8)$$

During post-processing of the experimental and numerical results of the decay test, time series are evaluated and successive pairs of positive and negative maxima are used to estimate the damping ratios:

$$D_i = \frac{1}{2\pi} \ln \left[ \frac{\psi_{a,i} - \psi_{a,i+1}}{\psi_{a,i+2} - \psi_{a,i+3}} \right]. \quad (4.9)$$

Journée advises in [103] to use double amplitudes in Equation 4.9 to avoid a potential spreading of the successively calculated damping ratios, which may be caused by a zero-shift of the measuring signal. The resulting damping ratios  $D_i$  are plotted against the mean pitch amplitudes:

$$\overline{\psi_{a,i}} = \left| \frac{\psi_{a,i} - \psi_{a,i+1} + \psi_{a,i+2} - \psi_{a,i+3}}{4} \right|. \quad (4.10)$$

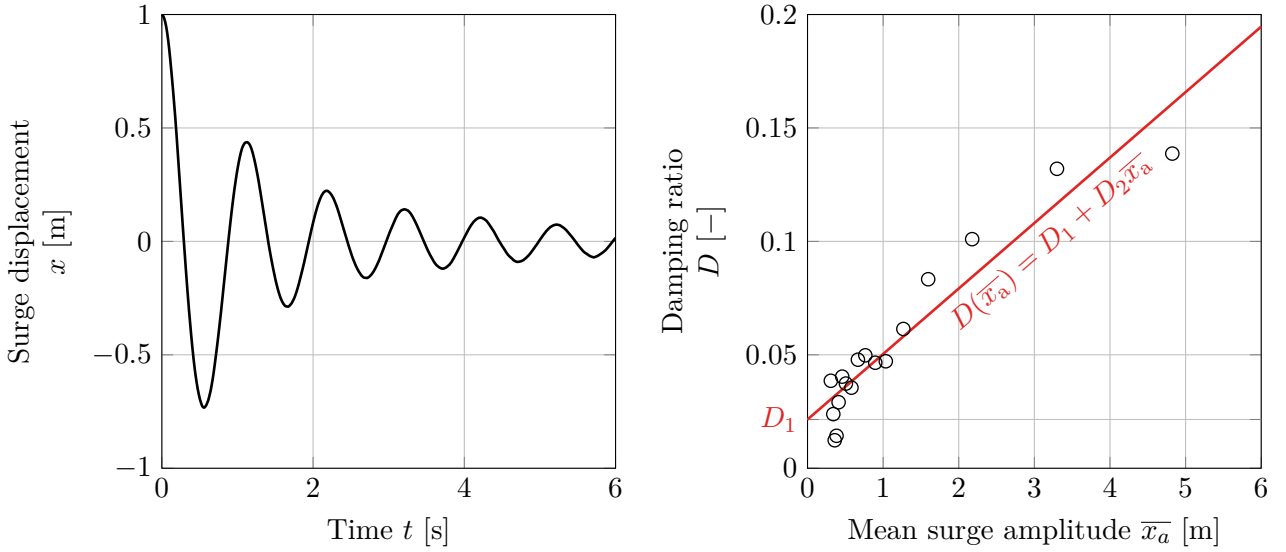
As a consequence, the damping ratio is determined by a regression analysis of the data points  $(\overline{\psi_{a,i}}, D_i)$  as shown in Figure 4.6. This procedure is strictly valid only for small values of  $\delta$ . For a linearised system, the gradient  $dD/d\overline{\psi_a} = 0$  and damping ratios  $D_i$  are constant in relation to  $\overline{\psi_{a,i}}$ :

$$D(\overline{\psi_a}) = D_0 \quad (4.11)$$

However, the damping behaviour of floating systems is often non-linear and a damping function with linear and higher-order terms – here quadratic – is applied in Equation 4.2:

$$D(\overline{\psi_a}) = D_1 + D_2 \overline{\psi_a} \quad (4.12)$$

with the linear and quadratic damping coefficients  $D_1$  and  $D_2$  respectively.



(a) Exemplary surge displacement during a free-decay (b) Calculated damping ratios over the mean surge amplitudes marked as circles.

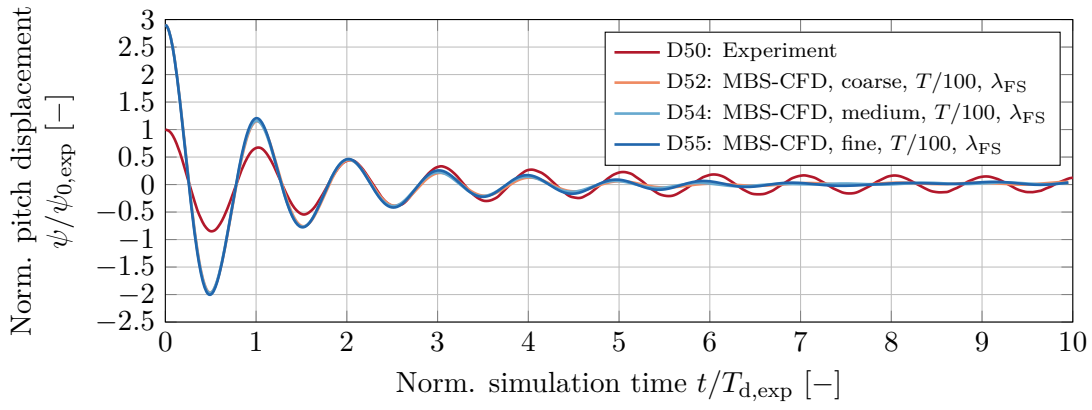
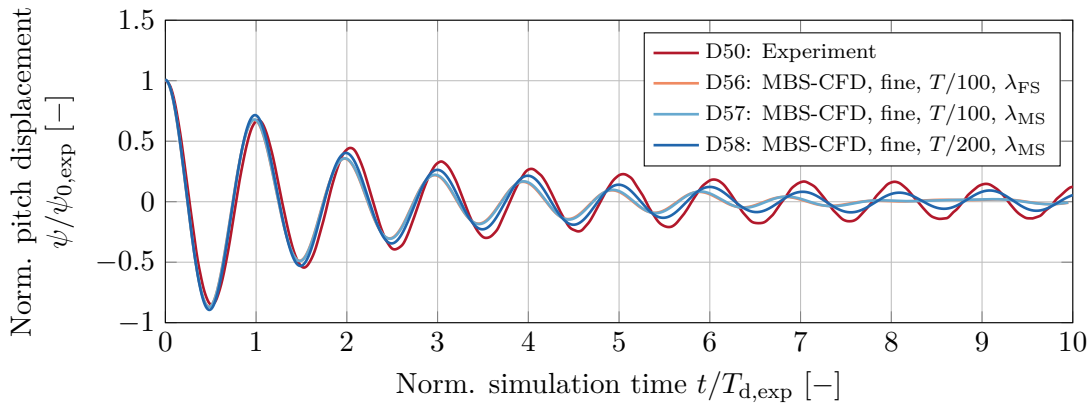
**Figure 4.6:** Illustration of the procedure for damping assessment. The positive and negative maxima of the damped oscillation of the platform DOF (left) are fitted to a straight line, represented by Equation 4.12, using a regression analysis (right). The intersection of the straight line with the  $y$ -axis relates to the linear damping coefficient  $D_1$  and the slope relates to the quadratic damping coefficient  $D_2$  respectively. The circle markers indicate the calculated damping ratios using Equation 4.9 at the double amplitudes applying Equation 4.10.

#### 4.4.2 Pitch Free-Decay

Pitch free-decay is examined in this Section. First, the platform is deflected about  $\psi_{0,1} = 10^\circ$  in the MBS-CFD simulation from its neutral position, which is approximately three times the initial pitch inclination of the experiment. A time step of  $t_{\text{step}} = T/100$  is applied and all three mesh variations fine, medium and coarse are simulated. The pitch displacement is shown in Figure 4.7a normalised to the initial, maximum value of the experiment. In order to match the initial pitch inclination of the experiment of  $\psi_{0,2} = \psi_{0,\text{exp}} = 3.3225^\circ$ , additional simulations are conducted with the finest mesh and temporal discretisation of  $t_{\text{step}} = T/100$  and  $t_{\text{step}} = T/200$  at model and full scale, see Figure 4.7b. A fit to the experimental data is calculated by applying a smoothing spline function to remove the measurement noise. This procedure is similar to a low-pass filter that cuts off the high frequency content of the signal. The normalised simulation time  $t/T_{d,\text{exp}}$  refers to the natural period of the pitch displacement of the experiment  $T_{d,\text{exp}}$ . It is calculated from the average of successive pairs of maximum and minimum values of the time series.

The damping characteristics and the natural frequencies and periods of the pitch DOF are analysed according to the procedure described in Section 4.4.1. The results are summarised in Table 4.4 for the experiment and the MBS-CFD simulation at model and full scale for



(a) D52, D54 and D55 with  $\psi_0/\psi_{0,\text{exp}} = 3$  at full scale  $\lambda_{\text{FS}}$ .(b) D56 to 58 with  $\psi_0/\psi_{0,\text{exp}} = 1$  at full scale  $\lambda_{\text{FS}}$  and model scale  $\lambda_{\text{MS}}$ .

**Figure 4.7:** Normalised pitch displacement over the normalised simulation time during the free-decay. A comparison is made between the results of the wave tank model test and variations of the MBS-CFD simulation.

three grid resolutions, three time step sizes and two initial pitch inclinations. The wave basin measurements are used as reference for the calculation of the ratios  $f_d/f_{d,\text{exp}}$  and  $T_d/T_{d,\text{exp}}$ .

#### 4.4.2.1 Discussion of Natural Period

Generally speaking, the natural period of the system is influenced by the spring stiffness and mass according to Equation 4.4. The magnitude of damping changes the eigenfrequency as can be seen in Equation 4.6. For the pitch free-decay, the time period of successive pairs of positive and negative peaks is nearly constant from the beginning of the decay until the floating system reaches equilibrium.

The influence of grid resolution is evaluated in simulations D52, D54 and D55 at full scale while keeping a constant  $t_{\text{step}} = T/100$  and  $\psi_0/\psi_{0,\text{exp}} = 3$ , see also Figure 4.7a. It is noticeable that the pitch natural frequency and period using the numerical MBS-CFD approach agree very well with the measurements in D50 with a small deviation of 1% to 2%. The natural period using the coarse mesh is overpredicted slightly, while the medium and fine mesh show

**Table 4.4:** Summary of the normalised eigenfrequency, period, damping and simulation wall clock time resulting from the pitch free-decay tests of the experiment and the MBS-CFD simulations.

ID	Method	Mesh	$t_{\text{step}}$	$\lambda$	$\frac{\psi_0}{\psi_{0,\text{exp}}}$	$\frac{f_d}{f_{d,\text{exp}}}$	$\frac{T_d}{T_{d,\text{exp}}}$	$D_0$	$D_1$	$D_2$	$\frac{T_{\text{calc}}}{T_{\text{calc,ref}}}$
D50	Experiment			32	1	1.0000	1.0000	0.0371	0.0285	0.0114	
D51	MBS-CFD	coarse	$T/50$	1	3	1.0283	0.9725	0.1598	0.1439	0.0093	0.1595
D52	MBS-CFD	coarse	$T/100$	1	3	0.9957	1.0043	0.1248	0.1165	0.0056	0.3212
D53	MBS-CFD	coarse	$T/200$	1	3	1.0016	0.9984	0.0704	0.0459	0.0203	0.6291
D54	MBS-CFD	medium	$T/100$	1	3	1.0239	0.9766	0.1143	0.0995	0.0098	0.4914
D55	MBS-CFD	fine	$T/100$	1	3	1.0093	0.9908	0.1000	0.0818	0.0131	1.0000
D56	MBS-CFD	fine	$T/100$	1	1	1.0242	0.9764	0.0746	0.0690	0.0065	
D57	MBS-CFD	fine	$T/100$	32	1	1.0197	0.9807	0.0733	0.0670	0.0072	
D58	MBS-CFD	fine	$T/200$	32	1	0.9892	1.0110	0.0449	0.0215	0.0282	

an underprediction with the highest deviation for the medium mesh. However, the absolute differences are very small and depend on the number of data points used for the averaging. Hence, even the coarse mesh delivers satisfactory results for the natural period.

Numerical simulation always depend on the combination of the spatial and temporal discretisation. Thus, the time step size is varied for D51 to D53 from  $t_{\text{step}} = T/50$  to  $t_{\text{step}} = T/100$  and, finally,  $t_{\text{step}} = T/200$ . Only a combination applying the largest time step of  $t_{\text{step}} = T/50$  with the coarse mesh in D51 shows increased underprediction of the natural period of around 3% compared to the experiment. Increasing the temporal resolution by a factor of two or four reduces the deviation to less than 1%. In conclusion, a sensitivity to grid resolution and temporal discretisation is observed for the coarse mesh and the highest time step size. Refinement only reduces the deviation to the measurements until a certain spatial and temporal discretisation, which demonstrates a convergence behaviour.

Next, the influence of initial pitch amplitude, from which the floating substructure is released, is analysed. The underestimation of the natural period compared to the experiment is slightly higher for D56 with  $\psi_0/\psi_{0,\text{exp}} = 1$  than for D55 with  $\psi_0/\psi_{0,\text{exp}} = 3$ , fine mesh and  $t_{\text{step}} = T/100$ . This can be explained by Equation 4.6, that describes the inevitable influence of damping on the natural angular frequency. As damping reduces for D56 compared to D55, the natural period is decreased.

Finally, the impact of the scaling factor is investigated by comparing MBS-CFD simulation D56 at full scale to D57 at model scale. Only small differences are found for the natural period with slightly higher values for D56. In general, scaling factor of experiment and MBS-CFD simulation should be identical for validation purposes to avoid a mismatch in Reynolds number.

#### 4.4.2.2 Discussion of Damping Behaviour

Spatial discretisation has an influence on numerical damping and the effect is quantified for simulations D52, D54 and D55 in Figure 4.7a and Table 4.4. The damping ratios are calculated following the procedure described in Section 4.4.1. The values decrease from  $D_0 = 0.1248$  for D52 to  $D_0 = 0.1000$  for D55 because the mesh is refined, especially in the vicinity of the floating substructure. Thus, damping decreases with higher grid resolution until convergence is reached.

Additionally, the effect of temporal discretisation is investigated for D51 to D53. The damping ratios decrease significantly from  $D_0 = 0.1598$  for D51 to  $D_0 = 0.0704$  for D53. This is explained by the temporal discretisation which is refined by a factor of two from D51 to D52 and again from D52 to D53. Consequently, damping reduces for smaller time step sizes until convergence is reached. Similar qualitative trends for spatial and temporal discretisation were shown in the sensitivity analysis in Section 3.4 using a two-dimensional NWT.

If a linear damping behaviour is assumed for the rigid body, the components of the equation of motion that are associated with the damping are proportional to the velocity (to the power of one), see Equation 4.2. However, the damping behaviour of floating systems is often characterised by non-linear functions with linear and quadratic components. For this reason, damping forces are also proportional to the velocity squared, see Equation 4.12. Maximum velocities and accelerations increase if the initial amplitude of the decay is increased. Consequently, parameters such as natural period and damping ratio are sensitive to the initial amplitude as demonstrated in simulation D55 and D56. Higher damping of  $D_0 = 0.1000$  for D55 is associated with higher initial amplitude compared to  $D_0 = 0.0746$  for D56. Especially the quadratic terms of the damping function are reduced by around 50% from  $D_2 = 0.0131$  for D55 to  $D_2 = 0.0065$  for D56, because of reduced pitch velocities in the first oscillations for  $\psi_0/\psi_{0,\text{exp}} = 1$  compared to  $\psi_0/\psi_{0,\text{exp}} = 3$ .

For simulations D56 and D57 the damping ratios are comparable, whether the platform is simulated in model scale or full scale. The scaling factor has no distinct impact on the damping. In order to match the reference damping ratios of the experiment, simulation D58 is performed with a reduced time step size of  $t_{\text{step}} = T/200$  at model scale and  $\psi_0/\psi_{0,\text{exp}} = 1$ . In comparison to simulation D57, the linear damping ratios reduce significantly to  $D_0 = 0.0449$  and  $D_1 = 0.0215$  for D58 and the quadratic damping ratio increases to  $D_2 = 0.0282$ . Simulation D58 shows the best fit to the damping behaviour of the experiment, although discrepancies are still present. Deviations could potentially be decreased further by simulating at even smaller time step sizes or running the simulation at a higher-order temporal discretisation scheme, see the last paragraph below. Damping ratios based on successive pairs of positive and negative maxima (Equation 4.9) are plotted against the mean pitch amplitudes (Equation 4.10) in Figure 4.8 for the experimental data D50 and MBS-CFD simulation D58.

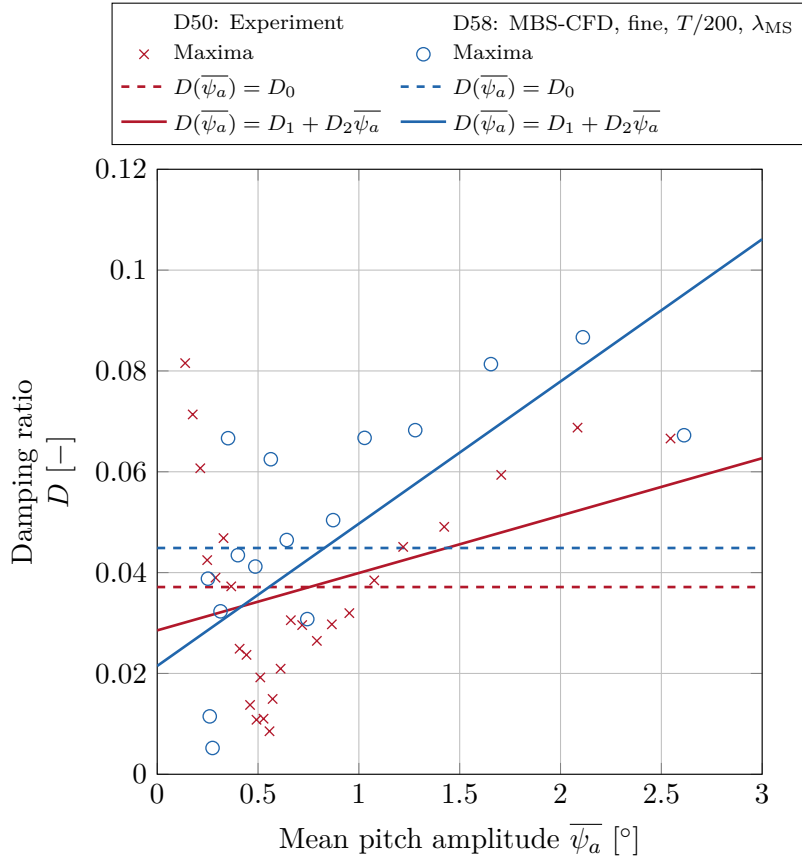


**Figure 4.8:** Damping ratios versus the mean pitch amplitudes. Regression functions are illustrated for the experiment and the MBS-CFD simulation.

The damping behaviour is approximated by a regression analysis. A fit to Equations 4.11 and 4.12 is made to find the values for  $D_0$ ,  $D_1$  and  $D_2$ . The graph demonstrates that a linear damping function is not sufficient to describe the behaviour of the floating system during the pitch-free decay because the data points show a large scatter around the horizontal, dashed lines for D50 and D58. Adding quadratic damping (solid lines) improves the goodness of fit of the data but higher-order terms are required to improve the fit.

Besides parameters, such as the grid resolution, temporal discretisation, initial amplitude of the free-decay and scaling factor, the numerical integration scheme of the coupled fluid and structural solvers influences the solution process. The fluid solver of the implicit MBS-CFD coupling methodology, introduced in Section 3.2, is limited to first-order Backward Euler time stepping scheme only. Higher-order implementations are beneficial in terms of numerical damping and accuracy but require further access to the MBS and CFD codes because more than one time step would have to be iterated in the communication data [37]. However, this is not possible as the applied commercial tools ANSYS CFX and SIMPACK are only open to a limited extend to user functions. The CFD results tend to predict higher damping than that of the experiment. This can be explained by the limitation of the numerical integration scheme. To achieve the same

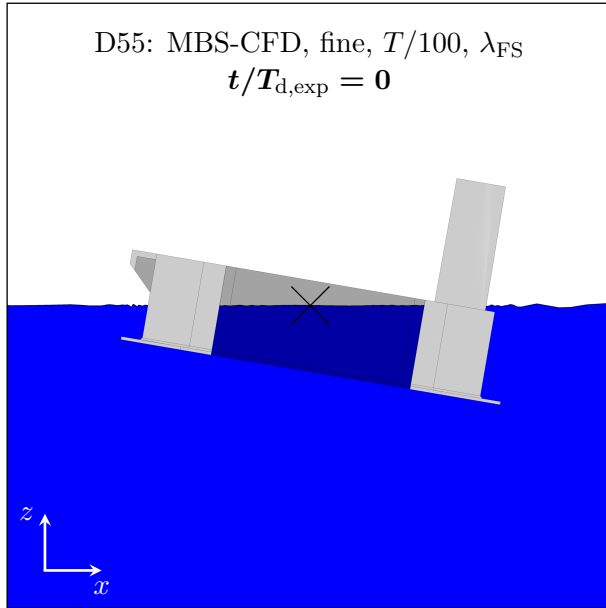
level of numerical damping with schemes of first-order instead of the second-order schemes, the temporal and spatial discretisation must be refined significantly, which increases the required computational resources. If no coupling to MBS is required, for example for a two-dimensional wave calibration analysis in CFD during pre-processing, the second-order Backward Euler time stepping scheme can be used. The derived settings from 2D are only fully transferable to 3D if the same time stepping scheme is applied. A discussion on the influence of the time stepping scheme on the numerical damping is included in Appendix A.2.

#### 4.4.2.3 Flow Field Visualisation

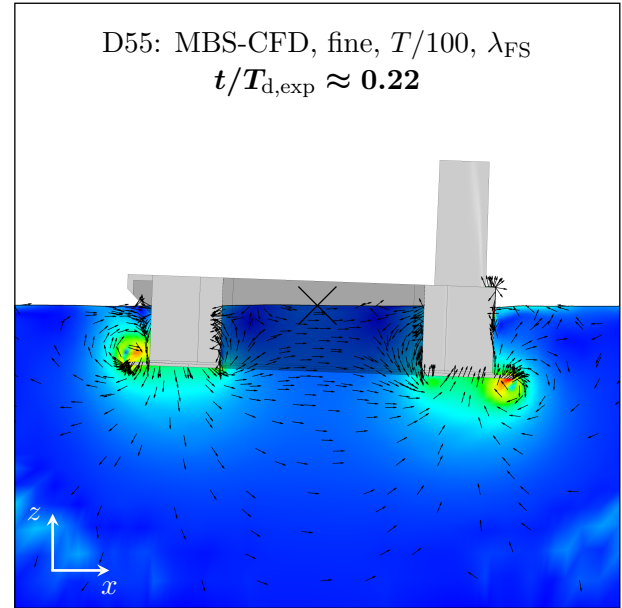
The normalised magnitude of the fluid velocity and normalised tangential velocity vectors are visualised for the simulation D55. Successive time steps are plotted in Figure 4.9 during the pitch free-decay starting from the initial position. A higher initial pitch amplitude than the experiment is chosen because the characteristic flow phenomena are amplified and better visible in the plots. The most relevant feature is strong three-dimensional vortex shedding that occurs at the skirt of the floating substructure after it is released from the initial position. The vortices rotate in clockwise direction both above and below the skirt. When the negative turning point of the first pitch oscillation is reached at  $t/T_{d,exp} \approx 0.49$  in Figure 4.9d and the platform starts to pitch back in the opposite direction, the vortex structures flow around the skirt and rotate anti-clockwise, while now being shed on the other side of the skirt. This vortex formation and interaction occurs during every maxima and minima of the pitch oscillation until the decay is finished and a static equilibrium is reached. Figure 4.9g highlights double vortices that rotate in opposite directions and form an eight-shape at the aft of the platform. The process how damping is generated can be shown using flow visualisation, which highlights the effects of the wall friction, the displacement of water particles below the floating substructure as well as the flow separation and associated vortex shedding. The water level in the moonpool stays nearly constant during the decay.

#### 4.4.2.4 Discussion of Computational Effort

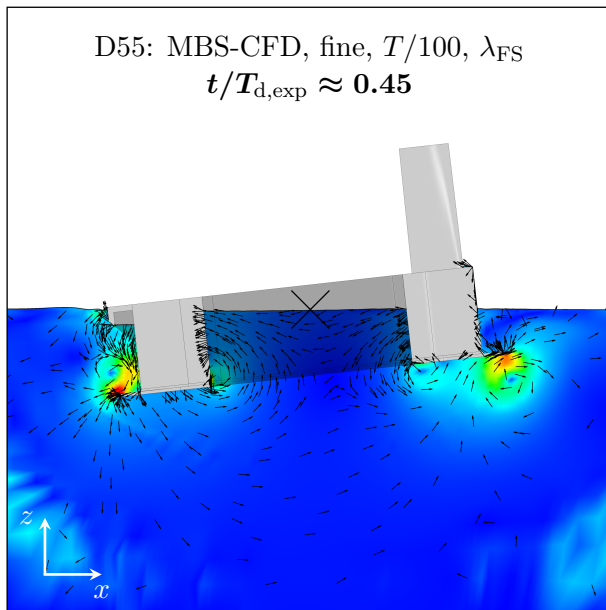
The wall clock time, that is needed to calculate the free-decay motion of ten periods, is recorded because of increased computational efforts for high-fidelity simulation methods. Table 4.4 quantifies the normalised calculation time  $T_{calc}/T_{calc,ref}$  with respect to the highest grid resolution in D55 for a selection of simulation cases. A large speed-up factor of over three is achieved using the coarse mesh in simulation D52 compared to the fine mesh in D55. If assessment of natural periods is of main interest, D52 is preferred in terms of the calculation time because both setups show small deviations from the experimental reference value of below 1% for the natural periods. However, if damping is to be modelled precisely, higher spatial and temporal discretisation is absolutely necessary as discussed in Section 4.4.2.2.



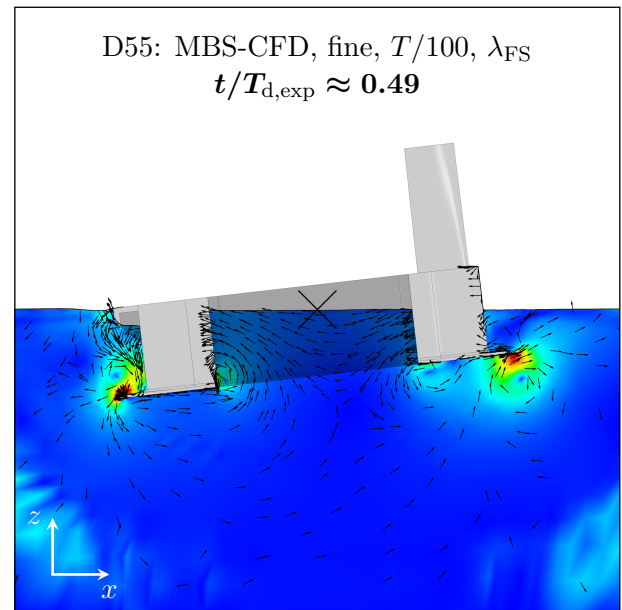
(a) Initial position.



(b) Maximum negative pitch velocity.



(c) Maximum positive pitch acceleration.



(d) Maximum negative pitch displacement.

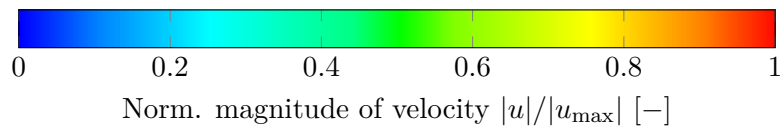
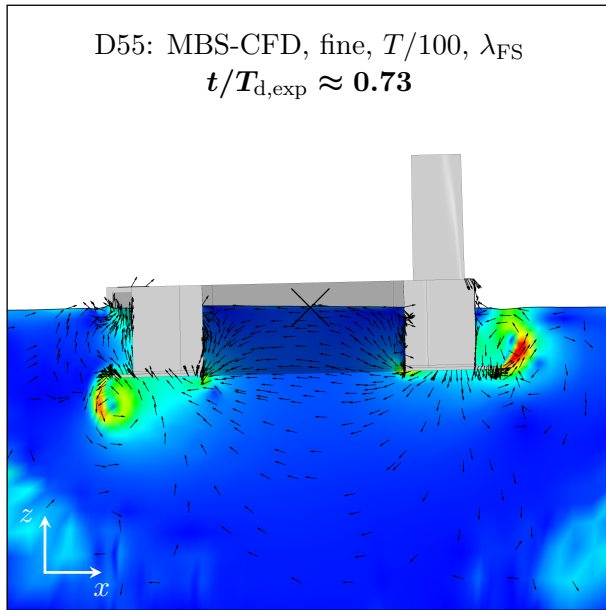
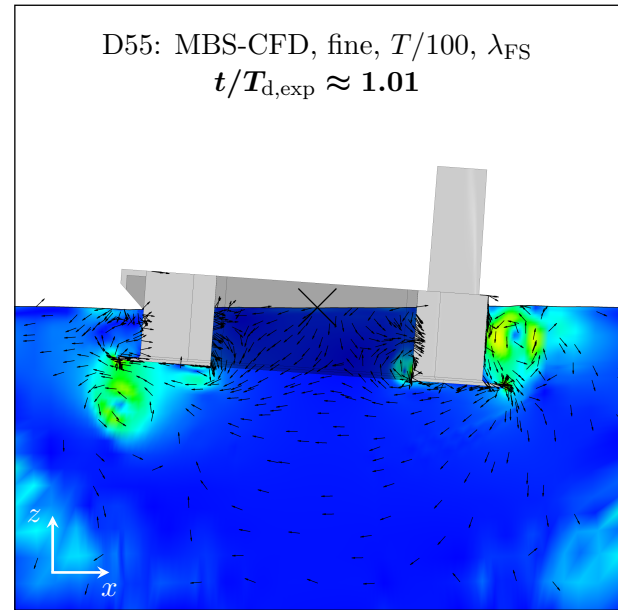


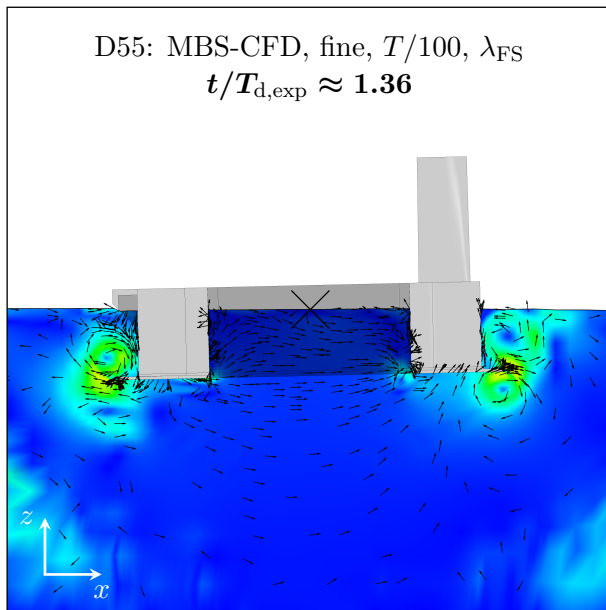
**Figure 4.9:** Visualisation of the normalised magnitude of the fluid velocity and the normalised tangential velocity vectors. The Figures are shown in the  $xz$ -plane at  $y = 0$  for successive time steps during the pitch free-decay. The initial position at the coordinate  $[0,0,0]$  is marked as reference by two crossed lines.



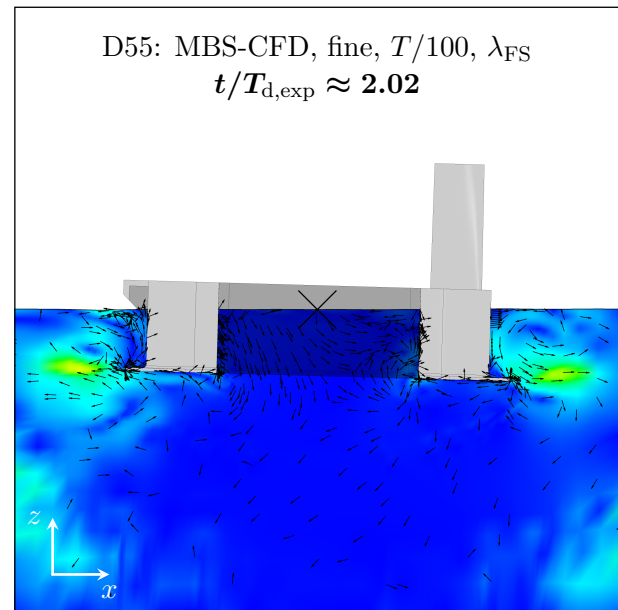
(e) Maximum positive pitch velocity.



(f) Maximum positive pitch displacement.



(g) Display of vortex shedding and dissipation.



(h) Display of vortex shedding and dissipation.

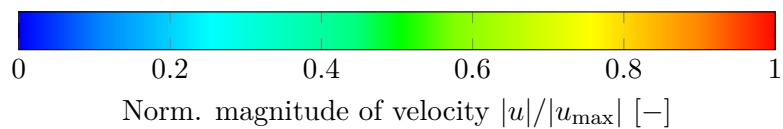
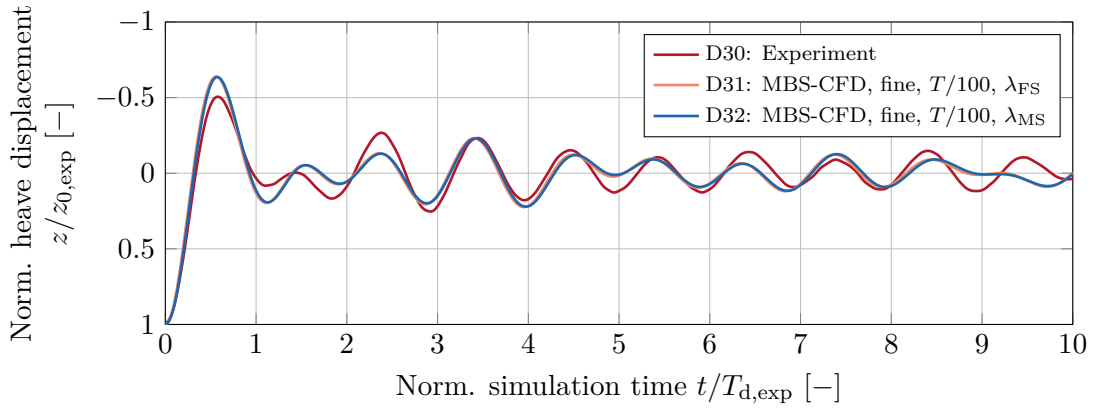


**Figure 4.9:** Visualisation of the normalised magnitude of the fluid velocity and the normalised tangential velocity vectors. The Figures are shown in the  $xz$ -plane at  $y = 0$  for successive time steps during the pitch free-decay. The initial position at the coordinate  $[0,0,0]$  is marked as reference by two crossed lines.

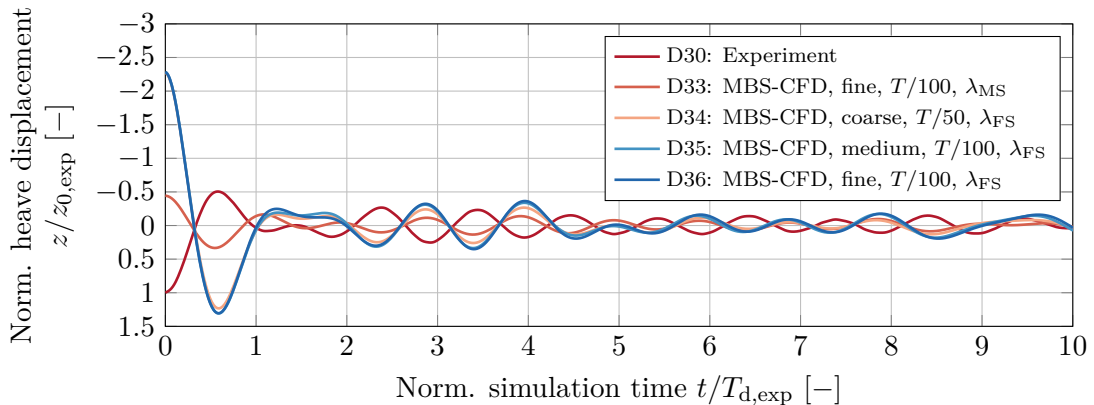
Similar trends were found by Arnold [176] for the MBS-CFD simulation of the free-decay of a spring pendulum in water with associated vortex shedding at the mass cube. The natural frequency of the damped oscillation was quite insensitive to a change in the grid resolution and even a very coarse mesh was sufficient to match the value of the experiment. However, the prediction of damping required higher spatial and temporal resolutions.

#### 4.4.3 Heave Free-Decay

Heave free-decay is evaluated in this Section. The model is pushed down vertically in MBS-CFD from its equilibrium position to  $z_{0,1} = z_{0,\text{exp}} = -1.25$  m and released. Additional simulations are performed with  $z_{0,2} = 0.62$  m and  $z_{0,3} = 3$  m by pulling the platform upwards. A time step of  $t_{\text{step}} = T/100$  is chosen and all three mesh variations fine, medium and coarse are simulated. The resulting vertical heave translational displacement, shown in Figure 4.10, is normalised to the initial, maximum value of the experiment.



(a) D31 and D32 with  $z_0/z_{0,\text{exp}} = 1$  at full scale  $\lambda_{FS}$  and model scale  $\lambda_{MS}$ .



(b) D33 to 36 with  $z_0/z_{0,\text{exp}} = -0.5$  and  $z_0/z_{0,\text{exp}} = -2.4$  at full scale  $\lambda_{FS}$  and model scale  $\lambda_{MS}$ .

**Figure 4.10:** Normalised heave displacement over the normalised simulation time during the free-decay. A comparison is made between the results of the wave tank model test and variations of the MBS-CFD simulation. The direction of the  $y$ -axis is reversed so that the downward movement of the substructure, for example in D36, after it is released corresponds to a descending line.



For simplification, the  $y$ -axis is shown in the opposite direction so that an upward movement of the model corresponds to an ascending line. Measurement noise of the experimental data is removed with a smoothing spline fitting function. Mean values and linear trends are removed from the signals. The normalised simulation time  $t/T_{d,\text{exp}}$  uses the natural period of the heave displacement of the experiment  $T_{d,\text{exp}}$  as reference. In contrast to the procedure applied for pitch free-decay, the value of  $T_{d,\text{exp}}$  is calculated from the Power Spectral Density (PSD) of the experimental data, see Section 4.4.3.1 for more details.

Natural frequencies and periods in heave are shown in Table 4.5 for all variations at model and full scale with three grid resolutions, two time step sizes and three initial heave displacements. The experimental data are used as reference to calculate the ratios  $f_d/f_{d,\text{exp}}$  and  $T_d/T_{d,\text{exp}}$ .

**Table 4.5:** Summary of the normalised eigenfrequency, period and simulation wall clock time resulting from the heave free-decay tests of the experiment and the MBS-CFD simulations. The damping ratios are not included.

ID	Method	Mesh	$t_{\text{step}}$	$\lambda$	$\frac{z_0}{z_{0,\text{exp}}}$	$\frac{f_d}{f_{d,\text{exp}}}$	$\frac{T_d}{T_{d,\text{exp}}}$	$\frac{T_{\text{calc}}}{T_{\text{calc,ref}}}$
D30	Experiment			32	1.0	1.0000	1.0000	
D31	MBS-CFD	fine	$T/100$	1	1.0	1.0150	0.9852	
D32	MBS-CFD	fine	$T/100$	32	1.0	1.0150	0.9852	
D33	MBS-CFD	fine	$T/100$	32	-0.5	1.0150	0.9852	
D34	MBS-CFD	coarse	$T/50$	1	-2.4	1.0188	0.9816	0.1724
D35	MBS-CFD	medium	$T/100$	1	-2.4	1.0150	0.9852	0.5062
D36	MBS-CFD	fine	$T/100$	1	-2.4	1.0150	0.9852	1.0000

#### 4.4.3.1 Discussion of Natural Period

The relation between frequency, period and angular frequency of a periodic signal is given by:

$$f = \frac{1}{T} = \frac{\omega}{2\pi}. \quad (4.13)$$

For pitch free-decay the reference value  $t/T_{d,\text{exp}}$  is calculated from the average of successive pairs of maximum and minimum values of the time series. This procedure is not applicable for the heave free-decay because of the large non-linear interference from vortex shedding on the heave motion. Therefore, the determination of peak values is not as straight forward as for the pitch free-decay. Instead,  $T_{d,\text{exp}}$  is derived from the PSD of the heave displacement using a Fast Fourier Transform (FFT) analysis. In order to improve the estimates, 30 periods are simulated compared to only 10 periods for the pitch free-decay. Results are plotted over the normalised frequency  $f/f_{d,\text{exp}}$  in Figure 4.11 using a linear  $y$ -axis. The natural frequency  $f_d$  in heave corresponds to the main peak of the signal in the frequency domain. It is used to

calculate the natural period of the experimental data  $T_{d,exp}$  according to Equation 4.13 and the normalised simulation time  $t/T_{d,exp}$  in Figure 4.10.

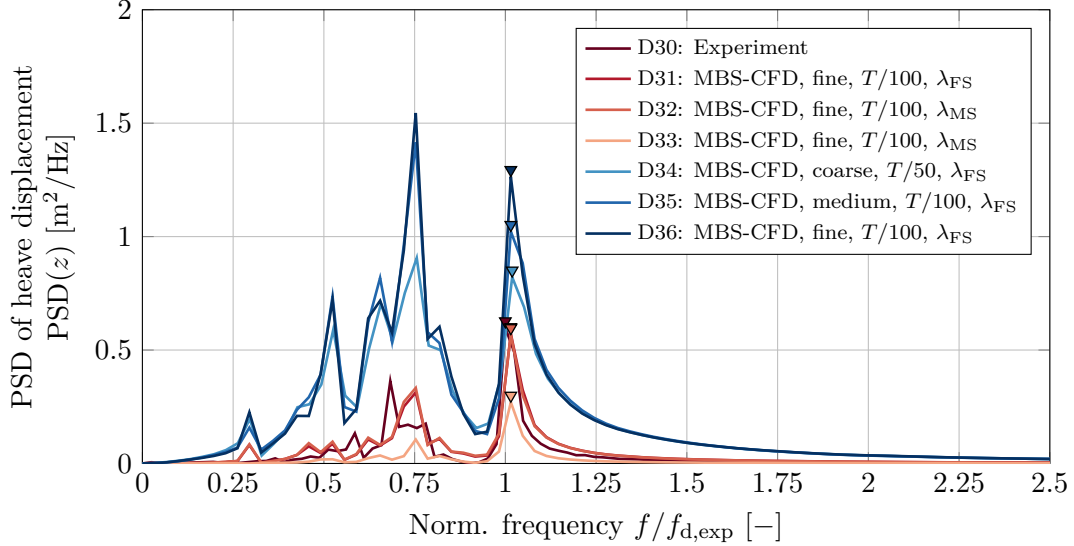


**Figure 4.11:** PSD of the heave displacement over the frequency normalised to the natural frequency of the experiment. The triangles indicate the peak values at the natural period.

The influence of grid size on the natural period is studied using the simulations D34, D35 and D36, shown in Figure 4.10b. Similar to the findings for pitch free-decay, the numerical results agree very well with the experimental data with a small overestimation of 1% to 2%. The coarse mesh in conjunction with the largest time step size of  $t_{step} = T/50$  shows a higher discrepancy than the medium and fine mesh, but this difference is insignificant. Still, D34 demonstrates the possibility to determine the natural period using MBS-CFD with a relatively coarse but still reasonable discretisation and this translates into a high computational speed-up of  $T_{calc,D36}/T_{calc,D34} \approx 5.8$  compared to the finest mesh.

The scaling factor has little to no influence on the natural period for simulations D31 and D32 as demonstrated in Table 4.5. A visual inspection of Figure 4.10a does not contradict this conclusion.

More relevant is the initial heave displacement from which the platform is released. Although the natural periods for D32 with  $z_0/z_{0,exp} = 1$ , D33 with  $z_0/z_{0,exp} = -0.5$  and D36  $z_0/z_{0,exp} = -2.4$  agree very well with the experiment with a deviation of around 1.5%, significant differences in the PSD plot can be seen, see Figure 4.11. The higher the initial heave displacement, the higher the magnitude of the peak of  $PSD(z)$  at the heave natural frequency. The peak values also depend on differences in the numerical damping due to the variations in grid resolution, temporal discretisation etc. In general, this behaviour is expected because more potential energy is available for the free-decay at the natural frequency with larger initial heave amplitude. Consequently, the peak values of D31 and D32 with  $z_0/z_{0,exp} = 1$ , marked by triangles in Figure 4.11, coincide with the experiment D30. The initial heave displacement for D33 is

smaller than for the experiment  $|z_{0,2}| < |z_{0,\text{exp}}|$  and also the magnitude of the peak in the PSD at the natural frequency is lower than for D30. In contrast, for D34 to D36 with higher initial heave amplitudes  $|z_{0,3}| > |z_{0,\text{exp}}|$  the peaks are also higher.

Looking at the spectral energy distribution below the natural frequency  $f/f_{d,\text{exp}} < 1$ , some interesting physical phenomena of this particular platform concept can be seen. Besides the peak at the natural frequency, high spectral energy content is present at around  $f/f_{d,\text{exp}} \approx 0.75$ . The magnitude of the second peak can be even larger than the peak at the natural frequency if the initial heave displacement increases, see D36 compared to D30. This is caused by interactions between the fluid and the square-shaped substructure that is combined with a moonpool. The water column inside the moonpool can be excited at its natural frequency, which results in large vertical motion. The literature describes this as piston mode. Faltinsen [105] considers the water column as a mass-spring system without damping and calculates the natural period of the moonpool  $T_n$  with the draught  $h$ . The square cross-section  $A$  of the moonpool is taken into account in [22] with:

$$T_n = 2\pi \sqrt{\frac{h + 0.473\sqrt{A}}{g}}. \quad (4.14)$$

Equation 4.14 provides an approximation of the piston mode, which is close to the observed peak at  $f/f_{d,\text{exp}} \approx 0.75$ . Furthermore, Molin [181] describes a method to obtain the piston mode of moonpools. Gaillardet et al. [182] state that the heave motion of a floating structure itself is excited when the volume of water oscillating in the moonpool is large enough. The analysis of moonpool effects is described in recommended practices, for instance [22, 183].

Generally speaking, the ability of the fluid boundary layer to follow the hull contour during movement of the structure diminishes with increasing pressure gradient, which ultimately leads to boundary layer detachment. Flow separation is also triggered in particular by geometric singularities such as sharp edges and corners in the geometry instead of rounded corners. The boundary layer detaches, folds and forms vortices that dissipate after time. Large vortex structures are shed during the heave free-decay below the SWL at the skirt and bottom of the hull, which introduces non-linearities in the heave motion. Higher absolute initial heave amplitudes increase the fluid-structure-interaction due to increased vortex dimensions, strength and maximum rotational velocities during the heave decay.

Small differences in the estimates of natural periods from the MBS-CFD simulation may also result from random errors during the execution of the wave basin test. Only one experimental dataset is available for the heave free-decay, which is less reliable than analysing repeated tests. Systematic errors are introduced because of the measurement accuracy of the optical motion tracking system of  $\pm 0.03$  m and  $\pm 0.1^\circ$  at full scale, which is approximately 2.4% of the initial heave displacement of the experiment. Only the mooring interface structure at the fore of the

platform is included in the simplified numerical domain, compare Figure 4.2 and 4.13. However, additional drag in heave is missing from the mooring interface structure at the aft of the hull, which may increase the natural period slightly.

#### 4.4.3.2 Discussion of Damping Behaviour

In contrast to pitch free-decay, the procedure described in Section 4.4.1 for determination of the damping behaviour is not applied for the heave free-decay. This is caused by significant non-linearities in the heave motion, which are introduced by strong vortex shedding and interactions with the moving water inside the moonpool. Assessment of damping ratios is not straightforward for the heave DOF because successive pairs of maxima during the damped oscillation decrease and increase in magnitude, see the time series in Figure 4.10. This makes a similar regression analysis as the one performed in Figure 4.8 unreliable. Beyond that, the damping calculation procedure is very sensitive to, for example, the minimum peak height and distance and the amount of data included. Higher damping is observed for the simulation D34 in Figure 4.10 compared to D35 and D36 because both the spatial and temporal resolution of D34 are lower. A similar relation between the damping and the grid and time step size is described for the pitch free-decay in Section 4.4.2.2.

Different physical phenomena are responsible for the viscous damping forces. First, geometric singularities such as edges trigger vortex shedding because of changes in the pressure field and resulting flow separation. The higher the initial heave amplitude, the higher the maximum vertical velocity during the decay and the higher the damping because of the quadratic, non-linear terms caused by increased vortex shedding. Second, wall friction from, for example, water entering and leaving the moonpool or the oscillating water column inside the moonpool, introduce additional damping. It is noticeable that the floating substructure continues to oscillate at low amplitude for both the experiment and simulation after  $t/T_{d,exp} > 5$ . With small heave amplitudes and small vertical velocities, small damping is created because of little vortex shedding and small wall friction from the water column oscillating vertically inside the moonpool.

#### 4.4.3.3 Flow Field Visualisation

The flow field with the normalised magnitude of fluid velocity and normalised tangential velocity vectors is visualised for simulation D36. Successive time steps are plotted in Figure 4.13 starting from the initial heave position. Similar to pitch free-decay in Section 4.4.2.3, the initial displacement is higher than that of the experiment in order to amplify characteristic flow phenomena.

Vortices rotate in clockwise direction at the fore of the hull and anti-clockwise at the aft in Figure 4.13b after release. When the negative turning point of the first heave oscillation is

reached at  $t/T_{d,exp} \approx 0.59$  in Figure 4.13c and the substructure heaves back in the positive  $z$ -direction, vortex structures flow around the skirt in Figure 4.13d before they rotate beneath the bottom side of the skirt in the opposite direction as before. As a consequence, the floating substructure repeatedly interacts with shed vortices while moving up and down during the heave oscillation until it reaches a static equilibrium. For example, after the maximum heave displacement is reached and the platform heaves downwards, newly shed vortices above and already existing vortex structures beneath the skirt touch each other, see Figure 4.13h, while rotating in opposite direction.

In contrast to pitch free-decay the water column inside the moonpool is not constant during heave free-decay but is excited at the heave natural period after release. The relative wave elevation is recorded at wave probe  $WP_0$  in the middle of the moonpool at  $x = y = 0$  m for D36, see a schematic arrangement in Figure 4.3. Together with the normalised heave displacement, the results are plotted in Figure 4.12. The wave elevation signal is phase shifted and lags behind the heave motion because of inertia effects. In general, a downward movement of the platform as shown in Figure 4.13b results in an inflow of water at the bottom of the moonpool, which increases the water level. Contrary, if the floater moves upward fluid flows out of the moonpool at the keel which decreases the water level, see Figure 4.13d. The moving water column inside the moonpool influences the heave motion of the floating substructure as discussed in Section 4.4.3.1. This effects is clearly visible in Figure 4.12 at the maximum moonpool water level at  $t/T_{d,exp} \approx 1.5$ , see Figure 4.13g. One would expect the platform to heave downward after reaching the maximum positive heave displacement, see Figure 4.13f, but instead the structure stays at nearly the same  $z$ -position until the moonpool sinks again. At the maximum water level in Figure 4.13g, the free surface is elevated in the middle and lowered at the walls of the moonpool, which shows small wave radiation inside the moonpool.

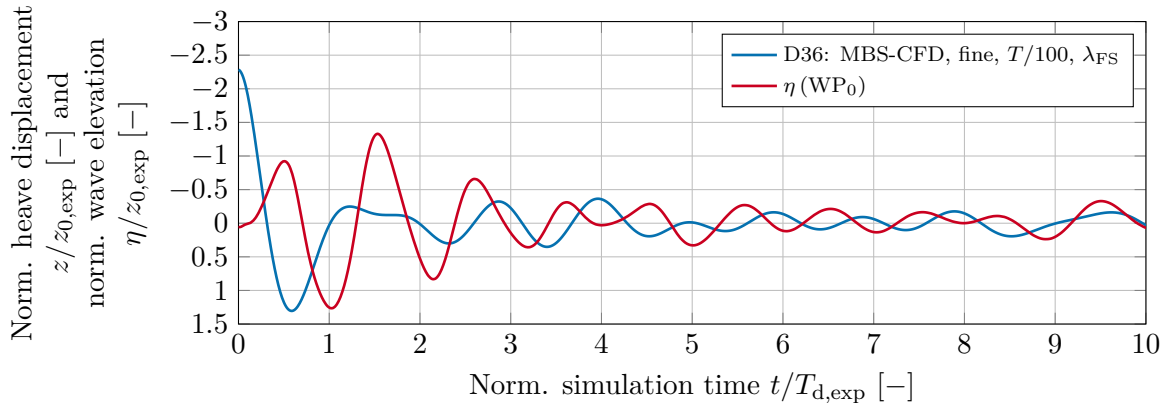


**Figure 4.12:** Comparison of the normalised heave displacement (blue) over the normalised simulation time during free-decay for D36 with the relative wave elevation (red) inside the moonpool at wave probe  $WP_0$ , see the schematic arrangement in Figure 4.3. The direction of the  $y$ -axis is reversed so that the downward movement of the substructure in D36 after it is released corresponds to a descending line.

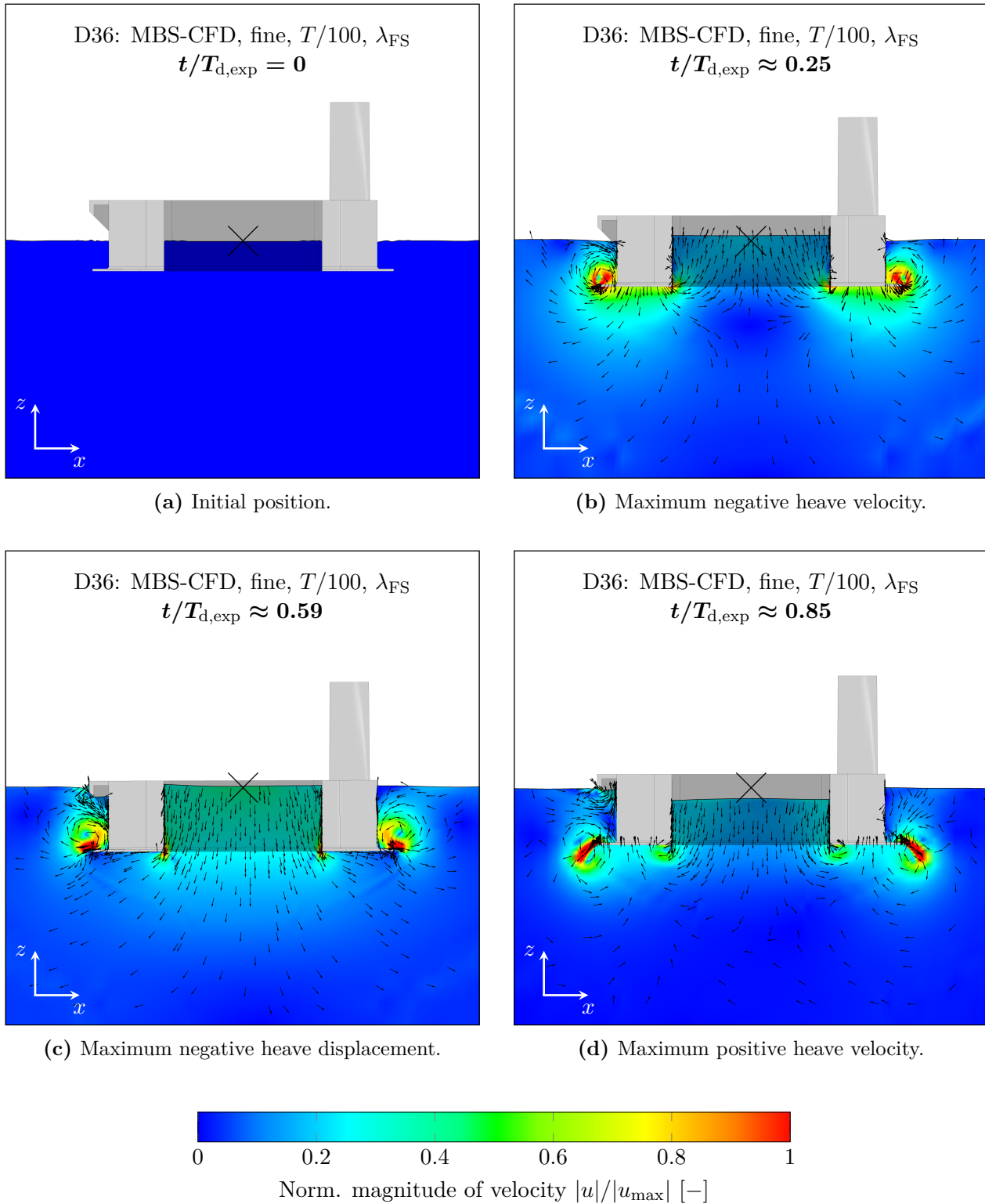
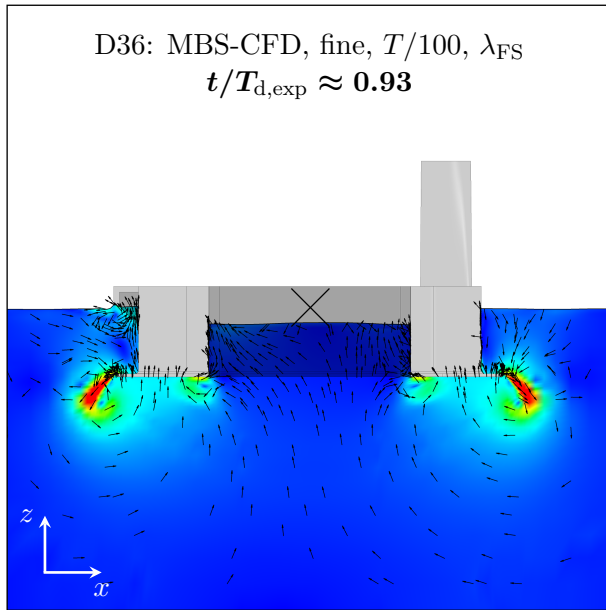
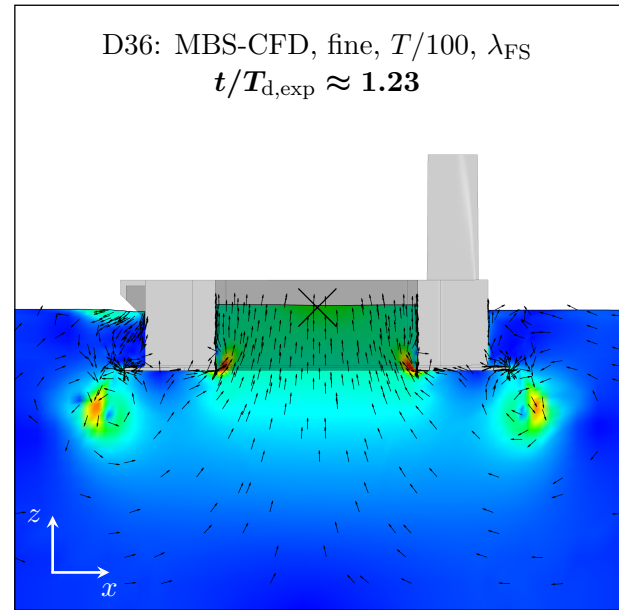


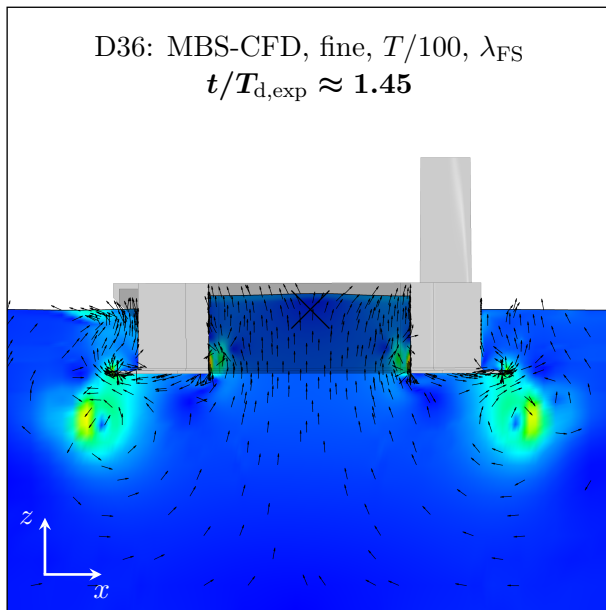
**Figure 4.13:** Visualisation of the normalised magnitude of the fluid velocity and the normalised tangential velocity vectors. The Figures are shown in the  $xz$ -plane at  $y = 0$  for successive time steps during the heave free-decay. The initial position at the coordinate  $[0,0,0]$  is marked as reference by two crossed lines.



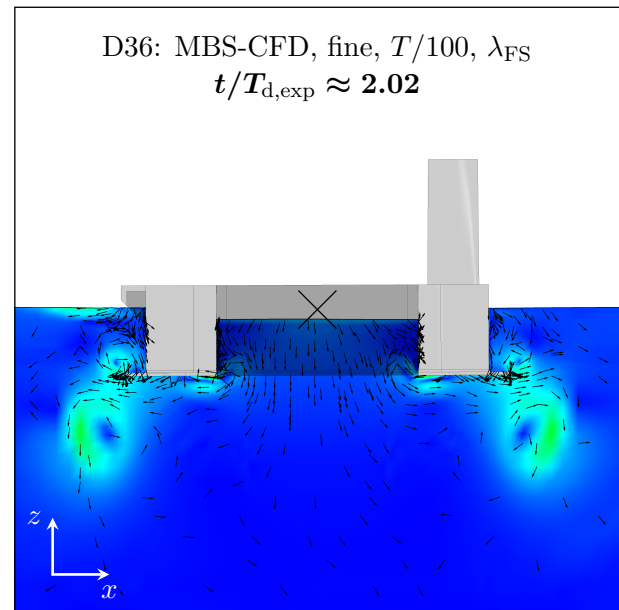
(e) Minimum water level in moonpool.



(f) Maximum positive heave displacement.



(g) Maximum water level in moonpool.



(h) Display of vortex shedding and dissipation.

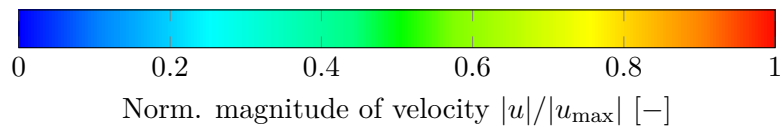
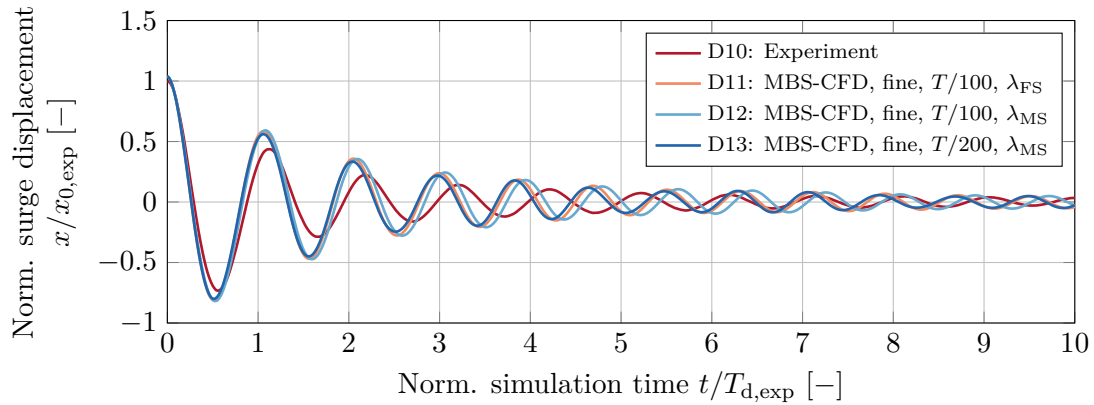


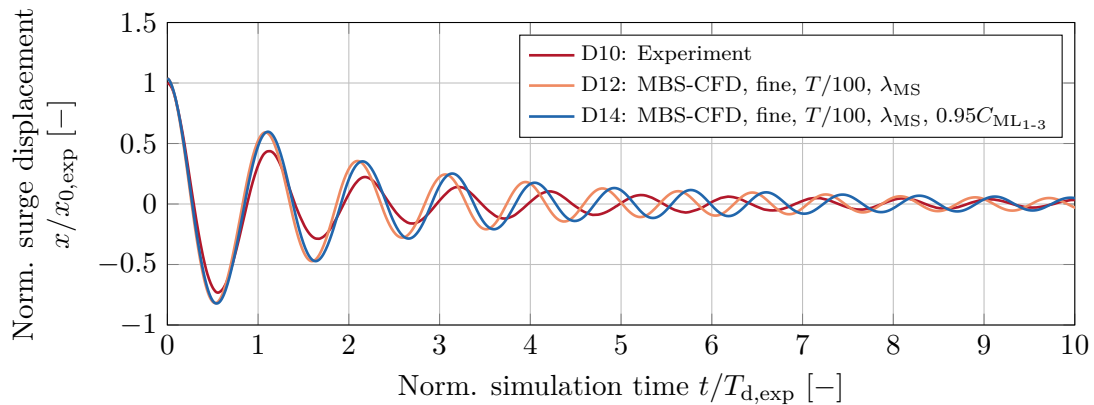
**Figure 4.13:** Visualisation of the normalised magnitude of the fluid velocity and the normalised tangential velocity vectors. The Figures are shown in the  $xz$ -plane at  $y = 0$  for successive time steps during the heave free-decay. The initial position at the coordinate  $[0,0,0]$  is marked as reference by two crossed lines.

#### 4.4.4 Surge Free-Decay

Surge free-decay is discussed in this Section. The model is pulled horizontally in MBS-CFD from its equilibrium position to  $x_{0,1} = x_{0,\text{exp}} = 8$  m and released. The initial surge displacement is the same for all performed MBS-CFD simulations. Also, the spatial discretisation is identical with the application of the fine mesh for all cases. The baseline time step is  $t_{\text{step}} = T/100$ . As comparison, a case with increased temporal discretisation of  $t_{\text{step}} = T/200$  is simulated. The resulting horizontal surge translational displacement is shown in Figure 4.14 relative to the initial, maximum value of the experiment. Measurement noise of the experimental data as well as mean values and linear trends are removed from the signals. The normalised simulation time  $t/T_{d,\text{exp}}$  uses the natural period of the surge displacement of the experiment  $T_{d,\text{exp}}$ , which is calculated from successive pairs of maxima similarly as for the pitch free-decay.



(a) D11 to 13 with  $x_0/x_{0,\text{exp}} = 1$  at full scale  $\lambda_{\text{FS}}$  and model scale  $\lambda_{\text{MS}}$ .



(b) D12 and D14 with  $x_0/x_{0,\text{exp}} = 1$  at model scale  $\lambda_{\text{MS}}$ . The mooring line stiffness is reduced by 5% in D14 compared to D12.

**Figure 4.14:** Normalised surge displacement over the normalised simulation time during the free-decay. A comparison is made between the results of the wave tank model test and variations of the MBS-CFD simulation.

Natural frequencies and periods in surge are quantified in Table 4.6 for all variations at model and full scale with one grid resolution, two time step sizes and one initial surge displacement.



**Table 4.6:** Summary of the normalised eigenfrequency, period, damping and simulation wall clock time resulting from the surge free-decay tests of the experiment and the MBS-CFD simulations. For simulation D14, the global stiffness ( $0.95C_{ML1-3}$ ) and the pre-tension of each mooring line are reduced by 5% to account for measuring and modelling errors.

ID	Method	Mesh	$t_{\text{step}}$	$\lambda$	$\frac{x_0}{x_{0,\text{exp}}}$	$\frac{f_d}{f_{d,\text{exp}}}$	$\frac{T_d}{T_{d,\text{exp}}}$	$D_0$	$D_1$	$D_2$	$\frac{T_{\text{calc}}}{T_{\text{calc,ref}}}$
D10	Experiment			32	1	1.0000	1.0000	0.0552	0.0215	0.0289	
D11	MBS-CFD	fine	$T/100$	1	1	1.1627	0.8601	0.0418	0.0188	0.0153	1.0000
D12	MBS-CFD	fine	$T/100$	32	1	1.1389	0.8781	0.0420	0.0191	0.0152	0.9181
D13	MBS-CFD	fine	$T/200$	32	1	1.1673	0.8567	0.0421	0.0176	0.0174	
D14	MBS-CFD	fine	$T/100$	32	1	1.1124	0.8990	0.0420	0.0192	0.0150	

#### 4.4.4.1 Discussion of Natural Period

The natural period is derived from the average of successive pairs of maximum and minimum values of the time series. In contrast to pitch decay, it reduces in magnitude for both experiment and simulation from the start of the decay until reaching a static equilibrium. D11 shows noticeable maximum and minimum deviations from the mean of  $T_{d,\text{max,exp}}/T_{d,\text{exp}} = 1.1258$  and  $T_{d,\text{min,exp}}/T_{d,\text{exp}} = 0.9029$ .

Considering the influence of the scaling factors on the numerical results, the natural period of the full scale simulation D11 of  $T_d/T_{d,\text{exp}} = 0.8601$  can be determined, which is 2% smaller than  $T_d/T_{d,\text{exp}} = 0.8781$  for the model scale case D12. Figure 4.14a shows a phase shift of  $\theta \approx \pi/2$  after  $t/T_{d,\text{exp}} = 10$  and D11 lags behind D12. Differences in Reynolds number between model and full scale are inevitable because the Froude scaling was applied in the wave basin experiment. The Reynolds number of Equation 2.24 describes the influence of the viscous forces relative to the inertial forces. Differences in the natural period of the simulated free-decay can be caused by the drag load predictions in CFD at model and full scale.

However, significant underestimations of more than 10% compared to the natural period of the experiment D10 can be observed. Similar discrepancies of the natural period between numerical model and experiment are not seen for the pitch and heave free-decay, which excludes fundamental modelling errors in the numerical CFD setup for surge. Additionally, measurements of the restoring forces in the surge direction indicate very good agreement with the MBS representation of the mooring system as shown in Figure 4.5.

The sensitivity of the restoring forces from the mooring system to the natural period in surge is analysed. For simulation D14, the global stiffness and the pre-tension of each mooring line are reduced by 5% to account for measuring and modelling errors. A decrease of the mooring stiffness increases the natural period according to Equations 4.4 and 4.6 for the linear equation of motion because of the relation  $T_d \propto 1/\sqrt{k}$ . As the natural period in surge only increases by

2.4% with  $T_d/T_{d,\text{exp}} = 0.8990$ , see also Figure 4.14b, other sources for the observed deviations need to be identified.

As simplification, only surge, heave and pitch DOFs are considered in the numerical simulation. In reality, the other platform DOFs sway, roll and yaw are also excited during surge free-decay, albeit with lower amplitude than the main DOFs. Only one measurement data set is available for the surge free-decay. Therefore, the standard deviation cannot be determined. When looking at the experimental time series, it can be seen that the mock-up is pulled from its equilibrium position to the initial surge displacement  $x_{0,\text{exp}}$  within a couple of seconds. Not only surge is excited, but also sway by  $|y_{\text{max,exp}}| \approx 1.5$  m, which indicates that the pulling operation was not carried out completely aligned to the global  $x$ -axis. After releasing the model in the wave basin, the platform experiences sway and yaw oscillations with a mean value of zero. Platform yaw shows maximum amplitudes of  $|\chi_{\text{max,exp}}| \approx 6^\circ$ , resulting in increasing drag forces during the surge free-decay compared to the MBS-CFD simulation. A constant yaw angle of zero degree is applied in the simulation because of symmetry in the  $xz$ -plane at  $y = 0$  in the CFD domain, and the yaw-surge coupling is not taken into account.

The surface area below SWL projected on the  $yz$ -plane mainly creates resistance during surge free-decay. The higher the platform yaw, up to  $|\chi| = 45^\circ$ , the higher the projected surface area. This directly affects the drag force because it is proportional to the reference area. For example, for this hull geometry a yaw angle of six degrees increases the projected surface area and the resulting drag force by 10% compared to a platform yaw of zero degrees. The yaw oscillation is damped after a few periods. Changes in platform draft also affect the wetted surface area but this seems not to be dominating here. Consequently, it is assumed that higher resistance and added mass is present in the experiment, leading to higher natural periods in D10 than natural periods in D11 to D14. This assumption is supported by findings from regular wave tests in Section 4.5.1 demonstrating very good agreement between experimental and numerical results. Ideally, initial positions, velocities and accelerations must be defined for all six platform DOFs in the numerical model, so that the initial conditions of the experiment can be captured correctly.

Refining the temporal discretisation by a factor of two to  $t_{\text{step}} = T/200$  in simulation D13 increases the deviation to the experiment with  $T_d/T_{d,\text{exp}} = 0.8567$ . One would assume that the damping reduces with the decreasing time step size from D12 to D13. But in contrast to a similar study for pitch free-decay, the damping ratios are comparable in their magnitude. However, the mooring lines provide only very limited restoring forces in platform pitch, hence, showing only little influence on the motion. For surge motion, the restoring forces originate from the mooring system. In conclusion, different numerical behaviour between D12 and D13 may be caused by different temporal discretisations of the mooring model, which results in different mooring line forces.

## 4.4.4.2 Discussion of Damping

Similar to the pitch free-decay in Section 4.4.2.2, the damping behaviour of the investigated surge free-decay cases is insensitive to the applied scaling factor.

Major differences between the damping of the pitch and surge free-decay are observed. First, the magnitude of damping ratios  $D_0$ ,  $D_1$  and  $D_2$  is underestimated by the numerical simulations D11 to D14 compared to the results of experiment D10, see Table 4.6. Given the mutual influence of natural period on damping, see Equation 4.6, this is expected because of an underestimation of the natural period of above 10%. Second, a significant reduction of the temporal discretisation to  $t_{\text{step}} = T/200$  for D14 does not noticeably influence the damping ratios at all. This indicates that either the temporal resolution for surge free-decay has already converged or the influence of the restoring forces from the mooring lines exceeds considerably other contributions to the damping forces, for example wall friction, vortex shedding or wave radiation. Damping ratios are plotted against the mean surge amplitudes in Figure 4.15 for the experimental data D10 and MBS-CFD simulation D13.

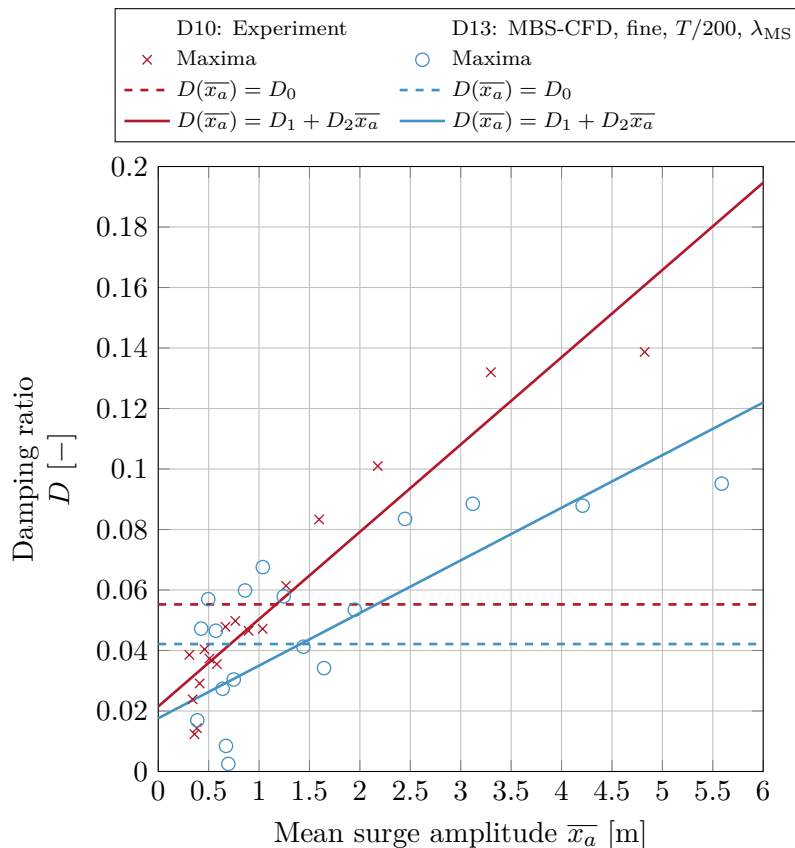


**Figure 4.15:** Damping ratios versus the mean surge amplitudes. Regression functions are illustrated for the experiment and the MBS-CFD simulation.

A regression analysis, similar to the one performed for the pitch free-decay, shows the damping behaviour of the floating system in surge. A linear damping function with the damping ratio

$D_0$  using dashed lines is not representing the behaviour shown by the data points. Only if a quadratic damping is taken into account with the damping ratios  $D_1$  and  $D_2$  using the solid lines, a better fit can be found. The graphs show that although the values for  $D_1$  are comparable between the experiment and simulation, higher damping is present in the experiment for  $D_2$  because the slope of the solid line is higher. Quadratic damping is more relevant especially during the first oscillations when the velocities are higher.

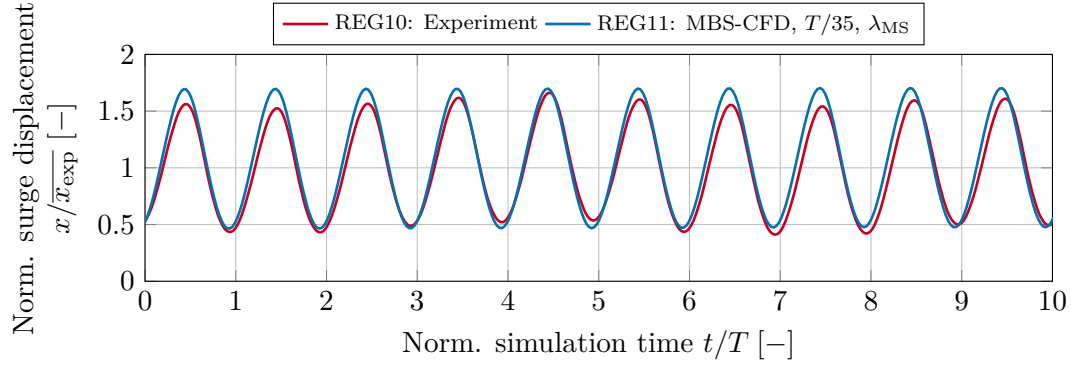
## 4.5 Regular Wave Test

During a validation, the level of complexity is increased gradually. Free-decay tests reveal the behaviour of a floating system for each individual DOF. Interactions between DOFs and external forcing from, for example, the mooring system need to be analysed in more complex load cases. For this reason, a regular wave test with  $H = 6$  m and  $T = 10$  s, as specified in Table 4.2, was conducted in the wave basin and compared to a MBS-CFD simulation. Platform motion in surge, heave and pitch, as considered in the numerical model in Table 4.1, are excited by incident waves. Restoring forces are provided by the mooring system. However, depending on the mooring line characteristics and wave kinematics, the floating substructure is pushed in the direction of the wave propagation and oscillates around a mean drift position. In order to save time during the initialisation of the numerical simulation, the platform is positioned at the mean surge location in the CFD mesh based on the evaluation of the measurement data. In addition, spring-damper elements are included in the MBS model to fix the structure at the initial surge displacement until waves are fully developed in the numerical CFD domain after a couple of wave periods, see also Section 3.5 and 3.6. One experimental data set is available per regular wave test and results of one numerical simulation are presented for the platform kinematics in surge, heave and pitch, for the relative wave elevations around the floater and for the flow field visualisation of one wave passing.

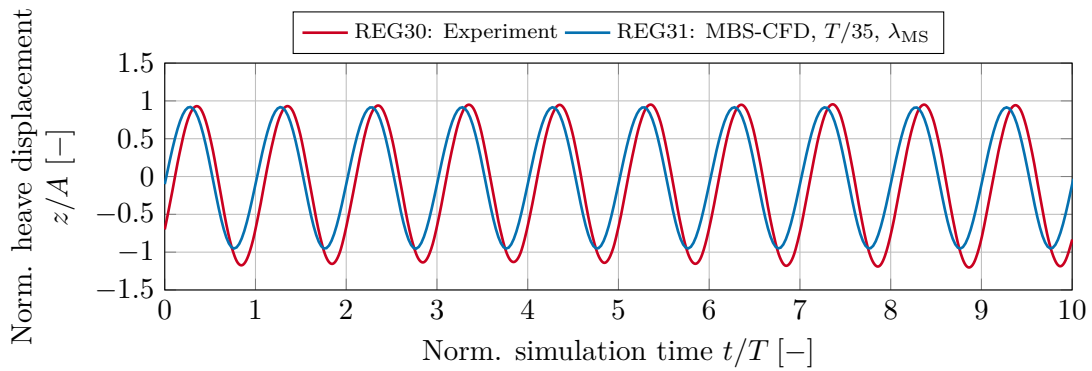
In the following analysis, IDs are used to distinguish between the measurements and different simulation results. Each plot line is associated with a five-character ID:

- Character 1-3: “REG” representing regular wave load cases,
- Character 4: One digit representing a sensor (“1” for surge translational displacement, “3” for heave translational displacement and “5” for pitch rotational displacement),
- Character 5: One digit that is either “0” for the experiment or “1” for the simulation.

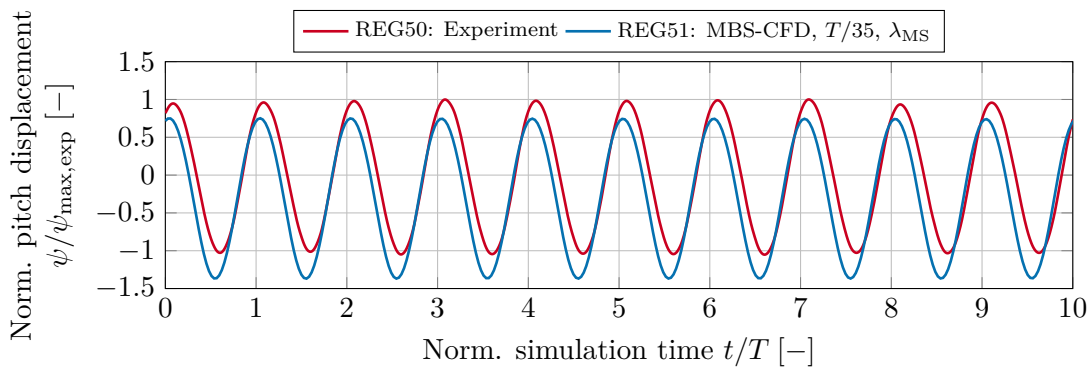
As an example, REG51 refers to the platform pitch displacement of the regular wave simulation.



(a) Surge displacement normalised to the mean surge position of the experiment  $\overline{x_{\text{exp}}}$  over the normalised simulation time.



(b) Heave displacement normalised to the wave amplitude  $A$  over the normalised simulation time.



(c) Pitch displacement normalised to the maximum platform pitch  $\psi_{\text{max,exp}}$  of the experiment over the normalised simulation time.

**Figure 4.16:** Comparison of the normalised platform motion in surge, heave and pitch between the experiment and the MBS-CFD simulation for the regular wave case defined in Table 4.2.

### 4.5.1 Discussion of Platform Kinematics

Following the simulation procedure described in Section 3.5 and Figure 3.17, wave calibration is performed in the two-dimensional CFD domain. Platform kinematics of the experimental data are analysed, especially the mean surge position, to find initial conditions of the numerical model. Linear Airy waves are generated at the inlet boundary condition with the WAVE2CFX numerical wave generator, introduced in Section 3.3.1.1, and increased in height using a ramp function of two full wave periods. Afterwards, the three-dimensional, transient, coupled MBS-CFD simulation is conducted applying a pre-deformed mesh based on the known initial surge displacement. In order to accelerate the initialisation process and avoid long transient platform motions because of the relatively high natural periods in surge, the floating substructure is fixed at the initial surge position by spring-damper elements in the MBS model. Constraining forces are released after the waves are fully developed and reach the platform. Finally, the floating system is free to oscillate around the mean surge position after some transients under the influence of incident waves. A processing window of ten wave periods is extracted from both the measurements and the numerical results after the transients. Normalised surge, heave and pitch displacement are plotted against the normalised simulation time in Figure 4.16. Phase differences between the two data sets are corrected for all sensors by shifting the simulation results in time with respect to the surge translational displacement.

Platform surge, resulting from mean wave drift forces, is presented normalised to the mean surge displacement of the experiment  $\overline{x_{\text{exp}}}$  in Figure 4.16a. The cases REG10 and REG11 show very good agreement between experiment and MBS-CFD simulation for platform surge motion, especially for  $3 \leq t/T \leq 5$ . This behaviour is better than expected given the deviations in the natural period and the sensitivity to mooring stiffness observed for the surge free-decay in Section 4.4.4. For regular waves, maximum, minimum and mean values in surge of both experiment and simulation agree very well. This indicates that the restoring forces from the mooring lines in the numerical model are comparable to those of the experiment.

Heave displacement of the floating substructure is normalised with respect to the wave amplitude  $A$ , see Figure 4.16b. A small phase shift between REG30 and REG31 is visible and the minimum heave displacement is slightly underestimated by the numerical model. Besides, frequency and maximum heave are predicted correctly, demonstrating an overall good match between the experimental and numerical results.

Platform pitch rotational displacement is normalised with respect to the maximum pitch displacement of the experiment  $\psi_{\text{max,exp}}$  in Figure 4.16c. Similarly to the findings for heave, the pitch signal of the experiment is leading with a small phase shift. In addition, an offset in pitch is found for the MBS-CFD simulation resulting in a lower mean value compared to the experiment. Platform pitch and heave displacement are coupled, meaning that a non-zero pitch value also changes the heave. Differences may be explained by, firstly, geometrical deviations between

the mock-up used in the experiment and the CFD mesh of the platform. Only the mooring interface structure at the fore of the floating substructure is included in the numerical domain for simplification purposes, compare Figure 4.2 and 4.18. Secondly, wave excitation may be different due to not perfectly matched wave kinematics at the floating substructure between the experiment and simulation. The reference wave probe  $WP_{\text{ref}}$  may be influenced by wave reflection at the substructure and walls of the wave tank. In general, the MBS-CFD methodology is capable of reproducing the behaviour of the floating substructure in the experiment for this regular wave test case.

### 4.5.2 Discussion of Relative Wave Elevation

Wave probes for measuring relative wave elevations around the floating substructure are defined in Figure 4.3 and time series of five successive wave periods are shown in Figure 4.17. The data are influenced by the motion of the floating substructure relative to the water level at the sensor location. For this reason, relative wave elevations give the current water level in the body fixed, moving coordinate system. They are presented with respect to the wave amplitude  $A$  and the initial normalised simulation time  $t/T = 0$  from Figure 4.16.

At first, reference wave probe  $WP_{\text{ref}}$  is considered. The curves show a very good agreement between the experiment and simulation, with respect to the amplitude, period and phase. Only small deviations at the wave troughs are observed with higher minimum values for the MBS-CFD simulation. This indicates the possible presence of additional non-linearities in the numerical results, since the absolute amplitudes of wave troughs are smaller than for the wave crests.

For the remaining wave probes a distinction is necessary between locations inside ( $WP_4$  and  $WP_7$ ) and outside ( $WP_5$ ,  $WP_6$  and  $WP_8$ ) of the moonpool, respectively, as well as at the fore ( $WP_8$ ) and aft ( $WP_5$  and  $WP_6$ ) of the floating substructure. Relative wave elevations are, in general, higher outside of the moonpool compared to those inside due to the blockage effect. The flow is hindered to enter the moonpool, resulting in a sheltered water level compared to the open ocean. Moreover, amplitudes are higher at the fore compared to the aft, since incident waves first reach the mooring interface structure and fore of the floating substructure at a wave propagation heading direction of  $\beta = 0^\circ$ . Figure 4.18 illustrates these effects described above. In general, the simulation results of relative wave elevations follow the trends given by the experiment with the best match for  $WP_6$  at the aft of the platform. Differences occur in the prediction of the maximum amplitudes. For example,  $WP_4$  experiences stagnation and, thus, run-up of water but only the experiment shows green water on deck with  $\eta/A \approx 1$ . Based on deviations found for global platform motions, refer to Figure 4.16, it can be expected that the relative wave elevations do not match perfectly. However, characteristics such as phase and period show a much better agreement than the amplitudes.

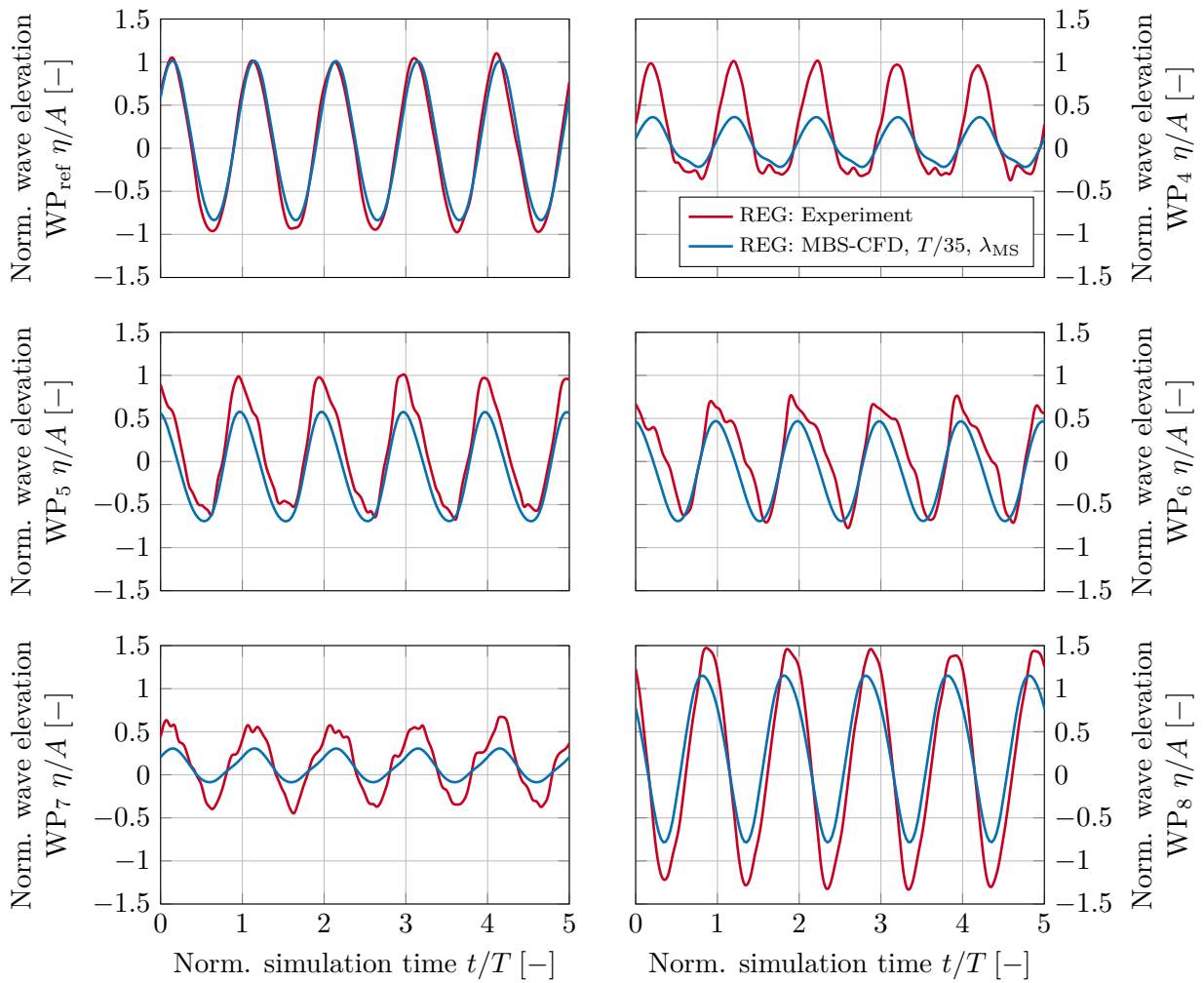


**Figure 4.17:** Comparison of the relative wave elevation sensors, defined in Figure 4.3, between the experiment and the MBS-CFD simulation.

### 4.5.3 Flow Field Visualisation

Visualisation of the flow field shows the normalised magnitude of the fluid velocity and normalised tangential velocity vectors. Successive time steps are plotted in Figure 4.18 for one wave passing  $0 \leq t/T \leq 1$ . Snapshots in time at multiples of the wave period, for instance  $t/T = 0$  in Figure 4.18a and  $t/T = 1$  in Figure 4.18h, show very similar flow characteristics because of the regularity of incident waves. Vortex formation and separation at the skirt of the substructure are dominant during regular waves, similar to free-decay results for pitch and heave in Figures 4.9 and 4.13. However, vortex shedding indicated by the normalised magnitude of fluid velocity is stronger and larger at the fore of the platform compared to the aft, see for example Figure 4.18e. This behaviour is explained by shadowing effects at the rear and the fact that incident waves first reach and excite the platform at the front.



---

Hence, the fore is washed over, resulting in green water loads on deck, and subsequent inflow of water into the moonpool. Wave run-up at the TP and tower at the aft is not observed for the simulated regular wave condition. During wave passing and overflowing, the mooring interface structure at the front is completely submerged under water, and air entrapped in the remaining chamber is compressed and decompressed as described in [25]. Differences in water level inside the moonpool and outside are present, for example in Figure 4.18d, similar to observations for heave free-decay in Figure 4.13. This is due to significant in- and outflow of water at the keel of the moonpool during one wave period.

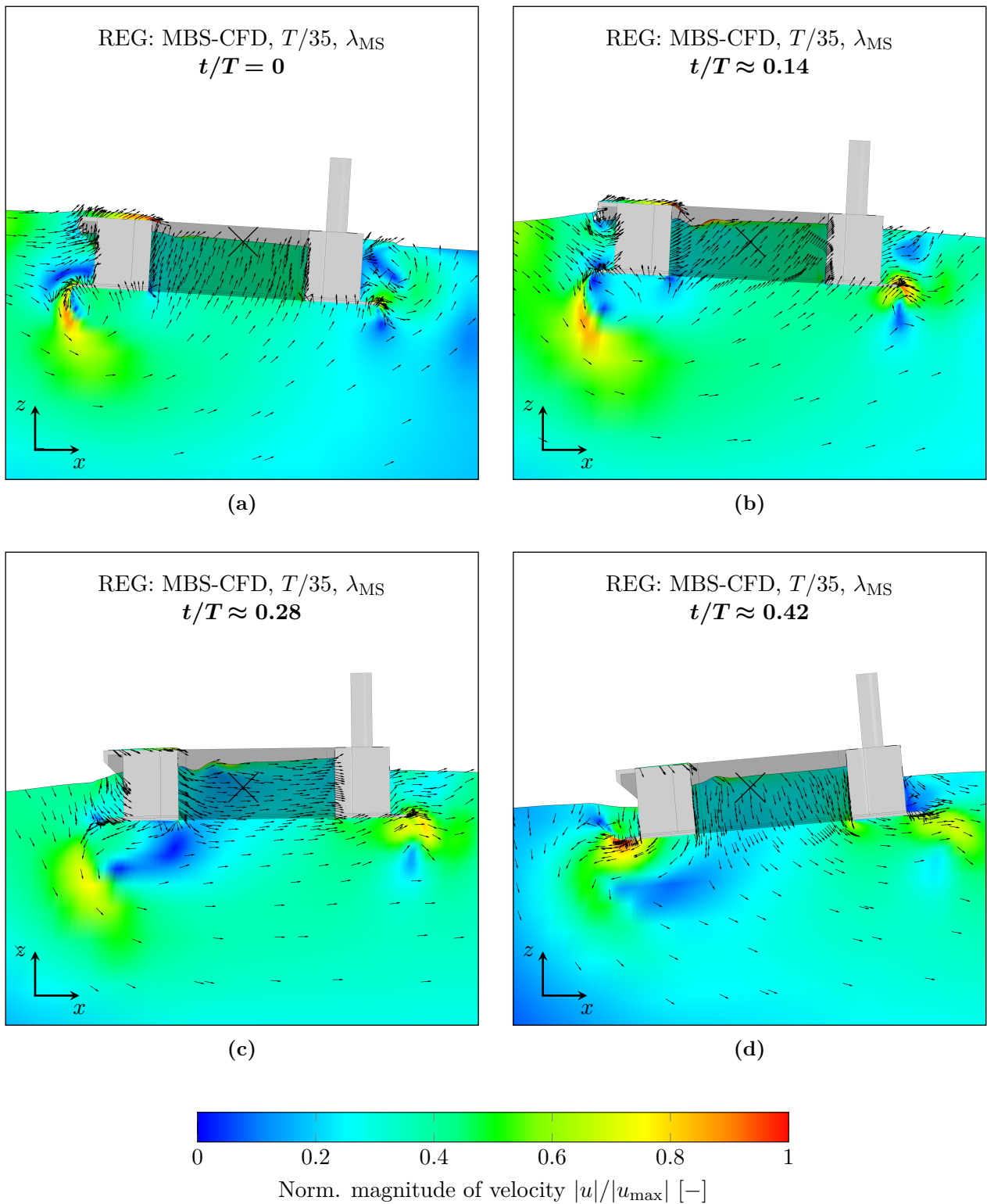


**Figure 4.18:** Visualisation of the normalised magnitude of the fluid velocity and the normalised tangential velocity vectors. The Figures are shown in the  $xz$ -plane at  $y = 0$  for successive time steps during one period of regular waves. The initial position at the coordinate  $[0,0,0]$  is marked as reference by two crossed lines.

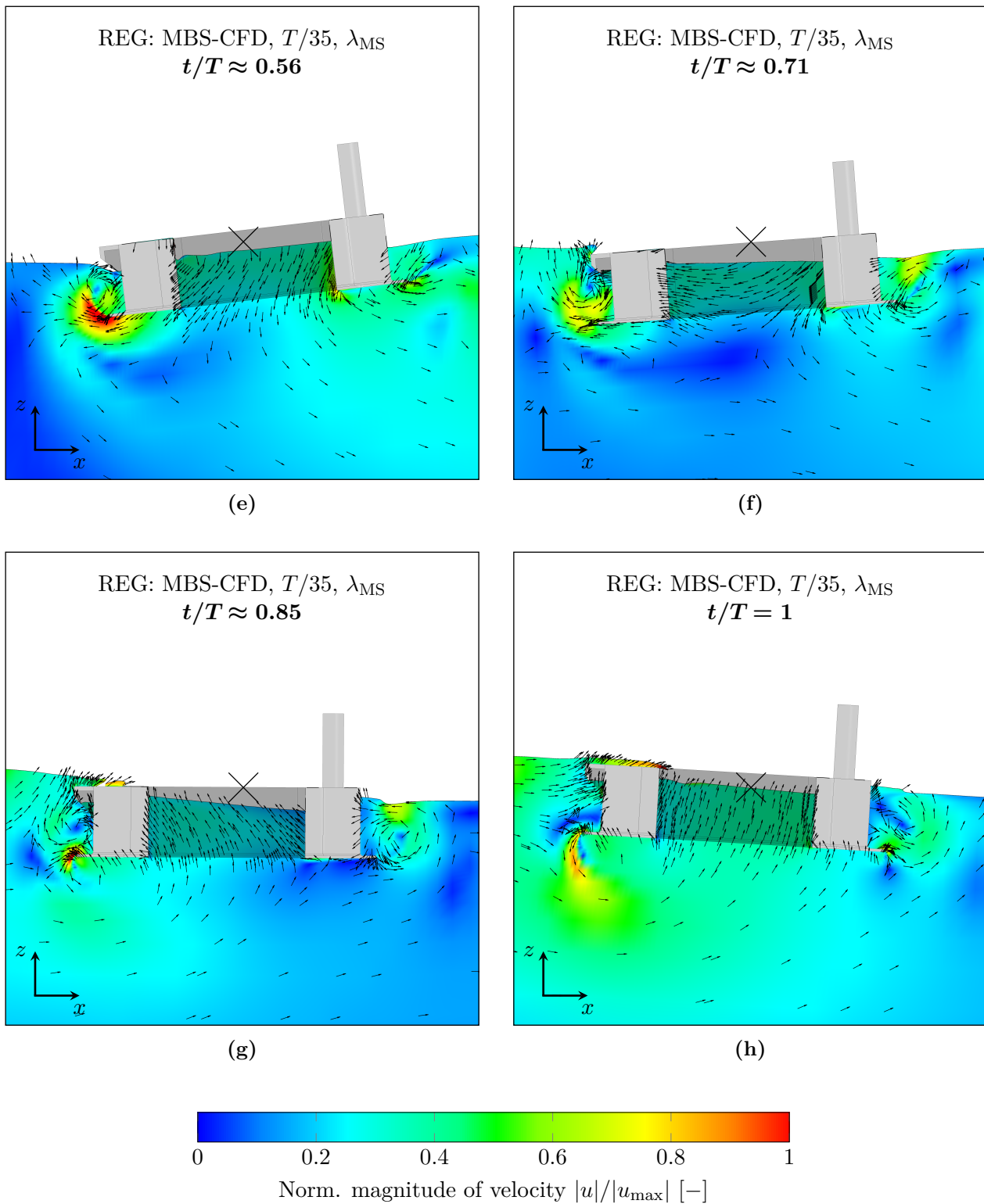


**Figure 4.18:** Visualisation of the normalised magnitude of the fluid velocity and the normalised tangential velocity vectors. The Figures are shown in the  $xz$ -plane at  $y = 0$  for successive time steps during one period of regular waves. The initial position at the coordinate  $[0,0,0]$  is marked as reference by two crossed lines.



# 5

## Extreme Wave and Wind Conditions

In this Chapter, the simulation environment, validated previously by free-decay and regular-wave tests, is modified to simulate extreme environmental conditions and the resulting coupled MBS-CFD model is outlined in Section 5.1. Investigated extreme load cases are summarised in Section 5.2 before measurements and sensor locations are explained in Section 5.3. Finally, simulations are performed and analysed for extreme wave-only conditions in Section 5.4 and followed by simulations of combined extreme wave and wind conditions in Section 5.5.

### 5.1 Description of Coupled MBS-CFD Model

For the setup of numerical models for analysis of extreme wave and wind conditions, experience and recommended practices are drawn from the previous free-decay and regular wave validation studies. In the following, similarities between the applied coupled MBS-CFD models for extreme load analysis are described before details on differences are provided.

In general, a NWT is setup in CFD with modified spatial limits and discretisation as illustrated in Figure 5.1. The seabed is located at a water depth of  $d = 32$  m based on the reference site. The draft of the platform in equilibrium, free floating position is the same as for the free-decay and regular wave tests resulting in the same still water level at  $z_{\text{SWL}}$ . The inlet is located 50 m in front of the platform and focus point  $x_f$  in order to limit the computational efforts. The velocity profile and wave elevation are imposed at the inlet boundary condition using the BCPROFILE2CFX approach of Section 3.3.1.2. In addition, a small distance between the inlet and the focus point is beneficial for the numerical damping, which reduces the wave height with increasing distance, see the sensitivity analysis in Section 3.4. The substructure is

released at the start of the simulation at its undisplaced position, in contrast to regular wave test that used an initial mean surge position to reduce the transient phase. Numerical damping in  $x$ - and  $z$ -direction is enforced in the NB, starting behind the platform at  $x_{nb}$  to avoid wave reflections, see modelling details in Section 3.3.2. Besides the introduced momentum sources for the wave damping, the cells increase in size towards the outlet and seabed. An influence of wave reflections from radiated or diffracted waves travelling from the floating substructure to the inlet and back is not observed in the simulations.

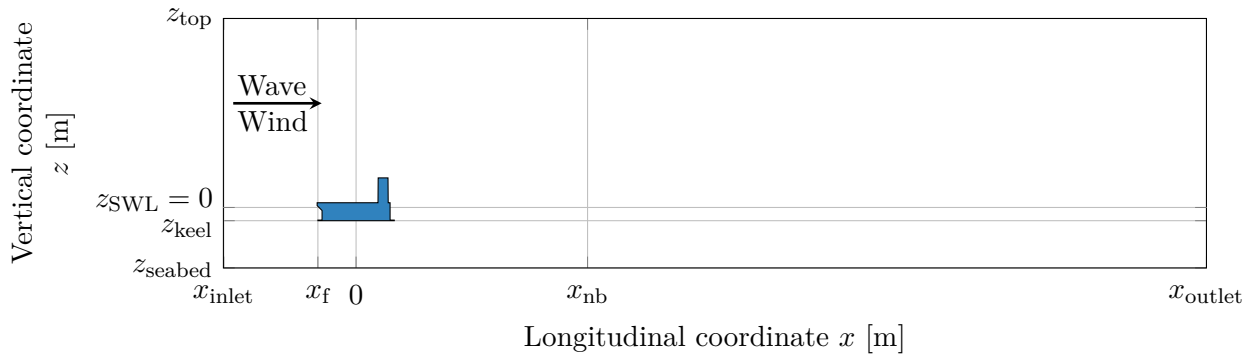


**Figure 5.1:** Illustration of the NWT in the  $xz$ -plane at  $y = 0$  from the seabed to the top boundary condition. The longitudinal location of inlet  $x_{inlet}$ , outlet  $x_{outlet}$ , focus point  $x_f$ , starting location of the numerical beach  $x_{nb}$  and the still water level  $z_{SWL}$  are included as reference.

Only one spatial discretisation of the numerical model of approximately 2.1 million cells is applied, as listed in Table 5.1. The resulting mesh in the vicinity of the floating substructure is modified to account for extreme wave heights present in the simulation as shown in Figure 5.2. Compared to the regular wave validation test, a new TP is incorporated in accordance with the reference design at the FLOATGEN site.

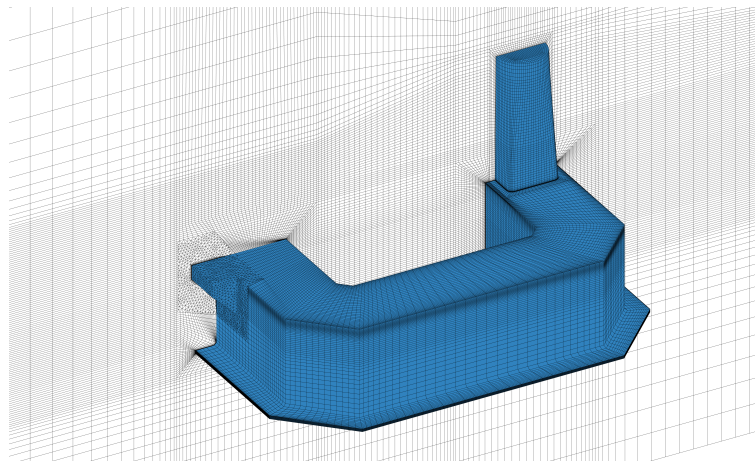


**Figure 5.2:** Illustration of the surface mesh of the floating substructure and the TP in blue as well as the symmetry plane at  $y = 0$  in white used for MBS-CFD simulation of extreme wave and wind conditions. Compared to the mesh used for the validation studies in Figure 3.9, refinement is done in the free surface region to account for extreme wave heights and in the boundary layer near the walls.

No experimental data set was available for comparison of extreme events. Reference marker for communication between the CFD and MBS solver is the coordinate  $[0,0,z_{\text{keel}}]$ , which is also used for the analysis of platform movement.

**Table 5.1:** Mesh discretisation used for the simulations of extreme wave and wind conditions.

ID	Number of elements
EXT3000, EXT4000	2,102,381

### 5.1.1 MBS Model Topology for Extreme Wave Conditions

The MBS model for analysis of extreme wave conditions without wind is based on the setup used for free-decay and regular wave validation tests. This means that the structural model is reduced to one rigid body representing the floating substructure, tower and RNA. Structural properties, such as the total mass, COG and moments of inertia are scaled to full scale with  $\lambda = 1$  based on the data from the measurement campaign. Also, symmetry of the investigated platform in  $y$ -direction is exploited to cut the numerical domain in half and save computational time. This simplification is possible because wave propagation in the positive  $x$ -direction is used for the focused wave group. As a consequence, only the following three platform DOFs are used: surge and heave translational displacement as well as pitch rotational displacement. The movement of the platform requires a mesh deformation scheme as described in Section 3.3.5. Force elements are included in the MBS model to account for the restoring forces from the mooring lines, which are modelled with the same methodology as done for the regular wave test, see Section 4.2.2. One has to bear in mind that this approach is simplified compared to modelling techniques of state-of-the-art dynamic mooring system models. Additionally, start-up behaviour is controlled by a spring-damper element which is released after ten initial time steps to increase stability of the coupled MBS-CFD simulation. Hydrodynamic forces are accounted for by the force element FLUID2SPCK, which is described in detail in Section 3.2. The reduced MBS model topology for extreme wave analysis is presented in Figure 5.3.

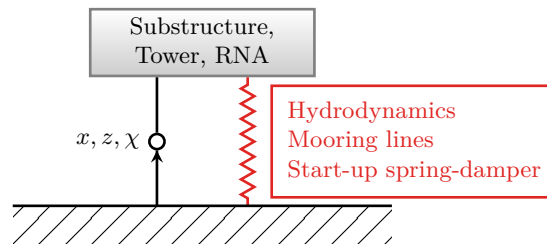


**Figure 5.3:** Topology of the reduced MBS model used for the analysis of extreme wave conditions.

### 5.1.2 MBS Model Topology for Extreme Wave and Wind Conditions

For the investigation of extreme wave and wind conditions a fully resolved MBS model of the floating system, which represents the floating substructure, the tower and the RNA, is implemented as presented in Figure 5.4. Based on the baseline MBS topology, illustrated in Figure 3.2, modifications and simplifications are incorporated in the model. MBS substructures for the seabed, floating substructure, tower, yaw bearing, nacelle, hub and rotor blades are included together with external force and results elements.

The number of rigid body DOFs is limited to the three rigid body motions of the platform in surge, heave and pitch and the free rotation of the rotor caused by aerodynamic loads. The later is modelled by a free rotation of the low speed shaft, which is coupled to the high speed shaft by the gear box ratio.

Also the number of flexible DOFs is limited. Flexible bodies are implemented in the model by definition of the number of eigenmodes starting from  $f_{\min} = 0$  Hz with 2% of critical damping for all modes. It would be more precise to increase the damping for higher eigenfrequencies in a verification and tuning study, which is not conducted here in order to limit the scope of the study. For the tower, modelled by 26 structural nodes, ten eigenmodes are used to account for deformation in fore-aft, side-side and torsional direction. Each rotor blade, modelled by 51 structural nodes, is described by four eigenmodes, two modes for in-plane and out-of-plane motion each. A higher number of eigenmodes for flexible bodies could be implemented but with the drawback of increased simulation time. In addition, verification of the flexible bodies is not possible due to the lack of publicly available reference design data at the reference site. However, this test case considers an idling rotor and a steady, uniform wind field with vertical shear so that an increased modelling fidelity of flexible bodies is not necessary to draw main conclusions.

Other joints in the model are fixed with zero DOF so that a total number of 32 DOFs are considered for analysis of extreme wave and wind conditions. The rotor blades are fixed at  $90^\circ$  during the simulation and the controller for blade pitch and generator torque is deactivated, representing a non-operational, parked situation.

Identical to the reduced MBS model for extreme wave analysis, force elements for hydrodynamics, restoring forces from mooring lines and start-up behaviour are implemented. For consideration of aerodynamic loads of extreme wind, two different approaches are followed. First, rotor aerodynamic loads are setup by the internal implementation of AeroDyn v13.00.00, which is a package of subroutines based on BEM theory with correction models developed by NREL [89], see Section 2.4.3. Second, dynamic wind loads on the tower are taken into account by a user-defined force element. It reads the wind field, which is also used for rotor aerodynamics, at a specified number of markers along the vertical  $z$ -axis of the tower at each time step of the simulation. The resulting drag force on sectional elements is calculated in Equation 5.1:



$$F_d(z) = 0.5\rho u_{\text{rel}}(z) |u_{\text{rel}}(z)| C_d A_{\text{TWR}} \quad (5.1)$$

The tower is divided into ten equally spaced sections of length  $L_{\text{TWR}} = (z_{\text{top}} - z_{\text{base}})/10$  and varying cross sections with a marker in the middle of each tower section, at which the wind loads are applied. Wind loads are related to the projected area of  $A_{\text{TWR}} = 0.5(D_n + D_{n+1})L_{\text{TWR}}$ , representing a trapezium. Translation and rotation of the markers relative to the wind field are considered, resulting in relative wind loads. For example, if the floating system pitches into the wind field due to wave excitation, the relative wind speed  $u_{\text{rel}}$  at the respective tower marker is increased. The same applies if the platform moves towards the negative  $x$ -axis, representing negative surge. In contrast, the relative wind speed at the tower markers is decreased in case of positive surge motion. A fully turbulent flow is assumed leading to an assumption of  $C_d = 0.6$  [95, 172].

### 5.1.3 Reference Wind Turbine and Reference Site

A 2.2 MW onshore wind turbine based on the research of Bortolotti, described in [184] and [185], is selected as reference wind turbine because the rating is similar to the Vestas V80 with 2.0 MW rated capacity, installed at the FLOATGEN demonstration site [44]. The reference model is a horizontal-axis, three-bladed, upwind wind turbine with a steel tower and glass-fiber-reinforced blade configuration. Further properties are given in Table 5.2.

**Table 5.2:** Overview of characteristic properties of the reference wind turbine. The mass properties are given with approximate values.

Property	Value
Rated capacity	2.2 MW
Rotor diameter	92.0 m
Hub height	60.0 m
Nacelle uptilt angle	6.0°
Rotor cone angle	2.0°
Blade mass	7,500 kg
Hub mass	20,000 kg
Nacelle mass	70,000 kg
Tower mass including TP	290,000 kg
Airfoils	DU airfoils [186]

The flexible reference tower model is modified to include an exemplary structural representation of the TP. In order to compare results between the load cases, the structural properties, such as mass, COG and moments of inertia of the floating substructure, are adapted to achieve the

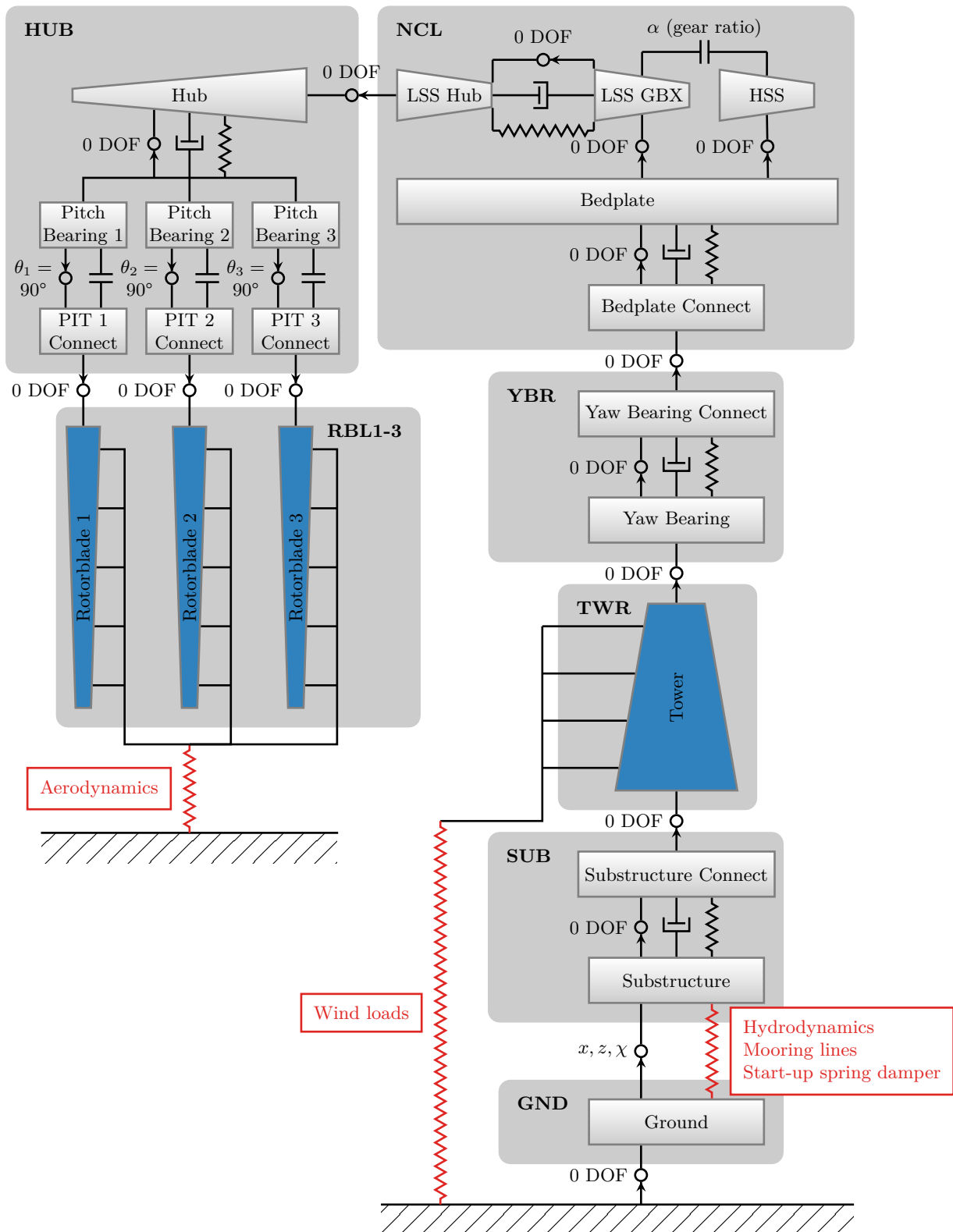


**Figure 5.4:** Topology of the MBS model for extreme wave and wind conditions with flexible bodies displayed in blue and force elements in red. The DOFs are indicated. Substructures are given by GND = Ground, SUB = Substructure, TWR = Tower, YBR = Yaw bearing, NCL = Nacelle, HUB = Hub and RBL = Rotorblade.

same design draft and equilibrium position as for the reduced MBS model. The later uses a single lumped mass as presented in Figure 5.3.

With respect to the reference site, modelling parameters, such as water depth and metocean conditions for extreme waves, are necessary. Based on the location of the FLOATGEN demonstrator, the SEM-REV offshore test site is selected which is a  $1 \text{ km}^2$  maritime zone approximately 20 km off the coast from Le Croisic and operated by École Centrale de Nantes. The floating substructure was constructed between 2016 and 2017 in Saint Nazaire and towed out to the test site in April 2018 for open ocean testing at a water depth of  $d = 32 \text{ m}$ . Table 5.3 summarises most relevant reference site data.

## 5.2 Investigated Load Cases

A summary of main load case parameters, used for simulation of extreme conditions, is given in Table 5.3. Load cases for extreme wave and wind conditions are conducted at full scale with  $\lambda = 1$ . Only one mesh resolution is investigated, which is based on the spatial discretisation of the fine mesh for free-decay MBS-CFD simulations as listed in Table 4.3. Modifications to the mesh are made to account for wave propagation in the NWT at extreme conditions and resulting wave impact on the floating substructure and TP, see Figure 5.2. A time step of  $t_{\text{step}} = T/100$  is chosen for implicit iterations in CFD and communication to the MBS solver. This choice is based on findings from the validation in Section 4.4 on free-decay and 4.5 on regular wave tests considering a good balance between computational time, temporal resolution, stability, numerical damping etc.

**Table 5.3:** Overview of the main load cases settings used for the simulation of extreme wave and wind conditions.

Section	Load case description	Time step	Wave	Wind	Initial conditions
5.4	Extreme wave at $\lambda = 1$ ID = EXT3000	$t_{\text{step}} = T/100$	$d = 32 \text{ m}$ $H_{\text{max}50} = 16.32 \text{ m}$ $T_p = 16 \text{ s}$ $\beta = 0^\circ$ $x_f = -0.5L_{\text{PTFM}}$ $t_f = 6T_p = 96 \text{ s}$	none	$x_0 = 0 \text{ m}$ $z_0 = 0 \text{ m}$ $\psi_0 = 0^\circ$
5.5	Extreme wave and wind at $\lambda = 1$ ID = EXT4000	$t_{\text{step}} = T/100$	$d = 32 \text{ m}$ $H_{\text{max}50} = 16.32 \text{ m}$ $T_p = 16 \text{ s}$ $\beta = 0^\circ$ $x_f = -0.5L_{\text{PTFM}}$ $t_f = 6T_p = 96 \text{ s}$	steady, uniform vertical shear with $\alpha = 0.11$ $u_{e50}(z)$ with $u_{e50,\text{hub}} = 70 \text{ m s}^{-1}$ (Equation 5.2)	$x_0 = 0 \text{ m}$ $z_0 = 0 \text{ m}$ $\psi_0 = 0^\circ$ $\Omega_0 = 0 \text{ min}^{-1}$ $\theta_{1,2,3} = 90^\circ$

In this study, deterministic environmental conditions are applied instead of turbulent wind and irregular waves because of necessary simplifications to limit the computational resources. The implicit iteration scheme of the coupled MBS-CFD simulation has the drawback that the structural solver needs to be restarted for each time step iteration from the results of the last converged time step, see Section 3.2.4. The wind field is loaded at the beginning of each integration of the structural solver. The implication is that for the investigated load cases this leads to several thousand repetitions, which requires a significant amount of time for turbulent wind fields, depending on the length and resolution. In contrast, the time needed to load a deterministic wind field is insignificant. Simulation of irregular waves relies on statistically relevant timescales, which requires very long run times of several weeks with the applied MBS-CFD simulation environment.

Environmental conditions are based on DLC 6.1 of IEC 61400-3-1 [8] for parked design situation and idling rotor. For consideration of extreme wind conditions, the Extreme Wind Speed Model (EWM) is used according to IEC 61400-1 [67]. In contrast to the standard, the steady extreme wind model is applied uniformly across the lateral coordinate  $y$  and the extreme wind speed  $u_{e50}$  with a return period of 50 years is computed as a function of height  $z$  following Equation 5.2:

$$u_{e50}(z) = 1.4u_{\text{ref}} \left( \frac{z}{z_{\text{hub}}} \right)^{0.11} \quad (5.2)$$

$$u_{\text{ref}} = 50 \text{ m s}^{-1} \quad (5.3)$$

with the power law exponent  $\alpha = 0.11$  to account for vertical wind shear and the reference wind speed  $u_{\text{ref}}$  in Equation 5.3 according to IEC wind turbine class I [67]. To put this value into perspective, the newest edition of the standard includes a T class for very high extreme winds from tropical cyclones with  $u_{\text{ref}} = 57 \text{ m s}^{-1}$ . The amplification factor of 1.4 is included in Equation 5.2 to simulate with conservative assumptions of the wind speed as the turbulent extreme wind speed model in [67] inherently includes wind speed fluctuations above the mean wind speed during gusts.

The wave focusing technique as described in Section 2.5.3 is applied to simulate an Extreme Sea State (ESS). Based on [8] it shall be assumed, that the extreme 10-min mean wind speed with a 50-year return period occurs during the extreme 3-hour sea state with a 50-year return period in the absence of long-term joint probability distribution of extreme wind and waves. The maximum wave height with a return period of 50 years is  $H_{\text{max}50} = 16.32 \text{ m}$  with a wave period of  $T_p = 16 \text{ s}$  derived from 3-hour sea state environmental data measured at SEM-REV, École Centrale de Nantes' offshore test site and location of the FLOATGEN demonstrator. The wave field propagates along the positive  $x$ -axis with a value of  $\beta = 0^\circ$  and focuses at the location  $x_f = -0.5L_{\text{PTFM}}$ . The focus point is located directly in front of the floating substructure at the mooring interface structure as shown in Figure 5.5. After six wave periods the focus time

$t_f = 6T_p$  is reached. The wave propagation direction of the focused wave groups is collinear with the wind direction, which is most likely a conservative assumption with respect to the level of utilisation and the damage.

The undisplaced position is chosen as initial condition for the floating wind turbine system. When wind is present, rotor blades are pitched to  $90^\circ$  during the parked situation and the rotor speed is set to zero at the start of the simulation. The controller for blade pitch and generator torque is switched off.

### 5.3 Measurements and Sensor Locations

The incident wave field is recorded by the reference wave probe  $WP_{ref}$ , which is located sufficiently away from the substructure at the focus location  $x_f$  and lateral coordinate  $y_{WP,ref}$  as illustrated in Figure 5.5. Wave probes are attached to the substructure at  $WP_1$  (in front of the substructure),  $WP_2$  (in front of the TP) and  $WP_3$  (behind the TP) with  $y = 0$  to capture the relative wave elevations.

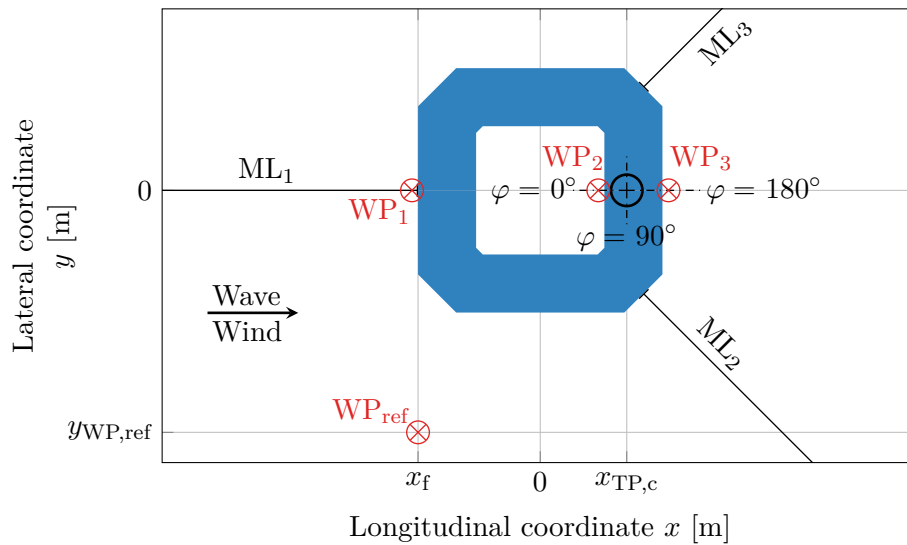


**Figure 5.5:** Schematic view of the floating substructure in the MBS-CFD simulation at 0 m initial surge displacement. The wind direction and the wave propagation direction of focused wave groups is collinear with a value of  $\beta = 0^\circ$ . The reference wave elevation is measured at  $WP_{ref}$ . The TP is represented by a circle with the centre  $x_{TP,c}$  together with selected azimuthal positions at  $\varphi = 0^\circ$ ,  $\varphi = 90^\circ$  and  $\varphi = 180^\circ$ . The orientation of the mooring lines  $ML_1$  to  $ML_3$  is displayed.

IDs are introduced to distinguish between different simulations and considered sensor channels. Each plot line is associated with a seven-character ID:

- Characters 1-3: “EXT” representing load cases with extreme environmental conditions,
- Characters 4-5: Two digits representing individual simulations (“30” represents extreme wave-only and “40” represents combined extreme wave and wind conditions),

- Characters 6-7: Two digits representing a sensor (“01” for surge translational displacement, “03” for heave translational displacement, “05” for pitch rotational displacement, “07” for longitudinal force, “09” for vertical force and “10” to “13” for wave elevations).

As an example, EXT3010 refers to the sensor ID “10” (reference wave probe) of the extreme wave simulation with the ID “30”.

## 5.4 Extreme Wave

The extreme waves are modelled by the wave focusing technique and applied to three-dimensional MBS-CFD simulation EXT3000 using a reduced MBS model with floating substructure and mooring lines only. Wind is not included as summarised in Table 5.3.

### 5.4.1 Discussion of Focused Wave Development

The incident wave field is measured at  $WP_{\text{ref}}$  during the simulation and results of the three-dimensional MBS-CFD case EXT3010, with the floating substructure, are compared to an empty two-dimensional NWT case EXT2010. Figure 5.6 shows the typical development of the wave elevation signal using the wave focusing technique. The wave elevation increases with each wave period and reaches its maximum at the focus time  $t_f = 6T_p$ . Afterwards, the wave height approaches zero. A numerical ramp function in CFD is disadvantageous for the focused wave group because the focus time and location would be shifted caused by the missing wave energy contributions during the ramp-up. Hence, a ramp function is not applied in the following analysis.

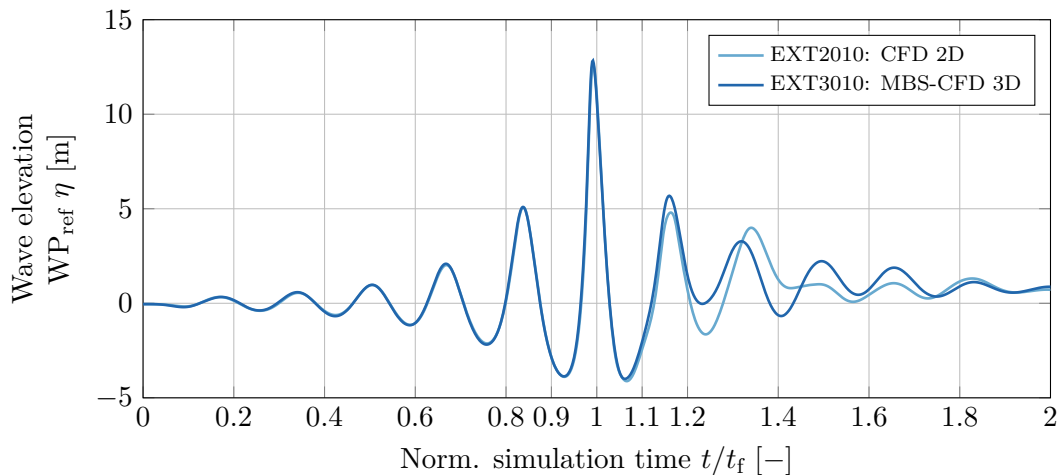


**Figure 5.6:** Comparison of the reference wave elevation  $WP_{\text{ref}}$  over the normalised simulation time for the two- and three-dimensional NWT. Line EXT4010, which represents the wave elevation of extreme wave and wind conditions, matches the line EXT3010 and is not included for reasons of clarity.

Based on the metocean data of the FLOATGEN site the maximum wave height with a return period of 50 years is  $H_{\max50} = 16.32$  m with a wave period of  $T_p = 16$  s. The procedure to achieve the input wave in the MBS-CFD simulation is divided in three steps. First, the analytical solution of the focused wave is pre-computed based on several input parameters according to the methodology described in Section 2.5.3. Second, the resulting time-dependent velocity profile and water volume fractions are imposed at the inlet boundary condition of a two-dimensional NWT at each time step. This is beneficial to save computational time before using the full model in three dimensions. In case the wave elevation at the reference wave probe  $WP_{\text{ref}}$  does not reach the target value, steps one and two need to be repeated iteratively. Finally, the three-dimensional MBS-CFD simulation is performed after tuning the input wave. At the end of this process time series are evaluated to determine the maxima and resulting wave height. The results are shown in Table 5.4.

**Table 5.4:** Overview of the maximum and minimum wave elevations from the MBS-CFD simulation of the focused wave.

ID	Method	Wave probe	$\eta_{\max}$	$\eta_{\min}$	$H_{\max}$	$\frac{H_{\max}}{H_{\max50}}$	$\frac{t(\eta_{\max})}{t_f}$
			[m]	[m]	[m]	[-]	[-]
EXT2010	CFD 2D	$WP_{\text{ref}}$	12.6260	-3.8894	16.5154	1.0176	0.9917
EXT3010	MBS-CFD 3D	$WP_{\text{ref}}$	12.8363	-3.9974	16.8337	1.0372	0.9917
EXT3011	MBS-CFD 3D	$WP_1$	6.3945	-4.0737	10.4682	0.6450	0.9850
EXT3012	MBS-CFD 3D	$WP_2$	5.3086	-2.1420	7.4507	0.4591	1.0183
EXT3013	MBS-CFD 3D	$WP_3$	3.8034	-3.1325	6.9359	0.4274	1.1000
EXT4010	MBS-CFD 3D	$WP_{\text{ref}}$	12.8441	-3.9959	16.8400	1.0376	0.9917
EXT4011	MBS-CFD 3D	$WP_1$	6.2648	-4.2304	10.4952	0.6467	0.9867
EXT4012	MBS-CFD 3D	$WP_2$	5.4104	-1.9664	7.3768	0.4545	1.0183
EXT4013	MBS-CFD 3D	$WP_3$	3.7957	-2.4337	6.2294	0.3838	1.0983

The best agreement is found for the two-dimensional CFD simulation EXT2010 with  $H_{\max} = 16.52$  m, measured slightly above the target value of  $H_{\max50}$  with less than 2% deviation. A similar trend is found for the 3D MBS-CFD simulation EXT3010, that shows a small increase of the maximum wave height of below 4%. As the floating substructure is included in EXT3010 in contrast to EXT2010, which solely simulates an empty NWT filled with water, the wave field is affected by the movement of the platform. Differences in wave propagation between the 2D and 3D case and potential wave reflection and diffraction are possible. However, the curves for EXT2010 and EXT3010 in Figure 5.6 are very close to each other up to the focus time, which is a prerequisite for the comparison between cases. For  $t/t_f > 1.1$ , deviations for the wave elevation signal are observable but this behaviour is influenced by the presence of the floating substructure, see also flow field visualisation during wave impact in Section 5.4.5. In addition,

the velocity field in the numerical domain after the focus time is significantly affected by the intensity of the applied wave damping in the numerical beach, see Section 3.3.2. Reflections at the beginning of the damping zone or outlet move back into the domain and interact with the incident waves. A case study confirmed, that a ratio of  $C_{M,x} = 10C_{M,z}$ , refer to Equations 3.12 and 3.13, is sufficient to achieve enough wave damping, to allow water mass to flow out of the outlet and to avoid reflections as much as possible. Moreover, it is observed that the maximum wave height in the CFD domain occurs shortly before the focus time at  $t(\eta_{\max})/t_f = 0.9917$ .

#### 5.4.2 Discussion of Relative Wave Elevation

Relative wave elevations are presented for EXT3010 in Figure 5.7. While the maximum wave height at  $WP_{\text{ref}}$  is  $H_{\max} = 16.83$  m, wave probes  $WP_1$  to  $WP_3$  measure smaller values because they are fixed to the substructure and move with it in the CFD domain, see also Table 5.4 and Figure 5.5. Two general trends can be observed. First, the further away the wave probe is positioned from the focus location  $x_f$ , the later the maximum relative wave elevation occurs. This is easily explainable by the wave propagation in the positive  $x$ -axis. Second, the resulting maximum relative wave height decreases with increasing distance to the focus location  $x_f$ . With respect to  $WP_1$ , which is located right in front of the floating substructure, the time series show an increase and decrease of wave elevation comparable to the input focused wave but significantly lower in amplitude and superimposed by the platform motion.  $WP_2$  is positioned in the moonpool and, thus, is very much sheltered from the incident waves similar to the behaviour found during the validation of a regular wave test in Section 4.5.3. Only small waves are measured in the moonpool until the focus time, but then the wave crest washes over the deck of the platform into the moonpool as shown in Figure 5.10d. After that, the wave crest reaches the TP and tower leading to significant wave run-up and a steep rise in relative wave elevation at  $t(\eta_{\max})/t_f = 1.0183$ , see Figure 5.10g for illustration. Water flows around the TP and back into the open ocean again. For  $WP_3$ , the maximum water level is not captured during the passage of the focused wave but later at  $t(\eta_{\max})/t_f = 1.0998$ . At this time the substructure reaches the minimum heave displacement, while moving back towards the positive  $x$ -axis, refer to Figure 5.8b. As visible in Figure 5.10p, the deck at the aft of the hull is then flooded again.



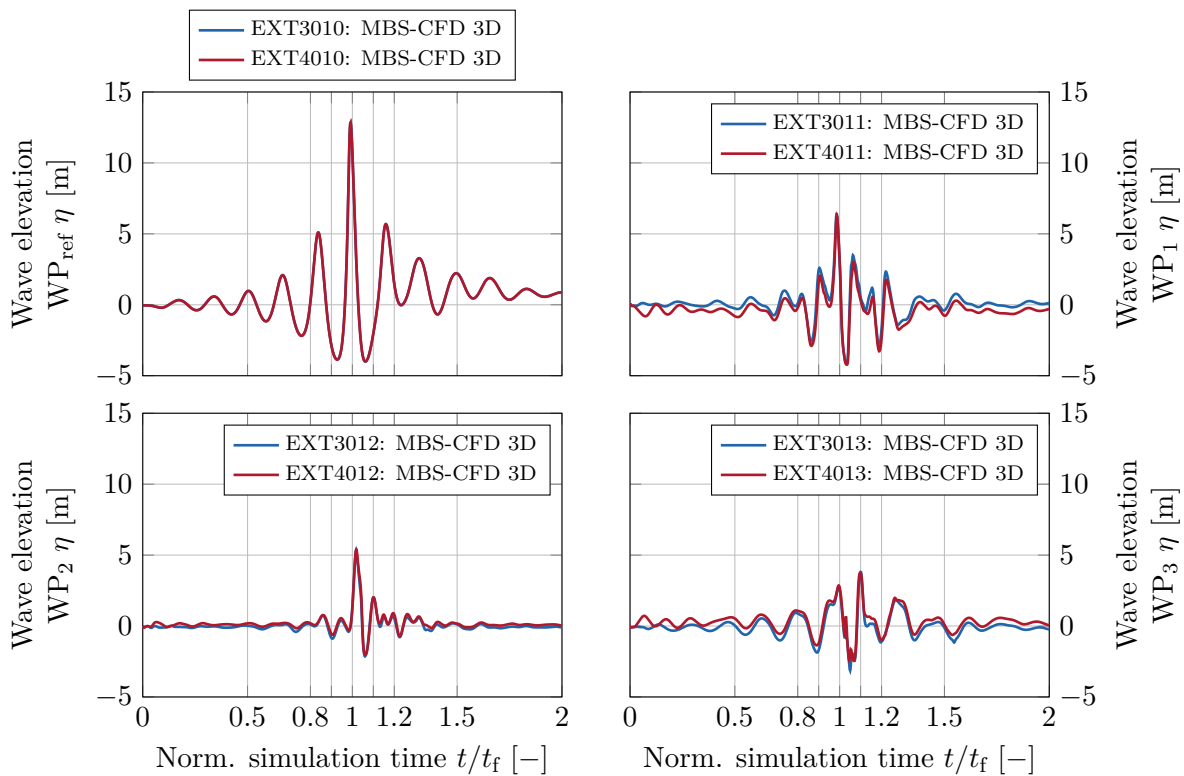


**Figure 5.7:** Measurements of the relative wave elevation sensors defined according to Figure 5.5 over the normalised simulation time.

### 5.4.3 Discussion of Platform Kinematics

In contrast to the procedure for regular wave validation described in Section 4.5.1, no initial platform surge is applied for extreme wave conditions because the focused wave impact is a deterministic event, which does not repeat as for regular waves. Thus, the substructure moves back to its initial, undisplaced position after passage of the focused wave in order to regain a static equilibrium. As a consequence, the initial mesh does not need to be deformed. The platform body in MBS is fixed at the initial position using a spring-damper element, which is released after ten time steps to increase solver stability at the start of the simulation, see step 4 in Section 3.5. The normalised surge, heave and pitch displacements are plotted against the normalised simulation time in Figure 5.8. An assessment of the maximum excursions and the associated normalised simulation time is summarised in Table 5.5.

Platform surge is highly excited by the extreme wave event leading to a maximum excursion relative to the water depth of  $|x_{\max}|/d = 0.7439$ . This is the outcome of the extreme longitudinal forces that impact the substructure during the passage of the focused wave, see Figure 5.9a. With respect to the temporal progression one can see that the maximum platform surge occurs at  $t/t_f = 1.0467$  after the wave travelled through the hull, while the longitudinal force  $F_x$  already switched its sign. This is due to the associated platform inertia and mooring resistance.

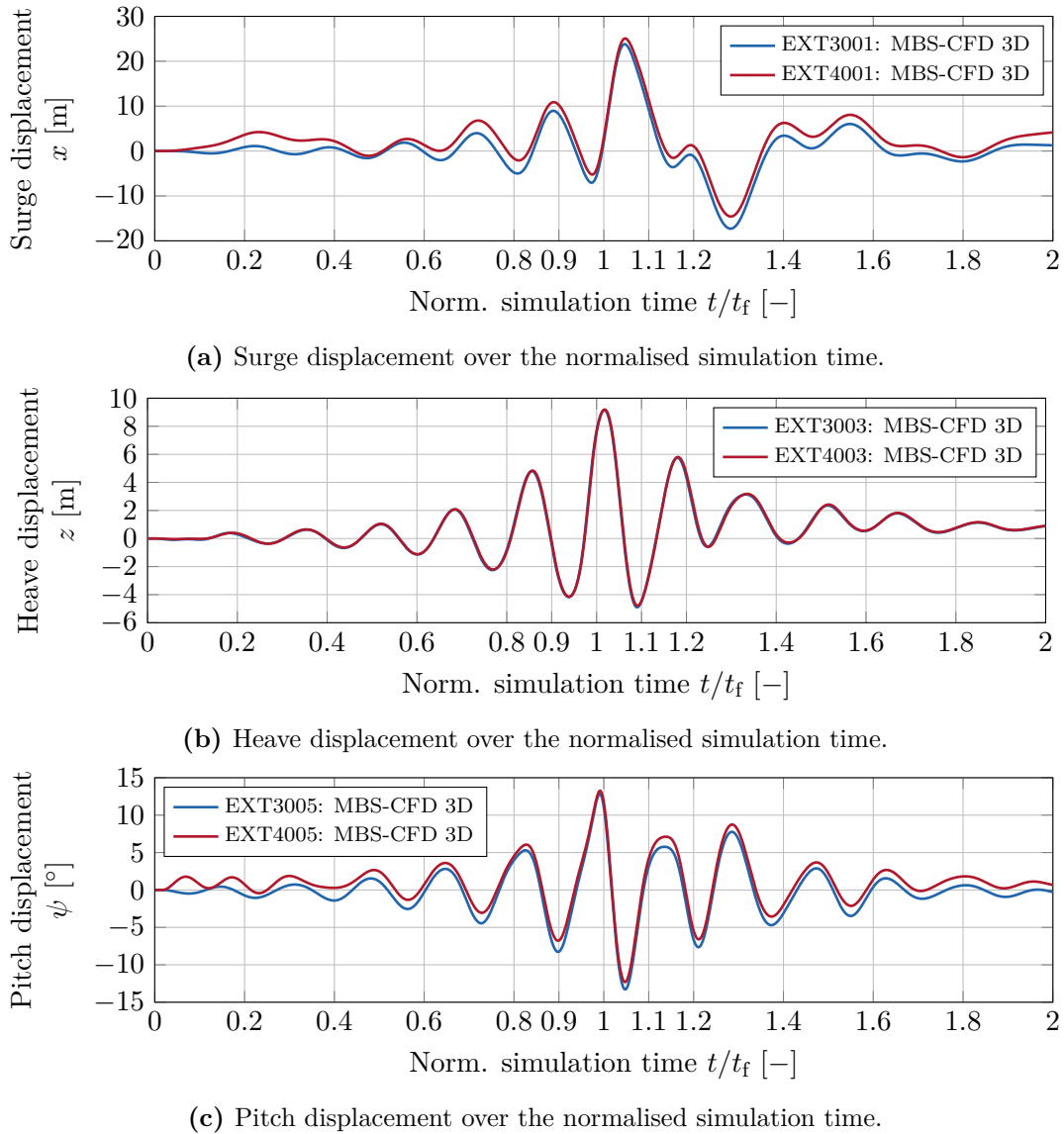


**Figure 5.8:** Illustration of the platform motion in surge, heave and pitch for the focused wave MBS-CFD simulations defined in Table 5.3.

In this study the mooring system is simplified and calibrated to the global linear stiffness matrix of the wave basin test campaign, see Section 4.2.2. The mooring stiffness is not high enough to limit the surge excursion to one third of the water depth, which is a commonly used estimate in early design phases of FOWTs. A limitation of the excursions is required for the dynamic cable, which is designed for a certain mooring system envelope to avoid clashes with mooring lines and damage from extreme stretching. The higher the maximum excursions of the mooring system, the higher the required length of the dynamic cable. A stricter limit for the maximum excursions results in a stiffer design and increases the peak loads on the mooring system, which can make it more costly. Hence, a softer mooring system with maximum excursions above the mentioned limit of one third of the water depth could be chosen by the designer

**Table 5.5:** Overview of the maximum excursions and the associated normalised simulation time of the floating substructure during the MBS-CFD simulation of the focused wave.

ID	Method	$ x_{\max} $	$ z_{\max} $	$ \psi_{\max} $	$\frac{t( x_{\max} )}{t_f}$	$\frac{t( z_{\max} )}{t_f}$	$\frac{t( \psi_{\max} )}{t_f}$
		[m]	[m]	[°]	[-]	[-]	[-]
EXT3000	MBS-CFD 3D	23.8042	9.1451	13.2807	1.0467	1.0167	1.0483
EXT4000	MBS-CFD 3D	25.0725	9.1924	13.2550	1.0483	1.0183	0.9917

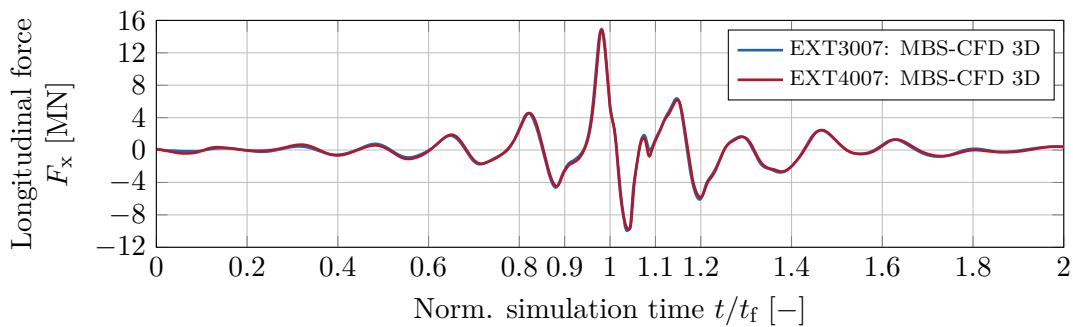
based on cost considerations. For deep water sites, the excursion limit is a function of the water depth based on Oil and Gas industry experience and ranges between 5% to 12% for intact and damaged load cases respectively. The as-built mooring system of the FLOATGEN demonstrator consists of six mooring lines (three clusters with two lines each) with synthetic fibre ropes made of Nylon and studless top and bottom chains [45]. Buoyancy elements are distributed along the mooring lines to prevent seabed contact of the fibre ropes and possible chafing damage. Additional clump weights keep the mooring lines under tension. In contrast to the simplified modelling approach of a global linear stiffness matrix in this study, the as-built mooring system configuration is characterised by a non-linear force-displacement behaviour. Hence, the maximum surge excursions observed in this load case cannot be directly related to the FLOATGEN demonstrator.

Timeseries of the platform heave are very much coupled to the wave elevation, meaning that an increase in wave height is translated directly into a higher platform heave and the other way around. In principle, the line in Figure 5.8b looks similar to line EXT3010 in Figure 5.6 with a small time offset because the wave probe is located  $x$ -wise in front of the floating substructure. The highest platform heave displacement occurs at  $t/t_f = 1.0167$  shortly after the focus time when the wave crest passes the middle of the moonpool.

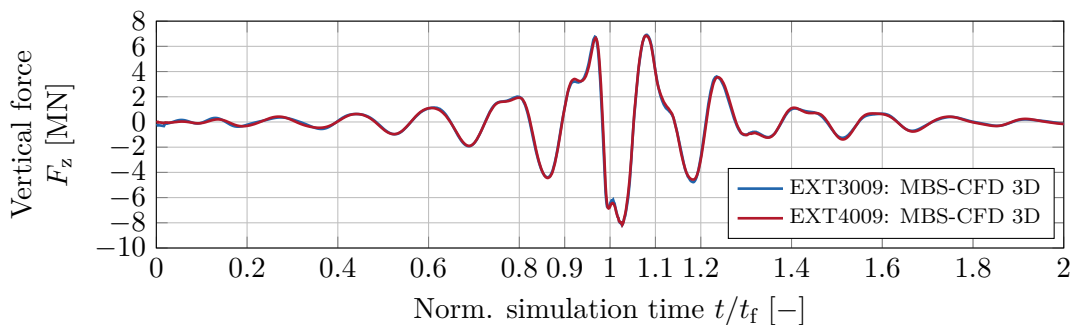
Platform pitch rotational displacement is also linked to the wave elevation. However, three major differences are visible. At first, the substructure experiences its maximum platform pitch, which is of negative sign, at a similar instance in time as for the maximum surge displacement at  $t/t_f = 1.0483$  after the wave travelled through the full length of the hull. Second, a comparable high value but of positive sign is found closely before the focus time at  $t/t_f = 0.9917$ . This occurs because of a very high pitching moment around the platform  $y$ -axis when the wave crest pushes the fore of the square-shaped hull upwards, refer to the illustration in Figure 5.10d. Third, platform pitch decays later in time compared to the wave elevation signal as well as platform surge and heave, and is influenced by pulling forces originating from the horizontal mooring lines, see Section 4.2.2. For example, the peak pitch signal at  $t/t_f = 1.2850$  is higher than  $t/t_f = 1.1350$  as the substructure reaches its maximum negative surge position.

#### 5.4.4 Discussion of Integrated Forces on the Structure

Hydrostatic and -dynamic forces, generated by the fluid, excite the floating substructure and TP and are calculated by the CFD solver using numerical integration of the pressure and wall shear stress across the full, three-dimensional hull surface area. The longitudinal and vertical force  $F_x$  and  $F_z$  are plotted in Figure 5.9 and do not represent the total forces acting on the platform as, for example, mooring line tensions are not considered in the fluid solver and are only made available by the MBS part of the coupled MBS-CFD simulation. The positive offset of the vertical force at  $t/t_f = 0$ , which originates from the hydrostatic buoyancy force, is removed. A value of  $F_z = 0$  represents the vertical force contribution present at static equilibrium. Forces calculated by the CFD solver are multiplied by a load factor of two to account for the full hull because a half model of the NWT is used to take advantage of the symmetric geometry of the substructure.



(a) Wave-induced longitudinal force over the normalised simulation time.



(b) Wave-induced vertical force over the normalised simulation time. The positive offset caused by the hydrostatic contribution in the equilibrium position in still water is removed from the vertical force component.

**Figure 5.9:** Illustration of the wave-induced longitudinal and vertical force components acting on the substructure and TP for the focused wave MBS-CFD simulations defined in Table 5.3.

Timeseries are evaluated for the absolute maximum values and the findings are summarised in Table 5.6. Two distinct peak values of the longitudinal force are visible, one closely before and the other after the focus time. At  $t/t_f = 0.9800$  the maximum positive longitudinal force is induced, which also represents the highest magnitude for this test case. It occurs when the

wave front of the extreme focused wave approaches the fore of the platform, which is pushed in positive  $x$ -direction following the increasing wave slope, see Figure 5.10b. The maximum negative longitudinal force occurs at  $t/t_f = 1.0383$  after the crest of the focused wave package passed the substructure, see Figure 5.10i for illustration. After the wave crest flushes over the deck and moonpool at the fore of the platform the water surface forms a plunging breaker, which impacts the TP at  $t/t_f = 1.0100$  in Figure 5.10f. The horizontal impact force and following wave run-up at the TP is not visible as a distinct peak in the signals of the longitudinal and vertical force components.

The maximum vertical force is of negative sign and occurs at  $t/t_f = 1.0267$ . Illustrated in Figure 5.10h, the fore of the platform moves out of the water almost up to the skirt at the bottom of the hull under the mooring interface structure, while the water column in the moonpool is higher in elevation than the surrounding free surface. Large quantities of green water are present on the deck and at the TP. This induces a strong downward-directed force, which reduces the buoyancy. The maximum positive vertical force is a combination of hydrostatic and -dynamic contributions. For example, at  $t/t_f = 0.9667$ , refer to Figure 5.10a and tangential velocity vectors, the floating substructure experiences an upward-directed force from the movement of water particles of the rising wave, as well as buoyancy force because of submerged hull sections. A second maximum occurs after the focus time at  $t/t_f = 1.0800$ , see Figure 5.10n, which is in line with the minimum heave displacement and results in an increase of the buoyancy force from the immersed hull parts.

**Table 5.6:** Overview of the maximum integrated longitudinal and vertical forces on the floating substructure and TP during the MBS-CFD simulation of the focused wave.

ID	Method	$ F_{x,\max} $	$ F_{z,\max} $	$\frac{t( F_{x,\max} )}{t_f}$	$\frac{t( F_{z,\max} )}{t_f}$
		[MN]	[MN]	[-]	[-]
EXT3000	MBS-CFD 3D	14.8368	8.1851	0.9800	1.0267
EXT4000	MBS-CFD 3D	14.8751	8.1686	0.9817	1.0267

### 5.4.5 Flow Field Visualisation

Visualisation of the flow field shows the normalised magnitude of fluid velocity and the normalised tangential velocity vectors. Successive time steps are plotted every  $\Delta t = T/20$  starting before the focus time at  $t/t_f = 0.9683$  in Figure 5.10a to  $t/t_f = 1.0933$  in 5.10p. A reference marker at  $[0,0,0]$  indicates the undisplaced, initial position by two crossed lines. To improve visibility of the zoomed images, screenshots are centred horizontally at the current surge position of floating substructure, while the vertical focus point is kept constant. Maximum values

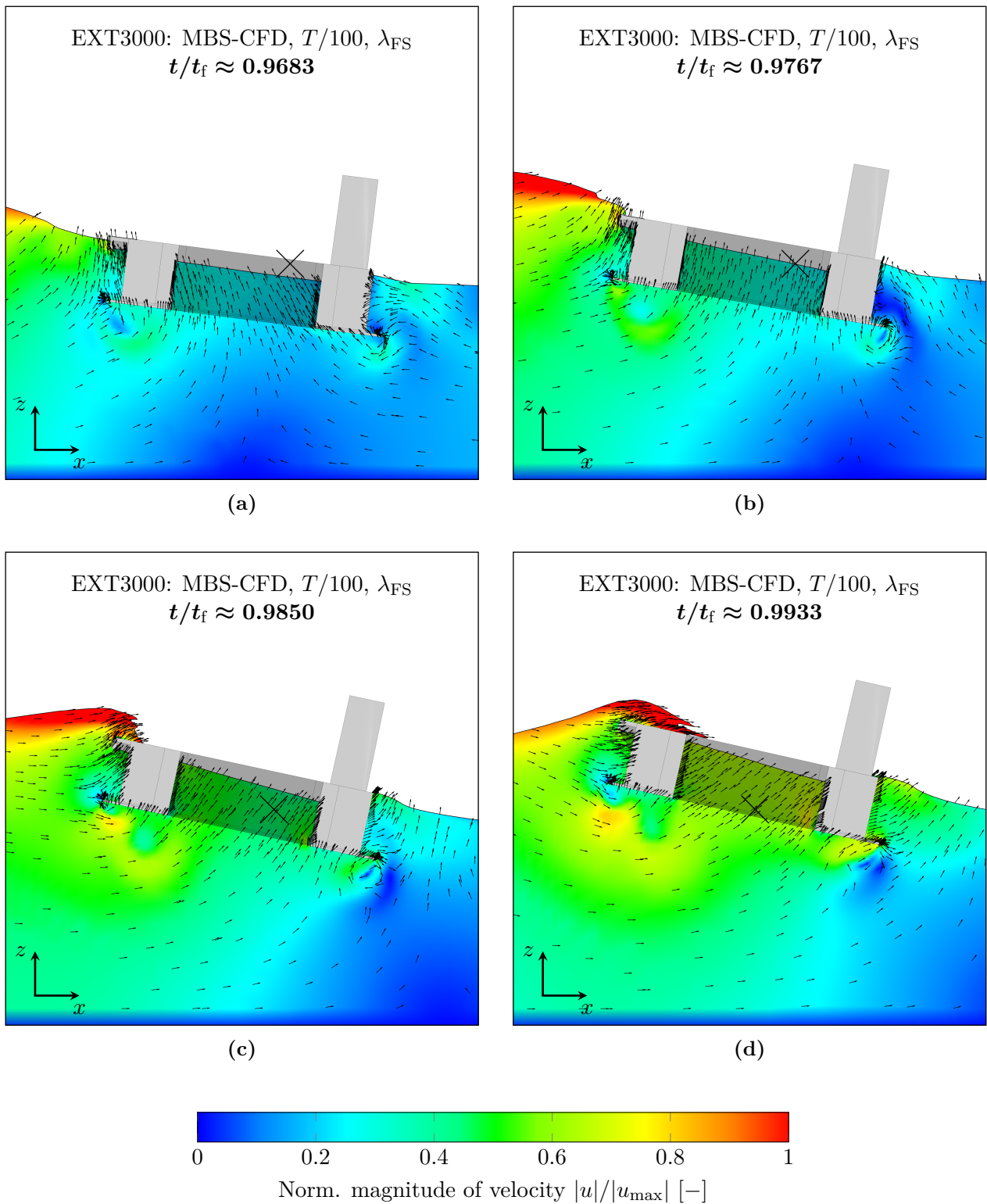


**Figure 5.10:** Visualisation of the normalised magnitude of the fluid velocity and the normalised tangential velocity vectors. The Figures are shown in the  $xz$ -plane at  $y = 0$  for successive time steps and are centred horizontally at the time-dependent platform surge. The initial position at the coordinate  $[0,0,0]$  is marked as reference by two crossed lines.

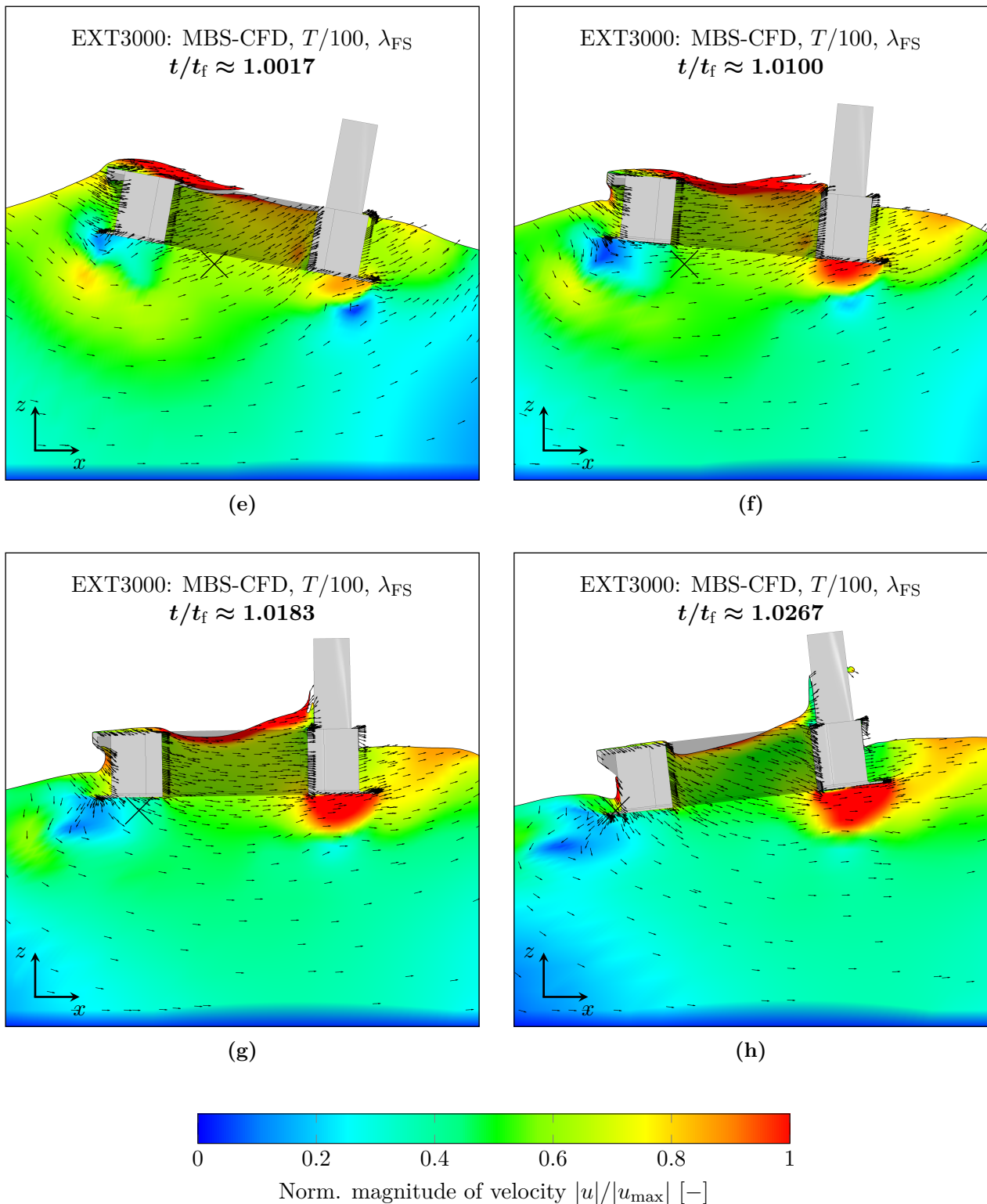


**Figure 5.10:** Visualisation of the normalised magnitude of the fluid velocity and the normalised tangential velocity vectors. The Figures are shown in the  $xz$ -plane at  $y = 0$  for successive time steps and are centred horizontally at the time-dependent platform surge. The initial position at the coordinate  $[0,0,0]$  is marked as reference by two crossed lines..

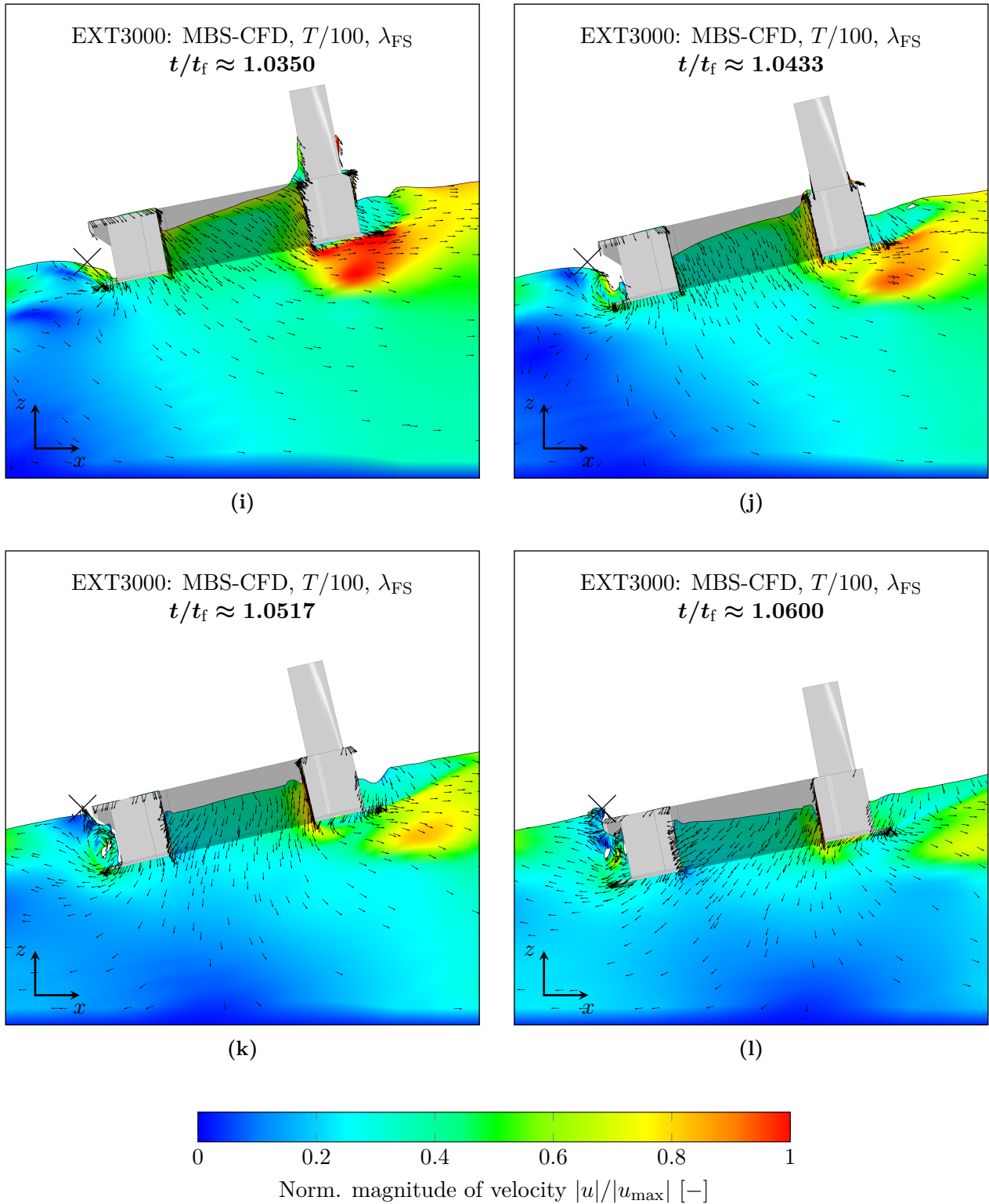


**Figure 5.10:** Visualisation of the normalised magnitude of the fluid velocity and the normalised tangential velocity vectors. The Figures are shown in the  $xz$ -plane at  $y = 0$  for successive time steps and are centred horizontally at the time-dependent platform surge. The initial position at the coordinate  $[0,0,0]$  is marked as reference by two crossed lines.



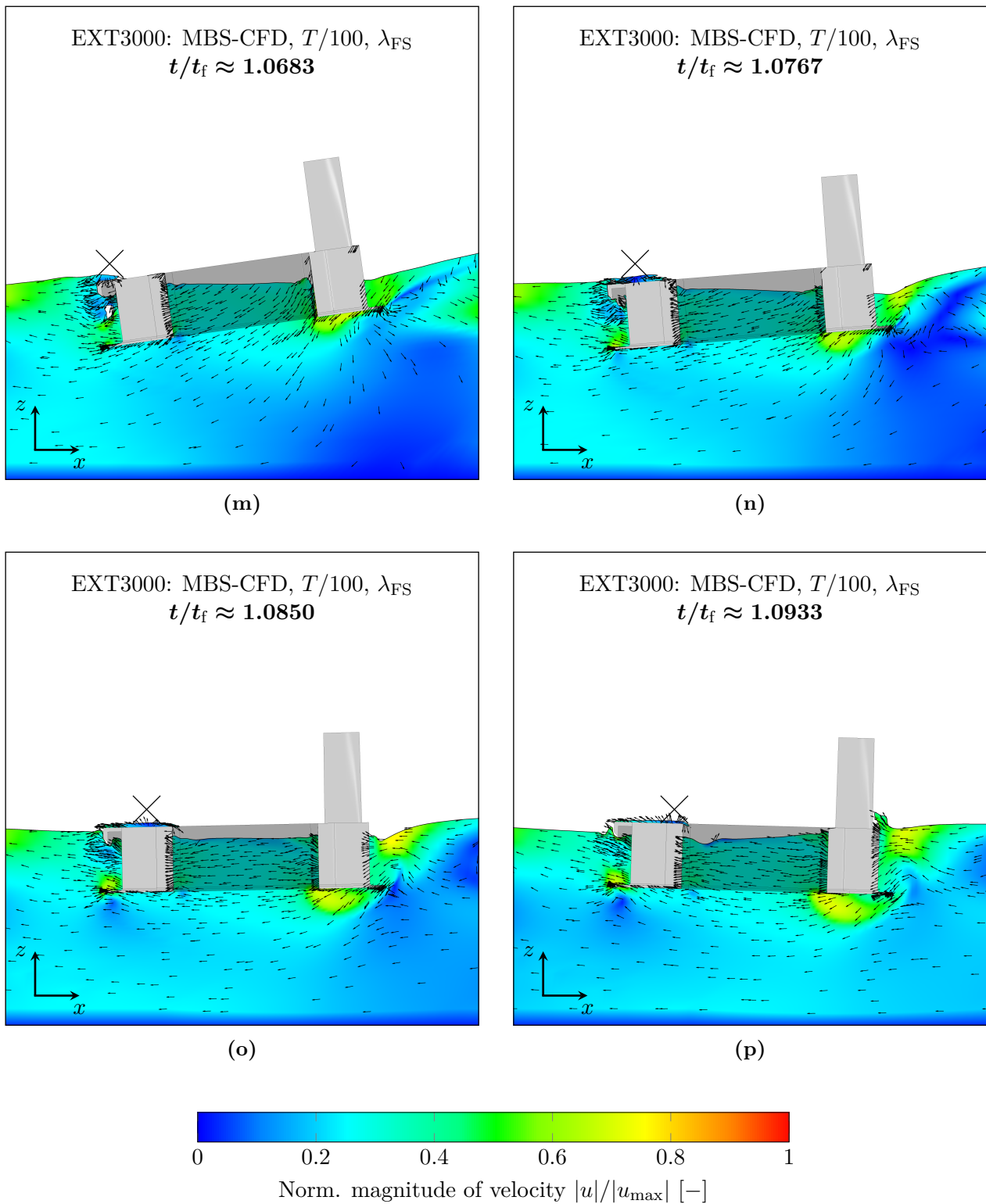


**Figure 5.10:** Visualisation of the normalised magnitude of the fluid velocity and the normalised tangential velocity vectors. The Figures are shown in the  $xz$ -plane at  $y = 0$  for successive time steps and are centred horizontally at the time-dependent platform surge. The initial position at the coordinate  $[0,0,0]$  is marked as reference by two crossed lines.

of positive and negative sign are associated to their respective time of occurrence and Figure number in Appendix A.3 for the the platform motion, integrated forces on the structure and the reference wave elevation.

The series of flow field visualisation starts before the focus time, when the focused wave is rising in front of the platform, see Figure 5.10a. The wave front approaches the mooring interface structure in Figure 5.10b and washes over the front deck in Figure 5.10c. The floating substructure is pushed in the direction of wave propagation, while the wave elevation reaches its maximum value close to Figure 5.10d. Afterwards the wave crest curls over and drops onto the moonpool, refer to Figure 5.10e, before it impacts the TP in Figure 5.10f. In the following, water runs up and around the TP, shown in Figure 5.10g and 5.10h, after the wave crest travelled through the full length of the hull. Then, the wave is falling and the platform pitches in the opposite direction, as the water surrounding the TP decreases again in Figure 5.10i. At the same time, the water level in front of the substructures decreases up to the skirt of the hull, while the water level inside the moonpool is higher than outside. The platform pitch increases further and the water, trapped inside the moonpool, flows out into the open ocean at the rear side of the keel, see Figure 5.10j. The mooring interface structure drops into the water in Figure 5.10k and 5.10l resulting in green water on the front deck in Figure 5.10m and 5.10n. At the end of the series of screenshots the wave elevation decays further as well as the platform motion, refer to Figure 5.10o. However, the aft deck and rear parts of the TP experience a wave run-up from behind in Figure 5.10p, while the platform heave increases and the hull is pulled towards the initial position by mooring line one, see Figure 5.5.

#### 5.4.6 Discussion of Impact of Wave Run-up on Structure

From the previous results, a main question arises how severe the impact of the focused wave crest is when it hits the TP at  $t/t_f = 1.0100$ , shown in Figure 5.10f. Physical properties of interest are the water volume fraction to determine the maximum water level, magnitude of fluid velocity, pressure and wall shear stress at the surface boundary of the structure. The CFD solver performs a statistical analysis of the above mentioned properties at each time step. Resulting maximum values at the end of the MBS-CFD simulation are extracted and stored together with associated grid coordinates for the TP. Using a data processing tool, the 4D data (physical quantity at the Cartesian coordinates  $x, y, z$ ) are reduced to 3D (physical quantity at the Cartesian coordinates  $x, z$ ).

Coordinate transformation is applied to derive data for the initial, undeformed mesh because the dataset written by CFD is available for the deformed mesh only. In addition, the TP is moved in such a way that its centre point at the bottom coincides with the coordinate origin  $[0,0,0]$ . With this procedure one can map the physical quantity of interest, for example the water volume fraction, from the surface of the TP to a cylinder surrounding it with identical

vertical  $z$ -axis. This represents a conversion from Cartesian to cylindrical coordinates. Unwrapping the resulting cylinder and flattening it provides the physical quantity of interest at the Cartesian coordinates  $x$  and  $z$ . The longitudinal coordinate  $x$  is plotted as azimuth  $\varphi$ , which starts at the TP with  $\varphi = 0^\circ$  at the front (facing the moonpool) and ends with  $\varphi = 180^\circ$  at the rear (facing the open ocean), as illustrated in Figure 5.5. The range of the azimuth is  $0^\circ \leq \varphi \leq 180^\circ$  because only a half model is simulated in this study. One needs to consider that small distortions of the physical quantities occur at the lower sections of the TP because of the applied projection method and the square-shaped base area with rounded corners.

In Figure 5.12 results based on the above mentioned data processing approach are plotted with contours ranging from the bottom of the TP to the top over the azimuth. For the water volume fraction in Figure 5.12a, a threshold of  $\varphi_{\text{water}} = 0.5$  is used for the definition of the boundary between the two phases water and air in each control volume. Based on the maximum relative wave elevations, captured by WP<sub>2</sub> in the moonpool directly in front of the TP as shown in Figure 5.7, one could assume that only little wave run-up on the structure occurs. However, water flows up and around the TP, resulting in significant wave run-up to a relative height of  $z_{\text{TP}} \leq 0.8$ . Also, one would assume that wave run-up is highest at the middle of the TP facing the incident focused wave. But wave run-up at  $\varphi = 0^\circ$  is lower in height than for  $45^\circ \leq \varphi \leq 135^\circ$ . This is because the floating substructure does not stand still but moves with the wave, which results in a relative movement. Even the rear of the TP is flooded by water flowing down again with a peak value at around  $\varphi = 150^\circ$  and with  $z_{\text{TP}} = 0.6$ . To obtain the volume fraction of air one must subtract one by the water volume fraction as given by  $\varphi_{\text{air}} = 1 - \varphi_{\text{water}}$ .

The magnitude of fluid velocities is shown in Figure 5.12c. A distinct hot spot is found at around  $\varphi = 45^\circ$  and  $0.2 \leq z_{\text{TP}} \leq 0.4$  with maximum velocities above  $|u_{\text{max}}| = 40 \text{ m s}^{-1}$ . The remaining surface area experiences smaller fluid velocities in the range of  $10 \text{ m s}^{-1} \leq |u| \leq 20 \text{ m s}^{-1}$ . Based on the findings one can question if the focused wave crest induces such high velocities at the described area as it impacts the TP centrally at the base. As the phases water and air share the same velocity field in a homogeneous multiphase CFD model as described in Section 3.3.7, a hypothetical fluid velocity – the superficial velocity – is calculated for the different fluids. The superficial velocity of air and water is defined as the fluid velocity times the volume fraction of air and water respectively. Figure 5.12i shows the water superficial velocity on the projected surface of the TP. It can be shown that the magnitude of the water velocity is much lower than that of the air. Maximum water velocities are induced, especially at the lower sections for  $z_{\text{TP}} \leq 0.4$ , and peaks of above  $|u_{\text{water,max}}| = 12 \text{ m s}^{-1}$  are visible at the corners of the TP at  $\varphi = 45^\circ$  and  $\varphi = 135^\circ$ . In general, air inside the NWT is at rest at the beginning of the simulation and maximum velocities at the TP are present shortly before the wave impacts the structure, as visualised in Figure 5.11a. The  $xz$ -plane at  $y = 0$  is clipped to show  $\varphi_{\text{air}} \geq 0.5$  and a white, semi-transparent isosurface at  $\varphi_{\text{water}} = 0.5$  illustrates the approaching focused wave surface. From the normalised tangential velocity vectors, the flow direction of air can

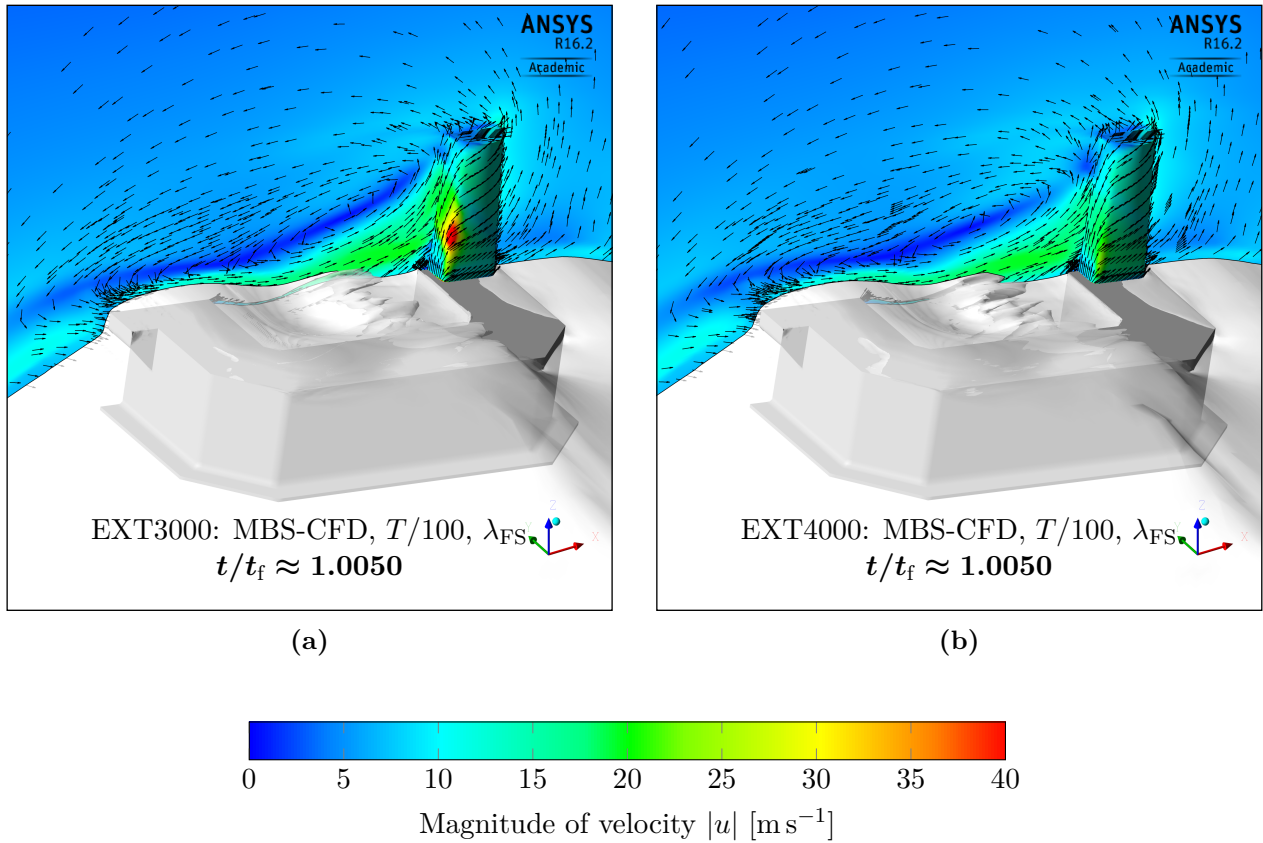


**Figure 5.11:** Visualisation of the magnitude of the fluid velocity and the normalised tangential velocity vectors for EXT3000 (left) and EXT4000 (right). The  $xz$ -plane at  $y = 0$  is clipped to show  $\varphi_{\text{air}} \geq 0.5$ . A white, semi-transparent isosurface at  $\varphi_{\text{water}} = 0.5$  illustrates the water surface.

be determined. An unsteady, large vortex structure forms in front of the TP because the air is accelerated by the propagating wave and pushed forward. The TP represents an obstacle with a moving flow stagnation point. At  $t/t_f = 1.0050$  the air velocity reaches a maximum value of over  $|u_{\text{air,max}}| = 50 \text{ m s}^{-1}$  when it flows around the corner of the TP at  $\varphi = 45^\circ$ . Air compressibility effects are not considered in this simulation. However, as demonstrated in [25] compression of entrapped gas can occur beneath the mooring interface structure.

For the evaluation of impact forces originating from the breaking wave and wave run-up on the TP, transient maximum values for pressure and wall shear stress are visualised in Figures 5.12e and 5.12g respectively. Pressure acts perpendicular to the surface, while wall shear is a tangential stress acting parallel to the surface and is caused by friction from fluid viscosity. In the CFD solver all pressures are calculated with respect to the reference pressure  $p_{\text{ref}} = 101,325 \text{ Pa}$ , which is used as datum. As can be expected, the pressure is very high at the wave impact zone close to the base area of the TP for  $z_{\text{TP}} \leq 0.4$  and  $0^\circ \leq \varphi \leq 30^\circ$ . The remaining parts of the structure experience only a small pressure increase, apart from a small area up to  $z_{\text{TP}} \leq 0.1$ , resulting from the hydrostatic pressure. Negative peaks exist at the corners of the TP at  $\varphi = 45^\circ$  and  $\varphi = 135^\circ$  and relate to the reference pressure  $p_{\text{ref}}$  defined in the CFD model. Following

Bernoulli's principle, if the fluid flow velocity along a streamline increases, the pressure will decrease at constant height for an incompressible fluid. As water flows around the structure, it is accelerated around the corners, resulting in higher velocities and lower pressures. The minimum pressure occurs at  $t/t_f = 1.0267$  after the wave impact and run-up.

Wall shear stresses are two orders of magnitude smaller than the pressure. Higher values of wall shear stress exist especially for the lower sections with  $z_{TP} \leq 0.4$ , where water flow is present. The maximum stresses are induced at the corners of the TP at  $\varphi = 45^\circ$  and  $\varphi = 135^\circ$  as a result of higher friction because the flow is redirected and follows the three-dimensional shape of the TP.

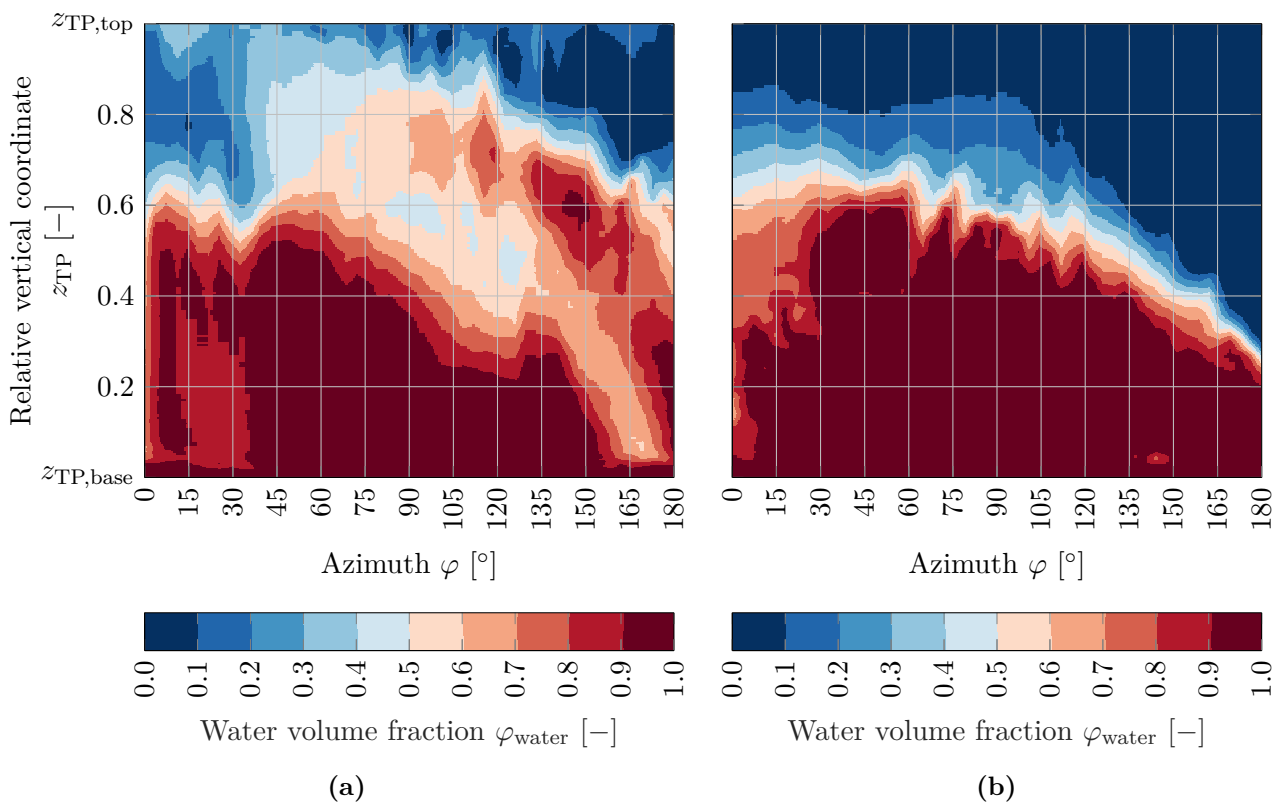


**Figure 5.12:** Illustration of the maxima of the physical properties occurring during the MBS-CFD simulation EXT3000 (left) and EXT4000 (right) at the TP. The 3D geometry is projected onto a flattened cylinder of same height, ranging from the azimuth of  $\varphi = 0^\circ$  to  $\varphi = 180^\circ$ , according to Figure 5.5.

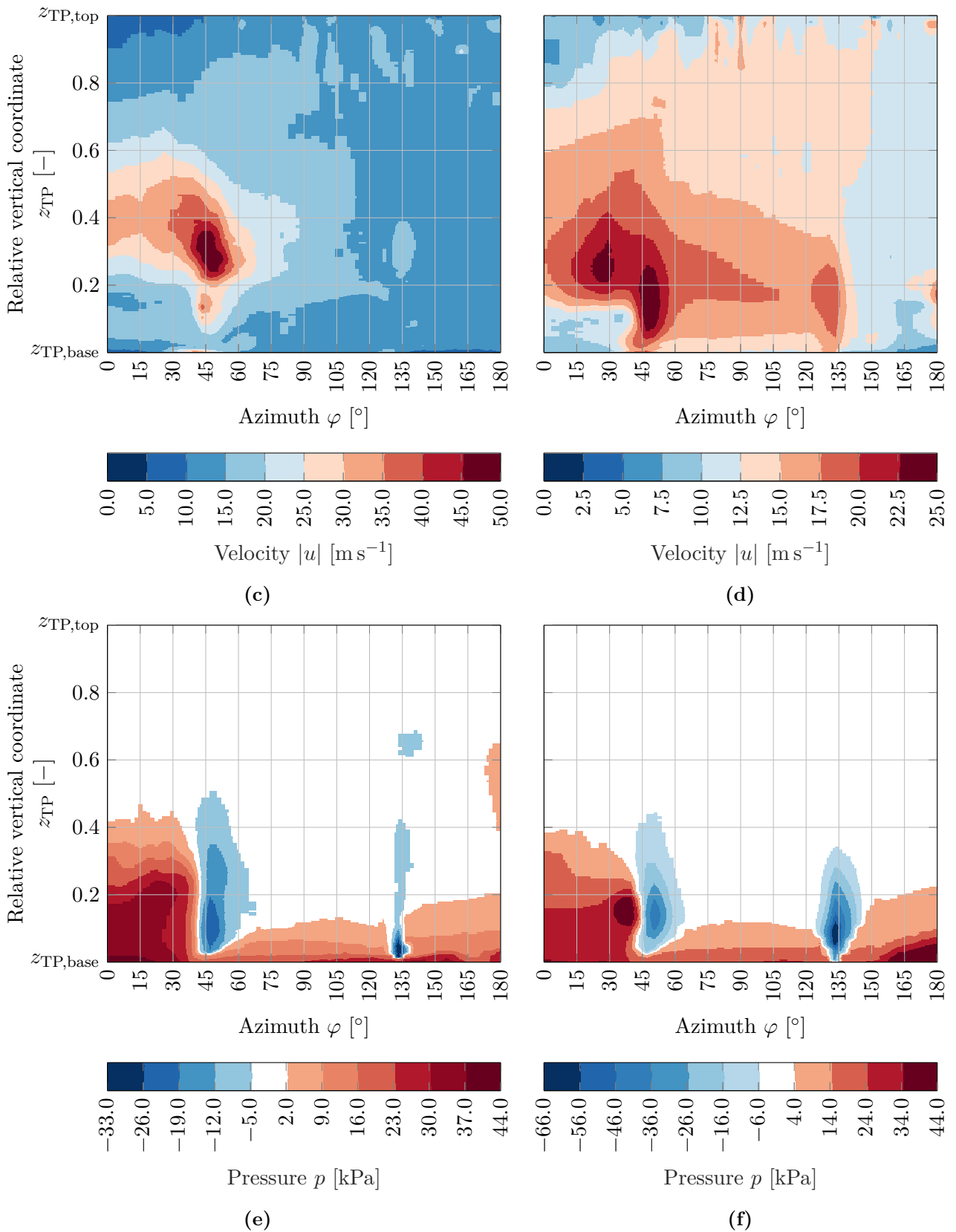


**Figure 5.12:** Illustration of the maxima of the physical properties occurring during the MBS-CFD simulation EXT3000 (left) and EXT4000 (right) at the TP. The 3D geometry is projected onto a flattened cylinder of same height, ranging from the azimuth of  $\varphi = 0^\circ$  to  $\varphi = 180^\circ$ , according to Figure 5.5.

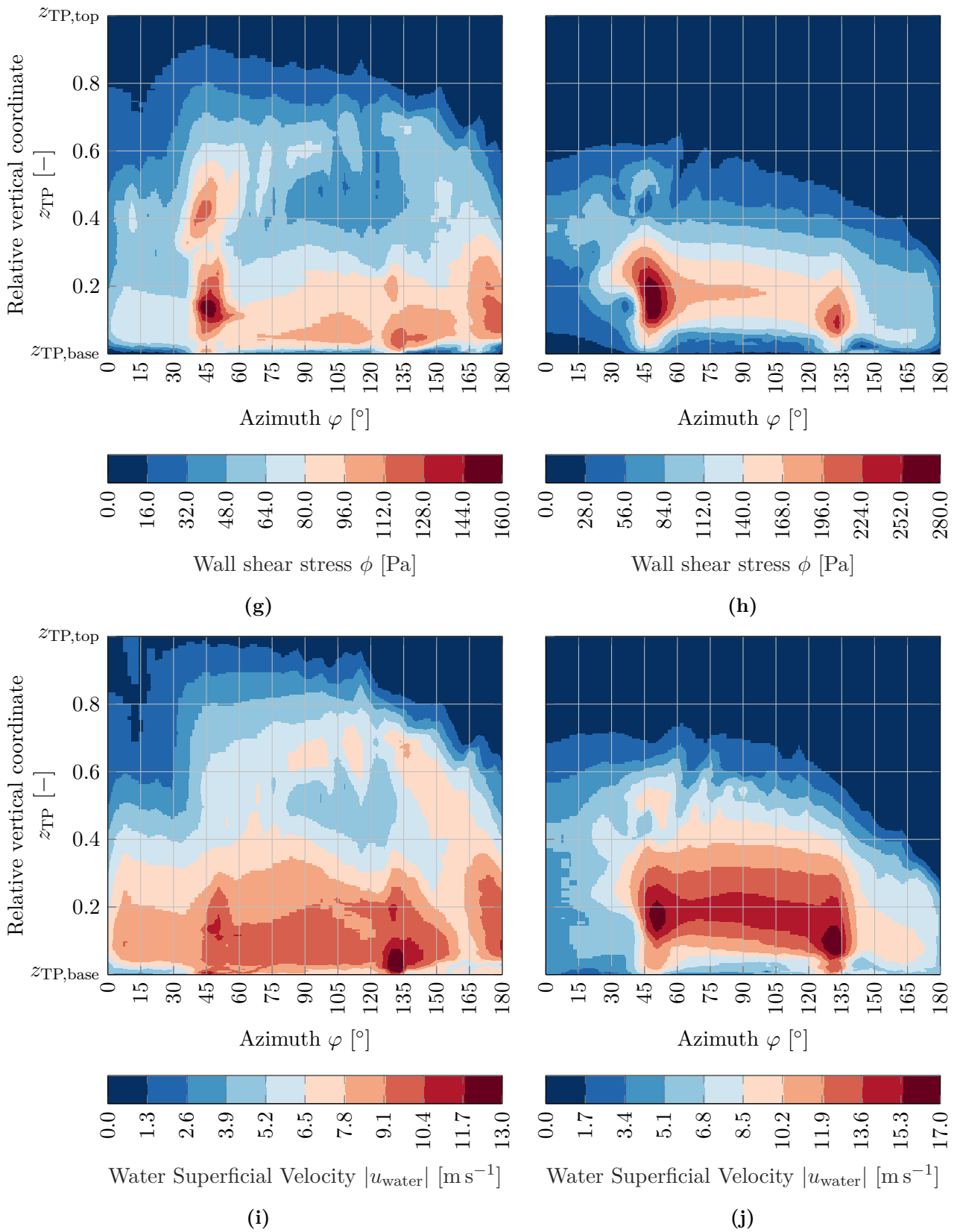


**Figure 5.12:** Illustration of the maxima of the physical properties occurring during the MBS-CFD simulation EXT3000 (left) and EXT4000 (right) at the TP. The 3D geometry is projected onto a flattened cylinder of same height, ranging from the azimuth of  $\varphi = 0^\circ$  to  $\varphi = 180^\circ$ , according to Figure 5.5.

## 5.5 Extreme Wave and Wind

The extreme wave from EXT3000, modelled by the wave focusing technique, is combined with the steady extreme wind speed model and applied to a MBS-CFD simulation of the floating substructure, mooring lines, tower and RNA. It is summarised in Table 5.3 with respect to load case EXT4000. The initial rotor speed is zero and the rotor blades are pitched to  $90^\circ$ . The main differences to the previously discussed load case in Section 5.4 are the fully resolved model of the wind turbine in MBS and the consideration of aerodynamic loads on the rotor and tower applying two different force elements (described in Section 5.1.2). In the following, results of EXT4000 are analysed with emphasis on differences to EXT3000. Table 5.7 provides quantitative comparison of the maximum and minimum values of velocities, pressure and wall shear stress and the associated relative time of occurrence. When comparing plots in Figure 5.12, one must take care of the differences in the maximum and minimum margins of the colourbars between EXT3000 and EXT4000.

**Table 5.7:** Summary of the maximum and minimum values and the time of occurrence of water superficial velocity, air superficial velocity, pressure and wall shear stress. The superficial velocity is determined by the fluid velocity in CFD times the volume fraction of water and air respectively.

ID	Method	Property	$ u_{\text{water}} $	$ u_{\text{air}} $	$p$	$\phi$
			[m s <sup>-1</sup> ]	[m s <sup>-1</sup> ]	[kPa]	[Pa]
EXT3000	MBS-CFD 3D	max	13.5054	52.6496	40.4386	180.8148
		min	0.0000	0.0000	-34.7603	0.0000
		$t_{\text{max}}/t_{\text{f}}$	1.0250	1.0083	1.0200	1.0200
		$t_{\text{min}}/t_{\text{f}}$	0.0000	0.0000	1.0267	0.0000
EXT4000	MBS-CFD 3D	max	17.4231	26.1073	54.2318	290.4824
		min	0.0000	0.0000	-73.1367	0.0000
		$t_{\text{max}}/t_{\text{f}}$	1.0233	1.0050	1.0167	1.0183
		$t_{\text{min}}/t_{\text{f}}$	0.0000	0.0000	1.0233	0.0000

### 5.5.1 Discussion of Relative Wave Elevation

The inlet boundary conditions for EXT4000 is defined in the same way as for extreme wave only case EXT3000. Therefore, reference wave probe  $WP_{\text{ref}}$  measures the same focused wave group as shown in Figure 5.6. Negligible differences in wave height below 0.1% are observed between EXT3010 and EXT4010 from numerics, see Table 5.4.

Comparing results in Figure 5.7, one only sees minor deviations between the curves for the simulations EXT3000 and EXT4000. The differences in the relative wave elevations must be related to the platform motion because the approaching focused wave is identical between the



test cases. For  $WP_1$  in front of the hull, it can be seen that the wave elevation signal EXT4011 shows a small negative mean offset of  $-0.43$  m compared to EXT3011, possibly caused by the increased positive platform pitch.  $WP_2$  inside the moonpool and directly in front of the TP shows similar values for EXT3012 and EXT4012. This indicates similar wave-run up behaviour. Small differences can be found for  $WP_3$ , which is shadowed by the TP at the rear of the platform. The signal EXT4013 shows a positive mean offset of  $0.35$  m compared to EXT3013, possibly due to the increased positive platform pitch. Furthermore, the measured wave amplitude is  $6.2294$  m for EXT4013 compared to  $6.9359$  m for EXT3013, which is a reduction of  $10\%$ . In general, relative wave elevations show only small differences when extreme wind is included in the simulation. This demonstrates a reduced influence of the aerodynamic forces.

### 5.5.2 Discussion of Platform Kinematics

After the wind increases from zero to  $u_{e50,hub} = 70 \text{ m s}^{-1}$  the floating system is pushed in the positive  $x$ -direction. High natural surge periods of the mooring system cause long transient motion until a steady state is reached at a new equilibrium position. For this reason, the initial positions for EXT3000 and EXT4000 are the same to save simulation time.

Figure 5.8 compares platform kinematics in surge, heave and pitch. The inclusion of extreme wind leads to an increased platform surge position as expected. A mean offset of  $1.97$  m can be shown between EXT3001 and EXT4001. The FOWT oscillates around this mean offset due to the high platform surge natural period and the incident waves. The maximum excursion increases by  $5.33\%$  to  $25.0725$  m for EXT4001 compared to  $23.8042$  m for EXT3001, see Table 5.5. But the time when the absolute maximum platform surge occurs is very similar in both cases.

Platform heave is not influenced by the aerodynamic forces from extreme wind because the signals EXT3003 and EXT4003 show almost the same behaviour. This indicates that platform heave motion is mainly driven by the waves and not coupled to platform surge or pitch.

Wind loads are higher at the top of the tower because the wind speed increases with height. The aerodynamic loads act on the rotor blades based on a sheared wind profile. Hence, a positive pitching moment around the  $y$ -axis of the floating system is induced, which leads to an increased platform pitch. Without extreme wind in EXT3005, the peak platform pitch before the focus time is of positive sign and smaller in magnitude than after the focus time, where the value is of negative sign with  $|\psi_{\max}| = 13.2807^\circ$ . A positive mean offset of  $1.07^\circ$  is observed for EXT4005 compared to EXT3005, which leads to a value of  $|\psi_{\max}| = 13.2550^\circ$  with extreme wind loads. The absolute maximum pitch angle does not increase when extreme wind is included in the simulation, see Table 5.5. Only the time of occurrence shifts from after the focus time for EXT3005 with  $t(|\psi_{\max}|)/t_f = 1.0483$  to slightly before the focus time for EXT4005 with  $t(|\psi_{\max}|)/t_f = 0.9917$ . This is caused by the pitching moment from the aerodynamic loads.

### 5.5.3 Discussion of Integrated Forces on the Structure

The longitudinal and vertical forces  $F_x$  and  $F_z$  shown in Figure 5.9 are determined by numerical integration of the pressure and wall shear stress across the hull surface area in CFD and include contributions from hydrostatics and hydrodynamics. The simulations show almost the same behaviour for EXT3007 and EXT4007 as well as EXT3009 and EXT4009. The absolute maximum vertical and longitudinal force components are summarised in Table 5.6. Only minor differences exist between both cases and the peak values occur at similar instances in time. This can be expected as the wave excitation forces dominate and the platform motion, as described in Section 5.5.2, is only affected to a very small extent when extreme wind is included in the simulation.

### 5.5.4 Discussion of Impact of Wave Run-up on Structure

Water volume fractions of EXT4000 are presented in Figure 5.12b. Compared to the case EXT3000 on the left one can see that the boundary between the surface areas around the TP covered by water is much clearer and more distinct. The water level rises up to  $z_{TP} \leq 0.6$  for  $\varphi_{water} \geq 0.5$ , which is lower in height than for EXT3000. In addition, the rear of the TP is less covered by water than the front, which is different when no extreme wind is included for EXT3000. Possibly, the inclusion of the extreme wind and the increase in platform pitch decreases the wave run-up and reduces the maximum water levels at the TP.

A similar tendency is found for the magnitude of fluid velocities as shown in Figure 5.12d. Maximum velocities measured during the simulation at the surface of the TP decrease by a factor of two, see also Table 5.7. This is explained by the decreasing air superficial velocities. Figure 5.11b is captured at the identical instance in time as for EXT3000 and clearly the hot spot of the velocity at the corner of the TP at  $\varphi = 45^\circ$ , originating from air accelerated by the approaching focused wave, is reduced significantly. The extreme wind and the associated effects on the platform motion change the breaking process of the focused wave at the fore of the floating substructure slightly. This results in differences in water particle motion and the following wave run-up. In contrast, the superficial velocity of water increases to over  $|u_{water,max}| = 17 \text{ m s}^{-1}$  on the surface of the TP when extreme wind is considered, refer to Figure 5.12j. Peak values are especially visible for  $\varphi = 45^\circ$  and  $\varphi = 135^\circ$ , and in between these values the water superficial velocity is higher compared to EXT3000. The extreme wind increases the maximum water superficial velocity by 29.01 %.

An increase of the maximum and the minimum pressure is observed for EXT4000 compared to EXT3000. This is based on Bernoulli's principle as higher water superficial velocities for EXT4000 reduce the pressure at the corners of the TP below the reference pressure  $p_{ref}$  defined in the CFD model. A relative decrease by 110.40 % is observed for the minimum pressure

between EXT3000 and EXT4000 in Figure 5.12f and Table 5.7. The maximum pressure is 34.11 % higher when extreme wind is included in the simulation. The impact zone at the front of the TP moves slightly towards the corner to  $30^\circ \leq \varphi \leq 45^\circ$ , possibly caused by changes in the wave crest development and wave breaking at the structure.

Peak values of the wall friction are found at  $\varphi = 45^\circ$  and  $\varphi = 135^\circ$  in Figure 5.12h. This is caused by water flowing around the surface of the TP after the wave impact. The maximum wall shear stress is increased by 60.65 % when extreme wind is included because of the higher water superficial velocities at the corners of the TP.

### 5.5.5 Discussion of Wind Turbine Motion and Loads

For the design of a FOWT, accelerations and especially loads at extreme environmental conditions are of major importance. Critical loads can be exceeded and the design can be driven by specific extreme load cases. At the same time, mechanical and electrical equipments are certified for a maximum acceleration, which should not be exceeded during the installation works and in all operating and non-operating conditions. Tolerances and operational limits are defined in the project design basis. For example, in the LIFES50+ project [187,188], the maximum pitch angle for non-operational load cases, such as DLC 6.1, was limited to  $15^\circ$ . This limit represents the maximum value in the time series of the simulation. For the same design load case, a maximum acceleration in longitudinal direction of  $0.6g \approx 5.89 \text{ m s}^{-2}$  was defined, with the gravitational acceleration of  $g = 9.81 \text{ m s}^{-2}$ . The operational limits are always dependent on the site conditions and characteristics of the selected type of floating substructure. Suitable limits for one platform design can result in severe loads at certain conditions or even unfeasible structural configurations for a different concept. Wind turbine designers also consider their own operational limits for the technical equipment. The same applies to designers of Offshore Substation (OSS), which will be placed on floating substructures for commercial floating wind farms in the near future. Recently, Aibel showed the readiness of high-voltage equipment and the assumed operational limits for floating OSS [189]. It is concluded that high-voltage equipment can require additional qualification and type approval for the dominant motions, but no supplier was able to confirm suitable high-voltage equipment yet.

In the following, the nomenclature of the legend entries is modified for sensors associated to the rotor and tower, so that the sensor is included by characters six to eight, instead of characters six to seven as for EXT3000 in Section 5.3.

### 5.5.5.1 Discussion of Wind Speed Variations

Thrust forces on the rotor and resulting tower base bending moments depend on the wind speed profile, which is calculated from Equations 5.2 and 5.3. The wind speed at hub height is unsteady because of dynamic motion of the floating substructure. Small oscillations around the mean value of  $u_{\text{hub}} = 70 \text{ m s}^{-1}$  can be observed with a maximum of  $u_{\text{hub}} = 71.11 \text{ m s}^{-1}$ , see left plot in Figure 5.13. Vertical shear also leads to variations of the wind profile across the rotor disk.

After initialisation of the wind field, the rotor begins to idle and a mean rotor speed of  $\Omega (t/t_f \geq 0.5) = 1.24 \text{ rpm}$  can be observed, see right plot in Figure 5.13. The maximum rotor speed of  $\Omega = 1.38 \text{ rpm}$  can be found considerably after the focus time  $t_f$ , which is explained by the rotor inertia and a time delay until changes of the wind speed can be seen in the rotor speed signal. The rotor idles at its minimum speed of  $\Omega = 1.10 \text{ rpm}$  at the focus time. This is caused by the mutual influence of the dynamic motion of the FOWT and the effective wind speed at the aerodynamic markers along the rotor blades. However, changes in rotor speed are only small due to a fixed blade pitch angle of  $\theta_{1,2,3} = 90^\circ$  to limit rotor loads at the extreme environmental conditions of DLC 6.1.

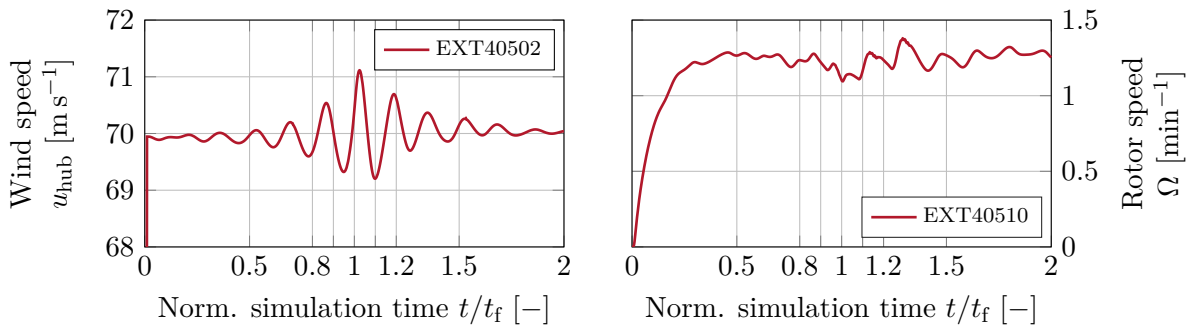


**Figure 5.13:** Response of the wind speed measured at the moving hub height (left) and the rotor speed (right) over the normalised simulation time for EXT4000.

The relative wind speed at the tower is shown for different heights in Figure 5.14. In general, the mean wind speed increases with the height because of the vertical wind shear. At the lowest tower marker at a height of  $0.05h_{\text{twr}}$ , the wind speed reduces to almost  $u_{\text{twr},01} = 0 \text{ m s}^{-1}$  in conjunction with the minimum platform heave at  $t/t_f = 1.0900$ , see Figure 5.8b. This is caused by the tower marker approaching a height of zero after the focus time, where the power law in Equation 5.2 gives a very small wind speed. The relative motion of the tower base is small and cannot compensate the drop in wind speed. Figure 5.10p shows that the lower tower sections are not covered by water at this time. For the upper tower markers at  $0.45h_{\text{twr}}$  and  $0.95h_{\text{twr}}$ , the measured wind speed  $u_{\text{twr},05}$  and  $u_{\text{twr},10}$  oscillates around a mean value with a range of several meters per second and a minimum value in the vicinity of the focus time  $t/t_f = 1$ .

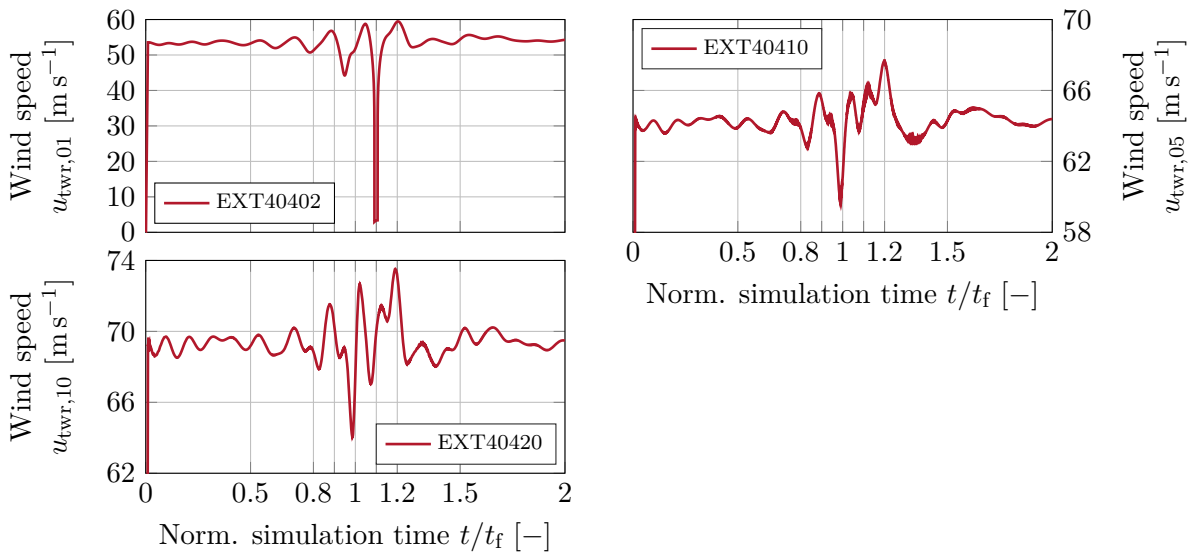


**Figure 5.14:** Response of the wind speed measured at the local tower markers over the normalised simulation time for EXT4000.  $u_{\text{twr},01}$  is captured at a tower height of  $0.05h_{\text{twr}}$ ,  $u_{\text{twr},05}$  at  $0.45h_{\text{twr}}$  and  $u_{\text{twr},10}$  at  $0.95h_{\text{twr}}$ .

### 5.5.5.2 Discussion of Tower Displacements

Figure 5.15 shows the translational and rotational displacement at the tower base and top marker over the normalised simulation time. The motion of the tower is mainly driven by the wave loads. The tower base, which represents the base of the TP, is fixed to the floating substructure. The surge, heave and pitch displacements at the tower base show almost the same behaviour as the platform motion, which is included for reference in grey colour based on Figure 5.8. For the tower top, a similar behaviour is seen for the vertical motion  $z$  and the pitch angle  $\psi$ . A maximum pitch of  $|\psi_{\text{max}}| = 13.69^\circ$  is observed, which is below the indicative limit for non-operational load cases of  $|\psi_{\text{max}}| = 15^\circ$  mentioned in Section 5.5.5.

The translational displacement of the tower in the  $x$ -direction is highly influenced by the platform pitch motion. The tower top fore-aft deflection is insignificant because it only represents approximately 1% of the maximum translational displacement at the tower top for the stiff-stiff tower configuration, see Section 5.5.5.4. The translational displacements in the  $x$ -direction deviates significantly between the tower base and the tower top, shown by the curves EXT40442 and EXT40460 respectively. This is observed close to the focus time  $t/t_f = 1$ , where the platform pitch motion is high, see also Figure 5.8c. The maximum and minimum displacements are  $x_{\text{TWR,top,max}} = 16.88\text{ m}$  and  $x_{\text{TWR,top,min}} = -9.08\text{ m}$  at the tower top, and  $x_{\text{TWR,base,max}} = 22.73\text{ m}$  and  $x_{\text{TWR,base,min}} = -13.31\text{ m}$  at tower base. As a conclusion, an observer situated at the tower top would experience smaller maximum translational displacements in the  $x$ -direction compared to the tower base during this extreme load case.

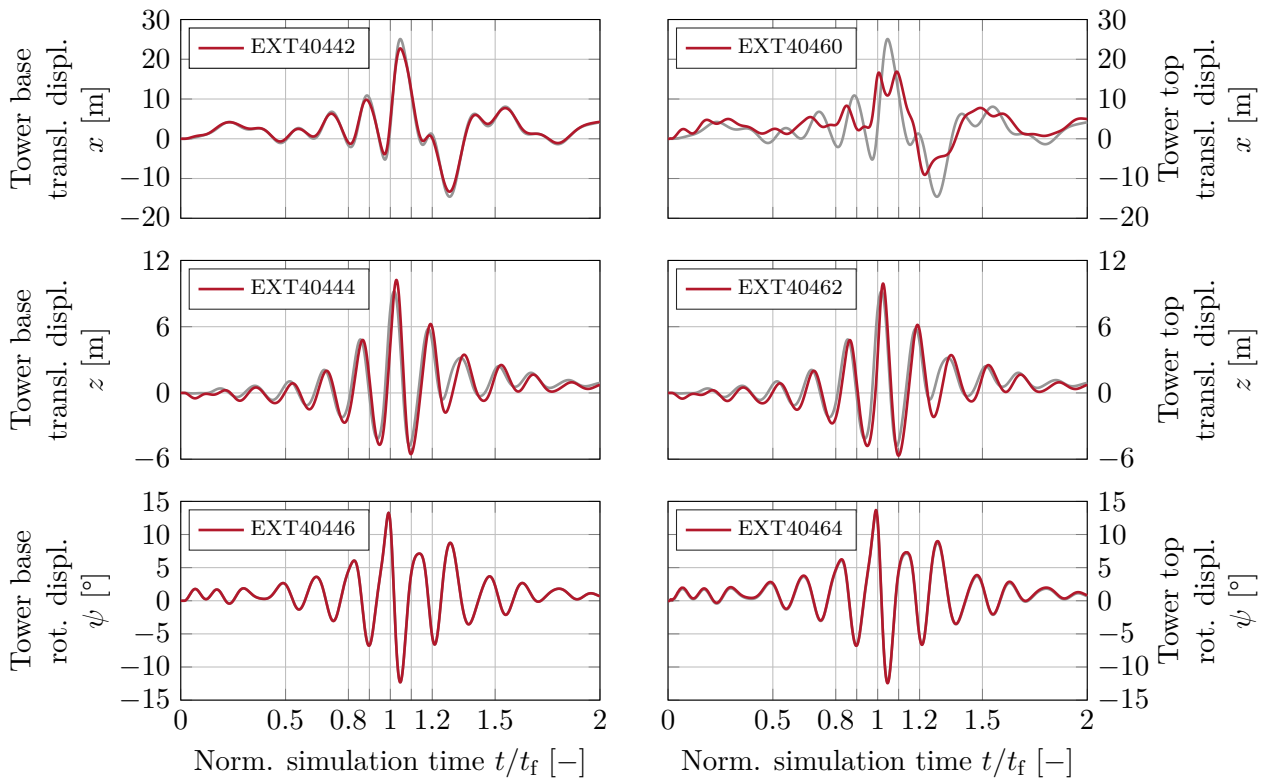


**Figure 5.15:** Response of the tower base (left) and the tower top (right) translational and rotational displacement relative to the undeflected initial position over the normalised simulation time for EXT4000. The platform motion from Figure 5.8 is included for reference in grey colour.

### 5.5.5.3 Discussion of Tower Accelerations

The accelerations at the tower top are presented in Figure 5.16 and Table 5.8. Considering the tower base, the magnitude of the maximum longitudinal accelerations is below  $0.3g \approx 2.94 \text{ m s}^{-2}$ . The highest value of  $\ddot{x}_{\text{base,max}} = 2.75 \text{ m s}^{-2}$  is observed slightly before the focus time at  $t_{\text{max}}/t_f = 0.9813$ , similar to the maximum longitudinal force  $F_x$  in Figure 5.9a. The tower top experiences higher accelerations. The maximum absolute acceleration in the longitudinal direction is  $|\ddot{x}_{\text{top,max}}| = 3.91 \text{ m s}^{-2}$  (negative sign), which is below the indicative limit for non-operational load cases of  $0.6g \approx 5.89 \text{ m s}^{-2}$  mentioned in Section 5.5.5. An increase of 42.08% is observed for the maximum longitudinal acceleration at the tower top compared to the tower base. A similar trend is seen for the vertical acceleration with a maximum absolute value of  $|\ddot{z}_{\text{top,max}}| = 2.74 \text{ m s}^{-2}$  (negative sign), which is 29.23% higher than at the tower base. The simulations show that the maximum tower top accelerations occur always very close to the focus time driven by the combined platform surge, heave and pitch motion. Furthermore, this load case may not be the most severe one for the accelerations depending on the environmental conditions and the operational behaviour of the wind turbine.

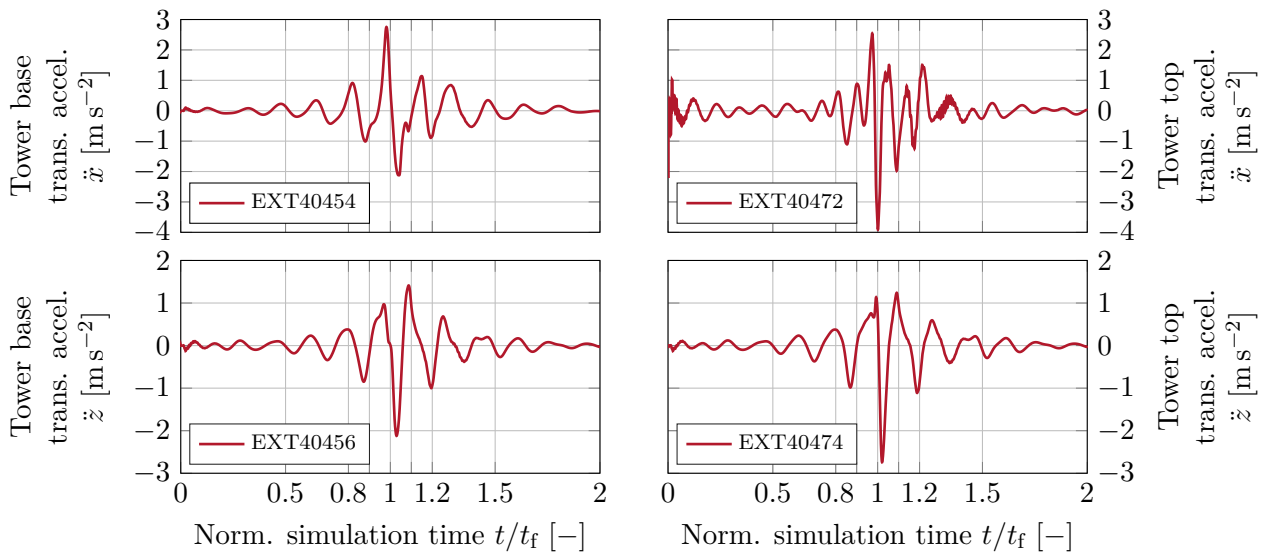


**Figure 5.16:** Response of the tower base (left) and the tower top (right) translational and rotational acceleration over the normalised simulation time for EXT4000.

#### 5.5.5.4 Discussion of Tower Loads

From a designer's perspective tower base bending moments are of major importance because rotor loads are transferred to the floating substructure through the connection at the tower base or TP. The tower base pitching moment is shown in Figure 5.17 on the left together with the tower top fore-aft deflection on the right. Extreme values of  $M_{y,\text{base,max}} = 80.15 \text{ MN m}$  at  $t_{\text{max}}/t_f = 1.0005$  and  $x_{\text{FA,max}} = 19.34 \text{ cm}$  at  $t_{\text{max}}/t_f = 1.0010$  can be shown. The maximum bending moments and fore-aft tower deflections occur at the focus time, where the platform pitch displacement is also at a maximum, see Figure 5.8c. A stiff-stiff tower design is included in this baseline configuration to shift the first eigenfrequency of the tower-fore aft mode above the 3P region as discussed in Section 2.3. This explains only little deflection at the tower top.

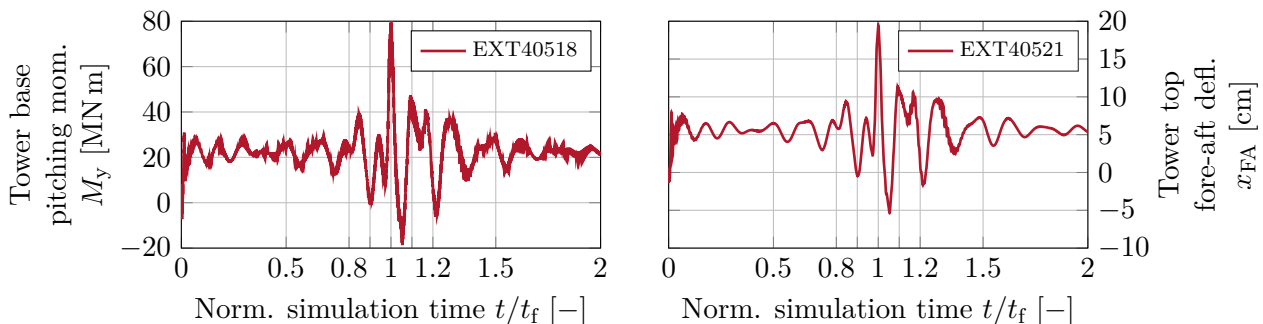


**Figure 5.17:** Response of the tower base pitching moment caused by the fore-aft forces (left) and the tower top fore-aft translational deflection relative to the moving undeflected position (right) over the normalised simulation time for EXT4000.

**Table 5.8:** Summary of the maximum and minimum accelerations measured at the tower base and tower top and the time of occurrence of EXT4000. The maximum absolute values are printed in bold.

ID	Method	Location	Property	$\ddot{x}$	$\ddot{z}$	
				[m s <sup>-2</sup> ]	[m s <sup>-2</sup> ]	
EXT4000	MBS-CFD 3D	Tower base	max	<b>2.7524</b>	1.4120	
			min	-2.1229	<b>-2.1208</b>	
			$t_{\max}/t_f$	<b>0.9813</b>	1.0875	
			$t_{\min}/t_f$	1.0417	<b>1.0297</b>	
			Tower top	max	2.5416	1.2398
				min	<b>-3.9107</b>	<b>-2.7408</b>
		$t_{\max}/t_f$		0.9742	1.0912	
		$t_{\min}/t_f$		<b>1.0013</b>	<b>1.0212</b>	

## 5.6 Summary and Final Remarks

In this research, a high-fidelity simulation environment was applied to analyse the system response of a FOWT under extreme wave and wind conditions. While engineering models for hydrodynamics need to be calibrated for the influence of added mass, viscous drag, drift loads, slamming loads etc., a CFD model inherently includes those effects. Instead, numerical modelling is more important for CFD, such as grid resolution for the pressure integration on the body surface, resolution of the boundary layer and turbulence modelling, discretisation of the free water surface in the NWT, consideration of the free body motion through mesh deformation, quality of the grid, adjustment of boundary conditions etc. This study is relevant because the developed MBS-CFD simulation environment can fill a gap between engineering models and experiments for the design of FOWTs. The methodology gives access to results, which cannot be obtained from other simulation techniques, such as ringing of the wind turbine after slamming loads, run-up heights along the TP, pressure distributions at any point under extreme conditions and pressure distributions in the vicinity of the skirt and corners to design I-tubes or power cable connections. Furthermore, the simulation environment can be used to complement wave tank model tests during the design phase of a FOWT to investigate extreme wave events, but also to predict hydrodynamic damping and viscous drag for engineering models.

The analysed barge-type floating substructure with a moonpool has very specific characteristics with respect to the hull geometry, the hydrodynamic properties, the mooring system and the motion response. In addition, the metocean conditions at the SEM-REV offshore test site, where the FLOATGEN demonstrator is operating, are very specific. For these reasons, general conclusions for the design of FOWTs are difficult to provide because the design is concept- and site-specific. The simulations of extreme wave-only and combined extreme wind-wave conditions were conducted to demonstrate the applicability of the methodology and to identify its



limitations. It is recommended to not only consider waves using a high-fidelity method, such as CFD, but also wind acting on the RNA and tower for reliable and conservative prediction of motion and loads in extreme conditions. Significant wave run-up was observed during the simulation at the TP up to 80 % of its height. Engineering models cannot capture such complex fluid-structure interactions. Further studies are required to verify, if and to what extent the motion of the floating substructure relative to the extreme wave can reduce the wave impact loads at the hull and TP in comparison to bottom-fixed substructures.

Furthermore, the observed maximum excursions, inclinations and accelerations may not be the most severe ones. More critical values can occur during the operation depending on the environmental conditions and the operational behaviour of the wind turbine. In general, it is a conservative assumption with respect to the level of utilisation and the damage if waves, wind and current are considered collinear.

Simulation of turbulent wind and irregular waves relies on statistically relevant timescales, which would require very long run times of several weeks with the applied MBS-CFD simulation environment. Therefore, deterministic environmental conditions were used in this study. Unidirectional, phase-focused wave groups were generated using a modification of the NewWave theory, which accounts for second-order Stokes waves to improve the accuracy. The method is recommended by offshore standards for the generation of design waves as an alternative to periodic regular wave theories. Other researchers used the same approach for numerical studies and it was also applied in experimental testing to investigate wave breaking on offshore structures. Hence, the wave focusing technique is expected to be reliable for modelling of the extreme design waves in this study. The effect of turbulent wind was not taken into account, but maximum wind speeds during gusts were considered by an amplification factor in the extreme wind modelling, which is based on the standard and assumed to be conservative.

The mooring system was simplified and calibrated to the global linear stiffness matrix of the wave basin test campaign. The simulations showed large maximum excursions caused by the extreme wave conditions. This finding does not need to be unreasonable. The mooring system design is very site-specific and soft configurations can be advantageous with respect to costs. It is recommended to implement an accurate mooring system model in future studies using a dynamic mooring model to account for the non-linear force-displacement relationship, the inertia forces and the fluid drag loads.



# 6

## Conclusions and Outlook

The final Chapter summarises main contributions and conclusions of this study in Sections 6.1, 6.2 and 6.3 and provides recommendations for future research in Section 6.4.

Based on previous and ongoing scientific studies, it was concluded that high-fidelity simulation techniques for assessment of extreme loads on offshore wind turbine substructures were primarily applied to bottom-fixed foundations. Hence, the main research question of this dissertation is to analyse how extreme environmental conditions influence the system response of a Floating Offshore Wind Turbine (FOWT) using high-fidelity modelling.

### 6.1 High-Fidelity Simulation Environment

Development of a high-fidelity simulation environment was based on a coupled methodology of the Multibody System (MBS) and Computational Fluid Dynamics (CFD) solvers SIMPACK and ANSYS CFX respectively, capable of simulating a FOWT in an integrated approach with consideration of aero- and hydrodynamics, structural dynamics as well as mooring and control system. This approach is beneficial, because modal reduction in MBS provides an efficient solution for complex FOWT systems, for which structural flexibilities of tower, rotor blades and drive train are of interest. In addition, assessment of model sensitivity to different levels of fidelity is possible both on a system and component level. A fully implicit iteration scheme was implemented and modules for sending, receiving and translating of loads and deformations were combined with a moderator, which controlled the iteration process.

A Numerical Wave Tank (NWT) was established in CFD and the free surface was modelled using the Volume of Fluid (VOF) method. Waves were generated at the inlet boundary con-

dition by specifying the velocity profile and the fluid volume fractions. Wave generation is ramped-up to increase solver stability and a numerical beach is used to damp wave reflections. Mesh deformations were considered for the boundary conditions of the floating substructure and Transition Piece (TP) through local deformations calculated by the structural solver. A three-dimensional, ellipsoidal transition function protected an inner mesh region around the structural components by specified displacements. From there, deformations were scaled by distance in an intermediate zone until the mesh was stationary in the outer region, depending on the geometrical limits and the maximum excursions of the floating substructure.

In the course of development of the coupled MBS-CFD methodology, a sensitivity study of grid resolution, time step size and turbulence model for a regular wave in a two-dimensional NWT was conducted to find an optimum between numerical accuracy and efficiency. Definition of the time step as a multiple of the wave period was found suitable. Refinement of the temporal discretisation beyond  $t_{\text{step}} = T/100$  has no additional benefits. Convergence was achieved for a spatial discretisation of 40 grid cells per wave length. In addition, the finer the hexahedral mesh is in the direction of gravity, the smaller the numerical damping. Lastly, the Shear Stress Transport (SST) turbulence model was chosen because of its advantages in numerical damping. In order to evaluate load cases efficiently, a simulation procedure was established. Wave generation was calibrated in a two-dimensional NWT in CFD standalone without the floating substructure to achieve the desired wave kinematics in the region of interest. Afterwards, the calibrated spatial discretisations and environmental input settings were used to create a three-dimensional mesh. Coupled MBS-CFD simulations were performed to assess hydrodynamic loads on a FOWT

## 6.2 Validation by Experiment

Experimental data from a wave tank model test were used to validate the simulation approach. It was generated in the course of the FLOATGEN project in 2014 to test the dynamic behaviour of Ideol's floating substructure in extreme wave conditions and shallow water depth by Froude scaling at 1:32. A reduced MBS model of the floating system was setup, consisting of one rigid body for representation of the floating substructure, tower and Rotor Nacelle Assembly (RNA). Platform surge, heave and pitch motion were considered based on the geometric symmetry. The mooring system was modelled in MBS by a calibrated, global linear stiffness matrix. Fluids were defined incompressible in CFD and initial mesh deflections were taken into account.

Free-decay of platform surge, heave and pitch motion were investigated. It was observed that linear damping is not sufficient to approximate the behaviour of the floating system and additional higher-order terms are needed. Damping was decreased by grid refinement and reduced time step size until convergence. However, reliable prediction of hydrodynamic damping is the weak point of the MBS-CFD coupling because the damping ratios calculated from CFD were

higher than those from the experiment. Unfortunately, the fluid solver of the coupled methodology is limited to first-order temporal discretisation. Higher-order implementations can increase the accuracy but cannot be implemented here because the commercial MBS and CFD codes only offer limited access to internal functions and system calls. Hence, a standalone CFD model is recommended for reliable assessment of damping characteristics using a rigid body solver. The mesh then needs to include a subdomain and interface for the floating substructure.

For the natural periods it was found that already moderate settings for grid resolution and time step size are sufficient for an accurate prediction. As viscous damping forces are proportional to the velocity squared, the natural period and damping ratio were sensitive to the initial amplitude of the pitch decay, which should agree between the simulation and the experiment. Variations of the initial heave displacement, though, had no influence on the natural period. But heave free-decay was characterised by significant spectral energy contributions below the natural frequency, which increased in magnitude for higher initial heave amplitudes and excited the heave motion of the floating substructure. This effect originates from the oscillating water column in the moonpool (piston mode), a strong vortex shedding at the skirt of the hull and interactions with the structure while it moves up and down repeatedly. High-fidelity CFD simulation can improve the understanding of observed physical phenomena. The natural period of the surge free-decay was underestimated by 10% in the simulation. This is because yaw and sway motions were present in the experiment due to an inaccurate alignment and the resulting platform drag and added mass were increased. But this additional motion was not considered in CFD due to the model simplifications based on the geometric symmetry of the structure. In order to estimate the influence of modelling errors, the stiffness and the pre-tension of the mooring lines were reduced by 5%, but this increased the natural period by only 2%. Representation at model or full scale did not influence the results noticeable.

Finally, validation was completed by regular wave tests and initial transients were reduced by spring-damper elements in MBS, which released the floating substructure from the mean drift position after waves were fully developed. A deflection of the initial mesh was needed. Resulting platform drift as well as maximum values of platform surge and heave motion showed very good agreement, which confirmed modelling of the mooring system. However, a small offset was observed in the pitch response, which is assumed to be caused by differences in numerical and experimental platform geometry. As a result, maximum relative water levels measured around the substructure and in the moonpool were underpredicted in CFD but matched in phase and frequency. Wave run-up at the TP was not discovered, however, green water was present and the front of the substructure was submerged regularly. Unfortunately, stability problems were encountered in CFD for parallel solver runs if a portion of a partition boundary was aligned with the free surface. Robustness was increased by implementation of additional parameters for solver control and alteration of the partitioning method.

### 6.3 Extreme Environmental Conditions

Evaluation of deterministic, extreme environmental conditions was performed to limit the computational resources. Simulation of turbulent wind and irregular waves would require very long run times of several weeks with the applied MBS-CFD simulation environment to achieve statistically relevant timescales. Design Load Case (DLC) 6.1 of IEC 61400-3-1 for parked design situation was adapted and a phase-focused wave group with  $H_{\max 50} > 16$  m and  $T_p = 16$  s was generated in CFD at full scale. It was based on metocean conditions with a return period of 50 years and water depth of 32 m, representative for the reference site SEM-REV, where the FLOATGEN demonstrator is installed. The wave propagation direction was collinear with the wind direction, which is most likely a conservative assumption with respect to the level of utilisation and the damage. A steady Extreme Wind Speed Model (EWM) with a return period of 50 years, vertical shear and reference wind speed of  $u_{\text{ref}} = 50 \text{ m s}^{-1}$  was used for computation of aerodynamic loads on the flexible rotor blades by Blade Element Momentum (BEM) theory modelled in SIMPACK's implementation of AeroDyn by National Renewable Energy Laboratory (NREL). Additional dynamic wind drag forces on the flexible tower were taken into account by a user-defined force element.

Two model variations with increasing level of fidelity were analysed. First, extreme wave-only conditions for a reduced MBS model of the FLOATGEN prototype were simulated, based on the numerical setup from the free-decay tests. Afterwards, extreme wave and wind conditions were investigated with a more complex model of a fully resolved MBS representation, based on a generic 2.2 MW wind turbine with modified tower to account for the TP. The MBS models for wave only and combined wind-wave conditions were characterised by the same physical properties of total mass, moments of inertia and Centre of Gravity (COG) to achieve the same draft of the FOWT. Besides rigid body modes for platform surge, heave and pitch, the low speed shaft could rotate freely and the flexible rotor blades were fixed at  $90^\circ$  without controller.

Subsequent analysis showed that the platform surge was highly excited by extreme wave conditions leading to maximum excursions of 24 m, which represents 75 % of the site-specific water depth. This is explained by applying a simplified mooring system with linear force-displacement relationship. Its stiffness is not high enough to limit the surge excursion to one third of the water depth, which is common estimate for the design of FOWTs. However, the mooring system design is very site-specific and soft configurations can be advantageous with respect to costs. Furthermore, the maximum heave occurred when the focused wave crest passed the middle of the moonpool so that the platform was elevated. Maximum pitch was found slightly before the focus time when the steep wave induced a high pitching moment.

Significant wave run-up was observed at the TP of up to 80 % of its height with water flowing around the structure and back into the open ocean. The surface pressure was highest in the wave impact zone of the TP at 20 % of its height, whereas wall shear stress was two orders of

magnitude smaller with maximum values at the corner edges. However, integrated hydrodynamic forces are only influenced to a small extent by the wave impact at the TP because of the relative motion of the floating substructure. It can be beneficial that the floating substructure moves with the wave and therefore possibly experiences lower wave impact loads compared to bottom-fixed foundations. Further studies are required to verify this statement. While maximum longitudinal forces occurred slightly before the focus time when the wave steepness was high, maximum vertical forces were observed when green water washed over the deck.

Aerodynamic loads on the rotor and tower increased the platform pitch by  $1^\circ$  due to an additional pitching moment. Moreover, rotor thrust forces enlarged the maximum platform surge by 2 m, an increase of 5 %, while the heave is dominated by wave-induced motion. Wave run-up at the TP only extended up to 60 % of its height if extreme wind is considered due to the offset in platform pitch. But higher water velocities, surface pressures and wall shear stresses were induced at the TP caused by different wave crest development and wave breaking.

Moreover, the longitudinal displacements at the tower top were significantly smaller compared to the tower base, which also corresponds to the base of the TP. The reason is that the FOWT is characterised as a two-mass oscillator with a system of two free masses – RNA and floating substructure. The tower base is more likely to follow the wave motion because it is closer to the floating substructure. The tower top fore-aft deflection is insignificant for the stiff-stiff tower configuration. A different picture was obtained for the accelerations and inclinations as the tower top experiences higher maximum values in longitudinal direction of  $4 \text{ m s}^{-2}$  and pitch rotational displacement up to  $14^\circ$  compared to the tower base. With respect to the time of occurrence, maximum accelerations, tower base pitching moment and tower top fore-aft deflection were found in the vicinity of the focus time of the focused wave group. However, maximum inclinations and accelerations are still within indicative survival design margins of  $15^\circ$  and  $0.6g \approx 5.89 \text{ m s}^{-2}$  of a barge-type floating substructure. These values only provide first indications before detailed load calculations are carried out with engineering models on a site-specific basis to assess design driving load cases for ultimate and fatigue loads. As a result, different design conditions may even be more critical for the accelerations and loads. The steady extreme wind model represents a conservative modelling approach of the wind speed as the turbulent extreme wind model inherently includes fluctuations above the mean wind speed during gusts. For mechanical components involving oil, lubrication system and sealings, adjustments may be required if extreme accelerations or inclinations exceed limits. Less critical is electronic equipment with usually high design values for accelerations.

Generalisation of above findings for different floating substructure concepts is difficult because the characteristic dynamic behaviour is very design- and site-specific. Since the geometry of the floating substructure was in accordance with the FLOATGEN prototype, but with simplifications, the transfer of findings from this study to the real application at the offshore test site must be evaluated carefully. Definition of maximum excursions, which depend on the water

depth, is necessary for the design of dynamic power cables and to avoid clashing. Increased limits compared to those found in this study impose stricter requirements on the mooring system design. In addition, application of a deterministic focused wave group is common in experimental and numerical wave tank testing but it does not represent real open ocean conditions, which are stochastic in nature. However, the approach is well-suited for analysis of extreme conditions, for example, freak waves, which represent a real extreme wave event.

In conclusion, the presented MBS-CFD simulation environment successfully filled the gap between engineering models and experiments with an integrated, high-fidelity analysis of FOWTs. Furthermore, consideration of extreme wind loads increased the modelling effort considerably, but it was needed for reliable prediction of motion and loads. A decoupled approach, similar in model fidelity to the reduced MBS model, would already provide first estimates if platform dynamics are of main interest, but it was not found to be conservative for all sensors.

## 6.4 Recommendations

High-fidelity modelling using CFD in the context of FOWT may be employed in further research. The methodology offers the potential to complement experiments in a combined wind and wave basin to a certain extent because relevant effects can be taken into account. Investigation of the influence of geometric design variations is feasible with the proposed methodology already at full scale. Another application is the assessment of characteristic properties such as hydrodynamic damping and drag coefficients, which may be computed for a wide range of environmental conditions. Here, the CFD solver should be applied standalone to avoid a limitation to first-order temporal discretisation and increased numerical damping. Even automatic processing of different geometries with increased parametrisation in CFD is possible. Finally, evaluation of extreme environmental conditions is very promising and provides insight into the prediction of extreme loads and associated dynamic motions.

Furthermore, discrepancies found for surge free-decay should be investigated by modelling of a different wave basin test. Depending on the number of experimental data sets and their quality, the six Degrees of Freedom (DOFs) of the platform motion should be considered to improve comparability with the experiment. Additional regular wave tests without green water should be analysed to understand the differences in relative wave elevation sensors. More important is the implementation of an accurate mooring system in the MBS to improve the results. This can be achieved using a dynamic mooring model, because a simplified approach cannot capture the large displacement effects at extreme conditions.

For modelling of extreme wave conditions, not only the maximum wave height should be taken into account but also the wave period at the platform pitch and heave natural periods to evaluate potential resonance effects. Moreover, relevance of modelled wave conditions could be improved by blending of an extreme wave with an irregular sea state (constrained NewWave).



# A

Appendix

## A.1 Derivation of Mesh Deformation Transition Function

In case of non-concentric ellipsoids applied for the mesh deformation transition function, Equation 3.25 with  $m_y = 0$  is solved analytically for the radius  $r$  using MATLAB's symbolic equation and system solver. After transformation of Equation 3.25 a function of  $r$  is obtained:

$$F(r) = \left( \frac{x - x_{m,1} - m_x(r - r_1)}{a} \right)^2 + \left( \frac{y - y_{m,1}}{b} \right)^2 + \left( \frac{z - z_{m,1} - m_z(r - r_1)}{c} \right)^2 - r^2 \quad (\text{A.1})$$

$$== 0.$$

On this basis, the analytical solution of the radius is:

$$r = \left[ bc^2m_x x - ac \right. \\ \left( a^2b^2m_z^2r_1^2 + 2a^2b^2m_zr_1z - 2a^2b^2m_zr_1z_{m,1} + a^2b^2z^2 - 2a^2b^2zz_{m,1} + a^2b^2z_{m,1}^2 \right. \\ \left. + a^2c^2x^2 - 2a^2c^2xy_{m,1} + a^2c^2y_{m,1}^2 - a^2m_z^2x^2 + 2a^2m_z^2xy_{m,1} - a^2m_z^2y_{m,1}^2 \right. \\ \left. + b^2c^2m_x^2r_1^2 + 2b^2c^2m_xr_1x - 2b^2c^2m_xr_1x_{m,1} + b^2c^2x^2 - 2b^2c^2xx_{m,1} + b^2c^2x_{m,1}^2 \right. \\ \left. - b^2m_x^2z^2 + 2b^2m_x^2zz_{m,1} - b^2m_x^2z_{m,1}^2 + 2b^2m_xm_zxz - 2b^2m_xm_zxz_{m,1} \right. \\ \left. - 2b^2m_xm_zx_{m,1}z + 2b^2m_xm_zx_{m,1}z_{m,1} - b^2m_z^2x^2 + 2b^2m_z^2xx_{m,1} - b^2m_z^2x_{m,1}^2 \right. \\ \left. - c^2m_x^2x^2 + 2c^2m_x^2xy_{m,1} - c^2m_x^2y_{m,1}^2 \right]^{1/2} \\ - bc^2m_x x_{m,1} + a^2bm_z z - a^2bm_z z_{m,1} + a^2bm_z^2 r_1 + bc^2m_x^2 r_1) \\ \left[ b \left( -a^2c^2 + a^2m_z^2 + c^2m_x^2 \right) \right]^{-1}.$$
(A.2)

Finally, Equation A.2 is used as input for the mesh deformation transition function  $f_D$  in Equation 3.24 to calculate the mesh deformation limiter  $D$  in Equation 3.22.

## A.2 Comparison of Influence of Time Stepping Scheme

In general, numerical integration is characterised by the order of accuracy, which quantifies how a numerical approximation  $Q_h$  improves if spatial or temporal discretisation is refined [190,191]. In particular, the order of accuracy indicates the rate of convergence of a differential equation to the exact solution  $Q$ . The big O notation is used in the following mathematical formulation to define the numerical order of accuracy  $k$ :

$$|Q - Q_h| = \mathcal{O}(h^k) \quad (\text{A.3})$$

with the characteristic parameter  $h$ , which describes, for example, the step size in a finite difference scheme of a numerical approximation. The higher the numerical order of accuracy  $k$ , the faster the numerical error reduces if  $h$  tends towards zero. Moreover, the order of accuracy does not give the magnitude of the numerical error for a given  $h$ , but rather indicates that if  $h$  is reduced, the results improve proportionally to  $h^k$ .

To identify the implications of numerical settings on the damping behaviour, a comparison is made for a two-dimensional NWT with first- and second-order temporal discretisation. For the applied CFD solver, this setting is distinguished by selecting either first- or second-order Backward Euler transient scheme. A mesh using  $N_\lambda = 40$  and  $N_H = 120$  is used in combination with the SST turbulence model and a time step of  $t_{\text{step}} = T/100$ . A snapshot of the NWT, in a similar way as for to sensitivity studies in Section 3.4, is presented in Figure A.1 together with quantification of numerical damping in Table A.1. Damping is assessed according to the Equation 3.32.

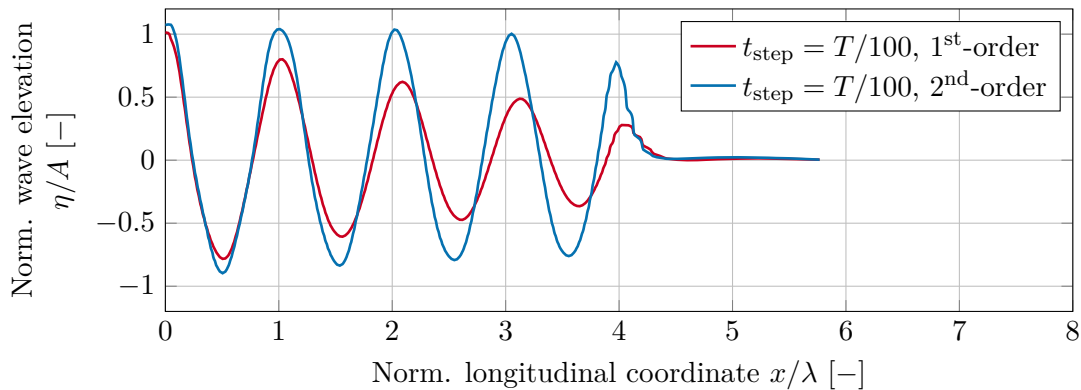


**Figure A.1:** Series of lines showing the normalised wave elevation over the normalised longitudinal coordinate with the variation of the order of time stepping scheme.

As expected, the damping ratio of the first-order solution is much higher than for the second-order solution at equal time step size. In addition, the magnitude of damping of the first-order Backward Euler time stepping scheme at  $T/100$  compares to the second-order temporal discretisation at  $t_{\text{step}} = T/25$ , see Table 3.3. Thus, a significantly higher temporal resolution

and also higher computational resources are needed for a first-order time stepping scheme to achieve comparable results of a second-order solution. Unfortunately, the fluid solver of the implicit MBS-CFD coupling methodology, introduced in Section 3.2, is limited to first-order Backward Euler time stepping scheme for the reasons explained in Section 4.4.2.2.

**Table A.1:** Damping ratios for the two-dimensional regular wave in relation to the time stepping scheme.

<b>Time stepping scheme</b>	1 <sup>st</sup> -order	2 <sup>nd</sup> -order
<b>Damping ratio <math>D</math> [%]</b>	3.94	0.29

### A.3 Maxima and Time of Occurrence for Extreme Wave Analysis

Table A.2 shows the maximum values of the platform motion, the integrated forces on the structure and the reference wave elevation according to the time of occurrence  $t/t_f$ . The values are sorted in ascending order by time and the associated Figure showing the visualisation of the flow field is referenced.

**Table A.2:** Overview of the maximum positive and negative properties and the corresponding Figures showing the flow field visualisation for the focused wave case EXT3000. A star symbol indicates Figures, which are not exactly at the instance in time given in column  $t/t_f$ , but very close to it. Values are sorted by the time of occurrence.

Property	Symbol	Sign of Maxima	$t/t_f$ [-]	Figure
Reference wave probe	$WP_{\text{ref}}$	-	0.9283	
Vertical force	$F_z$	+	0.9667	5.10a*
Longitudinal force	$F_x$	+	0.9800	5.10b*
Reference wave probe	$WP_{\text{ref}}$	+	0.9917	5.10d*
Pitch rotational displacement	$\psi$	+	0.9917	5.10d*
Wave approaches TP			1.0100	5.10f
Heave translational displacement	$z$	+	1.0167	5.10g*
Vertical force	$F_z$	-	1.0267	5.10h
Longitudinal force	$F_x$	-	1.0383	5.10i*
Surge translational displacement	$x$	+	1.0467	5.10j*
Pitch rotational displacement	$\psi$	-	1.0483	5.10k*
Reference wave probe	$WP_{\text{ref}}$	-	1.0617	5.10l*
Vertical force	$F_z$	+	1.0800	5.10n*
Heave translational displacement	$z$	-	1.0900	5.10p
Pitch rotational displacement	$\psi$	+	1.1350	
Surge translational displacement	$x$	-	1.2817	
Pitch rotational displacement	$\psi$	+	1.2850	



# Bibliography

- [1] L. Ramírez, D. Fraile, and G. Brindley, “Offshore Wind in Europe, Key trends and statistics 2019,” WindEurope, Brussels, Tech. rep., 2020. URL <https://windeurope.org/about-wind/statistics/offshore/european-offshore-wind-industry-key-trends-statistics-2019/>
- [2] F. Selot, D. Fraile, G. Brindley, and C. Walsh, “Offshore Wind in Europe, Key trends and statistics 2018,” WindEurope, Brussels, Tech. rep., 2019. URL <https://windeurope.org/about-wind/statistics/offshore/european-offshore-wind-industry-key-trends-statistics-2018/>
- [3] A. Arapogianni and A.-B. Genachte, “Deep Water - The next step for offshore wind energy,” European Wind Energy Association, Brussels, Tech. rep., 2013. URL <https://windeurope.org/about-wind/reports/deep-water/>
- [4] J. Murphy, K. Lynch, L. Serri, D. Airdoldi, and M. Lopes, “Site selection Analysis for offshore combined Resource Projects in Europe,” European Commission, ORECCA project, Tech. rep., 2011. URL [https://orecca.rse-web.it/doc\\_info/Site\\_Selection\\_Analysis\\_Report.pdf](https://orecca.rse-web.it/doc_info/Site_Selection_Analysis_Report.pdf)
- [5] D. Gielen, R. Gorini, G. Prakash, H. Anuta, N. Wagner, and G. Gallina, “Future of wind: Deployment, investment, technology, grid integration and socio-economic aspects,” International Renewable Energy Agency, Abu Dhabi, Tech. rep., 2019.
- [6] L. Cozzi, B. Wanner, C. Donovan, A. Toril, and W. Yu, “Offshore Wind Outlook 2019: World Energy Outlook Special Report,” International Energy Agency, Paris, Tech. rep., 2019. URL <https://www.iea.org/reports/offshore-wind-outlook-2019>
- [7] F. Borisade, J. Bhat, and D. Matha, “Deliverable D5.5 Overall summary of the industrialization process,” European Commission, LIFES50+ project, Tech. rep., 2019. URL [https://lifes50plus.eu/wp-content/uploads/2019/05/GA\\_640741\\_LIFES50\\_D5.5.pdf](https://lifes50plus.eu/wp-content/uploads/2019/05/GA_640741_LIFES50_D5.5.pdf)
- [8] IEC, *IEC 61400-3-1, Edition 1.0, 2019-04, Wind energy generation systems - Part 3-1: Design requirements for fixed offshore wind turbines*. Geneva: International Electrotechnical Commission, 2019.

- [9] K. Müller, F. Lemmer, F. Borisade, M. Kretschmer, J. Gruber, L. Hagemann, N.-D. Nguyen, and L. Vita, “Deliverable D7.4 State-of-the-Art FOWT design practice and guidelines,” European Commission, LIFES50+ project, Tech. rep., 2016. URL [https://lifes50plus.eu/wp-content/uploads/2015/11/GA\\_640741\\_LIFES50\\_D7.4.pdf](https://lifes50plus.eu/wp-content/uploads/2015/11/GA_640741_LIFES50_D7.4.pdf)
- [10] A. Pegalajar-Jurado, F. J. Madsen, H. Sarlak, H. Bredmose, F. Lemmer, R. Faerron-Guzman, F. Borisade, and M. Kretschmer, “Deliverable D4.8 Validation of advanced models and methods for cascading into simpler models,” European Commission, LIFES50+ project, Tech. rep., 2018. URL [https://lifes50plus.eu/wp-content/uploads/2019/01/GA\\_640741\\_LIFES50\\_D4.8-.pdf](https://lifes50plus.eu/wp-content/uploads/2019/01/GA_640741_LIFES50_D4.8-.pdf)
- [11] F. J. Madsen, A. Pegalajar-Jurado, H. Bredmose, M. Borg, K. Müller, and D. Matha, “Deliverable D7.8 Required numerical model fidelity in various design phases,” European Commission, LIFES50+ project, Tech. rep., 2018. URL [https://lifes50plus.eu/wp-content/uploads/2018/07/D78-GA\\_640741.pdf](https://lifes50plus.eu/wp-content/uploads/2018/07/D78-GA_640741.pdf)
- [12] E. Ferrer and A. Montlaur, *CFD for Wind and Tidal Offshore Turbines*, ser. Springer Tracts in Mechanical Engineering, E. Ferrer and A. Montlaur, Eds. Cham: Springer, 2015.
- [13] E. Ferrer and A. Montlaur, *Recent Advances in CFD for Wind and Tidal Offshore Turbines*, ser. Springer Tracts in Mechanical Engineering, E. Ferrer and A. Montlaur, Eds. Cham: Springer, 2019.
- [14] H. Bredmose and N. G. Jacobsen, “Vertical Wave Impacts on Offshore Wind Turbine Inspection Platforms,” in *Proceedings of the ASME 2011 30th International Conference on Ocean, Offshore and Arctic Engineering*. Rotterdam: American Society of Mechanical Engineers, 2011.
- [15] A. Ghadirian, H. Bredmose, and M. Dixen, “Breaking phase focused wave group loads on offshore wind turbine monopiles,” *Journal of Physics: Conference Series*, vol. 753, no. 9, 2016.
- [16] B. T. Paulsen, H. Bredmose, H. B. Bingham, and S. Schløer, “Steep Wave Loads From Irregular Waves on an Offshore Wind Turbine Foundation: Computation and Experiment,” in *Proceedings of the ASME 2013 32nd International Conference on Ocean, Offshore and Arctic Engineering*. Nantes: American Society of Mechanical Engineers, 2013.
- [17] B. T. Paulsen, H. Bredmose, H. B. Bingham, and N. G. Jacobsen, “Forcing of a bottom-mounted circular cylinder by steep regular water waves at finite depth,” *Journal of Fluid Mechanics*, vol. 755, pp. 1–34, September 2014.
- [18] A. Hildebrandt, “Hydrodynamics of Breaking Waves on Offshore Wind Turbine Structures,” Ph.D. dissertation, Gottfried Wilhelm Leibniz Universität Hannover, 2013.



- [19] F. Beyer, M. Arnold, and P. W. Cheng, “Analysis of Floating Offshore Wind Turbine Hydrodynamics using coupled CFD and Multibody Methods,” in *Proceedings of the 23rd International Offshore and Polar Engineering Conference*. Anchorage: International Society of Offshore and Polar Engineers, 2013.
- [20] J. Morison, J. Johnson, and S. Schaaf, “The Force Exerted by Surface Waves on Piles,” *Journal of Petroleum Technology*, vol. 2, no. 05, pp. 149–154, May 1950.
- [21] F. Lemmer, *Low-Order Modeling, Controller Design and Optimization of Floating Offshore Wind Turbines*. München: Verlag Dr. Hut, 2018, Ph.D. dissertation.
- [22] DNV, *DNV-RP-C205: Environmental conditions and environmental loads*. Høvik: Det Norske Veritas, 2019, no. December.
- [23] T. Sarpkaya and M. Isaacson, *Mechanics of Wave Forces on Offshore Structures*. Van Nostrand Reinhold Company, 1981.
- [24] F. Beyer, T. Choynet, M. Kretschmer, and P. W. Cheng, “Coupled MBS-CFD Simulation of the IDEOL Floating Offshore Wind Turbine Foundation Compared to Wave Tank Model Test Data,” in *Proceedings of the 25th International Offshore and Polar Engineering Conference*. Kona: International Society of Offshore and Polar Engineers, 2015.
- [25] F. Borisade, T. Choynet, and P. W. Cheng, “Design study and full scale MBS-CFD simulation of the IDEOL floating offshore wind turbine foundation,” *Journal of Physics: Conference Series*, vol. 753, no. 9, 2016.
- [26] W. Yu, K. Müller, and F. Lemmer, “Deliverable D4.2 Public Definition of the Two LIFES50+ 10MW Floater Concepts,” European Commission, LIFES50+ project, Tech. rep., 2018. URL [https://lifes50plus.eu/wp-content/uploads/2018/04/GA\\_640741\\_LIFES50\\_D4.2.pdf](https://lifes50plus.eu/wp-content/uploads/2018/04/GA_640741_LIFES50_D4.2.pdf)
- [27] M. Benitz, “Simulating the Hydrodynamics of Offshore Floating Wind Turbine Platforms in a Finite Volume Framework,” Ph.D. dissertation, University of Massachusetts Amherst, 2016.
- [28] A. Robertson, J. Jonkman, M. Masciola, H. Song, A. Goupee, A. Coulling, and C. Luan, “Definition of the Semisubmersible Floating System for Phase II of OC4,” National Renewable Energy Laboratory, Tech. rep. NREL/TP-5000-60601, 2014.
- [29] H. Sarlak, A. Pegalajar-Jurado, and H. Bredmose, “CFD Simulations of a newly developed floating offshore wind turbine platform using OpenFOAM,” in *Proceedings of the 21st Australasian Fluid Mechanics Conference*, Adelaide, 2018.
- [30] M. Borg, A. Pegalajar-Jurado, H. Sarlak, F. J. Madsen, H. Bredmose, F. Lemmer, and F. Borisade, “Deliverable D4.7 Models for advanced load effects and loads at component level,” European Commission, LIFES50+ project, Tech. rep., 2018. URL [https://lifes50plus.eu/wp-content/uploads/2018/06/D4.7-GA\\_640741\\_LIFES50.pdf](https://lifes50plus.eu/wp-content/uploads/2018/06/D4.7-GA_640741_LIFES50.pdf)

- [31] A. J. Dunbar, B. A. Craven, and E. G. Paterson, “Development and validation of a tightly coupled CFD/6-DOF solver for simulating floating offshore wind turbine platforms,” *Ocean Engineering*, vol. 110, pp. 98–105, December 2015.
- [32] S. Quallen, T. Xing, P. Carrica, Y. Li, and J. Xu, “CFD Simulation of a Floating Offshore Wind Turbine System Using a Quasi-Static Crowfoot Mooring-Line Model,” in *Proceedings of the 23rd International Offshore and Polar Engineering Conference*. Anchorage: International Society of Offshore and Polar Engineers, 2013.
- [33] J. Jonkman and W. Musial, “Offshore Code Comparison Collaboration (OC3) for IEA Task 23 Offshore Wind Technology and Deployment,” National Renewable Energy Laboratory, Tech. rep. NREL/TP-5000-48191, 2010.
- [34] A. N. Robertson, F. Wendt, J. M. Jonkman, W. Popko, H. Dagher, S. Gueydon, J. Qvist, F. Vittori, J. Azcona, E. Uzunoglu, C. G. Soares, R. Harries, A. Yde, C. Galinos, K. Hermans, J. B. De Vaal, P. Bozonnet, L. Bouy, I. Bayati, R. Bergua, J. Galvan, I. Mendikoa, C. B. Sanchez, H. Shin, S. Oh, C. Molins, and Y. Debruyne, “OC5 Project Phase II: Validation of Global Loads of the DeepCwind Floating Semisubmersible Wind Turbine,” *Energy Procedia*, vol. 137, pp. 38–57, 2017.
- [35] A. N. Robertson, S. Gueydon, E. Bachynski, L. Wang, J. Jonkman, D. Alarcón, E. Amet, A. Beardsell, P. Bonnet, B. Boudet, C. Brun, Z. Chen, M. Féron, D. Forbush, C. Galinos, J. Galvan, P. Gilbert, J. Gómez, V. Harnois, F. Haudin, Z. Hu, J. L. Dreff, M. Leimeister, F. Lemmer, H. Li, G. McKinnon, I. Mendikoa, A. Moghtadaei, S. Netzband, S. Oh, A. Pegalajar-Jurado, M. Q. Nguyen, K. Ruehl, P. Schünemann, W. Shi, H. Shin, Y. Si, F. Surmont, P. Trubat, J. Qvist, and S. Wohlfahrt-Laymann, “OC6 Phase I: Investigating the underprediction of low-frequency hydrodynamic loads and responses of a floating wind turbine,” *Journal of Physics: Conference Series*, vol. 1618, no. 3, 2020.
- [36] L. Wang, A. Robertson, J. Jonkman, J. Kim, Z. R. Shen, A. Koop, A. B. Nadal, W. Shi, X. Zeng, E. Ransley, S. Brown, M. Hann, P. Chandramouli, A. Viré, L. R. Reddy, X. Li, Q. Xiao, B. M. López, G. C. Alonso, S. Oh, H. Sarlak, S. Netzband, H. Jang, and K. Yu, “OC6 Phase Ia: CFD Simulations of the Free-Decay Motion of the DeepCwind Semisubmersible,” *Energies*, vol. 15, no. 1, 2022.
- [37] M. Arnold, *Simulation and Evaluation of the Hydroelastic Responses of a Tidal Current Turbine*. München: Verlag Dr. Hut, 2016, Ph.D. dissertation.
- [38] K. E. Steen, “Hywind Scotland - Status and plans,” in *EERA DeepWind 2015*, 2015.
- [39] B. Skaare, F. G. Nielsen, T. D. Hanson, R. Yttervik, O. Havmøller, and A. Rekdal, “Analysis of measurements and simulations from the Hywind Demo floating wind turbine,” *Wind Energy*, vol. 18, no. 6, pp. 1105–1122, June 2015.
- [40] F. Driscoll, J. Jonkman, A. Robertson, S. Srinivas, B. Skaare, and F. G. Nielsen, “Validation of a FAST Model of the Statoil-hywind Demo Floating Wind Turbine,” *Energy Procedia*, vol. 94, no. January, pp. 3–19, 2016.

- [41] D. Roddier, C. Cermelli, A. Aubault, and A. Peiffer, “Summary and Conclusions of the Full Life-Cycle of the WindFloat FOWT Prototype Project,” in *Proceedings of the ASME 2017 36th International Conference on Ocean, Offshore and Arctic Engineering*. Trondheim: American Society of Mechanical Engineers, 2017.
- [42] T. Choisnet, M. Favré, M. Lyubimova, and E. Rogier, “A Robust Concrete Floating Wind Turbine Foundation for Worldwide Applications,” in *Proceedings of the 9th Grand Renewable Energy Conference*, Tokyo, 2014.
- [43] T. Choisnet, B. Geschier, and G. Vetrano, “Initial Comparison of Concrete and Steel Hulls in the Case of Ideol’s Square Ring Floating Substructure,” in *Proceedings of the 15th World Wind Energy Conference and Exhibition*, Tokyo, 2016.
- [44] T. Choisnet, S. Vasseur, and E. Rogier, “Performance and Mooring Qualification in Floatgen: The First French Offshore Wind Turbine Project,” in *Proceedings of the 13th Grand Renewable Energy Conference*, Pacifico Yokohama, 2018.
- [45] T. Choisnet, E. Rogier, Y. Percher, A. Courbois, I. L. E. Crom, and R. Mariani, “Performance and Mooring Qualification in Floatgen: The First French Offshore Wind Turbine Project,” in *Proceedings of the 16th Journées de l’Hydrodynamique (JH2018)*, Marseille, 2018.
- [46] A. Alexandre, Y. Percher, T. Choisnet, R. Buils Urbano, and R. Harries, “Coupled Analysis and Numerical Model Verification for the 2MW Floatgen Demonstrator Project With IDEOL Platform,” in *Proceedings of the ASME 2018 1st International Offshore Wind Technical Conference*. San Francisco: American Society of Mechanical Engineers, 2018.
- [47] N. Jestin, P. Modiano, R. Bigard, C. Cremona, and B. Dumas, “FLOATGEN – Design and Construction of the First Floating Wind Turbine in France,” in *Proceedings of the 40th IABSE Symposium, Tomorrow’s Megastructures*, Nantes, 2018.
- [48] A. Courbois, E. Tcheuko, B. Bouscasse, Y. Choi, O. Kimmoun, and R. Mariani, “Study of Viscous Effects on Wave Drift Forces on a Rectangular Pontoon With a Damping Plate by Using CFD Code OpenFOAM,” in *Proceedings of the ASME 2018 37th International Conference on Ocean, Offshore and Arctic Engineering*. Madrid: American Society of Mechanical Engineers, jun 2018.
- [49] J. Cruz and M. Atcheson, *Floating Offshore Wind Energy*, ser. Green Energy and Technology, J. Cruz and M. Atcheson, Eds. Cham: Springer, 2016.
- [50] R. James and M. C. Ros, “Floating Offshore Wind: Market and Technology Review,” The Carbon Trust, London, Tech. rep., 2015. URL <https://www.carbontrust.com/resources/floating-offshore-wind-market-technology-review>
- [51] W. Musial, P. Beiter, P. Schwabe, T. Tian, T. Stehly, and P. Spitsen, “2016 Offshore Wind Technologies Market Report,” U.S. Department of Energy, Tech. rep., 2017. URL <https://www.energy.gov/eere/wind/downloads/2016-offshore-wind-technologies-market-report>

- [52] P. Beiter, P. Spitsen, J. Nunemaker, T. Tian, W. Musial, and E. Lantz, “2017 Offshore Wind Technologies Market Update,” U.S. Department of Energy, Tech. rep., 2018. URL <https://www.energy.gov/eere/wind/downloads/2017-offshore-wind-technologies-market-update>
- [53] WindEurope, “Floating Offshore Wind Vision Statement,” WindEurope, Tech. rep., 2017. URL <https://windeurope.org/about-wind/reports/floating-vision-statement/>
- [54] B. T. Pereyra, Z. Jiang, Z. Gao, M. T. Andersen, and H. Stiesdal, “Parametric Study of a Counter Weight Suspension System for the TetraSpar Floating Wind Turbine,” in *Proceedings of the ASME 2018 1st International Offshore Wind Technical Conference*. San Francisco: American Society of Mechanical Engineers, 2018.
- [55] M. T. Andersen, A. Tetu, and H. Stiesdal, “Economic Potential of Industrializing Floating Wind Turbine Foundations,” in *Proceedings of the ASME 2018 37th International Conference on Ocean, Offshore and Arctic Engineering*. Madrid: American Society of Mechanical Engineers, 2018.
- [56] A. Pegalajar-Jurado, F. J. Madsen, and H. Bredmose, “Damping Identification of the TetraSpar Floater in Two Configurations With Operational Modal Analysis,” in *Proceedings of the ASME 2019 2nd International Offshore Wind Technical Conference*. St. Julian’s: American Society of Mechanical Engineers, 2019.
- [57] M. Borg, A. Viselli, C. K. Allen, M. Fowler, C. Sigshøj, A. Grech La Rosa, M. T. Andersen, and H. Stiesdal, “Physical Model Testing of the TetraSpar Demo Floating Wind Turbine Prototype,” in *Proceedings of the ASME 2019 2nd International Offshore Wind Technical Conference*. St. Julian’s: American Society of Mechanical Engineers, 2019.
- [58] F. Lemmer, W. Yu, D. Schlipf, and P. W. Cheng, “Robust gain scheduling baseline controller for floating offshore wind turbines,” *Wind Energy*, no. June 2019, pp. 17–30, 2019.
- [59] T. J. Larsen and T. D. Hanson, “A method to avoid negative damped low frequent tower vibrations for a floating, pitch controlled wind turbine,” *Journal of Physics: Conference Series*, vol. 75, no. 1, p. 012073, July 2007.
- [60] J. Jonkman, “Influence of Control on the Pitch Damping of a Floating Wind Turbine,” in *Proceedings of the 46th AIAA Aerospace Sciences Meeting and Exhibit*. Reno: American Institute of Aeronautics and Astronautics, 2008.
- [61] P. A. Fleming, I. Pineda, M. Rossetti, A. D. Wright, and D. Arora, “Evaluating Methods for Control of an Offshore Floating Turbine,” in *Proceedings of the ASME 2014 33rd International Conference on Ocean, Offshore and Arctic Engineering*. San Francisco: American Society of Mechanical Engineers, 2014.
- [62] F. Savenije and J. Peeringa, “Control development for floating wind,” *Journal of Physics: Conference Series*, vol. 524, no. 1, p. 012090, June 2014.

- [63] DNV GL, *DNV-RP-0286: Coupled analysis of floating wind turbines*. Høvik: Det Norske Veritas, 2019, no. May.
- [64] P. Gujer and M. Kretschmer, “Deliverable D7.1 Review of FOWT guidelines and design practice,” European Commission, LIFES50+ project, Tech. rep., 2015. URL [https://lifes50plus.eu/wp-content/uploads/2015/12/GA\\_640741\\_LIFES50plus\\_D7.1.pdf](https://lifes50plus.eu/wp-content/uploads/2015/12/GA_640741_LIFES50plus_D7.1.pdf)
- [65] K. Müller, R. Faerron-Guzmán, S. Zhou, M. Lerch, R. Proskovics, G. Pérez, I. Medikoa, D. Matha, F. Borisade, J. Bhat, R. Scheffler, M. Thys, H. Bredmose, F. J. Madsen, and A. Pegalajar-Jurado, “Deliverable D7.11 Design Practice for 10MW+ FOWT Support Structures,” European Commission, LIFES50+ project, Tech. rep., 2019. URL [https://lifes50plus.eu/wp-content/uploads/2019/05/GA\\_640741\\_LIFES50\\_D7.11.pdf](https://lifes50plus.eu/wp-content/uploads/2019/05/GA_640741_LIFES50_D7.11.pdf)
- [66] IEC, *IEC 61400-3-2, Edition 1.0, 2019-04, Wind energy generation systems - Part 3-2: Design requirements for floating offshore wind turbines*. Geneva: International Electrotechnical Commission, 2019.
- [67] IEC, *IEC 61400-1, Edition 4.0, 2019-02, Wind energy generation systems - Part 1: Design requirements*. Geneva: International Electrotechnical Commission, 2019.
- [68] DNV, *DNV-ST-0119: Floating wind turbine structures*. Høvik: Det Norske Veritas, 2021, no. June.
- [69] DNV, *DNV-ST-0126: Support structures for wind turbines*. Høvik: Det Norske Veritas, 2018, no. July.
- [70] DNV, *DNV-ST-0437: Loads and site conditions for wind turbines*. Høvik: Det Norske Veritas, 2016, no. November.
- [71] DNV, *DNV-SE-0422: Certification of floating wind turbines*. Høvik: Det Norske Veritas, 2018, no. July.
- [72] D. Matha, M. Schlipf, and R. Pereira, “Challenges in Simulation of Aerodynamics , Hydrodynamics , and Mooring-Line Dynamics of Floating Offshore Wind Turbines,” in *Proceedings of the 21st International Offshore and Polar Engineering Conference*. Maui: International Society of Offshore and Polar Engineers, 2011.
- [73] M. Borg and H. Bredmose, “Deliverable D4.4 Overview of the numerical models used in the consortium and their qualification,” European Commission, LIFES50+ project, Tech. rep., 2015. URL [https://lifes50plus.eu/wp-content/uploads/2015/12/GA\\_640741\\_LIFES50-\\_D4.4.pdf](https://lifes50plus.eu/wp-content/uploads/2015/12/GA_640741_LIFES50-_D4.4.pdf)

- [74] A. Robertson, J. Jonkman, F. Vorpahl, W. Popko, J. Qvist, L. Frøyd, X. Chen, J. Azcona, E. Uzunoglu, C. Guedes Soares, C. Luan, H. Yutong, F. Pengcheng, A. Yde, T. Larsen, J. Nichols, R. Buils, L. Lei, T. A. Nygaard, D. Manolas, A. Heege, S. R. Vatne, H. Ormberg, T. Duarte, C. Godreau, H. F. Hansen, A. W. Nielsen, H. Riber, C. Le Cunff, F. Beyer, A. Yamaguchi, K. J. Jung, H. Shin, W. Shi, H. Park, M. Alves, and M. Guérinel, “Offshore Code Comparison Collaboration Continuation Within IEA Wind Task 30: Phase II Results Regarding a Floating Semisubmersible Wind System,” in *Proceedings of the ASME 2014 33rd International Conference on Ocean, Offshore and Arctic Engineering*. San Francisco: American Society of Mechanical Engineers, 2014.
- [75] K. Müller, R. Faerron-Guzmán, M. Borg, and A. Manjock, “Deliverable D7.7 Identification of critical environmental conditions and design load cases,” European Commission, LIFES50+ project, Tech. rep., 2018. URL [https://lifes50plus.eu/wp-content/uploads/2018/07/GA\\_640741\\_LIFES50\\_D7.7.pdf](https://lifes50plus.eu/wp-content/uploads/2018/07/GA_640741_LIFES50_D7.7.pdf)
- [76] C. Woernle, *Mehrkörpersysteme*. Berlin, Heidelberg: Springer Vieweg, 2016.
- [77] W. Schiehlen and P. Eberhard, *Technische Dynamik*. Wiesbaden: Springer Vieweg, 2017.
- [78] R. Schwertassek and O. Wallrapp, *Dynamik flexibler Mehrkörpersysteme*. Wiesbaden: Vieweg, 1999.
- [79] P. Wriggers, *Nonlinear Finite Element Methods*. Berlin, Heidelberg: Springer, 2008.
- [80] O. Zienkiewicz, R. Taylor, and J. Zhu, *The Finite Element Method: Its Basis and Fundamentals*, 7th ed. Oxford: Butterworth-Heinemann, 2013.
- [81] A. Pegalajar-Jurado, M. Borg, and H. Bredmose, “An efficient frequency-domain model for quick load analysis of floating offshore wind turbines,” *Wind Energy Science*, vol. 3, no. 2, pp. 693–712, October 2018.
- [82] M. Borg, H. Bredmose, and A. M. Hansen, “Elastic Deformations of Floaters for Offshore Wind Turbines: Dynamic Modelling and Sectional Load Calculations,” in *Proceedings of the ASME 2017 36th International Conference on Ocean, Offshore and Arctic Engineering*. Trondheim: American Society of Mechanical Engineers, 2017.
- [83] NREL, “OpenFAST Documentation - Release v3.1.0,” National Renewable Energy Laboratory, Tech. rep., 2022. URL <http://openfast.readthedocs.io/>
- [84] Q. Wang, M. A. Sprague, J. Jonkman, N. Johnson, and B. Jonkman, “BeamDyn: a high-fidelity wind turbine blade solver in the FAST modular framework,” *Wind Energy*, vol. 20, no. 8, pp. 1439–1462, August 2017.
- [85] S. Guntur, J. Jonkman, R. Sievers, M. A. Sprague, S. Schreck, and Q. Wang, “A validation and code-to-code verification of FAST for a megawatt-scale wind turbine with aeroelastically tailored blades,” *Wind Energy Science*, vol. 2, no. 2, pp. 443–468, August 2017.

- [86] B. Luhmann and P. W. Cheng, “Fatigue and extreme load reduction on two-bladed wind turbines using the flexible hub connection,” *Wind Energy*, no. January 2019, pp. 1–16, 2019.
- [87] J. F. Manwell, J. G. McGowan, and A. L. Rogers, *Wind Energy Explained*. Chichester: Wiley, 2009.
- [88] M. O. L. Hansen, *Aerodynamics of Wind Turbines*, 2nd ed. London: Earthscan, 2008.
- [89] P. J. Moriarty and A. C. Hansen, “AeroDyn Theory Manual,” National Renewable Energy Laboratory, Golden, Tech. rep. NREL/TP-500-36881, 2005.
- [90] M. R. Dhanak and N. I. Xiros, *Springer Handbook of Ocean Engineering*, ser. Green Energy and Technology, M. R. Dhanak and N. I. Xiros, Eds. Cham: Springer, 2016.
- [91] D. Matha, *Impact of Aerodynamics and Mooring System on Dynamic Response of Floating Wind Turbines*. München: Verlag Dr. Hut, 2016, Ph.D. dissertation.
- [92] L. Klein, C. Schulz, T. Lutz, and E. Krämer, “Influence of jet flow on the aerodynamics of a floating model wind turbine,” in *Proceedings of the 26th International Ocean and Polar Engineering Conference*. Rhodes: International Society of Offshore and Polar Engineers, 2016.
- [93] L. Klein, J. Gude, F. Wenz, T. Lutz, and E. Krämer, “Advanced computational fluid dynamics (CFD) – multi-body simulation (MBS) coupling to assess low-frequency emissions from wind turbines,” *Wind Energy Science*, vol. 3, no. 2, pp. 713–728, October 2018.
- [94] J. G. Leishman, *Principles of Helicopter Aerodynamics*, 2nd ed. Cambridge: Cambridge University Press, 2006.
- [95] J. D. Anderson, *Fundamentals of Aerodynamics*, 5th ed. New York: McGraw-Hill, 2011.
- [96] T. Burton, N. Jenkins, D. Sharpe, and E. Bossanyi, *Wind Energy Handbook*. Chichester: Wiley, 2011.
- [97] T. Sebastian, “The Aerodynamics and Near Wake of an Offshore Floating Horizontal Axis Wind Turbine,” Ph.D. dissertation, University of Massachusetts Amherst, 2012.
- [98] F. Beyer, D. Matha, T. Sebastian, and M. Lackner, “Development, Validation and Application of a Curved Vortex Filament Model for Free Vortex Wake Analysis of Floating Offshore Wind Turbines,” in *Proceedings of the 50th AIAA Aerospace Sciences Meeting including the New Horizons Forum and Aerospace Exposition*. Nashville: American Institute of Aeronautics and Astronautics, 2012.
- [99] B. Luhmann and P. W. Cheng, “Relevance of aerodynamic modelling for load reduction control strategies of two-bladed wind turbines,” *Journal of Physics: Conference Series*, vol. 524, no. 1, 2014.
- [100] J. M. Jonkman, “Dynamics Modeling and Loads Analysis of an Offshore Floating Wind Turbine,” Ph.D. dissertation, National Renewable Energy Laboratory, Golden, 2007, NREL/TP-500-41958.
- [101] J. N. Newman, *Marine Hydrodynamics*. Cambridge: The MIT Press, 2017.

- [102] M. E. McCormick, *Ocean Engineering Mechanics*. Cambridge: Cambridge University Press, 2009.
- [103] J. Journée and W. Massie, *Offshore Hydromechanics*. Delft: Delft University of Technology, 2001.
- [104] S. Chakrabarti, *Handbook of Offshore Engineering*. Elsevier, 2005.
- [105] O. Faltinsen, *Sea Loads on Ships and Offshore Structures*. Cambridge University Press, 1990.
- [106] R. MacCamy and R. Fuchs, “Wave Forces on Piles: A Diffraction Theory,” Beach Erosion Board Corps of Engineers, Washington, D.C., Tech. rep., 1954.
- [107] E. E. Bachynski and H. Ormberg, “Hydrodynamic Modeling of Large-Diameter Bottom-Fixed Offshore Wind Turbines,” in *Proceedings of the ASME 2015 34th International Conference on Ocean, Offshore and Arctic Engineering*. St. John’s: American Society of Mechanical Engineers, 2015.
- [108] M. Leimeister and B. Dose, “Validation and Development of Improved Methods for the Calculation of Wave Loads on XXL Monopiles,” in *Proceedings of the ASME 2018 37th International Conference on Ocean, Offshore and Arctic Engineering*. Madrid: American Society of Mechanical Engineers, 2018.
- [109] R. G. Dean and R. A. Dalrymple, *Water Wave Mechanics for Engineers and Scientists*, ser. Advanced Series on Ocean Engineering. World Scientific, January 1991, vol. 2.
- [110] L. Guignier, A. Courbois, R. Mariani, and T. Choynet, “Multibody Modelling of Floating Offshore Wind Turbine Foundation for Global Loads Analysis,” in *Proceedings of the 26th International Ocean and Polar Engineering Conference*. Rhodes: International Society of Offshore and Polar Engineers, 2016.
- [111] C. H. Lee and J. N. Newman, “WAMIT User Manual Version 7.3,” WAMIT, Inc., Chestnut Hill, USA, Tech. rep., 2019.
- [112] C. H. Lee and J. N. Newman, “WAMIT User Manual Versions 6.4, 6.4S,” WAMIT, Inc., Chestnut Hill, USA, Tech. rep., 2014.
- [113] T. M. Duarte, A. J. Sarmiento, and J. M. Jonkman, “Effects of Second-Order Hydrodynamic Forces on Floating Offshore Wind Turbines,” in *Proceedings of the 32nd ASME Wind Energy Symposium*. National Harbor: American Institute of Aeronautics and Astronautics, 2014.
- [114] J. H. Ferziger, M. Perić, and R. L. Street, *Computational Methods for Fluid Dynamics*. Cham: Springer, 2020.
- [115] J. D. Anderson, *Computational fluid dynamics - the basics with applications*. New York: McGraw-Hill, Inc, 1995.
- [116] J. Boussinesq, *Essai sur la théorie des eaux courantes, Mémoires présentés par divers savants à l’Académie des sciences de l’Institut de France*. Paris, France: Imprimerie Nationale, 1877.



- [117] F. R. Menter, “Two-equation eddy-viscosity turbulence models for engineering applications,” *AIAA Journal*, vol. 32, no. 8, pp. 1598–1605, August 1994.
- [118] P. Weihing, K. Meister, C. Schulz, T. Lutz, and E. Krämer, “CFD Simulations on Interference Effects between Offshore Wind Turbines,” *Journal of Physics: Conference Series*, vol. 524, no. 1, p. 012143, June 2014.
- [119] C. Schulz, P. Letzgus, P. Weihing, T. Lutz, and E. Krämer, “Numerical simulation of the impact of atmospheric turbulence on a wind turbine in complex terrain,” *Journal of Physics: Conference Series*, vol. 1037, no. 7, p. 072016, June 2018.
- [120] K. Müller, D. Matha, S. Tiedemann, R. Proskovics, and F. Lemmer, “Deliverable D7.5 Guidance on platform and mooring line selection, installation and marine operations,” European Commission, LIFES50+ project, Tech. rep., 2016. URL [https://lifes50plus.eu/wp-content/uploads/2015/11/GA\\_640741\\_LIFES50\\_D7.5.pdf](https://lifes50plus.eu/wp-content/uploads/2015/11/GA_640741_LIFES50_D7.5.pdf)
- [121] DNV, *DNV-OS-E301: Position mooring*. Høvik: Det Norske Veritas, 2018, no. July.
- [122] ISO, *ISO 19901-7:2013-05, Petroleum and natural gas industries - Specific requirements for offshore structures - Part 7: Stationkeeping systems for floating offshore structures and mobile offshore units*. Geneva: International Organization for Standardization, 2013.
- [123] API, *API RP 2SK:2005-10, Design and Analysis of Stationkeeping Systems for Floating Structures*. Washington, D.C.: American Petroleum Institute, 2005.
- [124] K.-T. Ma, Y. Luo, T. Kwan, and Y. Wu, *Mooring System Engineering for Offshore Structures*. Cambridge: Elsevier, 2019.
- [125] M. Masciola, “MAP++ Documentation - Release v1.20.10,” National Renewable Energy Laboratory, Tech. rep., 2015. URL <https://map-plus-plus.readthedocs.io/>
- [126] M. Hall and A. Goupee, “Validation of a lumped-mass mooring line model with DeepCwind semisubmersible model test data,” *Ocean Engineering*, vol. 104, pp. 590–603, August 2015.
- [127] M. Hall, “MoorDyn - Lumped-Mass Mooring Dynamics,” National Renewable Energy Laboratory, Tech. rep., 2021. URL <https://moordyn.readthedocs.io/>
- [128] M. Masciola, J. Jonkman, and A. Robertson, “Extending the Capabilities of the Mooring Analysis Program: A Survey of Dynamic Mooring Line Theories for Integration Into FAST,” in *Proceedings of the ASME 2014 33rd International Conference on Ocean, Offshore and Arctic Engineering*. San Francisco: American Society of Mechanical Engineers, jun 2014.
- [129] J. Azcona, D. Palacio, X. Munduate, L. González, and T. A. Nygaard, “Impact of mooring lines dynamics on the fatigue and ultimate loads of three offshore floating wind turbines computed with IEC 61400-3 guideline,” *Wind Energy*, vol. 20, no. 5, pp. 797–813, May 2017.

- [130] M. Masciola, A. Robertson, J. Jonkman, A. Coulling, and A. Goupee, "Assessment of the importance of mooring dynamics on the global response of the DeepCwind floating semisubmersible offshore wind turbine," in *Proceedings of the 23rd International Offshore and Polar Engineering Conference*. Anchorage: International Society of Offshore and Polar Engineers, 2013.
- [131] W.-t. Hsu, K. P. Thiagarajan, M. MacNicoll, and R. Akers, "Prediction of Extreme Tensions in Mooring Lines of a Floating Offshore Wind Turbine in a 100-Year Storm," in *Proceedings of the ASME 2015 34th International Conference on Ocean, Offshore and Arctic Engineering*. St. John's: American Society of Mechanical Engineers, may 2015.
- [132] R. Gasch and J. Twele, *Windkraftanlagen*. Wiesbaden: Springer Vieweg, 2005.
- [133] E. Hau, *Windkraftanlagen*, 6th ed. Berlin, Heidelberg: Springer Vieweg, 2016.
- [134] IEC, *IEC 61400-12-1, Edition 2.0, 2017-03, Wind energy generation systems - Part 12-1: Power performance measurements of electricity producing wind turbines*. Geneva: International Electrotechnical Commission, 2017.
- [135] W. J. Pierson and L. Moskowitz, "A proposed spectral form for fully developed wind seas based on the similarity theory of S. A. Kitaigorodskii," *Journal of Geophysical Research*, vol. 69, no. 24, pp. 5181–5190, December 1964.
- [136] K. Hasselmann, T. Barnett, E. Bouws, H. Carlson, D. Cartwright, K. Enke, J. Ewing, H. Gienapp, D. Hasselmann, P. Kruseman, A. Meerburg, P. Müller, D. Olbers, K. Richter, W. Sell, and H. Walden, "Measurements of wind-wave growth and swell decay during the Joint North Sea Wave Project (JONSWAP)," *Ergänzungsheft zur Deutschen Hydrographischen Zeitschrift*, vol. A8, no. 12, 1973.
- [137] H. Bredmose, S. E. Larsen, D. Matha, A. Rettenmeier, E. Marino, and L. Sætran, "Deliverable D2.4 Collation of offshore wind-wave dynamics," European Commission, MARINET project, Tech. rep., 2012. URL [https://orbit.dtu.dk/files/60086212/Collation\\_of\\_offshore.pdf](https://orbit.dtu.dk/files/60086212/Collation_of_offshore.pdf)
- [138] ISO, *ISO 19901-1:2015-10, Petroleum and natural gas industries - Specific requirements for offshore structures - Part 1: Metocean design and operating considerations*. Geneva: International Organization for Standardization, 2015.
- [139] B. Méhauté, *An Introduction to Hydrodynamics and Water Waves*. Berlin, Heidelberg: Springer, 1976.
- [140] G. Airy, "On tides and waves," *Encyclopaedia Metropolitana*, vol. 5, pp. 241–396, 1845.
- [141] L. Skjelbreia and J. Hendrickson, "Fifth order gravity wave theory," in *Coastal Engineering Proceedings*, 1960, pp. 184–196.
- [142] J. D. Fenton, "A fifth-order Stokes theory for steady waves," *Journal of Waterway, Port, Coastal, and Ocean Engineering*, vol. 111, no. 2, pp. 216–234, March 1985.
- [143] J. D. Fenton, "A high-order cnoidal wave theory," *Journal of Fluid Mechanics*, vol. 94, no. 1, pp. 129–161, September 1979.

- [144] J. D. Fenton, "Nonlinear Wave Theories," in *The Sea, Volume 9: Ocean Engineering Science*, B. L. MéHauté and D. M. Hanes, Eds. New York: Wiley, 1990, pp. 3–25.
- [145] R. G. Dean, "Stream function representation of nonlinear ocean waves," *Journal of Geophysical Research*, vol. 70, no. 18, pp. 4561–4572, September 1965.
- [146] M. M. Rienecker and J. D. Fenton, "A Fourier approximation method for steady water waves," *Journal of Fluid Mechanics*, vol. 104, pp. 119–137, March 1981.
- [147] T. S. Hedges, "Regions of validity of analytical wave theories," *Proceedings of the Institution of Civil Engineers: Water, Maritime and Energy*, vol. 112, no. 2, pp. 111–114, 1995.
- [148] S. Haver, "Design of offshore structures: impact of the possible existence of freak waves," in *Proceedings of the 14th Aha Hulikoá Hawaiian Winter Workshop on Rogue Waves*, 2005, pp. 161–175.
- [149] P. S. Tromans, A. R. Anaturk, and P. Hagemeyer, "A new model for the kinematics of large ocean waves - application as a design wave," in *Proceedings of the 1st International Offshore and Polar Engineering Conference*. Edinburgh: International Society of Offshore and Polar Engineers, 1991.
- [150] D. Ning, J. Zang, S. Liu, R. Eatock Taylor, B. Teng, and P. Taylor, "Free-surface evolution and wave kinematics for nonlinear uni-directional focused wave groups," *Ocean Engineering*, vol. 36, no. 15-16, pp. 1226–1243, November 2009.
- [151] J. Westphalen, D. Greaves, C. Williams, A. Hunt-Raby, and J. Zang, "Focused waves and wave-structure interaction in a numerical wave tank," *Ocean Engineering*, vol. 45, pp. 9–21, May 2012.
- [152] E. Ransley, M. Hann, D. Greaves, A. Raby, and D. Simmonds, "Numerical and physical modeling of extreme waves at Wave Hub," *Journal of Coastal Research*, vol. 165, no. 65, pp. 1645–1650, January 2013.
- [153] V. Sriram, T. Schlurmann, and S. Schimmels, "Focused wave evolution using linear and second order wavemaker theory," *Applied Ocean Research*, vol. 53, pp. 279–296, 2015.
- [154] M. L. McAllister, T. A. Adcock, P. H. Taylor, and T. S. Van Den Bremer, "A Note on the Second-Order Contribution to Extreme Waves Generated during Hurricanes," *Journal of Offshore Mechanics and Arctic Engineering*, vol. 141, no. 4, pp. 1–7, 2019.
- [155] M. J. Cassidy, "Non-Linear Analysis of Jack-Up Structures Subjected to Random Waves," Ph.D. dissertation, University of Oxford, 1999.
- [156] S. S. Bennett, D. A. Hudson, and P. Temarel, "A comparison of abnormal wave generation techniques for experimental modelling of abnormal wave-vessel interactions," *Ocean Engineering*, vol. 51, no. September, pp. 34–48, 2012.
- [157] K. Hasselmann, "On the non-linear energy transfer in a gravity-wave spectrum Part 1. General theory," *Journal of Fluid Mechanics*, vol. 12, no. 04, p. 481, April 1962.

- [158] J. Sharma and R. Dean, “Second-Order Directional Seas and Associated Wave Forces,” *Society of Petroleum Engineers Journal*, vol. 21, no. 01, pp. 129–140, February 1981.
- [159] J. Dalzell, “A note on finite depth second-order wave-wave interactions,” *Applied Ocean Research*, vol. 21, no. 3, pp. 105–111, June 1999.
- [160] G. Z. Forristall, “Wave Crest Distributions: Observations and Second-Order Theory,” *Journal of Physical Oceanography*, vol. 30, no. 8, pp. 1931–1943, 2000.
- [161] V. Sriram, T. Schlurmann, and S. Schimmels, “Focused Wave Evolution in Intermediate Water Depth Using First and Second Order Wave Maker Theory,” in *Proceedings of the 23rd International Offshore and Polar Engineering Conference*. Anchorage: International Society of Offshore and Polar Engineers, 2013.
- [162] A. J. Goupee, B. J. Koo, R. W. Kimball, K. F. Lambrakos, and H. J. Dagher, “Experimental Comparison of Three Floating Wind Turbine Concepts,” *Journal of Offshore Mechanics and Arctic Engineering*, vol. 136, no. 2, May 2014.
- [163] A. N. Robertson, J. M. Jonkman, A. J. Goupee, A. J. Coulling, I. Prowell, J. Browning, M. D. Masciola, and P. Molta, “Summary of Conclusions and Recommendations Drawn From the DeepCwind Scaled Floating Offshore Wind System Test Campaign,” in *Proceedings of the ASME 2013 32nd International Conference on Ocean, Offshore and Arctic Engineering*. Nantes: American Society of Mechanical Engineers, 2013.
- [164] K. Muller, F. Sandner, H. Bredmose, J. Azcona, A. Manjock, and R. Pereira, “Improved tank test procedures for scaled floating offshore wind turbines,” in *Proceedings of the 1st International Wind Engineering Conference*, Hannover, 2014.
- [165] F. Borisade, C. Koch, F. Lemmer, P. W. Cheng, F. Campagnolo, and D. Matha, “Validation of INNWIND.EU Scaled Model Tests of a Semisubmersible Floating Wind Turbine,” *International Journal of Offshore and Polar Engineering*, vol. 28, no. 1, pp. 54–64, March 2018.
- [166] H. Bredmose, F. Lemmer, M. Borg, A. Pegalajar-Jurado, R. F. Mikkelsen, T. S. Larsen, T. Fjelstrup, W. Yu, A. K. Lomholt, L. Boehm, and J. A. Armendariz, “The Triple Spar campaign: Model tests of a 10MW floating wind turbine with waves, wind and pitch control,” *Energy Procedia*, vol. 137, pp. 58–76, 2017.
- [167] W. Yu, F. Lemmer, H. Bredmose, M. Borg, A. Pegalajar-Jurado, R. F. Mikkelsen, T. S. Larsen, T. Fjelstrup, A. K. Lomholt, L. Boehm, D. Schlipf, J. A. Armendariz, and P. W. Cheng, “The Triple Spar Campaign: Implementation and Test of a Blade Pitch Controller on a Scaled Floating Wind Turbine Model,” *Energy Procedia*, vol. 137, pp. 323–338, 2017.
- [168] I. Bayati, M. Belloli, L. Bernini, and A. Zasso, “Wind tunnel validation of AeroDyn within LIFES50+ project: Imposed Surge and Pitch tests,” *Journal of Physics: Conference Series*, vol. 753, no. 9, 2016.

- [169] M. Thys, V. Chabaud, T. Sauder, L. Eliassen, L. O. Sæther, and Ø. B. Magnussen, “Real-Time Hybrid Model Testing of a Semi-Submersible 10MW Floating Wind Turbine and Advances in the Test Method,” in *Proceedings of the ASME 2018 1st International Offshore Wind Technical Conference*. San Francisco: American Society of Mechanical Engineers, 2018.
- [170] M. Thys, “Deliverable D3.4 Ocean Basin Test Report,” European Commission, LIFES50+ project, Tech. rep., 2018.
- [171] M. I. Kvittem, P. A. Berthelsen, L. Eliassen, and M. Thys, “Calibration of Hydrodynamic Coefficients for a Semi-Submersible 10 MW Wind Turbine,” in *Proceedings of the ASME 2018 37th International Conference on Ocean, Offshore and Arctic Engineering*. Madrid: American Society of Mechanical Engineers, 2018.
- [172] H. Schlichting and K. Gersten, *Grenzschicht-Theorie*, 10th ed. Berlin, Heidelberg: Springer, 2006.
- [173] Ansys, “ANSYS 16.2 Theory Manual,” Canonsburg, 2015.
- [174] F. Beyer, B. Luhmann, S. Raach, and P. W. Cheng, “Shadow Effects in an Offshore Wind Farm - Potential of Vortex Methods for Wake Modelling,” in *Proceedings of the 12th German Wind Energy Conference DEWEK*, Bremen, 2015.
- [175] B. Luhmann, F. Beyer, and P. W. Cheng, “Coupled Aero-Elastic Multi-Body Simulation of Two-Bladed Wind Turbines in Wind Farm Arrays,” in *Proceedings of the 34th Wind Energy Symposium*. San Diego: American Institute of Aeronautics and Astronautics, jan 2016.
- [176] M. Arnold, M. Kretschmer, J. Koch, P. W. Cheng, and F. Biskup, “A Validation Method for Fluid-Structure Interaction Simulations Based on Submerged Free Decay Experiments,” *Journal of Ocean and Wind Energy*, vol. 2, no. 4, pp. 202–212, 2015.
- [177] C. Förster, W. Wall, and E. Ramm, “The artificial added mass effect in sequential staggered fluid-structure interaction algorithms,” in *ECCOMAS CFD 2006: Proceedings of the European Conference on Computational Fluid Dynamics*, Egmond aan Zee, 2006.
- [178] M. Schildhauer, “Simulation von Fluid-Struktur-Interaktion mit ANSYS CFX,” Master’s thesis, Hochschule für Technik, Wirtschaft und Kultur Leipzig, 2011.
- [179] D. Uhlmann, “Numerische Simulation von irregulärem Seegang,” Master’s thesis, HAW Hamburg, 2012.
- [180] H. P. Piehl, “Ship Roll Damping Analysis,” Ph.D. dissertation, University of Duisburg-Essen, 2016.
- [181] B. Molin, “On the piston and sloshing modes in moonpools,” *Journal of Fluid Mechanics*, vol. 430, pp. 27–50, 2001.
- [182] G. Gaillardie and A. Cotteleer, “Water motion in moonpools empirical and theoretical approach,” Maritime Research Institute Netherlands, Tech. rep., 2005.

- 
- [183] DNV, *DNV-RP-N103: Modelling and analysis of marine operations*. Høvik: Det Norske Veritas, 2019, no. December.
- [184] P. Bortolotti, C. L. Bottasso, and A. Croce, “Combined preliminary-detailed design of wind turbines,” *Wind Energy Science*, vol. 1, no. 1, pp. 71–88, 2016.
- [185] P. Bortolotti, H. Canet Tarrés, K. Dykes, K. Merz, L. Sethuraman, D. Verelst, and F. Zahle, “IEA Wind TCP Task 37: Systems Engineering in Wind Energy - WP2.1 Reference Wind Turbines,” National Renewable Energy Laboratory, Tech. rep. NREL/TP-5000-73492, 2019.
- [186] W. A. Timmer and R. P. J. O. M. van Rooij, “Summary of the Delft University Wind Turbine Dedicated Airfoils,” *Journal of Solar Energy Engineering*, vol. 125, no. 4, pp. 488–496, November 2003.
- [187] A. Krieger, G. K. V. Ramachandran, L. Vita, P. G. Alonso, G. G. Almería, J. Berque, and G. Aguirre, “Deliverable D7.2 Design Basis,” European Commission, LIFES50+ project, Tech. rep., 2015. URL [https://lifes50plus.eu/wp-content/uploads/2015/11/D72\\_Design\\_Basis\\_Retyped-v1.1.pdf](https://lifes50plus.eu/wp-content/uploads/2015/11/D72_Design_Basis_Retyped-v1.1.pdf)
- [188] G. Ramachandran, L. Vita, A. Krieger, and K. Mueller, “Design Basis for the Feasibility Evaluation of Four Different Floater Designs,” *Energy Procedia*, vol. 137, pp. 186–195, 2017.
- [189] J. Wigaard, “Floating substations - what’s needed?” in *WindEurope Offshore 2019, NORWEP Seminar*, Copenhagen, 2019.
- [190] C.-D. Munz and T. Westermann, *Numerische Behandlung gewöhnlicher und partieller Differenzialgleichungen*, 4th ed. Berlin, Heidelberg: Springer Vieweg, 2019.
- [191] F. Beyer, “Curved Vortex Filaments in Free Vortex Wake Analysis of Floating Wind Turbines,” Master’s thesis, Universität Stuttgart, 2011.

# Curriculum Vitae

Friedemann Borisade (né Beyer) was born in 1985 in Stendal, Germany.

He received his Diplom-Ingenieur's degree (Dipl.-Ing.) in aerospace engineering in 2011 from the University of Stuttgart with specialisations in fluid dynamics and wind energy. Friedemann was awarded scholarships from the Konrad Adenauer Foundation (KAS) and German Academic Exchange Service (DAAD) for an internship in the field of infrared astronomy at the SOFIA Science Center, NASA Ames Research Center, Moffett Field, CA, USA in 2007. He spent one semester as research scholar studying floating wind aerodynamics at the University of Massachusetts Amherst, MA, USA, in 2011. After his return to Stuttgart he graduated with the thesis entitled "Curved Vortex Filaments in Free Vortex Wake Analysis of Floating Wind Turbines".

Friedemann continued as researcher at the University of Stuttgart and joined Stuttgart Wind Energy (SWE) at the Institute of Aircraft Design in November 2011. He specialised in system simulation applying multifidelity and multiphysics methods. Through his involvement in international demonstration and research projects on floating wind, such as European R&D projects FLOATGEN, INNWIND.EU, LIFES50+, COREWIND and the international simulation code comparison projects OC4 to OC6, he gained extensive experience in the fields of integrated loads analysis and dynamic simulation of floating offshore wind turbines. Friedemann supervised several Bachelor's and Master's theses, was engaged in teaching activities in the wind energy program at the University of Stuttgart and presented his research at several international conferences. During his work at SWE he led the research group "Conceptual Design and System Simulation".

In December 2018, Friedemann joined the engineering consultancy company Ramboll in Hamburg, Germany, where he is engaged in commercial consultancy projects on floating wind and in research and innovation projects, such as the European R&D project COREWIND.